Universität Hamburg
DER FORSCHUNG | DER LEHRE | DER BILDUNG

FAKULTÄT
FÜR MATHEMATIK, INFORMATIK
UND NATURWISSENSCHAFTEN

Processes of long-term crater modification inferred from scaled analogue experiments

- Dissertation -

with the aim of achieving the doctoral degree

Dr. Rer. Nat.

at the Faculty of Mathematics, Informatics and Natural Sciences

Department of Earth Sciences

at Universität Hamburg

Submitted by Jan Oliver Eisermann

from Hamburg, Germany

Hamburg, 2024

Accepted as Dissertation at the Department of Earth Sciences

Reviewers:	Prof. Dr. Ulrich Riller
	Dr. Matthias Rosenau
members of the examination commission:	Prof. Dr. Ulrich Riller (chair)
	Dr. Matthias Rosenau
	Prof. Dr. Christian Betzler (co-chair)
	Dr. Sebastian Lindhorst
	Prof. Dr. Christian Hübscher
Chair of the Subject Doctoral Committee:	Prof. Dr. Hermann Held
Dean of Faculty of MIN:	Prof. Dr.-Ing. Norbert Ritter
Date of Submission:	28.01.2024
Date of defense:	19.08.2024

„Und wenn ich geh, dann so, wie ich gekommen bin
Wie ein Komet, der zweimal einschlägt
Vielleicht tut es weh, doch will auf Nummer sicher geh'n
Dass ich für immer leb, lass uns nochmal aufdreh'n

Ich will ein'n Fußabdruck von mir, stärker als die Zeit
Und ich sage dir: "Kein anderer Fuß passt da noch rein“

Komet – Apache 207 & Udo Lindenberg

I dedicate this thesis to my proud parents Horst + Sabine Eisermann. I am forever grateful for their support which led me to where I am today. I also dedicate this work to my dearly beloved friend/teacher/mentor, Heidemarie "Angy" Thalmann, who did not live to see its completion. She unlocked my passion for science during our rebellious Jugend forscht adventure in 2012, which ultimately laid the foundation for this work. She taught me to be curious, to follow my intuition and not to be afraid to ask questions. In difficult times, she guided me back to the right path by seeing the bigger picture. She was as proud as anyone could be. Her legacy will live on. In the quiet recesses of our hearts, a deep sense of loss casts its shadow. The gentle echo of her presence lingers, a shimmering reminder of the beautiful soul we were fortunate to have known. May she rest in peace and may her memory be a blessing.

Abstract

Although the mechanisms of large-impact cratering have been extensively studied, the structural effects of long-term crater modification, operating for tens of thousands of years after impact, are poorly understood. Localised deformation in the form of crater floor fractures (CFFs) are known from large craters across celestial bodies. On Earth, CFFs in large craters are radial and concentric and filled with impact melt. Similarly, fractured crater floors are prominent post-cratering structural vestiges of lunar impact craters. Two mechanisms have been proposed to explain the formation of CFFs: emplacement of horizontal igneous intrusion, and long-term isostatic re-equilibration of target rocks beneath crater floors.

Using scaled analogue experiments, I systematically investigated the structural consequences of both mechanisms on long-term crater floor deformation. Craters with specified morphologies, depths and radii were excavated into the material using a novel rotating blade. Analogue modelling observes the deformation of granular and viscous materials, acting as rock analogues, on a laboratory scale. In order to apply appropriate scaling, it is necessary to know the properties of the materials used. I present the characteristics of 22 granular and 4 viscous materials used at the UHH-Tec laboratory. These include the mechanical properties of a novel flour-sand mixture developed to model crater modification processes. In addition, I provide measurements of the relative permittivity values of common analogue materials. The experimental surfaces were monitored using 3D digital image correlation, which allowed me to quantify key structural parameters such as the distribution and evolution of surface fractures. This provides, for the first time, a quantitative relationship between diameter, depth and fracture geometry of crater floors. I used granular materials simulating the brittle upper crust of the Moon to investigate the structural consequences of sill formation below crater floors. Sills were simulated by flat, circular balloons emplaced in the granular material at varying depths below model craters. For each experiment, the model sill was inflated and then deflated to simulate intrusion and evacuation of magma.

My experiments showed that fracture patterns were controlled more by the depth of the flat balloons below the surface than by the morphology of the crater floor. The model

craters are characterised by radial and polygonal fracture patterns. In nature, these fracture patterns may allow magma to erupt immediately from sill reservoirs. I conclude that natural lunar sill systems are unlikely to reach the structural maturity previously proposed.

The deformation behaviour of the upper crust, scaled to Earth, following crater formation was modelled using a two-layer modelling setup to investigate the structural and kinematic consequences of crustal relaxation. The structural evolution was systematically analysed for different initial crater floor depths and diameters. The uplift of the crater floor is achieved by long wavelength subsidence of the crater periphery and can operate on time scales of thousands of years in nature. I conclude that the observed patterns of floor fractures, including impact melt dykes, may be caused by long-term crater floor uplift compensated by lateral crustal flow towards the crater centre.

Zusammenfassung

Obwohl die Mechanismen der Kraterbildung in großen Einschlagskratern gut erforscht sind, sind die strukturellen Auswirkungen langfristiger Kraterveränderungen, die über Zehntausende von Jahren nach dem Einschlag wirken, kaum bekannt. Lokale Deformationen in Form von Kraterbodenbrüchen (CFFs) sind von großen Kratern auf anderen Himmelskörpern bekannt. Auf der Erde sind CFFs in großen Kratern radial und konzentrisch und mit Einschlagschmelze gefüllt. In ähnlicher Weise sind zerklüftete Kraterböden auffällige strukturelle Überreste in Mondkratern nach der Kraterbildung. Zwei Mechanismen wurden vorgeschlagen, um die Bildung von CFFs zu erklären: die Einlagerung von horizontalen magmatischen Intrusionen und die langfristige isostatische Anpassung des Gesteins unter den Kraterböden.

Mit Hilfe von skalierten Analogexperimenten habe ich systematisch die strukturellen Auswirkungen beider Mechanismen auf die langfristige Deformation des Kraterbodens untersucht. Krater mit definierter Morphologie, Tiefe und Radius wurden mit einer neuartigen rotierenden Klinge in das Material gegraben. Die Analogmodellierung beobachtet die Verformung von granularen und viskosen Materialien, die als Gesteinsanaloga dienen, im Labormaßstab. Um eine geeignete Skalierung anwenden zu können, muss man die Eigenschaften der verwendeten Materialien kennen. Ich stelle die Eigenschaften von 22 granularen und 4 viskosen Materialien vor, die im UHH-Tec Labor verwendet werden. Dazu gehören auch die mechanischen Eigenschaften einer neuartigen Mehl-Sand-Mischung, die zur Modellierung von Kratermodifikationsprozessen entwickelt wurde. Darüber hinaus werden Messungen der relativen Dielektrizitätskonstanten gängiger analoger Materialien vorgestellt. Die experimentellen Oberflächen wurden mit Hilfe der digitalen 3D-Bildkorrelation überwacht, die es mir ermöglichte, wichtige strukturelle Parameter wie die Verteilung und Entwicklung von Oberflächenbrüchen zu quantifizieren. Dies liefert zum ersten Mal eine quantitative Beziehung zwischen Durchmesser, Tiefe und Bruchgeometrie von Kraterböden.

Ich habe granulare Materialien verwendet, die die spröde obere Kruste des Mondes simulieren, um die strukturellen Konsequenzen der Sillbildung unter Kraterböden zu

untersuchen. Die Sills wurden durch flache, kreisförmige Ballons simuliert, die in verschiedenen Tiefen unter den Modellkratern in das Granularmaterial eingebracht wurden. Bei jedem Experiment wurde der Modell-Sill aufgeblasen und wieder entleert, um das Einströmen und Austreten von Magma zu simulieren. Meine Experimente zeigten, dass die Bruchmuster eher durch die Tiefe der flachen Ballons unter der Oberfläche als durch die Morphologie des Kraterbodens bestimmt wurden. Die Modellkrater zeichnen sich durch radiale und polygonale Bruchmuster aus. In der Natur könnten diese Bruchmuster den sofortigen Ausbruch von Magma aus Sill-Reservoirs ermöglichen. Ich komme zu dem Schluss, dass es unwahrscheinlich ist, dass natürliche Sill-Systeme auf dem Mond die zuvor vorgeschlagene strukturelle Reife erreichen.

Das Deformationsverhalten der oberen Kruste nach der Kraterbildung wurde mit Hilfe eines Zweischichtenmodells modelliert, um die strukturellen und kinematischen Konsequenzen der Krustenrelaxation zu untersuchen. Die strukturelle Entwicklung wurde systematisch für verschiedene anfängliche Kraterbodentiefen und -durchmesser analysiert. Die Hebung des Kraterbodens wird durch eine langwellige Absenkung des Kraterrandes erreicht und kann in der Natur auf Zeitskalen von Jahrtausenden wirksam werden. Ich komme zu dem Schluss, dass die beobachteten Bruchmuster im Kraterboden, einschließlich der Einschlagsschmelzen, durch eine langfristige Anhebung des Kraterbodens verursacht werden können, die durch einen lateralen Krustenfluss in Richtung des Kraterzentrums kompensiert wird.

Table of Contents

Abstract ..... **iii**

Zusammenfassung ..... **v**

Table of Contents ..... **vii**

List of derived publications: ..... **xi**

1. Introduction **1**

1.1 Cratering 1

1.2 Floor-fractured craters 1

1.3 Crater Modification 3

1.4 Analogue modelling 4

1.5 Objectives of the thesis 5

2. Catalogue of granular and viscous materials and their physical properties used for quantitative analogue modelling of geological processes at the UHH-Tec laboratory, Universität Hamburg, Germany **7**

2.1. Introduction 8

2.2. Methods 10

2.2.1 Density 10

2.2.2 Angle of internal friction 10

2.2.3 Grain size distribution 11

2.2.4 Relative permittivity 12

2.2.5 Rings shear test data 13

2.2.7 Macro photography 14

2.3. Coloured quartz sands 14

2.4. Data records 16

2.4.1 Quartz sands 17

2.4.1.1 Quartz sand G12T 17

2.4.1.2 Quartz sand G23T 19

2.4.1.3 Quartz sand G23T coloured 21

2.4.2 Heavy minerals 23
2.4.2.1 Corundum sand 23
2.4.2.2 Iron powder 25
2.4.3 Technical minerals 26
2.4.3.1 Glass spheres fine 26
2.4.3.2 Glass spheres coarse 28
2.4.3.3 Expanded glass 29
2.4.4 Organic materials 31
2.4.4.1 Flour 31
2.4.4.2 Starch 33
2.4.5 Elastic granulate 34
2.4.5.1 Rubber black 34
2.4.5.2 Rubber green 36
2.4.5.3 Rubber blue 37
2.4.6 Soluble granulate 38
2.4.6.1 Salt grit 38
2.4.6.2 Table salt 40
2.4.7 Mixtures 40
2.4.7.1 G23T DIC 41
2.4.7.2 G12T Elastic 42
2.4.7.3 Flour 2:1 44
2.4.7.4 Flour 1:1 46
2.4.8 Viscous materials 47
2.4.8.1 Water 48
2.4.8.2 PDMS 48
2.4.8.3 PDMS + corundum 48
2.4.8.4 Laponite 49
2.5. Discussion 50
2.5.1 Ring shear data 50
2.5.3 Material relative permittivity 53
2.5.4 Grain size distribution 55
2.6. Conclusion 55
2.6.1. Disclosure of competing interests 56
3. Structural consequences of sill formation below lunar craters inferred from scaled analogue experiments 57

3.1. Introduction 58
3.1.1 Lunar examples 60
3.2. Experimental setup 63
3.2.1 Sill formation 63
3.2.2 Setup process 64
3.2.3 Crater generation 65
3.2.4 Experimental sets 66
3.2.5 Digital Image Correlation 66
3.3. Scaling 67
3.4. Model limitations 69
3.5. Results 70
3.5.1 Set 1: Balloon and crater at equal diameter 70
3.5.2 Set 2: Balloon larger than crater 70
3.5.3 Set 3: Balloon offset from crater 73
3.5.4 Set 4: Balloon without crater 75
3.5.5 Crater floor uplift 75
3.6. Discussion 77
3.6.1 Fractures 79
3.6.2 Influence of crater morphology 81
3.6.3 Terraced crater walls 82
3.6.4 Magmatic system 83
3.6.5 Sill emplacement model 85
3.7 Conclusions 86
4. Long-term Isostatic Relaxation of Large Terrestrial Impact Structures: Structural Characteristics Inferred from Scaled Analogue Experiments 87
4.1. Introduction 88
4.2. Experimental setup 91
4.3. Scaling 94
4.4. Results 95
4.4.1 Vertical surface displacements 95
4.4.2 Horizontal surface displacements 98

4.4.3 Fracture patterns 98
4.5. Discussion 101
4.5.1 Buoyancy and material strength in experiments 101
4.5.2 Kinematics of crustal relaxation 103
4.5.3 CCFs in nature and experiment 104
4.5.4 Model limitations 105
4.6. Conclusions 106
5. Conclusion 107
5.1 Outlook 110
6. Acknowledgments 112
7. References 113
8.1. Supplement to chapter 2 122
8.2. Supplement to chapter 3 123
8.3. Supplement to chapter 4 133
Versicherung an Eides statt 140

List of derived publications:

Eisermann, J. O.; Lindhorst, S.; Kanzler, L.; Riller, U.: Catalogue of granular and viscous materials and their physical properties used for quantitative analogue modelling of geological processes at the UHH-Tec laboratory, Universität Hamburg, Germany. (In preparation for submission to Data in Brief)

Eisermann, J. O.; Riller, U.: Ring shear test data of flour sand mixtures – low density quartz sand flour mixture for analog modelling crater modification processes. (In preparation for submission to GFZ Data Services)

Eisermann, J. O.; Riller, U.: Structural consequences of sill formation below lunar craters inferred from scaled analogue experiments. (In preparation for submission to JGR Planets)

Eisermann, J. O.; Riller, U.: Experimental data on structural consequences of sill formation below lunar craters inferred from scaled analogue experiments. (In preparation for submission to GFZ Data Services)

Eisermann, J. O.; Riller, U.: Long-term Isostatic Relaxation of Large Terrestrial Impact Structures: Structural Characteristics Inferred from Scaled Analogue Experiments. (In review at JGR Planets)

Eisermann, J. O.; Riller, U.: Experimental data on long-term Isostatic Relaxation of Large Terrestrial Impact Structures: Structural Characteristics Inferred from Scaled Analogue Experiments at the UHH-Tec Modelling Lab of the Universität Hamburg. GFZ Data Services (2023). https://doi.org/10.5880/fidgeo.2023.036

Additional publications during the PhD period:

Reolid, J.; Bialik, O. M.; Lindhorst, S.; **Eisermann, J. O.**; Petrovic, A.; Hincke, C.; Beaman, R. J.; Webster, J. M.; Betzler, C.: A new type of Halimeda bioherm on the Queensland Plateau, NE Australia. (Submitted to Coral Reefs)

Eisermann, J. O.; Göllner, P. L.; Riller, U.: Orogen-scale transpression accounts for GPS velocities and kinematic partitioning in the Southern Andes. Nature Communications Earth & Environment 2.1 (2021). https://doi.org/10.1038/s43247-021-00241-4

Eisermann, J. O.; Göllner, P. L.; Riller, U.: Experimental data on scaled analogue experiments modelling GPS velocity field variations and kinematic partitioning in the Southern Andes (34°S to 42°S). GFZ Data Services (2021). https://doi.org/10.5880/fidgeo.2021.023

Göllner, P. L.; **Eisermann, J. O.**; Balbis, C.; Petrinovic, I. A.; Riller, U.: Kinematic partitioning in the Southern Andes (39° S–46° S) inferred from lineament analysis and reassessment of exhumation rates. International Journal of Earth Sciences 110.7 (2021): 2385-2398. https://doi.org/10.1007/s00531-021-02068-y

Betzler, C.; Lindhorst, S.; Lüdmann, T.; Reijmer, J. J.; Braga, J. C.; Bialik, O. M.; Reolid, J.; **Eisermann, J. O.**; Emais, K.; Rixen T.; Bissessur, D.: Current and sea level control the demise of shallow carbonate production on a tropical bank (Saya de Malha Bank, Indian Ocean). Geology 49.12 (2021): 1431-1435. https://doi.org/10.1130/G49090.1

Hernando, I. R.; Bucher, J.; del Papa, C. E.; **Eisermann, J. O.**; Göllner, P. L.; Guzmán, S. R.; Balbis, C.; Petrinovic, I. A.: Unraveling the timing of the Caviahue depression, Andean Southern Volcanic Zone: insights from the sedimentary infill. International Journal of Earth Sciences 110.7 (2021): 2541-2558. https://doi.org/10.1007/s00531-020-01936-3

Reports (non peer-reviewed):

Betzler, C.; Artschwager, M.; Becking, J.; Bialik, O. M.; Eggers, D.; **Eisermann, J. O.;** Falkenberg, P.; Häcker, T.; Hübscher, C.; Hincke, C.; Lahajnar, N.; Lindhorst, S.; Lüdmann, T.; Maak, J. M.; Maul, J.; Petrovic, A.; Reolid, J.; Saitz, Y.; Schmidt, M. C.; et al.: . Towards an understanding of carbonate platforms in the icehouse world, Cruise No. SO292, 15.05.2022 – 21.06.2022, Nouméa (New Caledonia) - Nouméa (New Caledonia). In SONNE-Berichte (SO292, pp. 1-58). Begutachtungspanel Forschungsschiffe. (2022) https://doi.org/10.48433/cr_so292

Lindhorst, S.; Appoo, J.; Artschwager, M.; Bialik, O.; Birkicht, M.; Bissessur, D.; Braga, J.-C.; Budke, L.; Bunzel, D.; Coopen, P.; Eberhardt, B.; Eggers, D.; **Eisermann, J. O.;** El Gareb, F.; Emeis, K.; Geßner, A.-L.; Hüge, F.; Knaack-Völker, H.; Kornrumpf, N.; et al.: . Saya de Malha Carbonates, Oceanography and Biogeochemistry (Western Indian Ocean), Cruise No. SO270, 2019-09-06 – 2019-10-23, Hong Kong (China) - Port Louis (Mauritius). In SONNE-Berichte (SO270, pp. 1-102). Gutachterpanel Forschungsschiffe. (2019) https://doi.org/10.2312/cr_so270

1. Introduction

1.1 Cratering

The collision of solid matter has affected every planetary body, regardless of size. The result of such collisions leaves morphological features in the form of impact craters. Hypervelocity impact cratering is recognised as one of the most fundamental geological processes in the Solar System (Melosh, 1989). In particular, knowledge of large impact crater formation has gained significant importance in the geosciences for understanding punctuated geological events associated with drastic changes in climate (Artemieva et al., 2017; Gulick et al., 2019), post-impact hydrothermal circulation associated with possible niches for early life (Goderis et al., 2021; Kring & Bach, 2021; Lowery et al., 2021), and the generation of giant mineral deposits (Lightfoot, 2006; Lightfoot, 2017). The formation of large impact craters is typically considered to be a matter of minutes (Melosh, 1989). Accordingly, numerical models of large impact craters are generally tailored to elucidate cratering mechanisms on this time scale (Melosh & Ivanov, 1999; Ivanov, 2005; Wünnemann et al., 2008; Collins et al., 2012; Morgan et al., 2016).

1.2 Floor-fractured craters

Crater morphology is best preserved on rocky celestial bodies, where atmospheric and endogenous processes are largely absent. The Moon and planets such as Venus and Mercury serve as analogues to the Earth in the study of impact crater morphology. Studies of lunar craters during the era of the Apollo programme led to the first description of then unexpected morphological features. A collection of more than 170 lunar impact craters characterised by anomalously flat and shallow floors cut by fractures are known as Floor-Fractured Craters (FFCs) (Melosh, 1976; Schultz, 1976; Hall et al., 1981; Jozwiak et al., 2012). Lunar FFCs range from about 10 km to 300 km in diameter, and therefore predominantly have complex crater morphologies with central peaks and terraced crater walls (Jozwiak et al., 2012; Jozwiak et al., 2015). FFCs are also spatially associated with lunar mare regions.

A characteristic morphological feature within FFCs are radially, concentric or polygonal oriented Crater Floor Fractures (CFFs), which can be tens of kilometres long (Fig. 1.1a; Jozwiak et al., 2012). Other features observed in FFCs include moats, ridges and rootless patches or fills of mare material. First observed on the Moon, FFCs are now also known from Mars and Mercury. For example, the Caloris Basin on Mercury, with a

diameter of more than 1000 km, is characterised by a distinct radial pattern of CFFs and grabens in its centre (Watters et al., 2005; Murchie et al., 2008; Freed et al., 2009; Mohit et al., 2009; Watters et al., 2009; Klimczak et al., 2010; Watters et al., 2012; Klimczak et al., 2013). Martian FFCs are less pronounced due to the planet's atmospheric processes (Schultz & Orphal, 1978; Mohit & Phillips, 2007; Mohit et al., 2009).

On Earth, evidence of FFCs is less obvious because large impact structures are partially eroded, covered by sedimentary rocks or deformed (Grieve & Therriault, 2000; Grieve et al., 2008). Two impact structures, Sudbury (Canada) and Vredefort (South Africa), are known to host impact melt filled fractures (Wichman & Schultz, 1993). At Sudbury (Fig. 1.1b), the fractures are known as Offset Dykes because of the tectonic segmentation that has taken place since their emplacement (Grant et al., 1984). The dykes are arranged concentrically and radially around the remnant of the deformed impact melt sheet (Fig. 1.1b; Grieve, 1991; Riller, 2005) to which some of the radial ones are connected (Hecht et al., 2008; Pilles et al., 2018). Similar to Sudbury, the Vredefort impact structure hosts impact melt dykes known as Granophyre dykes (Reimold & Gibson, 2006). These dykes are interpreted to be derived from the overlying, now eroded, impact melt rock sheet (Lieger & Riller, 2012; Huber et al., 2020, 2022). The formation of these dykes was originally attributed to the cratering process (Riller, 2005). More recently, however, the dykes have been interpreted as the equivalent of lunar crater floor fractures (Wichman & Schultz, 1993; Riller, 2005; Hecht et al., 2008).

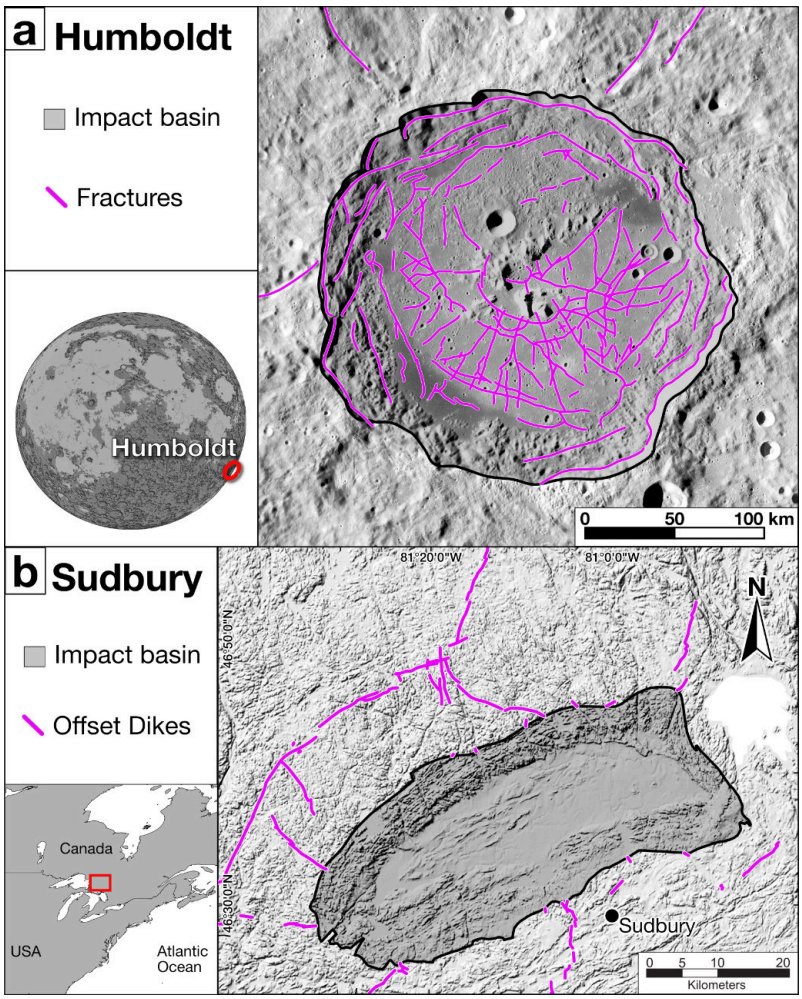

Figure 1.1: Examples of large floor-fractured craters on Earth and the Moon with radial and concentric fractures, shown in purple. (a) Floor-fractured lunar crater Humboldt with flat and mare covered floor (NASA LROC-WAC image data). (b) Sudbury impact structure, Canada. Geometry of offset dykes based on Pilles et al. (2018).

1.3 Crater Modification

CFFs and other characteristic of FFCs are generally considered to be prominent post-cratering structures. Despite the importance of understanding deformation processes resulting from impact cratering itself, long-term processes are generally understudied (Kenkmann et al., 2014). Modification of craters is assumed to occur on timescales of tens to possibly millions of years after impact, but operating times are not well understood. An ongoing debate in the scientific community concerns the mechanism of long-term crater modification. Two conceptual models for the formation of FFCs have been proposed: emplacement of horizontal igneous sheets beneath the crater floor (Fig. 1.2a; Schultz, 1976; Jozwiak et al., 2012) and isostatic re-equilibration of crust underlying the crater floor (Fig. 1.2b; Hall et al., 1981; Riller, 2005; Hecht et al., 2008).

The 'igneous intrusion model' postulates the emplacement of a horizontal intrusion beneath the crater, which lifts the crater floor as it inflates (Jozwiak et al., 2015). The sudden mass removal during cratering causes local crustal unloading apparently generating melt at depth (Michaut et al., 2020). The melt travels upward in dykes before transitioning to a horizontal intrusion at a relatively shallow depth below the crater (Fig. 1.2a; Michaut et al., 2020; Walwer et al., 2021). The dike then expands laterally, forming a sill that may not extend beyond the diameter of the crater (Jozwiak et al., 2015).

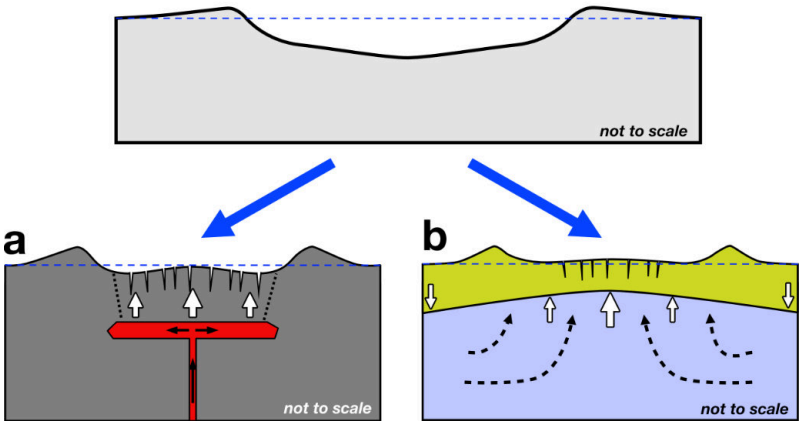

Figure 1.2: Schematic overview of the main conceptual models for the formation of FFCs. (a) Sketch outlining the emplacement of horizontal igneous sheets uplifting the crater floor. (b) Sketch outlining the isostatic relaxation of the crust beneath meteorite impact craters.

Isostatic re-equilibration of the crust beneath large craters is attributed to the mass deficit caused by the ballistic ejection of target rock during cratering, resulting in buoyancy-driven uplift of the crater floor (Fig. 1.2b; Hall et al., 1981; Riller, 2005; Hecht et al., 2008). This process requires a viscously deforming lithosphere. Upward bending of the crater floor is thought to be compensated for by subsidence of the crater rim and its periphery (Hall et al., 1981). Both mechanisms are thought to be independently capable of uplifting the crater floor, resulting in radial stretching of the crater floor accomplished by extensional fractures.

To date, long-term crater modification has mainly been studied numerically using topography and gravity data. The numerical studies have focused on the influence of crustal rigidity and thickness. Studies have been limited by considering only 2D systems or low-resolution numerical modelling (Wichman & Schultz, 1993; Jozwiak et al., 2012; Thorey & Michaut, 2014; Michaut et al., 2020). However, the structural consequences of both proposed mechanisms on surface uplift and deformation in combination with crater morphology have not been systematically analysed in 3D space and time.

1.4 Analogue modelling

The study of crater dynamics is challenged by the timescales involved. On geological timescales, impact craters form instantaneously (Collins et al., 2012). To study the processes involved, we need to change our timescale from seconds to minutes. As the speed of the processes involved in impact cratering diminishes exponentially, subsequent processes become seemingly imperceptibly slow, as we now have to consider changes over thousands of years (Collins et al., 2002). In the past, this shift in timescale led to the assumption that impact cratering was practically finished after a few minutes, as such numerical models could not account for much longer timescales and observed only small changes.

Laboratory experiments, which take place under the influence of all laws of physics, allow us to gain a detailed insight into the evolution of crater floor deformation. Experiments by design take into account detailed multi-scale processes, complex material properties, complex experimental geometries, randomisation and natural inhomogeneities that exceed the capabilities of numerical models. However, experiments must be performed with high precision. By now, analogue modelling has been a fundamental tool in exploring geological processes for over a century (Ranalli, 2001). It is used to study scaled-down geodynamic processes and hypotheses on a laboratory scale. Analogue modelling observes the deformation of granular and viscous materials, acting as rock analogues, within a finite domain of known boundary conditions. The first experiments date back to 1815 (Hall, 1815). Despite the time elapsed since its first application, the method is still relevant today (Zwaan et al., 2022). The method has improved greatly over time from a qualitative to a highly quantitative approach. Laboratory experiments are scaled to the physical properties of natural prototypes (Ranalli, 2001). Scaling is based on the theory of similarity, which ensures comparability with nature (Hubbert, 1937). Two physical systems of different sizes are governed by the same processes if all the corresponding lengths are proportional. To obtain accurate quantitative results and proper scaling, it is necessary to know the properties of the materials used in the experiment (Hubbert, 1937). While most raw material properties are provided by the manufacturer, they are often not accurate enough for scientific use. It is, therefore, important to know the material properties to ensure accuracy and comparability between laboratories. I used a special 2:1 flour-sand mixture tailored for modelling crater modification and quantified its mechanical properties.I

facilitate state of the art optical recording of experiments. Imaging and processing of the recorded surface allows me the calculation of displacement vectors and scalar derivatives of the vector field at sub-millimetre scales. Digital Image Correlation (DIC) allows me to get a quantitative sense of surface processes, both in time and in 3D space (Adam et al., 2005; Stamhuis & Thielicke, 2014; Boutelier, 2016).

The precise creation of realistic model craters in granular material is critical for FFC case studies. The model craters were created using a curved plastic blade with a base in the shape of the inverse radial crater profile. The final concave shape of the craters was constructed based on the scaled depth and diameter of a fresh crater. The curved blade was fabricated using a 3D printer and mounted on an axis for rotation. A gantry kept the plastic blade horizontal. As it rotated, the plastic blade was gently lowered into the upper part of the granular material, excavating a specific crater profile. During excavation, the ejected material was evenly distributed, similar to the distribution of natural ejecta deposits.

1.5 Objectives of the thesis

I employed novel analogue modelling techniques to quantitatively assess the mechanism of long-term crater modification. I performed scaled analogue experiments to study the surface deformation induced by the emplacement of a crustal intrusion beneath an impact crater. Moreover, I took the emplacement of a horizontal intrusion as the starting point for my structural analysis. For different crater diameters, depths and sill locations below the crater floor, I analysed the resulting surface deformation associated with sill inflation and evacuation. Using two-layer scaled analogue experiments, I investigated the feasibility of isostatic re-equilibration of the crust beneath large impact craters, and the evolution of the resulting CFFs in terms of pattern and kinematics during this process (Fig. 1.3). In particular, I systematically analysed the influence of initial crater depth and diameter on CFF formation. Using state-of-the-art digital image correlation, the results of my physical experiments allowed me to quantitatively project the duration of vertical displacements, horizontal surface motions and the localisation of brittle deformation at the surface onto natural equivalents. The modelling results were compared with terrestrial and lunar impact structures.

Knowledge of the mechanical properties of the materials used in my experiments is crucial to understanding the processes observed. I present an extensive description of the granular materials used in the UHH-Tec laboratory. By quantifying the analogue materials used to model crater modification, I ensure proper scaling of the experiment. I also document the technical processes used to colour the quartz sand used in all the experiments.

The aim of the thesis is to fill important knowledge gaps in planetary geology and comparative planetology. In particular, the thesis will improve our knowledge of crater modification, which occurs over thousands of years after impact. Its structural

consequences have not been systematically analysed in 3D space. In particular, knowledge of crater floor fracturing is directly relevant to assessing the duration, spatial extent and mechanisms of advective heat transport from post-impact hydrothermal cells beneath impact craters on Earth (Bralower et al., 2020; Kring & Bach, 2021) as well as the formation of the economically most valuable ore deposits on Earth (Lightfoot, 2006). The analogue experiments will provide quantitative constraints on the spatial and temporal extent of floor fractures, which are based on the patterns and types of crater floor fractures resulting from the analogue experiments.

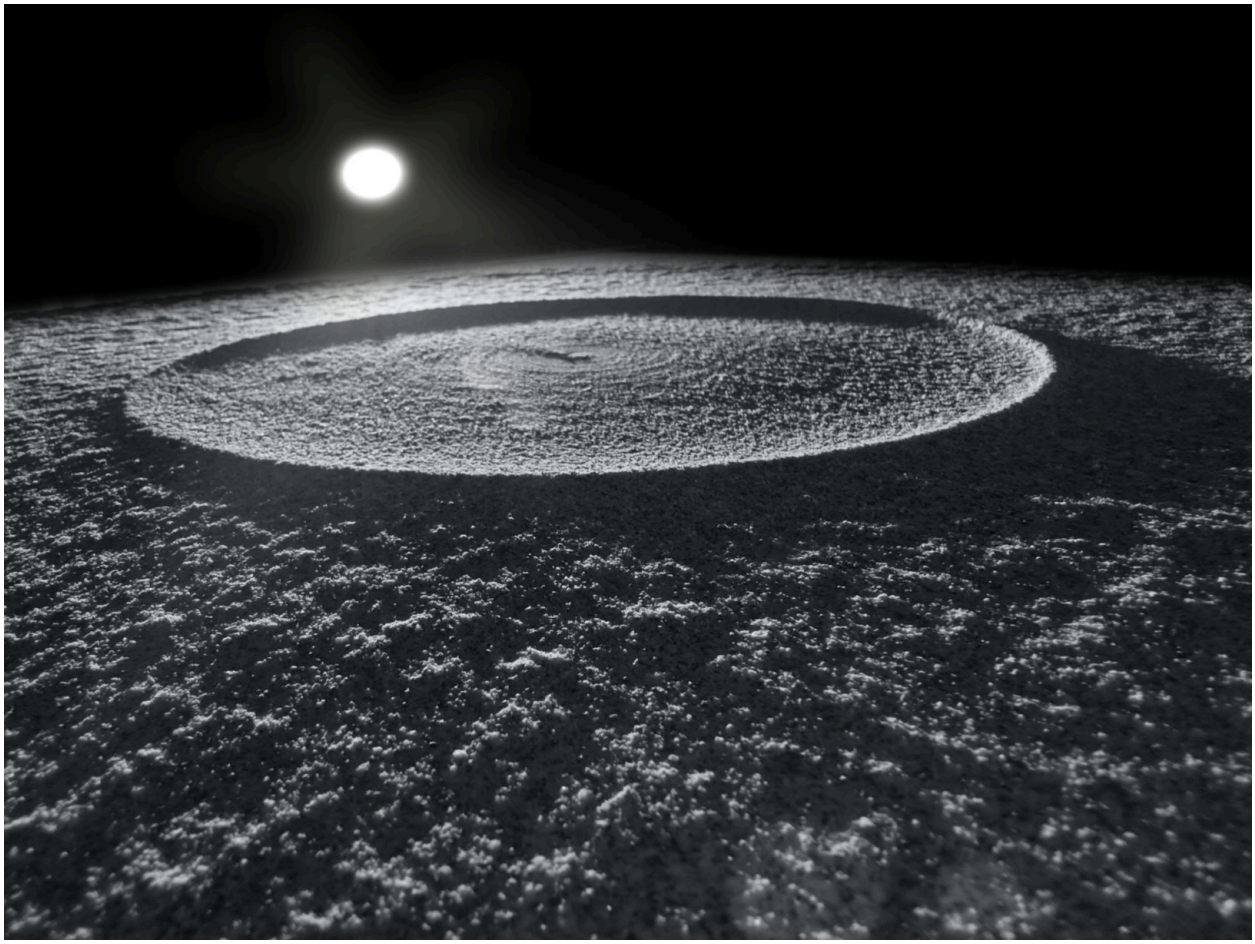

Figure 1.3: Artistically modified photograph (adapted background) of an actual physical model crater after experiencing isostatic re-equilibration. Taken from experiments carried out in thesis chapter 4.

2. Catalogue of granular and viscous materials and their physical properties used for quantitative analogue modelling of geological processes at the UHH-Tec laboratory, Universität Hamburg, Germany

Abstract

Analogue modelling has been a fundamental tool in geology for over a century. It is used to study scaled-down geodynamic processes and hypotheses on a laboratory scale. Analogue modelling observes the deformation of granular and viscous materials, acting as rock analogues, within a finite domain of known boundary conditions. Laboratory experiments can be scaled to the physical properties of natural prototypes and are often used to quantitatively assess the deformation mechanics and kinematics of a given geodynamic system. In order to apply appropriate scaling, it is necessary to know the properties of the materials chosen for the experiment. As most of the materials employed are natural resources, their quality may vary. While the properties of the most common materials have been published in detail, the materials used are generally not standardised between laboratories. I present a comprehensive description of 22 granular and 4 viscous materials used in the UHH-Tec laboratory. These are grouped into 8 categories. I present parameters measured in our laboratory such as density and angle of internal friction. I also present ring shear test data and mechanical properties of a novel flour-sand mixture developed and used e.g. to model crater modification processes. In addition, I provide comprehensive measurements of relative permittivity values of common analogue materials. Finally, I also describe and quantify the technical procedure for colouring quartz sand. As analogue modelling involves a large amount of manual labour, I provide general recommendations for material handling. This study contributes previously unavailable parameters and serves as a cross-laboratory reference.

2.1. Introduction

The study of Earth dynamics is challenged by the slow and imperceptible nature of geological processes. Field observations provide valuable insights into the geological past. However, we can only observe a moment in time. Many geological processes, such as the movement of plates, the opening of oceans or the formation of mountain ranges, unfold gradually over vast periods of time that are too slow for direct human observation. While geophysical measurements give us a glimpse of the Earth's dynamics over the past few decades, we can only observe processes that manifest themselves in these time frames. Experimental approaches that take into account natural factors are needed to study such processes on timescales that can be perceived by humans. Besides the emerging possibility of numerical modelling of such processes, analogue modelling has been a fundamental tool in geology for over a century (Ranalli, 2001). It is used to study scaled-down geodynamic processes and hypotheses on a laboratory scale. The first experiments date back to 1815 (Hall, 1815). It has since made a major contribution to the modern understanding of geodynamic processes that are now considered fundamental. Despite the time that has elapsed since its first application, the method is still relevant today. Analogue modelling observes the deformation of granular and viscous materials, acting as rock analogues, within a finite domain of known boundary conditions, in most cases a box with moving walls. The method has improved greatly over the centuries from a qualitative to a highly quantitative approach (Adam et al., 2005). Laboratory experiments can be scaled to the physical properties of natural prototypes and are often used to quantitatively assess the deformation mechanics and kinematics of a given geodynamic system (Ranalli, 2001). Scaling is based on the theory of similarity, which ensures comparability with nature (Hubbert, 1937). Two physical systems of different sizes are governed by the same processes if all the corresponding lengths are proportional. Since the first definition of scaling laws that allowed quantitative assessment, dimensionless scaling laws have further improved the definition of scaling (Galland et al., 2015).

Analogue experiments, which are controlled by the laws of physics, allow us to gain a detailed insight into the evolution of brittle and ductile deformation. Experiments by design take into account detailed multiscale processes, complex material properties, complex experimental geometries, randomisation and natural inhomogeneities that exceed the capabilities of numerical models. Compared to numerical simulations, analogue models are highly intuitive as one can directly interact with the process, making them excellent for research, teaching and public outreach.

Modern deformation analysis methods allow us to visualise what is invisible to the naked eye of the observer and to measure parameters for truly quantitative experiments. Optical recording of experiments is one of the most common methods. To visualise deformation activity, the recording of surface processes can be further accelerated. Advances in imaging and processing of the recorded surface allows one to calculate displacement vectors and scalar derivatives of vector fields. Digital Image Correlation

(DIC) and Particle Image Velocimetry (PIV) allow us to get a very sensitive quantitative sense of surface processes both in time and in 2D and 3D space (Adam et al., 2005; Stamhuis & Thielicke, 2014; Boutelier, 2016). Optical methods such as DIC and PIV require marker grains that allow the formation of a random, high-contrast speckle pattern. Since it is most convenient to image the observable surfaces of an experiment, such methods have become standard today. More recently, computed tomography (CT) has been used to image internal processes and structures (Poppe et al., 2015; Zwaan & Schreurs, 2017; Zwaan et al., 2018; Poppe et al., 2019; Zwaan et al., 2022). However, analysing experiments with CT requires adjusting material densities to achieve sufficient density contrast between model geological materials. In addition, CT scans are cost-intensive and limited in the size of accessible experiments. Other more exotic methods are evaluating the use of lab-scale seismic surveys (Sherlock & Evans, 2001; Krawczyk et al., 2013). The use of reflection seismic has been evaluated, but compromises in experimental design make it unsuitable for most analogue modelling objectives. At the UHH-Tec laboratory in Hamburg, Germany, tomographic scans of experiments based on high-frequency ground penetrating radar (GPR) have been pioneered. This low-cost method is generally not limited in the area it can cover and promises potential as radar technology advances. Experiments can also be fixed at the end of a given run and cut into thin slices to give an idea of their internal configuration of model materials. By using layers of coloured sand, internal deformation can be visualised. However, this process requires the experiment to be completed and, thus, may destroy it.

To obtain accurate quantitative results and proper scaling, it is necessary to know the properties of the materials chosen for the experiment. Although most material properties are provided by the manufacturer, they are often not accurate enough for scientific use. As most of the materials used are derived from natural resources, their quality can vary from batch to batch of the materials. It is not uncommon for analogue materials to be blends of different raw materials to achieve a specific property. While the properties of the most common materials have been described in detail, the materials used are generally not standardised between laboratories (Panien et al., 2006; Klinkmüller et al., 2016; Montanari et al., 2017; Galland et al., 2018). Furthermore, sourced materials can be of varying quality between different suppliers. Therefore, it is important to present material properties to ensure transparency and comparability between laboratories.

I present a description of 22 granular and 4 viscous materials used in the UHH-Tec laboratory. I give parameters measured in our own laboratory, such as density and angle of internal friction for brittle materials and refer to key references specific to the exact material used. I also present novel ring shear test data and mechanical properties of a flour-sand mixture material developed and used, for the first time, to model crater modification processes. I additionally present comprehensive measurements of empirically obtained relative permittivity values of common analogue materials as a reference for interpreting GPR scans of analogue models. I furthermore describe and quantify a technical procedure developed at the UHH-Tec laboratory for colouring quartz sand. As analogue modelling involves a large amount of manual labour, the respective

literature is largely devoid of the description of valuable information and 'lessons learned' in the handling and use of such materials. Based on a fair number of experiments conducted in the UHH-Tec laboratory over the past four years, I present common observations to help others. This study serves as a supplement to previously published material descriptions, adding previously unavailable parameters and serving as a cross-laboratory benchmark.

2.2. Methods

The following section describes the methods used to obtain the measurements presented. The following parameters were measured: Visible light macro photography, scanning electron microscope (SEM) photography, sifted density (ρ_s), compacted density (ρ_c), density difference compaction ($\Delta\rho$), porosity, angle of internal friction (ϕ), grain size distribution, relative permittivity (ε_r) of a 0.4 – 6 GHz and 2 GHz antenna, ring shear tester measurements of shear strength.

2.2.1 Density

Density was measured using a precision-milled stainless steel cylinder with an internal volume of 500 cm^3. Measurements were made under stable room conditions at 21°C and a stable humidity of around 30%. The material and cylinder were allowed several days to stabilise at room temperature and humidity. The material was loosely sieved into the cylinder from a height of approximately 20 cm, as is usually done in analogue modelling. Secondly, the material was poured into the cylinder and compacted using a vibrating table until no further compaction was possible. Excess material was carefully scraped off. The cylinder was weighed before and after filling using an electric laboratory balance (KERN EMS 3000-2). The weight of the cylinder was subtracted, and the density was calculated from the volume. Each density value given in the table is the average of 10 repeated measurements for statistical significance. The standard deviation of each average is shown in the table (staw). Grain density is derived from the typical mineral density. Porosity was calculated as a function of grain density and measured density.

$$Porosity = \left(1 - \left(\frac{\rho bulk}{\rho grain}\right)\right) * 100$$

2.2.2 Angle of internal friction

The angle of internal friction of a granular material can be derived from the critical angle of repose. The angle of repose is the maximum slope angle at which a pile of granular material resting on a flat surface will remain stable. The angle of repose is equal to the angle of internal friction. I designed a 3D printable measuring instrument for the

geometric calculation of the angle of internal friction (Fig. 2.1). The instrument is provided to the analogue modelling community as a printable stl file in the supplementary material. The instrument works by adding the sample to the upper funnel, which slowly dispenses the sample onto a lower platform that is 4 cm in width (side a on the right-angled triangle). Sample material is added until it begins to fall down the inner ledge. The rear surface of the instrument is provided with a cm scale. The resulting slope of the material is determined by the internal friction of the material. By reading the height of the material on the cm scale (side b on the right-angled triangle), one can mathematically determine the angle ϕ (Fig. 2.1). The measurements were made under stable room conditions at 21°C and a stable humidity of around 30%. The material and instrument were given several days to adjust to room temperature and humidity. Each angle in the table is the average of 15 repeated measurements for statistical significance. The standard deviation of each average is shown in the table (staw).

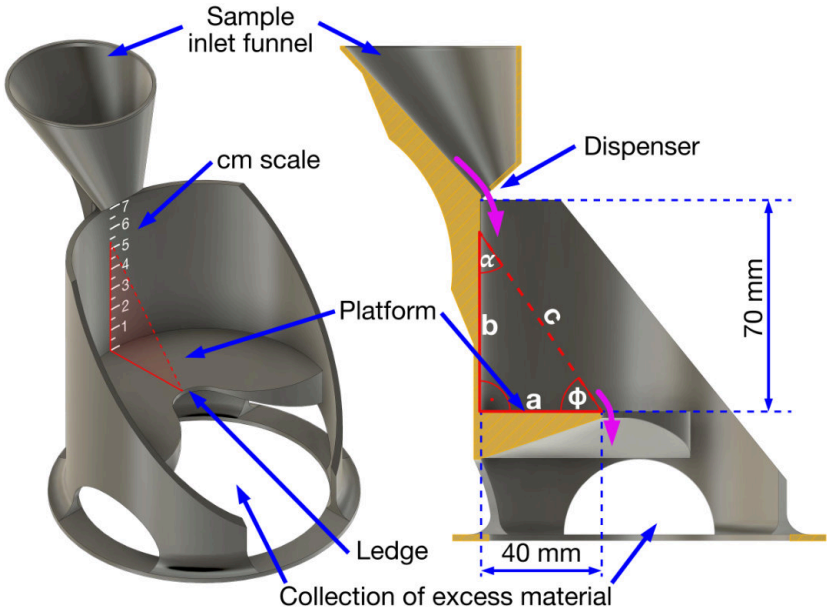

Figure 2.1: Rendering and cross-section of a 3D printable instrument for the geometric calculation of the angle of internal friction. The sample rests on the base platform. Red triangle indicates the geometric relationship to determine the angle of repose ϕ.

2.2.3 Grain size distribution

Grain size distributions were determined using a laser diffraction particle sizer (Sympatec HELOS/KF Magic; range 0.5/18 to 3200 µm, 32 grain size classes). Prior to measurement, material samples (1.5 cm^3 each) were suspended in water using tetra-sodium diphosphate decahydrate as a dispersing agent. To ensure the accuracy of the measurements, an in-house grain size standard was measured daily (standard deviation < 3.3 µm). Grain size statistics are based on the graphical method (Folk & Ward, 1957) calculated using the software Gradistat (Blott & Pye, 2001). All grain size parameters were rounded for use in the text.

2.2.4 Relative permittivity

Measurements to determine the material specific relative permittivity were made using a Proceq GP8800 Ground Penetrating Radar (400 - 6000 MHz FMCW) and a GSSI SIR 4000 equipped with a GSSI Model 62000 – 2 GHz Palm Antenna (2000 MHz centre frequency) in normal polarisation. Both systems were set up to take 5 scans per centimetre. Measurements were made under stable room conditions at 21°C and a stable humidity of around 30%. The material was allowed several days to acquire room temperature and ambient humidity. The measurement setup consists of a cardboard box measuring 31 x 11 x 14 cm (Fig. 2.2a). Cardboard was chosen as the material of choice because of its low relative permittivity to minimise electromagnetic wave reflections from the walls. The bottom of the cardboard box is lined with a thin layer of carbon fibre, which attenuates the electromagnetic wave and reduces the signal reflected from the bottom of the box, reducing return signal overpowering of the flat set-up. The sample is poured evenly into the box. A conductive brass tube 0.01 cm in diameter is placed horizontally at a depth of 7 cm as a radar target (Fig. 2.2a). A wooden plate is placed on top of the box to ensure correct movement of the survey wheel. The antenna is placed on top of the cardboard box and moved along the length. The brass tube will appear as a diffraction hyperbola in the recorded radargram (Fig. 2.2b). The antenna emits a wave in the shape of a wide cone. Electromagnetic waves propagate spherically through the medium. This allows the radar to get a reflection from the target not only when it is directly on top, but also several scans before and after its actual position. The hyperbola shape shows the antenna approaching and then moving away from the target, with the peak of the diffraction hyperbola being exactly where the target is actually located. The shape of the diffraction hyperbola is

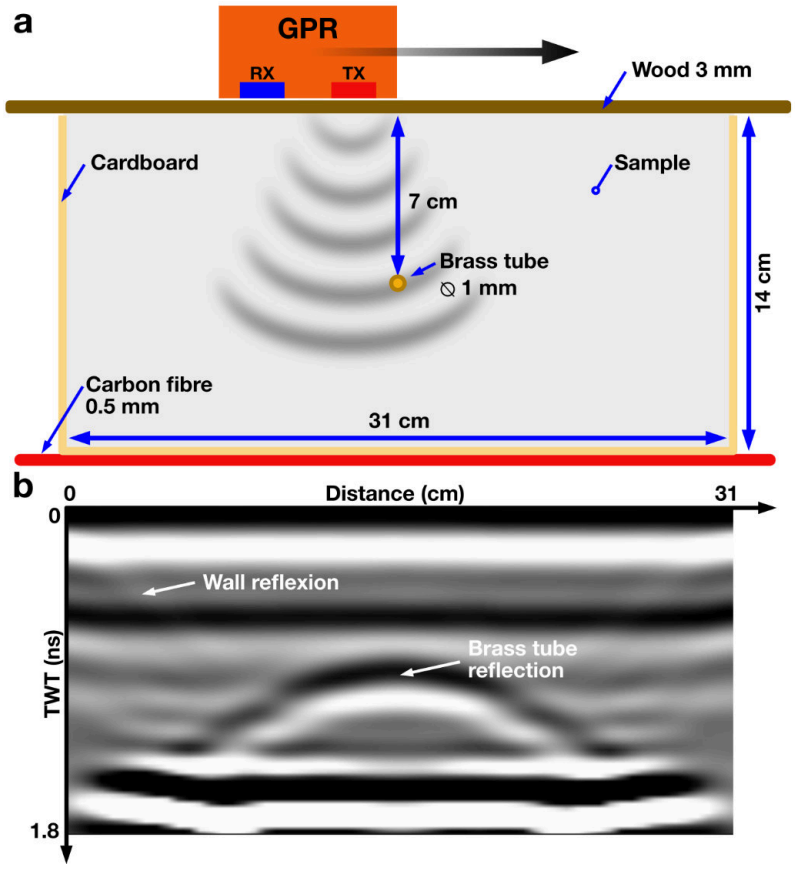

Figure 2.2: Sketch illustrating the setup used to measure the relative permittivity. (a) Diagram showing the setup with the GPR antenna on top, the cardboard box filled with the sample and the radar target (b) Actual radargram of the test setup. The hyperbola in the centre represents the radar target.

dependent on the propagation speed of the electromagnetic wave. The material specific relative permittivity ε_r is calculated from the recorded diffraction hyperbola. For the calculation of ε_r, I used the integrated software function of each system by fitting a reference hyperbola. Furthermore, due to the known depth of the brass target I could further calibrate the resulting relative permittivity ε_r value. Each value in the table is the average of 5 repeated measurements per antenna system for statistical significance. I also calculated the average based on both antenna systems. The standard deviation of each average is shown in the table (staw).

2.2.5 Rings shear test data

Selected materials were tested in a ring shear apparatus to determine their Mohr-Coulomb failure criterion. The measurements were performed in the Ring Shear Tester RST-01.pc. Access to the instrument at the HelTec laboratory Deutsches GeoForschungsZentrum Potsdam, Germany, was made possible with the kind assistance of the laboratory staff. The ring shear tester consists of a ring shear cell containing the sample. The shear cell used has dimensions of 5 cm inner radius, 10 cm outer radius and 4 cm height. A lid is pressed onto the sample at a predetermined normal load. The corresponding lid is fitted with radial blades and has dimensions of 17.9 mm at the inner edge, 30.2 mm at the outer edge, a blade height of 5 mm and a blade thickness of 0.9 mm. Blades pointing downwards from the lid ensure mechanical coupling with the sample. The shear cell is rotated by a motor. Sensors attached to the lid by tie rods record the torque of the rotating shear. From the known geometry of the shear cell, the torque measurements can be converted to shear stress (τ) and the rotation to displacement and plotted as shear curves. The RST-01.pc instrument is calibrated regularly using a certified standard bulk material (CRM-116 limestone powder).

The material is sieved into the shear cell according to the preparation of the experiments. Excess material is carefully scraped off. The shear cell is placed in the ring shear tester, the lid is fitted and the tie rods for torque measurement are installed. At the start of each measurement, a constant predefined normal load is applied, and the cell is rotated. Measurements were taken at a stable room temperature of 21°C. Measurements were repeated 3 times for each normal load to achieve statistical significance. A detailed description of the procedure and data analysis was published by Ritter et al. (2016).

2.2.6 Scanning electron microscope

Each sample was photographed using a Hitachi TM4000 scanning electron microscope (SEM). Each sample was imaged at 50x magnification and a detail view was taken at higher magnification to visualise the grain surface. A sample holder containing a carbon-induced adhesive was pressed into the sample. A layer of grains adhered to the sample holder. In preparation, each sample was sputtered with gold to avoid surface

charges on the sample and to improve image quality. The images were taken with the BSE detector at 15.0 kV.

2.2.7 Macro photography

Each sample was photographed using macro photography with a Canon 750D with a 24.2 megapixel sensor and a Canon 18 – 50 mm lens. Visible light photography is used as a reference for the optical appearance of a given material. White balance was set manually and kept constant throughout the images. The focus was set manually and the sample was uniformly illuminated with emphasis on oblique shading to improve visual representation. The sample was poured into a small tray. A scale in the field of view of each image was used as a length reference. All images represent the same area for comparability.

2.3. Coloured quartz sands

An essential requirement for many experiments is the use of coloured quartz sand, which performs several functions within the experiment. In particular, black and green sand, which make up a small percentage of the main lighter coloured granular materials, act as tracking markers for DIC analysis. The coloured quartz sand is also used as a marking layer and optical indicator. It is important to note that the added pigment does not affect the physical properties such as grain size, intergranular friction and shape of the quartz grains compared to their uncoloured counterparts. Given the typically low proportion of coloured sand in DIC applications, minor variations in its properties can be ignored. Although commercially available coloured sands exist, they are not well-suited to analogue experiments due to the lack of control over their mechanical properties among batches and their high costs. To address these issues and provide a cost-effective alternative, the following procedure was developed and applied to produce coloured quartz sand with specific properties.

Clean quartz sand type G23T is used as the raw material for grain dyeing. The quartz sand is placed in a large mixing vessel. A gypsum or concert mixing attachment is attached to a portable drill or laboratory mixer and lowered into the sand for mixing (Fig. 2.3a). Mixing of sand necessities a lot of torque. Acrylic paint, commonly found in art supplies stores, is added to the mixture in small portions while stirring (Fig. 2.3a). The dye is added under constant stirring until the sand reaches a vivid saturation. It is important to add the dye in small portions and to wait until the dye is evenly distributed before adding more. The mixture should feel dry at all times. A good indicator of the correct dye-to-sand ratio is minimal staining when touched. Oversaturation of the mixture may result in the formation of overly cemented grains when dried. Small clumps of residual colour may form (Fig. 2.3b). In weighting the amount of dye added, I concluded that 4% by volume of dye gave adequate saturation (Table 2.6). This proportion already considers dye losses along the processing steps. When an even

distribution of colour is achieved, the coloured sand mixture is spread flat and loosely on a surface to dry. The mixture should be left to dry for at least 24 hours until it develops a brittle, crusty texture (Fig. 2.3c). During the drying process, the dye loses approximately 62% by volume of its initial weight as evaporated solvent (Table 2.6). Chunks of coloured sand are coarsely pre-crushed by hand to improve handling. Grains stuck together by the dye need to be separated and clumps of pigment need to be removed from the final product. Approximately 40% by volume of dry pigment will be separated of the mixture as clumps (Table 2.6). Sieves and a sieve shaker are used to separate the individual grains and restore the initial grain size distribution (Fig. 2.3d). The sieve shaker, equipped with several test sieves arranged from coarser at the top to 360 µm at the bottom. The use of cm scale agate balls in each sieve improves mechanical separation of adherent grains. The stepped sieves allow efficient, step-by-step separation and fractionation of the grains. The final dyed sand is free of lumps and contains only individual grains. The surface of the grains show only a minimum of surface coating (Fig. 2.3d). The final coloured sand will contain approximately 0.9% by volume of dry pigment on the grains (Table 2.6).

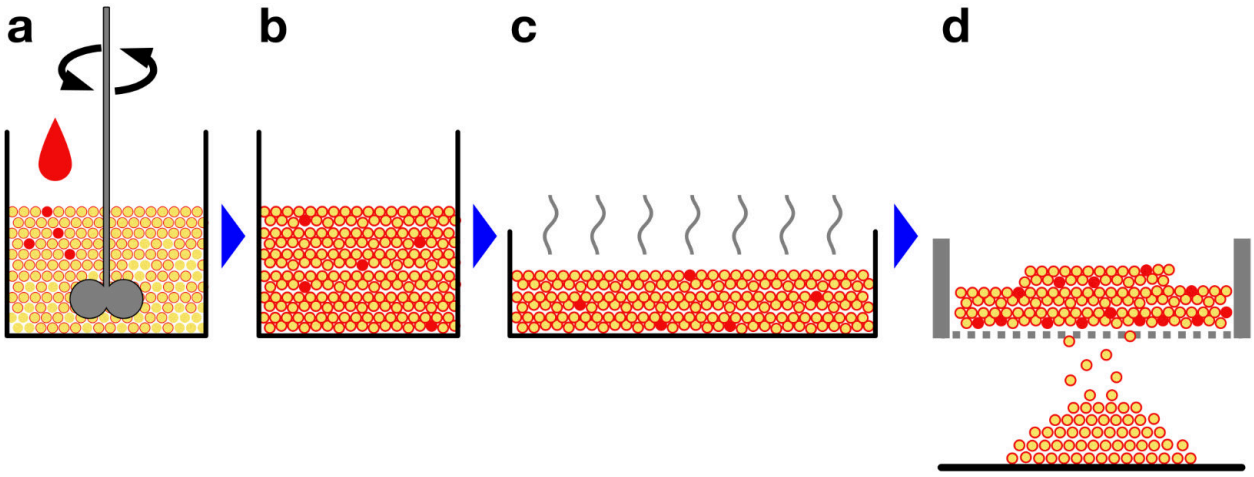

Figure 2.3: Sketch illustrating the process steps involved in dying of quartz sand. (a) Quartz sand is placed in a mixing vessel. A mixing attachment lowered into the sand for mixing. Paint is added to the mixture in small portions while stirring. The dye is added until the sand reaches a vivid colour. (b) When an even distribution of colour is achieved mixing is stopped. Grains may stick together and lumps of pigment may form (red dots). (c) The coloured sand mixture is spread flat and loosely on a surface to dry. (d) Sieves are used to separate the individual grains. Grains stuck together and lumps of pigment are removed from the final product. The final dyed sand is free of lumps and contains only individual grains.

2.4. Data records

22 granular and 4 viscous materials grouped into 8 categories:

2.4.1 Quartz sands

2.4.2 Heavy minerals

2.4.3 Technical minerals

2.4.4 Organic materials

2.4.5 Elastic granulate

2.4.6 Soluble granulate

2.4.7 Mixtures

2.4.8 Viscous materials

2.4.1 Quartz sands

Group of natural quartz sands

2.4.1.1 Quartz sand G12T

Material description:

White to light beige, well sorted, fine-grained fluvial sand with rounded grains (Figs. 2.4, 2.6). The manufacturer quotes a grain size distribution of 100 – 400 µm. Measured grain size is 50 – 450 µm with a mean of 274 µm (Fig. 2.5). The quartz sand grade G12T is supplied by Schlingmeier Quarzsand GmbH & Co. KG. The quarry is located in Uhry Königslutter am Elm, Germany. After mining, the silica sand is washed, sieved and fire-dried to remove water and organic compounds. It is characterised by a low iron and titanium content and is free of any salt or organic impurities. It has a high chemical and mineralogical purity and is free of any heavy minerals. G12T is commonly used in the glass industry.

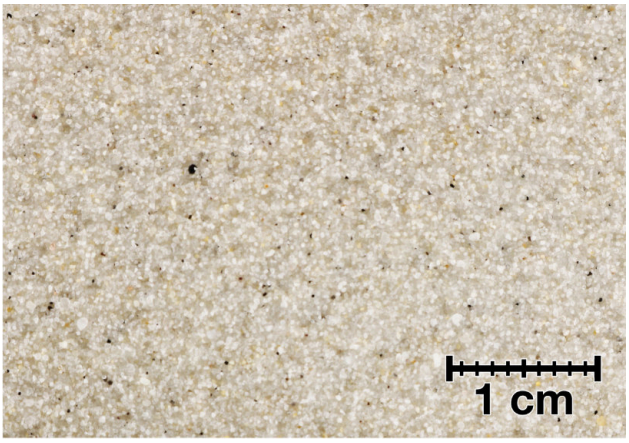

Figure 2.4: Macro photo of G12T.

Application and handling:

This type of quartz sand is commonly used in analogue experiments to model the brittle upper crust. Its small grain size is optimal for analogue experiments as it can resolve fine details. It is very clean and has a uniform sorting which does not require pre-processing. It is easily reused. Sieving for experimental preparation is unproblematic. Handling and sifting the sand causes electrostatic charging. The grains are small enough to be attracted to surfaces by the electrostatic charge and stick to utensils and surfaces.

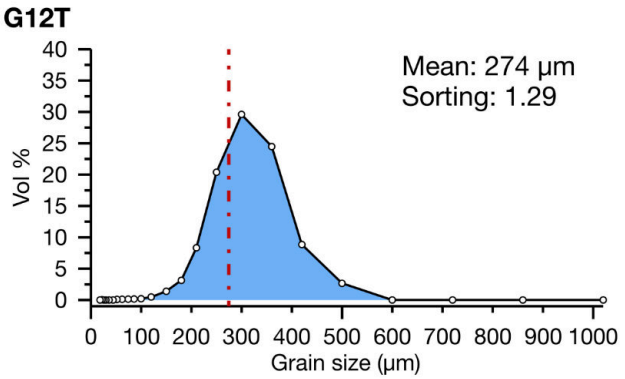

Figure 2.5: Grain size distribution of G12T.

References:

Detailed ring shear test data and further discussion on material properties are described by Klinkmüller et al. (2016).

Measured properties:

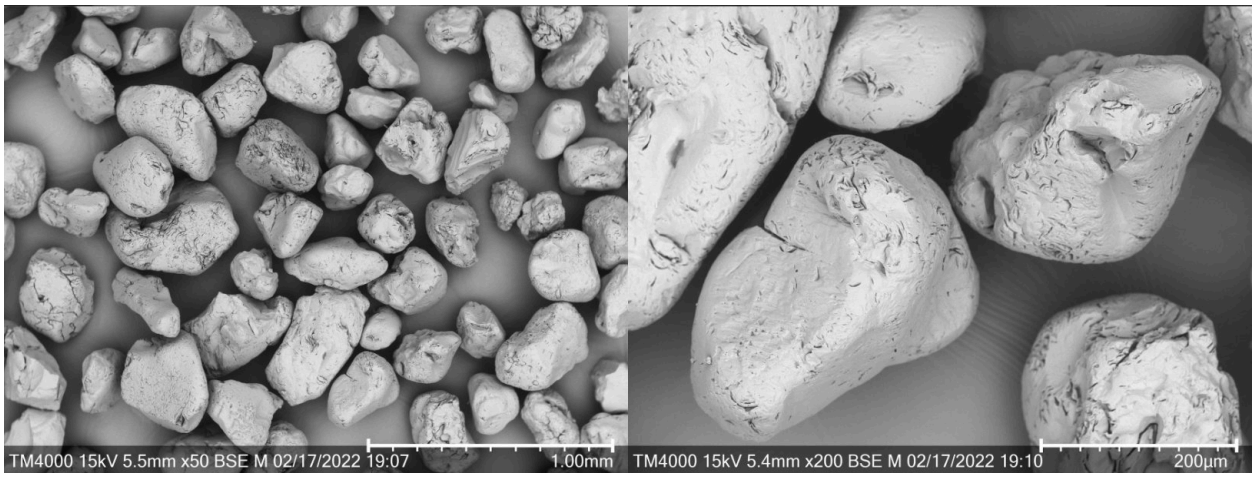

Figure 2.6: SEM images of G12T at 50x and 200x magnification.

G12T - density ρ								Friction angle ϕ	
Grain (kg/m³)	Sifted (kg/m³)	staw	Porosity	Compacted (kg/m³)	staw	Porosity	Δ ρ s-c (kg/m³)	(°)	staw
2680	1612.044	8.97	39.8 %	1635.896	7.10	39 %	-23.852	31.033	0.34

Table 2.1: Measured densities, calculated porosities and internal friction angle of G12T.

G12T - relative permittivity ε_r					
GP8800 (0.4-6 GHz)		GSSI (2 GHz)		Mean ε_r	
(ε_r)	staw	(ε_r)	staw	(ε_r)	staw
3.26	0.05	3.2	0.10	3.23	0.08

Table 2.2: Relative permittivity of G12T.

2.4.1.2 Quartz sand G23T

Material description:

White to light beige, well sorted, medium grained fluvial sand with rounded grains (Figs. 2.7, 2.9). The manufacturer quotes a grain size distribution of 100 – 600 µm. Measured grain size is 60 – 600 µm with a mean of 334 µm (Fig. 2.8). The quartz sand grade G23T is supplied by Schlingmeier Quarzsand GmbH & Co. KG. It is the coarse variant of G12T. The quarry is located in Uhry Königslutter am Elm, Germany. After mining, the quartz sand is washed, sorted and fire-dried to remove water and organic compounds. It has a low iron and titanium content and is free from salt and organic impurities. It has a high chemical and mineralogical purity and is free of heavy minerals. G23T is widely used in the glass industry.

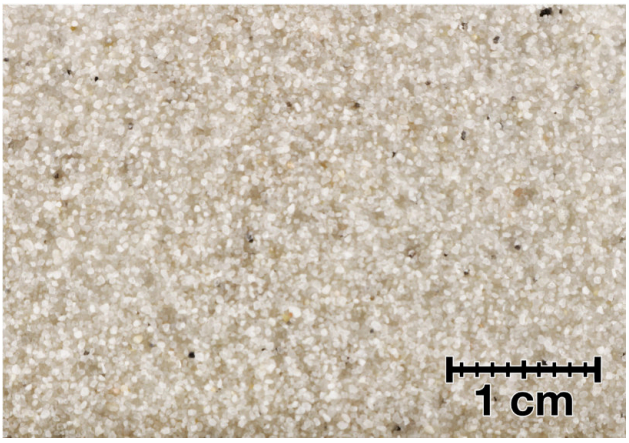

Figure 2.7: Macro photo of G23T.

Application and handling:

It is the standard material used for analogue modelling at UHH-Tec. This type of quartz sand is commonly used in analogue experiments to model the brittle upper crust. It represents a rather coarse variant of the sands used by the analogue modelling community. Its grain size is optimal for analogue experiments as it is still fine enough to resolve details. It is easily reused. Sieving for experimental preparation is unproblematic.

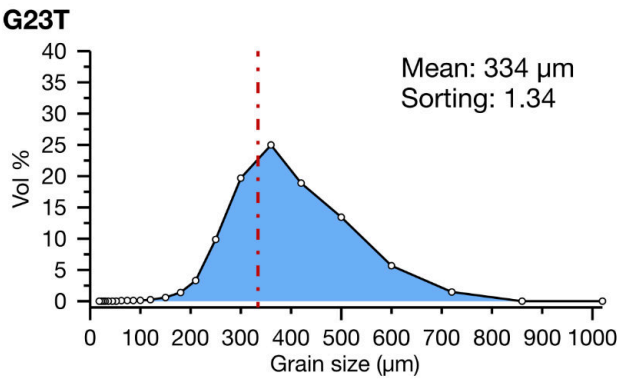

Figure 2.8: Grain size distribution of G23T.

References:

This type of quartz sand is commonly used in European analogue laboratories (Schreurs et al., 2006). Detailed data from the ring shear test and further discussion of the material properties have been published by Klinkmüller et al. (2016), Ritter et al. (2016) and Rosenau et al. (2018).

Measured properties:

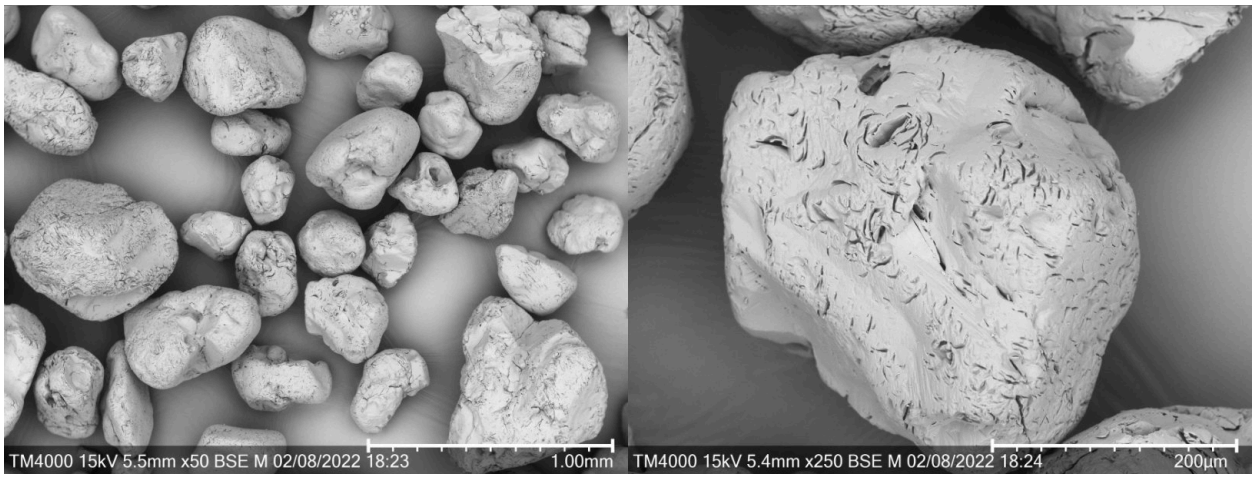

Figure 2.9: SEM images of G23T at 50x and 250x magnification.

G23T - density ρ								Friction angle ϕ	
Grain (kg/m³)	Sifted (kg/m³)	staw	Porosity	Compacted (kg/m³)	staw	Porosity	Δ ρ s-c (kg/m³)	(°)	staw
2680	1631.788	11.61	39.1 %	1647.238	9.68	38.5 %	-15.450	32.209	0.38

Table 2.3: Measured densities, calculated porosities and internal friction angle of G23T.

G23T - relative permittivity ε_r					
GP8800 (0.4-6 GHz)		GSSI (2 GHz)		Mean ε_r	
(ε_r)	staw	(ε_r)	staw	(ε_r)	staw
3.22	0.08	3.1	0.12	3.16	0.12

Table 2.4: Relative permittivity of G23T.

2.4.1.3 Quartz sand G23T coloured

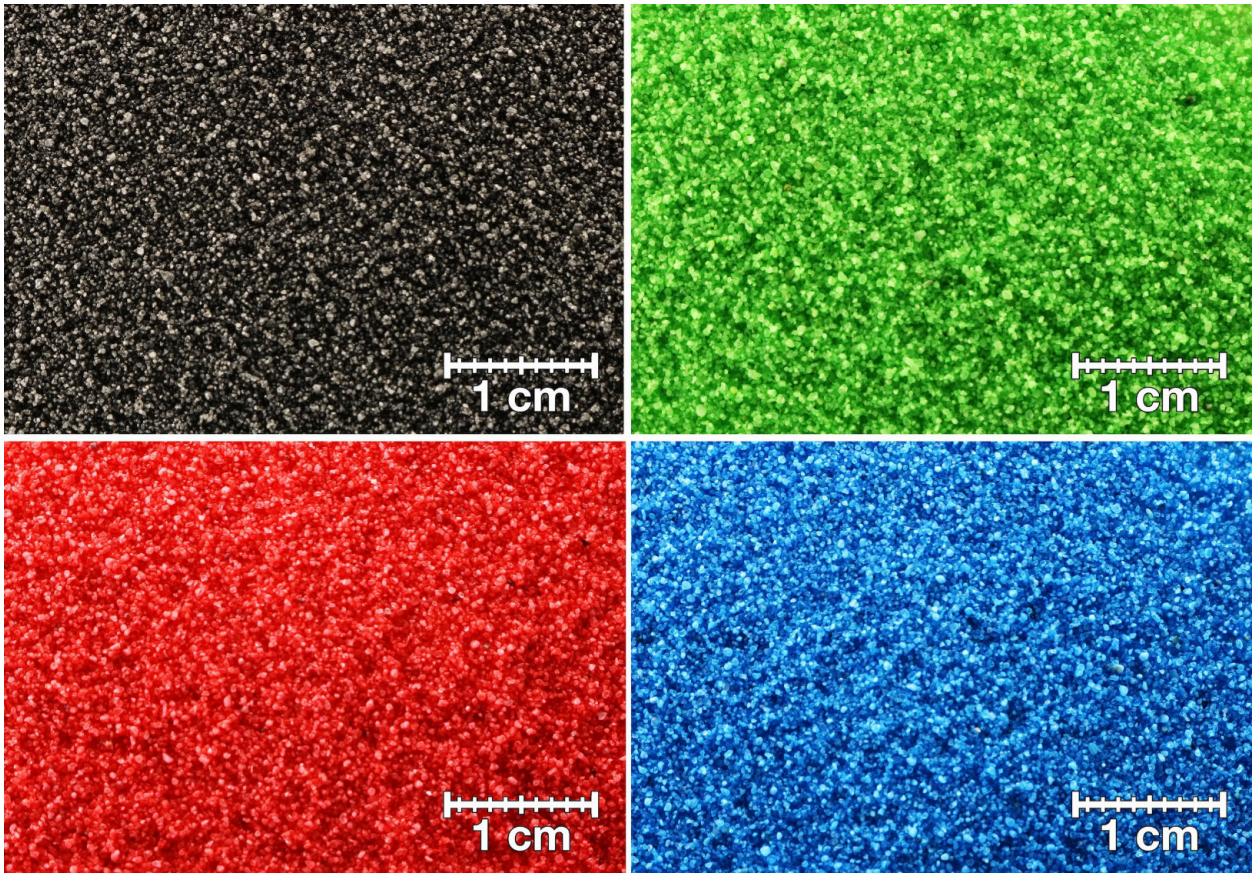

Figure 2.10: Macro photo of G23T coloured in black, green, red and blue.

Material description:

Black, green, blue and red well sorted quartz sand with rounded grains (Figs. 2.10, 2.12, 2.13). Grains have thin pigment coating on the surface. Measured grain size is 75 – 750 µm with a mean of 353 µm (Fig. 2.11). See G23T (2.4.1.2) for basic material properties.

Application and handling:

Coloured marker grains are primarily used to mix with other granular analogue materials in small proportions. Black marker grains are most commonly used to create random black and white patterns for cross-correlation with digital image correlation. A mixture of colours may be used depending on the camera specification. In addition, coloured sand can be used to visualise horizontal stratification or to draw patterns that act as markers to visualise strain. Coloured sand is usually used for visual purposes only. It is desirable that colouring the grains does not change the mechanical properties of the sand. For colouring, I use viscous `boesner - ACRYL STUDIO` acrylic paint in the following colours: Vermilion 506; Phthalo blue 616; Permanent green light 707 and Black

906. The pigments have a density of 1.0 – 1.5 g/ml. The coloured sand is waterproof. The coloured sands used are manufactured manually in the UHH-Tec laboratory to maintain full control over the colouring process and the final product. See section 2.3 for a detailed description of the colouring process. The coloured sands have the same properties as the regular G23T. However, they tend to stick together slightly.

Measured properties:

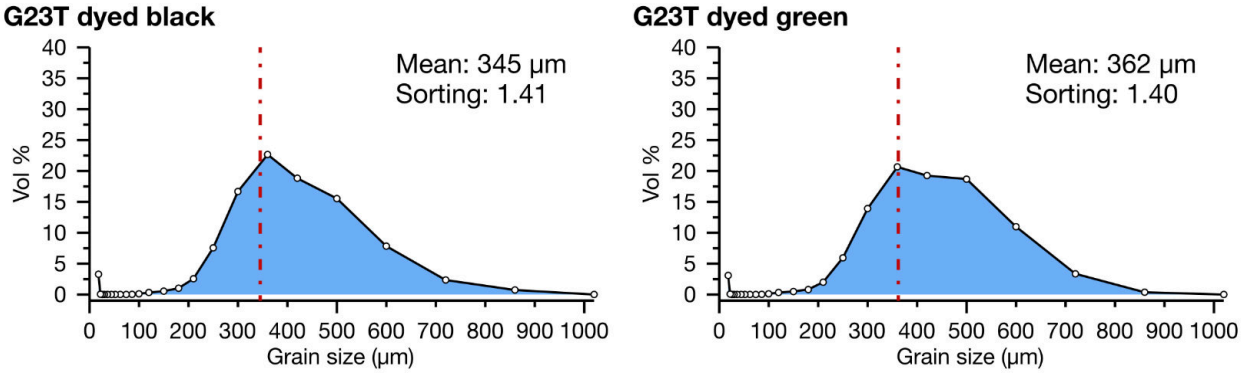

Figure 2.11: Grain size distribution of G23T coloured in black and green.

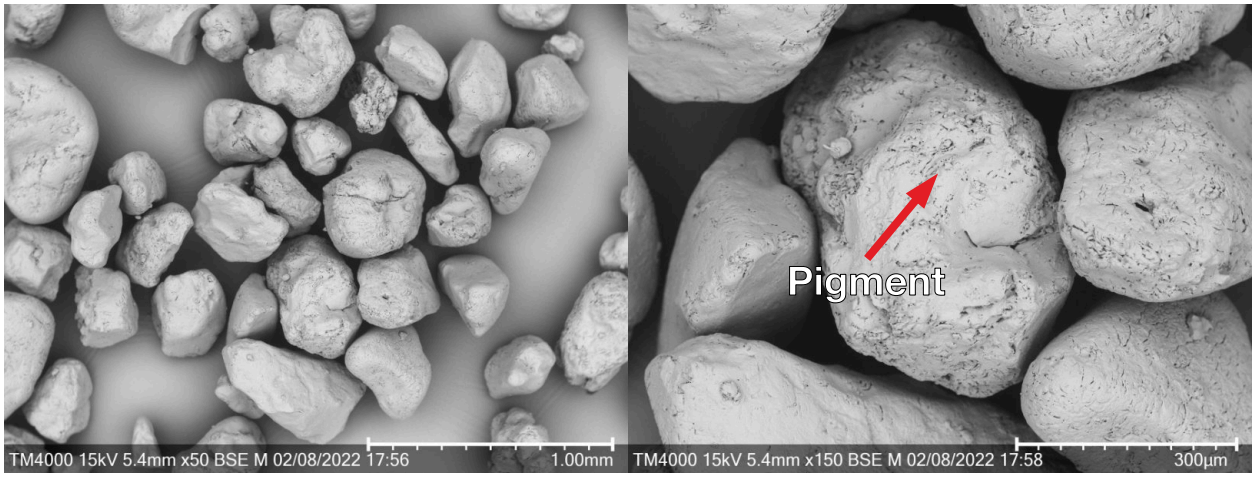

Figure 2.12: SEM images of G23T with black pigment coating (SEM image cannot resolve colour).

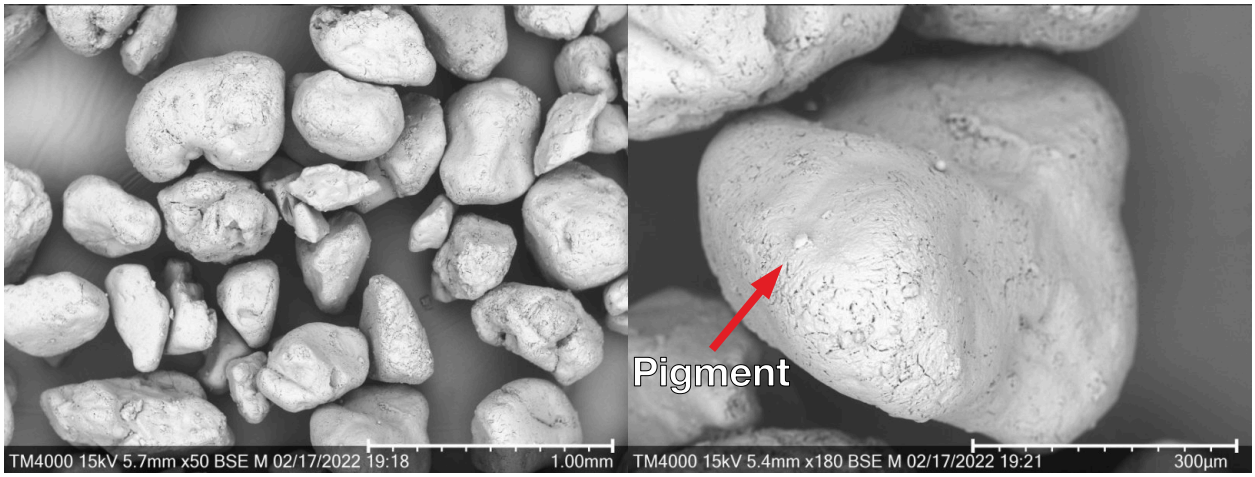

Figure 2.13: SEM images of G23T with green pigment coating (SEM image cannot resolve colour).

G23T dyed black - density ρ					Friction angle ϕ	
Sifted	staw	Compacted	staw	$\Delta \rho$ s-c	(°)	staw
1567.968	14.30	1582.474	11.81	-14.506	32.481	0.45
G23T dyed green						
1542.578	9.30	1554.078	4.52	-11.500	32.516	0.43

Table 2.5: Measured densities and internal friction angle of G23T coloured in black and green.

Processing steps	Average	G23T dyed black		G23T dyed green		G23T dyed blue		G23T dyed red	
Raw G23T		700 g		600 g		600 g		600 g	
Dye added	3.6 % vol	21 g	3 % vol	30.5 g	5.1 % vol	16.9 g	2.8 % vol	20.6 g	3.4 % vol
Mixing vessel dye loss ↓	26.9 % vol	-6.69 g	31.9 % vol	-17.7 g	58 % vol	-0.3 g	0.2 % vol	-3.6 g	17.7 % vol
G23T dyed, wet ↓		714.31 g		612.8 g		616.9 g		616.9 g	
Wet dye on grains ↓	2.5 % vol	14.31 g	2 % vol	12.8 g	2.1 % vol	16.9 g	2.8 % vol	16.9 g	2.8 % vol
Dye solvent loss ↓	61.9 % vol	-9.81 g	68.6 % vol	-8.1 g	63.3 % vol	-10.2 g	60.0 % vol	-7.9 g	46.9 % vol
Dry pigment ↓		4.5 g		4.7 g		8.9 g		8.8 g	
G23T dyed, dry ↓		704.5 g		604.7 g		606.8 g		609 g	
Dye aggregates ↓	40 % vol	-2.2 g	48.9 % vol	-2.3 g	48.9 % vol	-2.3 g	25.9 % vol	-3.2 g	36.4 % vol
Grain sieving loss ↓		-2 g	0.3 % vol	-2 g	0.3 % vol	-2 g	0.3 % vol	-2 g	0.3 % vol
G23T dyed, sifted		702.3 g		602.4 g		604.5 g		605.8 g	
Pigment on grains	0.9 % vol	4.3 g	0.6 % vol	4.4 g	0.7 % vol	6.5 g	1.1 % vol	4.4 g	1.3 % vol

Table 2.6: Measurements of dye concentration on coloured quartz sand grains. Results for different colours obtained by weighting along the dyeing process. The top two rows show the initial weight of sand and added dye. The middle group of rows, marked with arrows, represent changes along the colouring process. The final concentration of pigment remaining on the grain is shown in the bottom row.

2.4.2 Heavy minerals

Group of minerals with high density

2.4.2.1 Corundum sand

Material description:

Dark reddish, well sorted, fine-grained sand with angular grains (Figs. 2.12, 2.16). The manufacturer quotes a grain size distribution of 88 – 125 µm. Measured grain size is 50 – 350 µm with a mean of 127 µm (Fig. 2.15). The corundum sand is supplied by ARTEKA e.K., Germany. It is commonly used as an abrasive for blasting. The grains are

Figure 2.14: Macro photo of corundum sand.

physically crushed and sieved to the desired grain size to obtain sharp angular grains. Physical crushing of the grains leaves a silt component.

Application and handling:

This type of corundum sand is used in analogue modelling to model brittle upper crust. It is often used for its high density and angularity of its grains. The high density enhances the contrast on CT scans. The angular grains interlock and have a high overall shear strength. The corundum sand is highly abrasive, which can increase wear on clear acrylic glass and mechanical components. It can be reused. Sieving for experimental preparation is unproblematic. Fine dust is generated during handling.

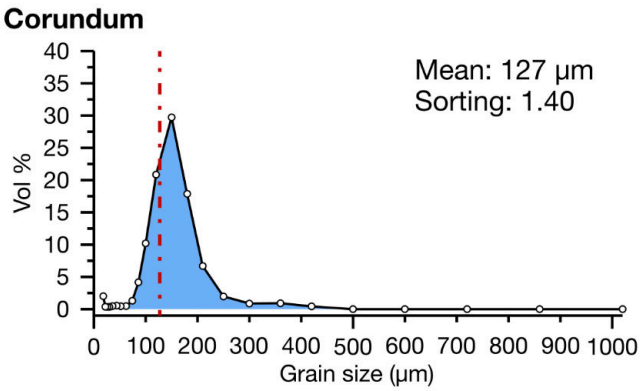

Figure 2.15: Grain size distribution of corundum sand.

References:

Detailed ring shear test data and further discussion on material properties are published by Panien et al. (2006).

Measured properties:

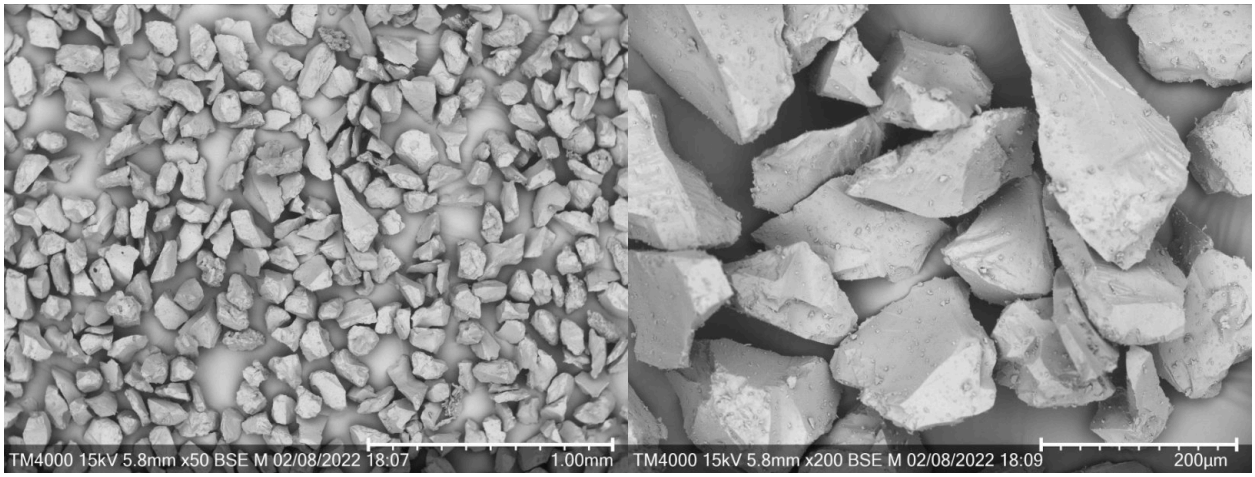

Figure 2.16: SEM images of corundum sand at 50x and 200x magnification.

Corundum - density ρ								Friction angle ϕ	
Grain (kg/m³)	Sifted (kg/m³)	staw	Porosity	Compacted (kg/m³)	staw	Porosity	$\Delta\rho$ s-c (kg/m³)	(°)	staw
4020	1868.216	11.33	53.5 %	2011.692	27.88	50 %	-143.476	34.990	0.45

Table 2.7: Measured densities, calculated porosities and internal friction angle of corundum sand.

Corundum - relative permittivity ε_r					
GP8800 (0.4-6 GHz)		GSSI (2 GHz)		Mean ε_r	
(ε_r)	staw	(ε_r)	staw	(ε_r)	staw
4.06	0.15	4.54	0.05	4.30	0.27

Table 2.8: Relative permittivity of corundum sand.

2.4.2.2 Iron powder

Material description:

Darkish-grey to graphitic-grey, well-sorted, angular sand (Figs. 2.17, 2.18).

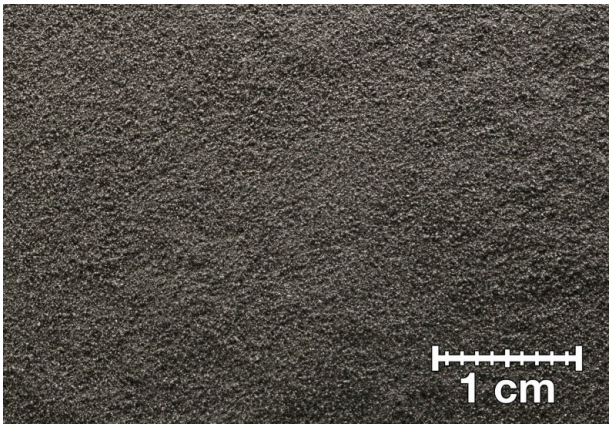

Figure 2.17: Macro photo of iron powder.

Application and handling:

Used as an additive to increase the specific density of a granular mixture or viscous fluid. The conductivity of the material can also be used to increase the relative permittivity of a compound to produce a greater response for GPR measurements.

References:

Detailed ring shear test data of a mixture of iron powder and quartz sand are published by Beekman et al. (2019).

Measured properties:

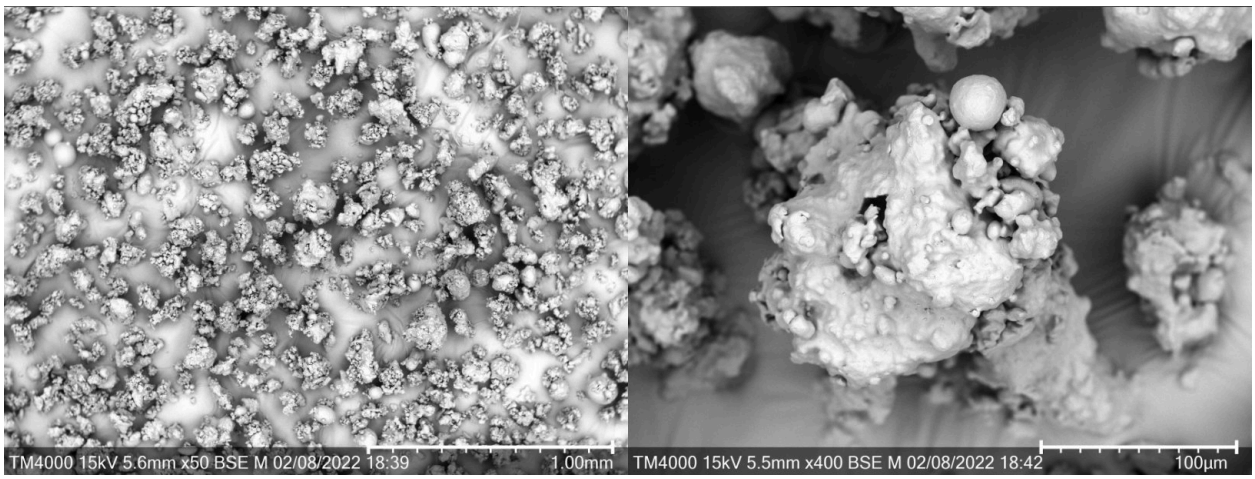

Figure 2.18: SEM images of Iron powder at 50x and 400x magnification.

Iron - density ρ	Friction angle ϕ	
Grain (kg/m³)	(°)	staw
7870	33.718	0.69

Table 2.9: Density and internal friction angle of iron powder.

2.4.3 Technical minerals

Group of artificially produced materials based on glass

2.4.3.1 Glass spheres fine

Material description:

White to slightly translucent, perfectly rounded and poorly sorted (Figs. 2.19, 2.21). The manufacturer quotes a grain size distribution of 40 – 80 µm. Measured grain size is 20 – 450 µm with a mean of 86 µm (Fig. 2.20). The glass beads are supplied by ARTEKA e.K., Germany. They are commonly used as blasting abrasives. This type of clear glass beads is also used in reflective coatings.

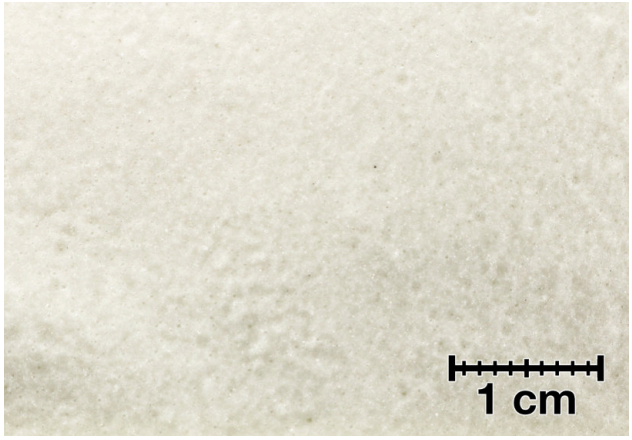

Figure 2.19: Macro photo of spheres fine.

They are artificially produced by evaporating soda lime silicate glass into a furnace.

Application and handling:

The glass beads are a fine-grained granular material with low friction and cohesion. In fact, the beads have the lowest friction of all commonly used granular analogue materials. They are often used to simulate detachment or weak layers of the upper crust. As an additive, they can be used to control the density and shear strength of a material. The fine powder can become very slippery if spilled during experimental preparation. It is difficult to reuse and next to

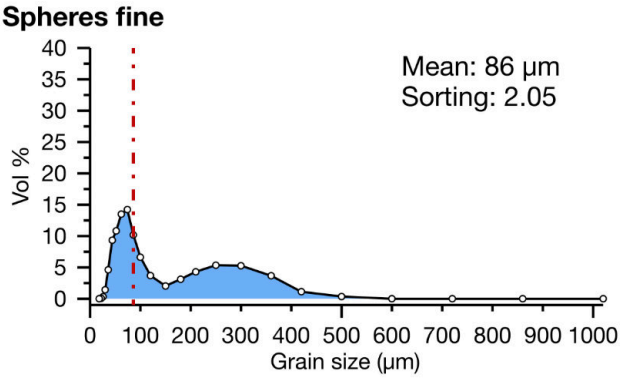

Figure 2.20: Grain size distribution of spheres fine.

impossible to sieve for experimental preparation. Dust may be generated during handling.

References:

Detailed ring shear test data and further discussion on material properties are published by Klinkmüller et al., (2016) and Pohlenz et al., (2020).

Measured properties:

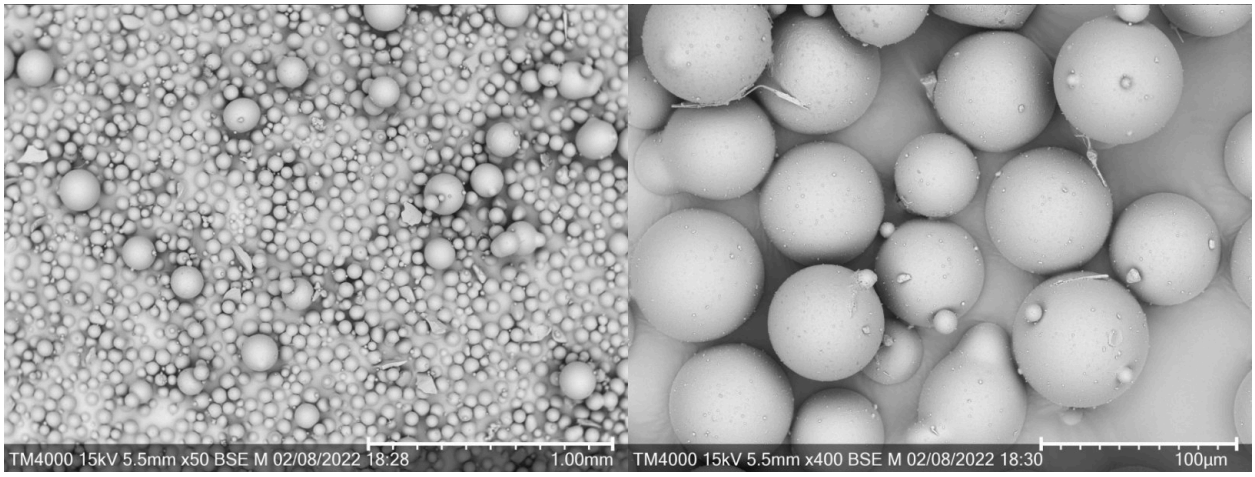

Figure 2.21: SEM images of spheres fine at 50x and 400x magnification.

Spheres fine - density ρ								Friction angle ϕ	
Grain (kg/m³)	Sifted (kg/m³)	staw	Porosity	Compacted (kg/m³)	staw	Porosity	Δ ρ *s-c* (kg/m³)	(°)	staw
2500	1515.530	12.65	39.4 %	1580.644	23.46	36.8 %	-65.114	26.218	0.48

Table 2.10: Measured densities, calculated porosities and internal friction angle of spheres fine.

Spheres fine - relative permittivity ε_r					
GP8800 (0.4-6 GHz)		GSSI (2 GHz)		Mean ε_r	
(ε_r)	staw	(ε_r)	staw	(ε_r)	staw
4.08	0.08	4.42	0.13	4.25	0.21

Table 2.11: Relative permittivity of spheres fine.

2.4.3.2 Glass spheres coarse

Material description:

White to slightly translucent perfectly rounded and very well sorted spheres (Figs. 2.22, 2.24). Manufacturer stated grain size distribution of 100 – 200 µm. Measured grain size is 90 – 300 µm with a mean of 161 µm (Fig. 2.23). The Glass beads are provided by ARTEKA e.K., Germany. They are commonly used as an abrasive blasting material. Furthermore, this type of clear glass spheres is used in reflective coatings. They are artificially produced by evaporating soda lime silicate glass into a furnace.

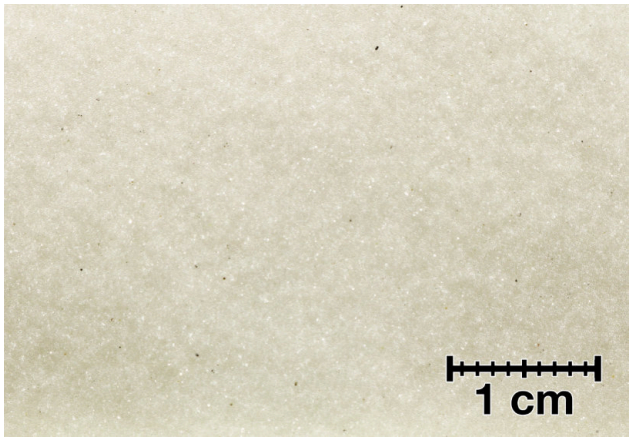

Figure 2.22: Macro photo of spheres coarse.

Application and handling:

The glass beads are a fine-grained granular material with low friction and cohesion, and have the lowest friction of all commonly used granular analogue materials. They are often used to simulate detachment or weak layers of the upper crust. As an additive, they can be used to control the density and shear strength of a material. The fine powder can become very slippery if spilled during experimental preparation. It is difficult to reuse and rather impossible to sieve for experimental preparation. Dust may be generated during handling.

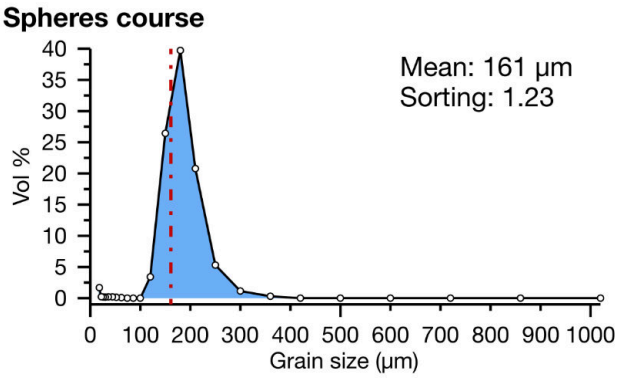

Figure 2.23: Grain size distribution of spheres coarse.

References:

Detailed ring shear test data and further discussion on material properties are published by Ritter et al., (2016) and Rosenau et al., (2022).

Measured properties:

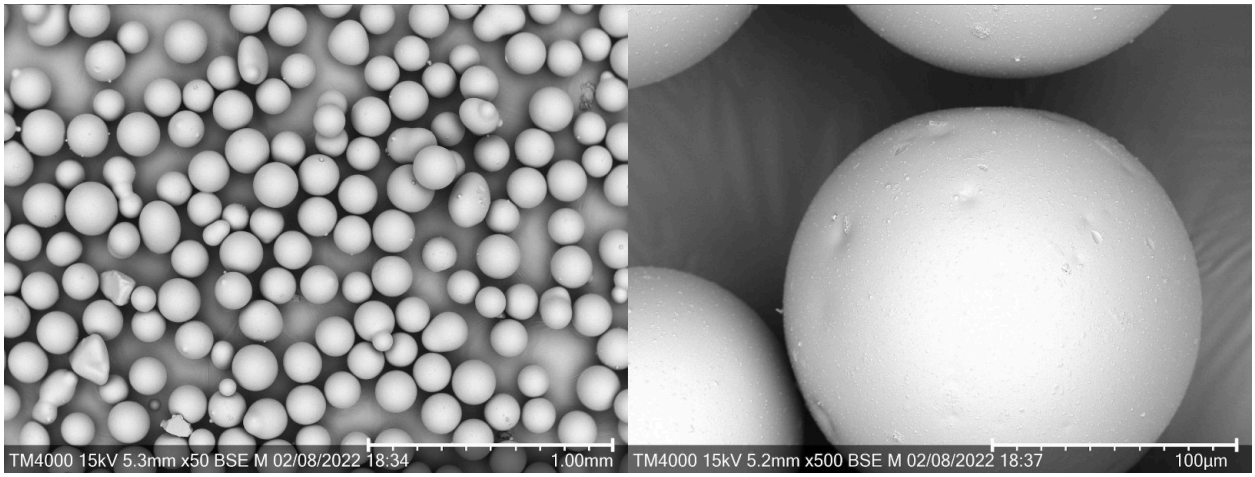

Figure 2.24: SEM images of spheres coarse at 50x and 500x magnification.

Spheres course - density ρ								Friction angle ϕ	
Grain (kg/m³)	Sifted (kg/m³)	staw	Porosity	Compacted (kg/m³)	staw	Porosity	Δ ρ s-c (kg/m³)	(°)	staw
2500	1486.170	9.56	40.6 %	1550.962	12.14	38 %	-64.792	25.328	0.54

Table 2.12: Measured densities, calculated porosities and internal friction angle of spheres coarse.

Spheres course - relative permittivity ε_r					
GP8800 (0.4-6 GHz)		GSSI (2 GHz)		Mean ε_r	
(ε_r)	staw	(ε_r)	staw	(ε_r)	staw
3.92	0.08	4.08	0.08	4.00	0.12

Table 2.13: Relative permittivity of spheres coarse.

2.4.3.3 Expanded glass

Material description:

Dark brown to greyish, rounded and moderately sorted spheres (Figs. 2.25, 2.27). The grain size distribution quoted by the manufacturer is 100 – 300 µm. Measured grain size is 50 – 600 µm with a mean of 360 µm (Fig. 2.26). The expanded gllass was supplied by Liaver GmbH & co. KG, Germany. The beads are produced by evaporation of recycled glass mixed with an unknown additive in

Figure 2.25: Macro photo of expanded glass.

a furnace. The glass forms small droplets while the additive becomes gaseous, expanding the droplet into a pumice-like structure. It is used industrially as a building material and as a concrete additive for material reduction.

Application and handling:

The expanded glass features an extremely low density. It can be used to model brittle upper crust and can be mixed with other granular or highly viscous fluids to reduce the overall density of a given mixture. It proved to be useful as a separation layer between viscous materials and granular top layer avoiding capillary creep of the fluid. Expanded glass floats on water. A layer of a couple centimetres can stay afloat while carrying a quartz sand layer. Mixing with granular materials is nearly impossible as the low density will lead to separation from any denser material such as quartz sands. The smallest available grain size is still rather large for meaningful analogue experiments. It can be reused but is difficult to sieve for experimental preparation, due to its low density. It can become very slippery if spilled during experimental preparation.

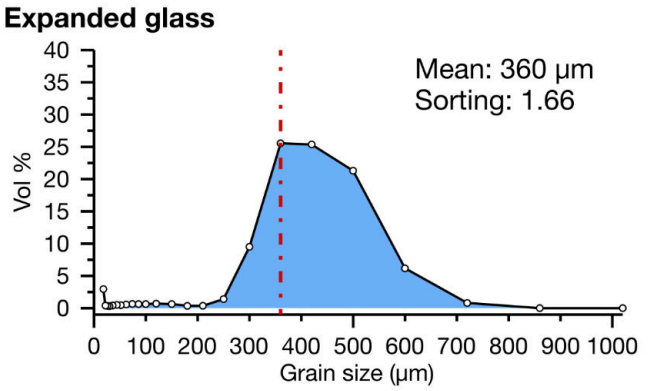

Figure 2.26: Grain size distribution of expanded glass.

References:

Ring shear test data are published by Warsitzka et al. (2019). A mixture for density reduction has been used by Ge et al. (2019).

Measured properties:

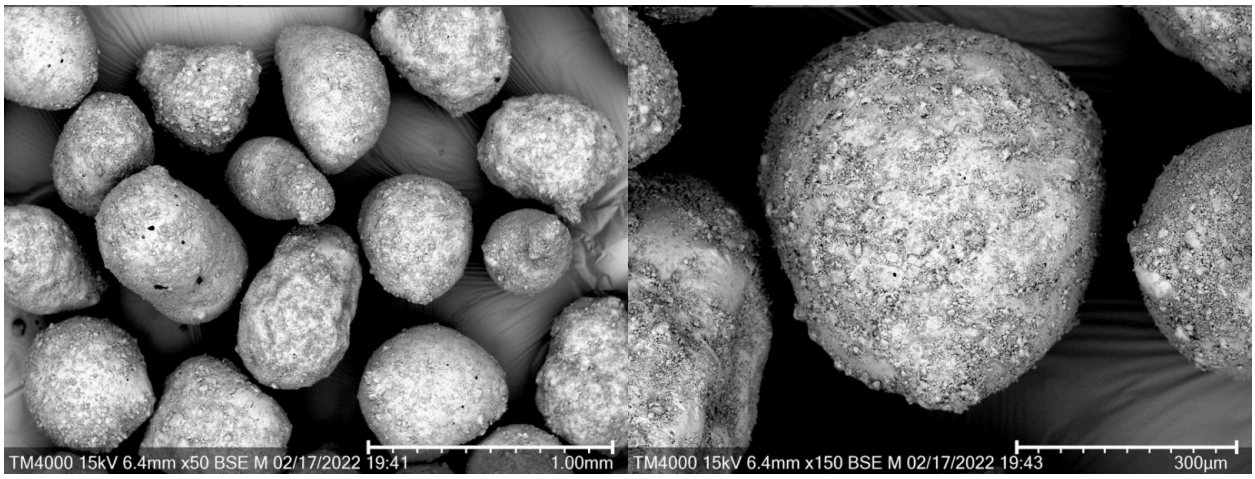

Figure 2.27: SEM images of expanded glass at 50x and 150x magnification.

Expanded glass - density ρ								Friction angle ϕ	
Grain (kg/m³)	Sifted (kg/m³)	staw	Porosity	Compacted (kg/m³)	staw	Porosity	$\Delta \rho$ s-c (kg/m³)	(°)	staw
2500	284.404	4.93	88.6 %	292.764	2.55	88.3 %	-8.360	29.501	0.48

Table 2.14: Measured densities, calculated porosities and internal friction angle of expanded glass.

Expanded glass - relative permittivity ε_r					
GP8800 (0.4-6 GHz)		GSSI (2 GHz)		Mean ε_r	
(ε_r)	staw	(ε_r)	staw	(ε_r)	staw
1.94	0.05	1.8	0.07	1.87	0.09

Table 2.15: Relative permittivity of expanded glass.

2.4.4 Organic materials

Group of organically derived materials

2.4.4.1 Flour

Material description:

White, opaque, pale beige powder, poorly sorted grains with spherical to aggregated grains (Figs. 2.28, 2.30). Measured grain size is 0.5 – 400 µm with a mean of 22 µm (Fig. 2.29). Broken starch spherules from ground wheat are distributed in a variety of different particle sizes. Based on standard food grade Wheat flour type 405.

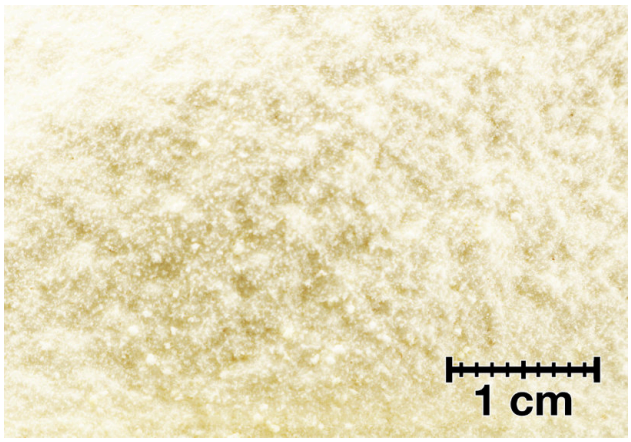

Figure 2.28: Macro photo of flour.

Application and handling:

Commonly used as a slightly cohesive, non-toxic upper crust analogue. Cohesion and fine grain size resolve even the smallest structures in great detail. It can be mixed with other analogue materials to reduce density and add cohesion. It is frequently used in models of volcanic plumbing systems and easily sifted into uniform layers. Flour is highly hygroscopic, changing its properties with adsorbed water content. It can be reused several times. Working with flour can cause significant dust development. Handling and sifting flour causes electrostatic charging. The grains are small enough to

be attracted to surfaces by the electrostatic charge and stick to utensils and surfaces.

References:

Ring shear test data are published by Warsitzka et al. (2022). Application in models of volcanic plumbing systems by Galland et al. (2018).

Measured properties:

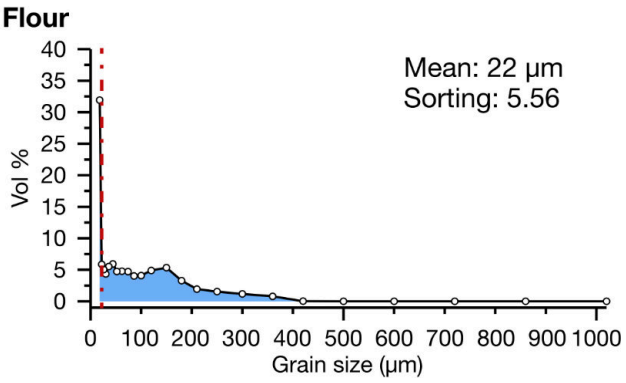

Figure 2.29: Grain size distribution of flour.

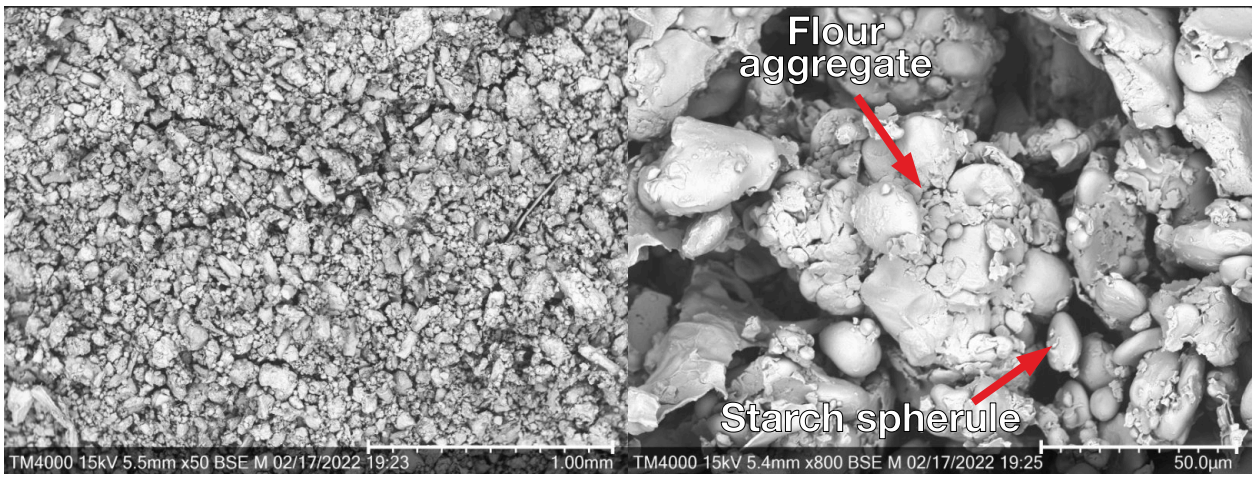

Figure 2.30: SEM images of flour at 50x and 800x magnification.

Flour - density ρ								Friction angle ϕ	
Grain (kg/m³)	Sifted (kg/m³)	staw	Porosity	Compacted (kg/m³)	staw	Porosity	$\Delta\ \rho$ s-c (kg/m³)	(°)	staw
1500	586.398	21.12	60.9 %	687.246	19.85	54.2 %	-100.848	50.372	0.95

Table 2.16: Measured densities, calculated porosities and internal friction angle of flour.

Flour - relative permittivity ε_r					
GP8800 (0.4-6 GHz)		GSSI (2 GHz)		Mean ε_r	
(ε_r)	staw	(ε_r)	staw	(ε_r)	staw
3.08	0.08	2.8	0.12	2.94	0.18

Table 2.17: Relative permittivity of flour.

2.4.4.2 Starch

Material description:

Pure white, slightly translucent powder, moderately sorted, spherical grains (Fig. 2.31, 2.33). Grain size ranges from 0.1 – 150 µm. Measured grain size is 0.1 – 150 µm with a mean of 36 µm (Fig. 2.32). Starch spherules are obtained from processed potato starch.

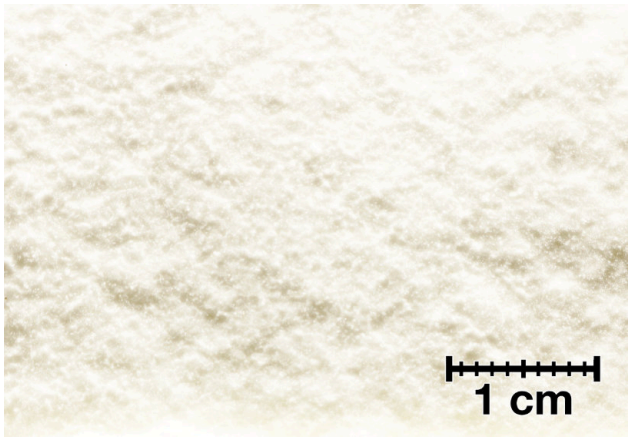

Figure 2.31: Macro photo of starch.

Application and handling:

Starch is used as a moderately cohesive, non-toxic analogue material. Its cohesion and fine grain size resolve even the smallest structures in great detail. It can be mixed with other analogue materials to reduce density and increase cohesion. It is finer and better sorted than flour. Mixing with water and drying the slurry produces a dense compact layer with brittle properties. Starch is highly hygroscopic, changing its properties with adsorbed water content. It can be reused several times and easily sifted into uniform layers. Working with starch can cause significant dust generation. Handling and sifting of flour cause electrostatic charging. The grains are small enough to be attracted to surfaces by the electrostatic charge and stick to utensils and surfaces.

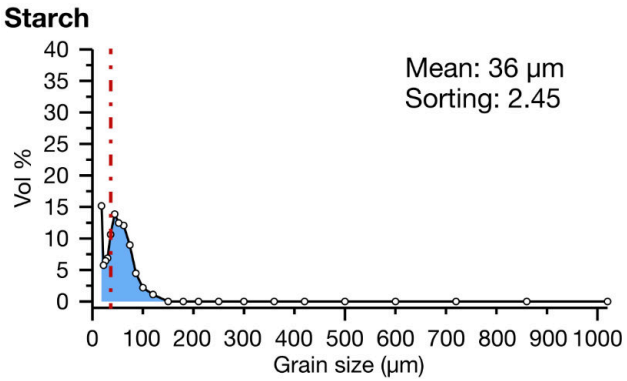

Figure 2.32: Grain size distribution of starch.

References:

Applications of dried starch slurry for modelling of basaltic columnar jointing (Müller, 1998; Toramaru & Matsumoto, 2004; Goehring et al., 2006). Density of individual starch spherules published by Dengate et al. (1978).

Measured properties:

Starch - density ρ								Friction angle ϕ	
Grain (kg/m³)	Sifted (kg/m³)	staw	Porosity	Compacted (kg/m³)	staw	Porosity	$\Delta\rho$ s-c (kg/m³)	(°)	staw
1500	678.588	10.93	54.8 %	746.416	16.04	50.2 %	-67.828	52.972	0.97

Table 2.18: Measured densities, calculated porosities and internal friction angle of starch.

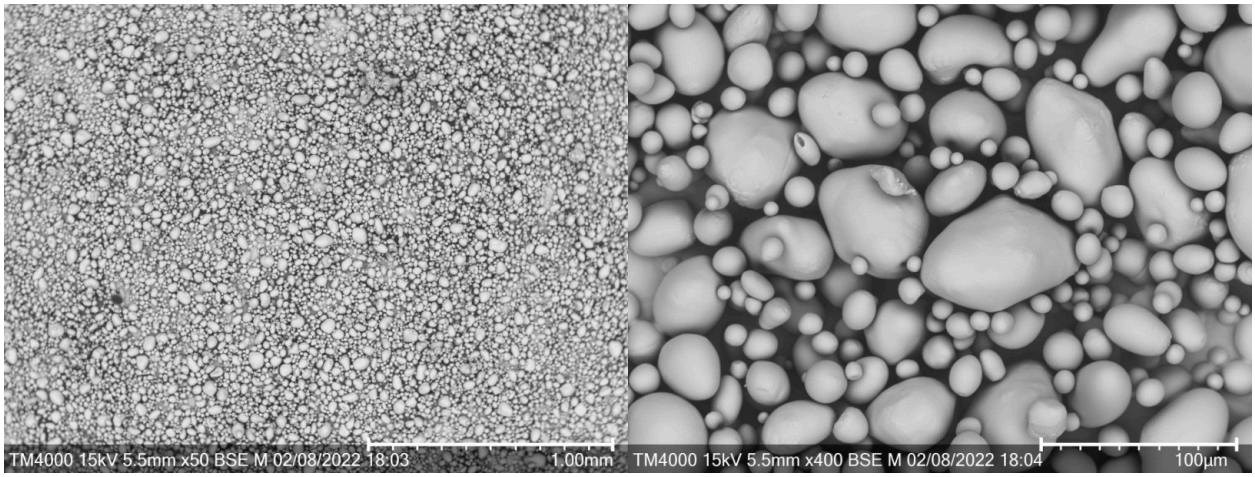

Figure 2.33: SEM images of starch at 50x and 400x magnification.

Starch - relative permittivity ε_r					
GP8800 (0.4-6 GHz)		GSSI (2 GHz)		Mean ε_r	
(ε_r)	staw	(ε_r)	staw	(ε_r)	staw
3.68	0.04	3.66	0.09	3.67	0.07

Table 2.19: Relative permittivity of starch.

2.4.5 Elastic granulate

Class of materials of organic origin with granular properties and elastic grains

2.4.5.1 Rubber black

Material description:

Black granules of poorly sorted, elongate aggregates (Figs. 2.34, 2.36). Manufacturer quoted grain size is 300 – 500 µm. Measured grain size is 20 – 1100 µm with a mean of 328 µm (Fig. 2.35). It comes as granules of ground ethylene propylene diene monomer rubber (EPDM) commonly used for sports surfaces and protective floor coatings.

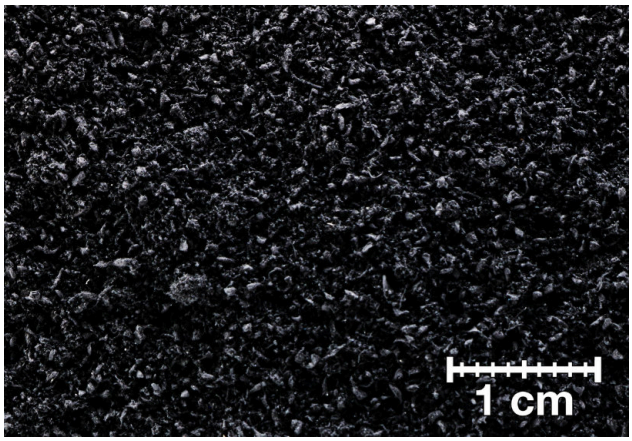

Figure 2.34: Macro photo of rubber granulate black.

Application and handling:

Rubber can be used as a standalone granulate with elastic properties. It can be mixed with other granular materials to provide a more elastic component. Its low density renders mixing with quartz sand difficult. Sieving is almost impossible due to the elongate, string-like shape of the aggregates. Handling causes electrostatic charging. Grains are light enough to be attracted to surfaces by electrostatic charge and stick to utensils and surfaces.

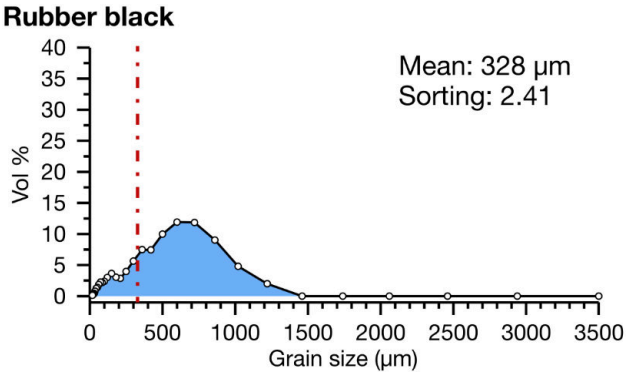

Figure 2.35: Grain size distribution of rubber granulate black.

References:

Elastic properties have been describes by Rosenau et al. (2017). Application of rubber granulate mixtures for the study of subduction earthquake cycles (Rosenau et al., 2009; Rosenau & Oncken, 2009; Rosenau et al., 2010).

Measured properties:

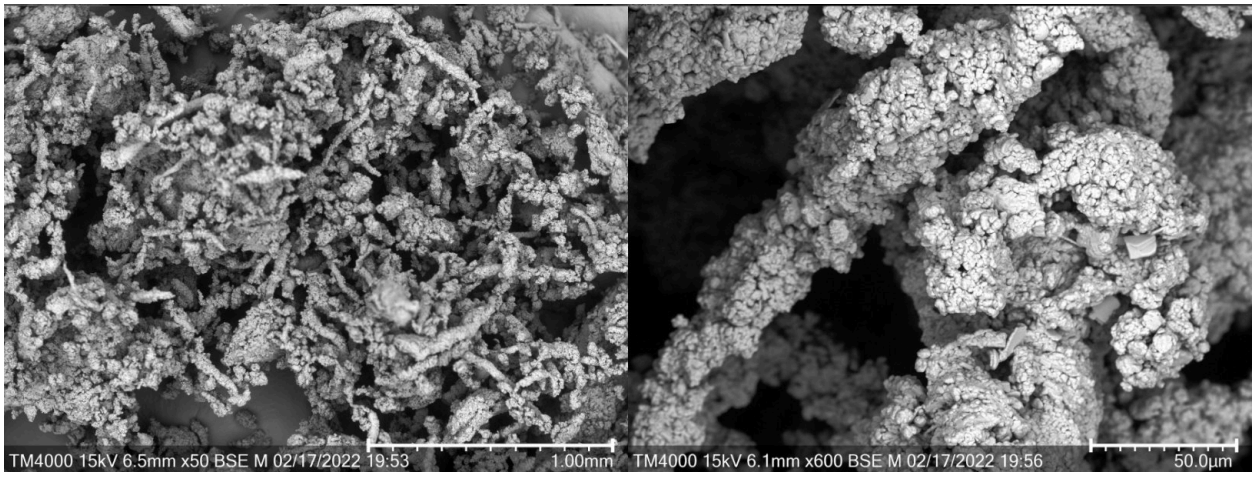

Figure 2.36: SEM images of rubber granulate black at 50x and 600x magnification (SEM image cannot resolve colour).

Rubber black - density ρ								Friction angle ϕ	
Grain (kg/m³)	Sifted (kg/m³)	staw	Porosity	Compacted (kg/m³)	staw	Porosity	Δ ρ s-c (kg/m³)	(°)	staw
1170	508.796	4.34	56.5 %	553.338	5.73	52.7 %	-44.542	42.344	0.83

Table 2.20: Measured densities, calculated porosities and internal friction angle of rubber granulate black.

2.4.5.2 Rubber green

Material description:

Moss green granules of poorly sorted, elongate aggregates (Fig. 2.37). The manufacturer quotes a grain size of 300 – 500 µm. Measured grain size is 60 – 1800 µm with a mean of 641 µm (Fig. 2.38). It comes as granules of ground ethylene propylene diene monomer rubber (EPDM) commonly used for sports surfaces and protective floor coatings.

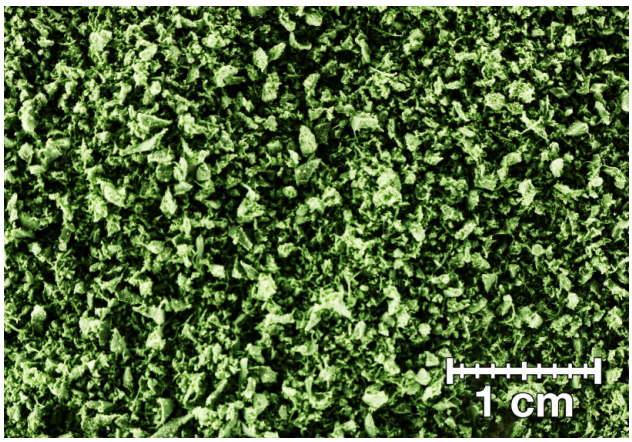

Figure 2.37: Macro photo of rubber granulate green.

Application and handling:

Rubber can be used as a standalone granulate with elastic properties and can be mixed with other granular materials to provide a more elastic component. Its low density renders mixing with quartz sand difficult. Sieving is almost impossible due to the elongate, string-like shape of the aggregates. Handling causes electrostatic charging and grains are light enough to be attracted to surfaces by electrostatic charge and stick to utensils and surfaces.

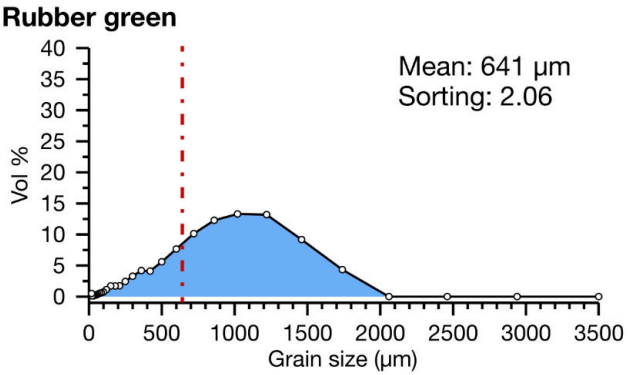

Figure 2.38: Grain size distribution of rubber granulate green.

References:

See 2.4.5.1

Measured properties:

Rubber green - density ρ								Friction angle ϕ	
Grain (kg/m³)	Sifted (kg/m³)	staw	Porosity	Compacted (kg/m³)	staw	Porosity	Δ ρ s-c (kg/m³)	(°)	staw
1170	528.236	4.23	54.9 %	572.172	7.71	51.1 %	-43.936	44.367	0.61

Table 2.21: Measured densities, calculated porosities and internal friction angle of rubber granulate green.

Rubber green - relative permittivity ε_r					
GP8800 (0.4-6 GHz)		GSSI (2 GHz)		Mean ε_r	
(ε_r)	staw	(ε_r)	staw	(ε_r)	staw
2.32	0.04	2.18	0.08	2.25	0.10

Table 2.22: Relative permittivity of rubber granulate green.

2.4.5.3 Rubber blue

Material description:

Blue granules of well sorted, angular grains (Fig. 2.39). Manufacturer quoted particle size of 500 – 1500 µm. Measured grain size is 250 – 2500 µm with a mean of 1383 µm (Fig. 2.40). It comes as granules of ground ethylene propylene diene monomer rubber (EPDM) commonly used for sports surfaces and protective floor coatings.

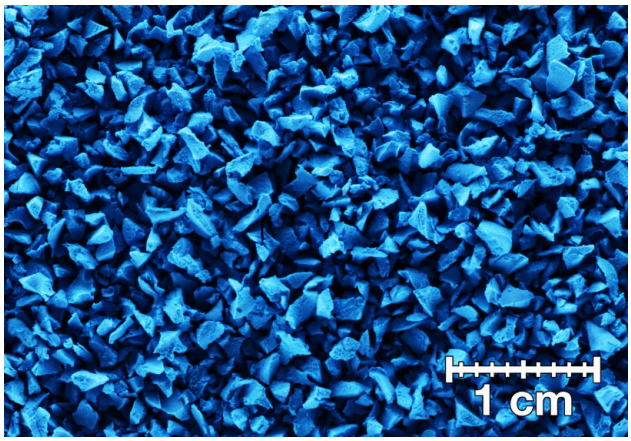

Figure 2.39: Macro photo of rubber granulate blue.

Application and handling:

Rubber can be used as a standalone granulate with elastic properties. It can be mixed with other granular materials to provide a more resilient component. Its low density renders mixing with quartz sand difficult. Its grain size is to coarse for experiments to resolve detailed structures. Handling causes electrostatic charging and grains may be attracted to surfaces by electrostatic charge and stick to tools and surfaces.

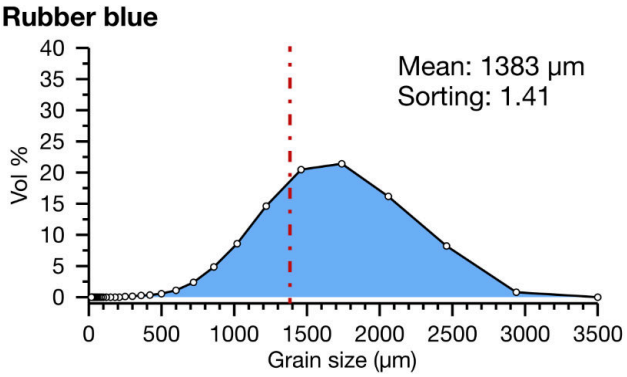

Figure 2.40: Grain size distribution of rubber granulate blue.

References:

See 2.4.5.1 of the finer grained version as a reference.

Measured properties:

Rubber blue - density ρ								Friction angle ϕ	
Grain (kg/m³)	Sifted (kg/m³)	staw	Porosity	Compacted (kg/m³)	staw	Porosity	Δ ρ s-c (kg/m³)	(°)	staw
1170	568.132	7.10	51.4 %	593.828	6.43	49.2 %	-25.696	37.705	0.92

Table 2.23: Measured densities, calculated porosities and internal friction angle of rubber granulate blue.

Rubber blue - relative permittivity ε_r					
GP8800 (0.4-6 GHz)		GSSI (2 GHz)		Mean ε_r	
(ε_r)	staw	(ε_r)	staw	(ε_r)	staw
2.28	0.04	2.04	0.09	2.16	0.14

Table 2.24: Relative permittivity of rubber granulate blue.

2.4.6 Soluble granulate

Group of natural minerals soluble in water

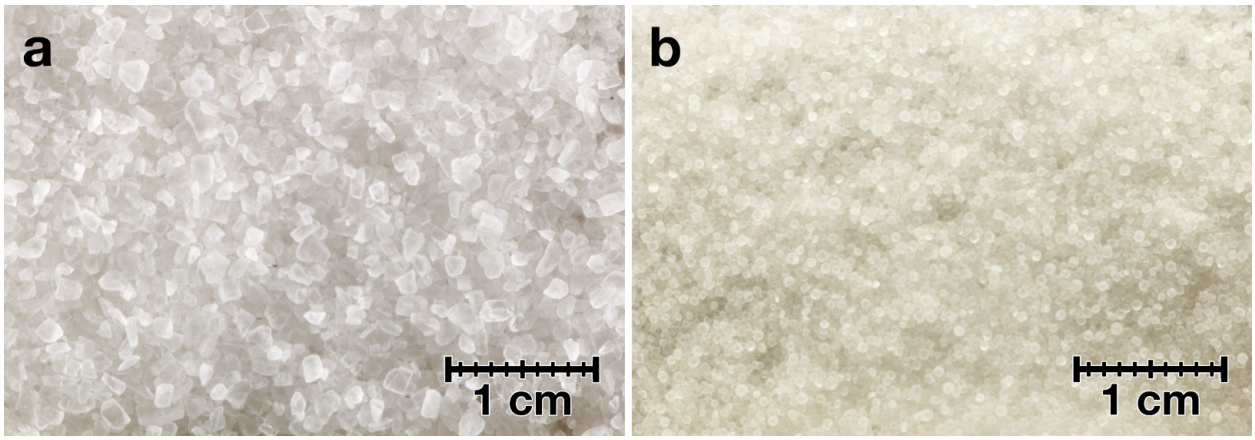

Figure 2.41: Macro photo of granular salts. (a) Salt grit. (b) Table salt.

2.4.6.1 Salt grit

Material description:

White to slightly translucent, sharp angular grains (Figs. 2.41a, 2.42). Commonly used as a de-icing salt.

Application and handling:

Can be used to model brittle upper crust. The angular grains interlock and have high overall shear strength. Dissolvable material can be used in conjunction with water to

model the dissolution of natural rocks. The dissolution of salt from the experiment can take a long time. Initial contact with water causes compaction and capillary creep of the fluid. It can be reused and sieving for experimental preparation is unproblematic.

Measured properties:

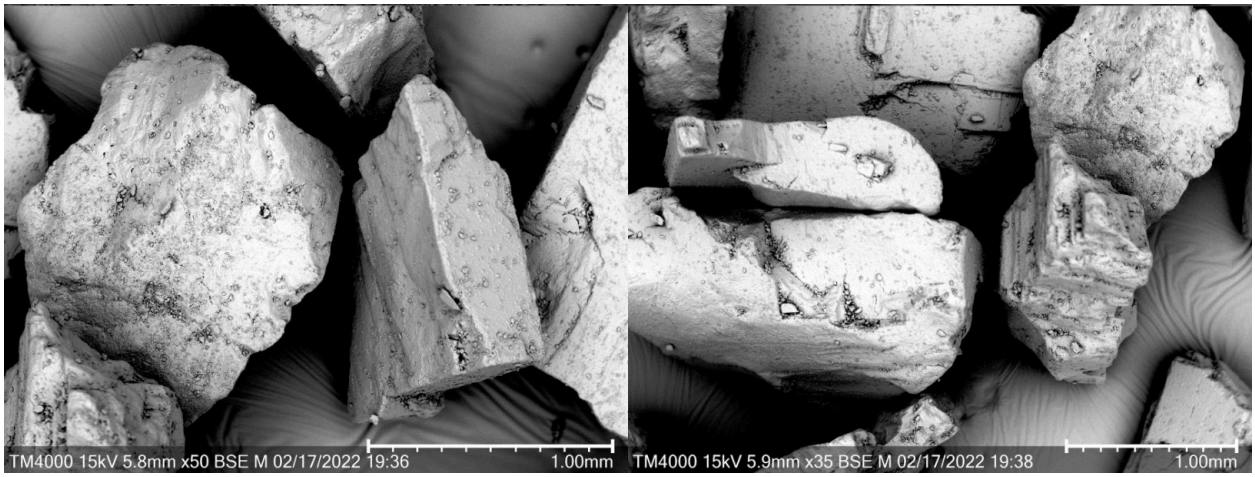

Figure 2.42: SEM images of salt grit at 50x and 35x magnification.

Salt grit - density ρ								Friction angle ϕ	
Grain (kg/m³)	Sifted (kg/m³)	staw	Porosity	Compacted (kg/m³)	staw	Porosity	Δ ρ s-c (kg/m³)	(°)	staw
2160	1207.710	9.51	44.1 %	1221.572	8.18	43.4 %	-13.862	32.719	0.46

Table 2.25: Measured densities, calculated porosities and internal friction angle of salt grit.

Salt grit- relative permittivity ε_r					
GP8800 (0.4-6 GHz)		GSSI (2 GHz)		Mean ε_r	
(ε_r)	staw	(ε_r)	staw	(ε_r)	staw
3.68	0.04	3.52	0.11	3.60	0.12

Table 2.26: Relative permittivity of salt grit.

2.4.6.2 Table salt

Material description:

White to slightly translucent rounded grains (Figs. 2.41b, 2.43). Commonly used as table salt for human consumption.

Application and handling:

Salt can be used to model brittle upper crust. Rounded salt crystals have low friction. Dissolvable material can be used in conjunction with water to model the dissolution of natural rocks. Dissolution of salt from the experiment may take a long time. Initial contact with water causes compaction and capillary creep of the fluid. It may not be reused and sieving for experimental preparation is not easy due to low friction.

Measured properties:

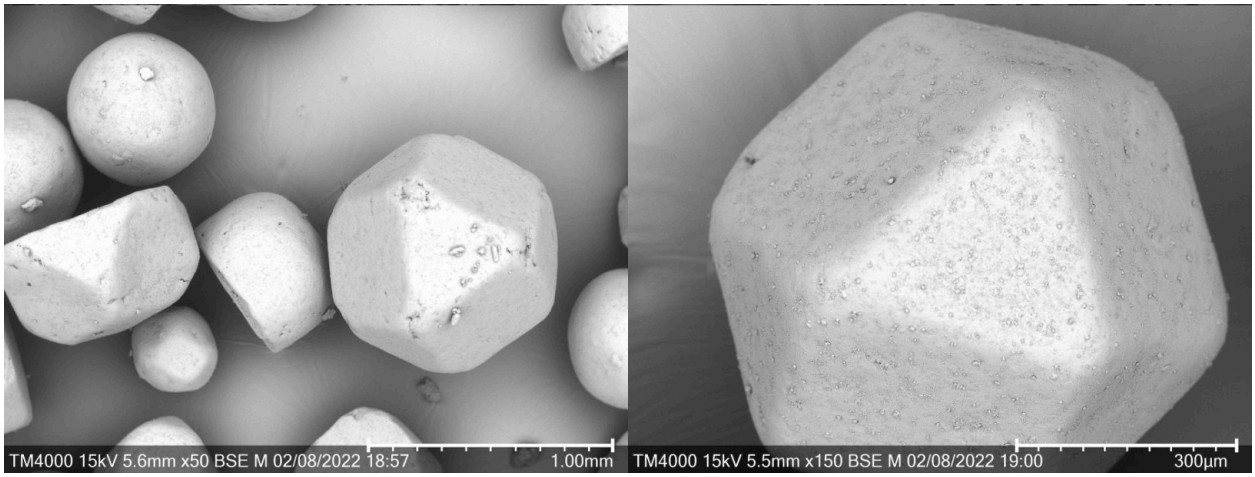

Figure 2.43: SEM images of salt at 50x and 150x magnification.

Salt - density ρ	Friction angle ϕ	
Grain (kg/m³)	(°)	staw
2160	30.503	0.44

Table 2.27: Internal friction angle of salt.

2.4.7 Mixtures

Combination of different material classes or types for the achievement of specific properties

2.4.7.1 G23T DIC

Material description:

White to light beige in colour with black and green coloured marker grains (Figs. 2.44, 2.46). Well sorted, medium-grained fluvial sand with rounded grains. Measured grain size is 100 – 900 µm with a mean of 383 µm (Fig. 2.45). See G23T for material specifications.

Figure 2.44: Macro photo of G23T DIC.

Application and handling:

Also known as the workhorse sand, it is used as the main brittle upper crust analogue material at UHH-Tec. The ratio of added marker grains is optimised for the resolution, distance and adsorption spectra of the DIC cameras used (LaVision GmbH, M-lite 12M CMOS black and white camera 12 megapixel). A mixture of black and green coloured grains is added to the colourless G23T. For every 12 parts of G23T, 1 part of black G23T is added and for every 20 parts of G23T, 1 part of green G23T is added. The white value of the camera used is in the green spectra. Plain G23T will appear as a light grey tone in images. Green grains will appear white and black grains will appear black, providing a clearer separation of the random speckle pattern for DIC. The mixture is easily recycled after experimental runs. Sieving for experimental preparation is straightforward.

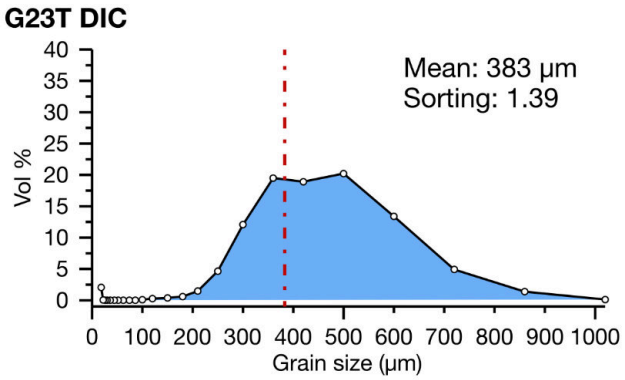

Figure 2.45: Grain size distribution of G23T DIC.

References:

Ring shear test data and material properties are identical to plain G23T described by Ritter et al. (2016). Used as upper crustal analogue by Eisermann et al. (2021).

Measured properties:

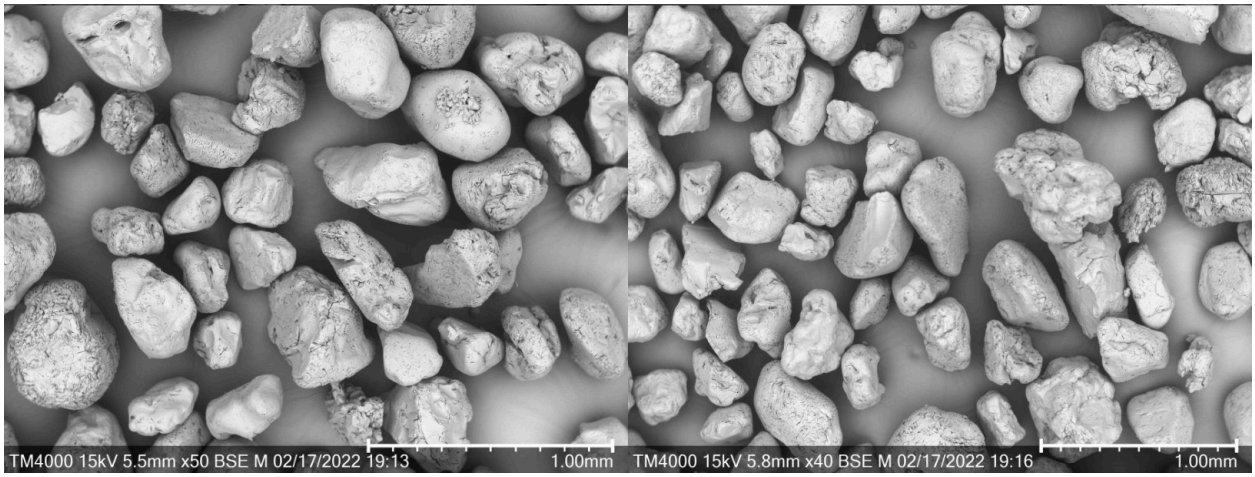

Figure 2.46: SEM images of G23T DIC at 50x and 40x magnification (SEM image cannot resolve colour).

G23T DIC - density ρ								Friction angle ϕ	
Grain (kg/m³)	Sifted (kg/m³)	staw	Porosity	Compacted (kg/m³)	staw	Porosity	$\Delta \rho$ s-c (kg/m³)	(°)	staw
2680	1656.016	9.19	38.2 %	1676.618	6.67	37.4 %	-20.602	31.241	0.52

Table 2.28: Measured densities, calculated porosities and internal friction angle of G23T DIC.

G23T DIC - relative permittivity ε_r					
GP8800 (0.4-6 GHz)		GSSI (2 GHz)		Mean ε_r	
(ε_r)	staw	(ε_r)	staw	(ε_r)	staw
3.26	0.11	3.14	0.15	3.20	0.14

Table 2.29: Relative permittivity of G23T DIC.

2.4.7.2 G12T Elastic

Material description:

White to light grey in colour with black and green rubber granules (Fig. 2.47). Moderately sorted, medium-grained fluvial sand with rounded grains. Measured grain size is 90 – 650 µm with a mean of 270 µm (Fig. 2.48). See G12T and rubber granules for material specifications.

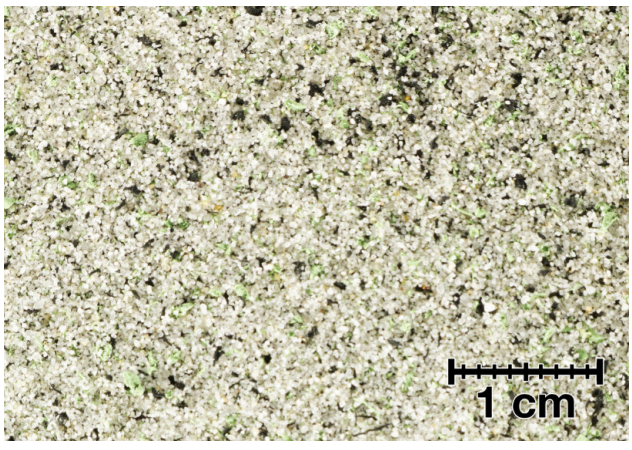

Figure 2.47: Macro photo of G12T Elastic.

Application and handling:

It is used as a brittle upper crust analogue material at UHH-Tec and qualifies as a second-generation workhorse sand and as an improved successor to G23T DIC. Material mix consists of 1 part black rubber granules for every 12 parts G12T quartz sand and 1 part green rubber granules for every 15 parts G12T. The added rubber granules act as markers for DIC image post-processing. Adding rubber reduces the overall density. The finer grain size of the G12T improves resolution of fine structures. The rubber adds elasticity to the otherwise non-elastic quartz sand. Mixture is easily recycled after experimental runs however vacuuming leads to separation between rubber and sand. Sieving for experimental preparation is somewhat possible. Handling and sifting the sand causes electrostatic charging. The grains are small enough to be attracted to surfaces by the electrostatic charge and stick to utensils and surfaces.

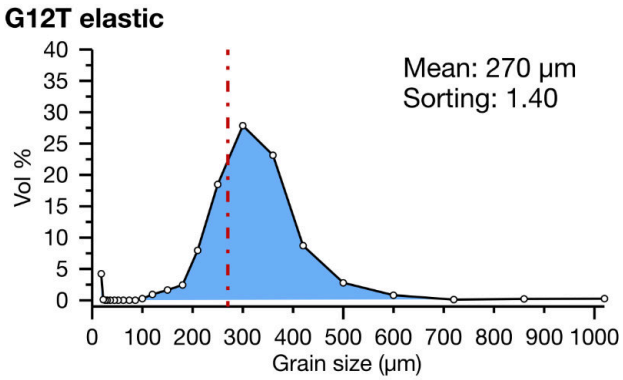

Figure 2.48: Grain size distribution of G12T Elastic.

References:

Properties related to those published by Rosenau et al. (2009).

Measured properties:

G12T elastic - density ρ					Friction angle ϕ	
Sifted (kg/m³)	staw	Compacted (kg/m³)	staw	Δ ρ s-c (kg/m³)	(°)	staw
1279.886	6.76	1409.360	12.02	-129.474	32.547	0.65

Table 2.30: Measured densities and internal friction angle of G12T Elastic.

2.4.7.3 Flour 2:1

Material description:

White, opaque, pale beige powder with black and green coloured quartz marker grains, poorly sorted with spherical to aggregated grains (Figs. 2.49, 2.51). Measured grain size is 0.5 – 800 µm with a mean of 80 µm (Fig. 2.50). See flour and G23T for individual compound properties.

Figure 2.49: Macro photo of flour 2:1.

Application and handling:

The mixture is used as a slightly cohesive, non-toxic, brittle upper crust analogue. It sieves easily into uniform layers and is designed for modelling isostasy-controlled crater modification processes. Cohesion and fine grain size resolve even the smallest structures in detail. The mixture of 1 part of G23T with 2 parts of flour to achieve a specific target bulk density of 961.5 kg/m^3 which is slightly below the density of PDMS (see 2.4.8.2). The colour of the added marker grains is optimised for the resolution, distance and adsorption spectra of the DIC cameras used (LaVision GmbH, M-lite 12M CMOS black and white camera 12 megapixel). Black and green coloured grains are added to the colourless flour for DIC compatibility. For every 2 parts of flour, ½ part of black G23T and ½ part of green G23T is added. The white value of the cameras is in the green spectra. Plain flour will appear as a light grey tone in the images. Green grains will appear white, and black grains will appear black, giving a clearer separation of the random speckle pattern for DIC. The mixture has a very high albedo. Flour is highly hygroscopic and changes its properties with adsorbed water content. The mixture is easily recycled after experimental runs. Working with flour can cause significant dust generation. Handling and sifting flour causes electrostatic charging. The grains are small enough to be attracted to surfaces by the electrostatic charge and stick to utensils and surfaces.

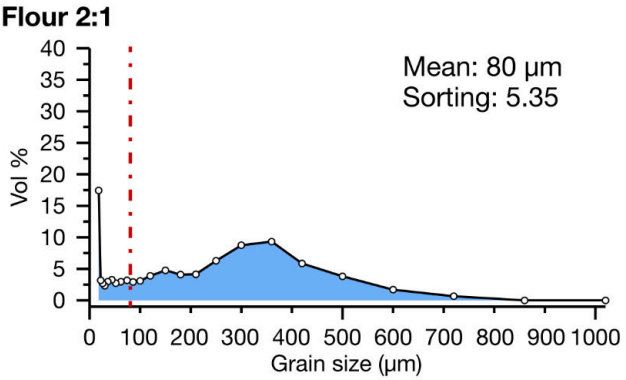

Figure 2.50: Grain size distribution of flour 2:1.

Measured properties:

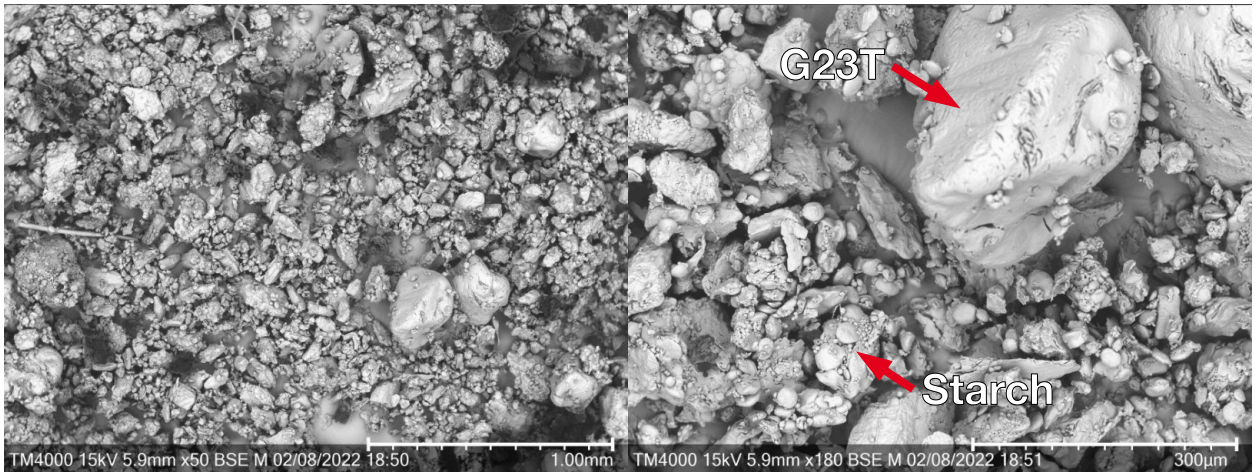

Figure 2.51: SEM images of flour 2:1 at 50x and 180x magnification (SEM image cannot resolve colour).

Flour 2:1 - density ρ					Friction angle ϕ	
Sifted (kg/m³)	staw	Compacted (kg/m³)	staw	Δ ρ s-c (kg/m³)	(°)	staw
961.558	5.87	1132.780	18.22	-171.222	46.390	0.63

Table 2.31: Measured densities and internal friction angle of flour 2:1.

Flour 2:1 - relative permittivity ε_r					
GP8800 (0.4-6 GHz)		GSSI (2 GHz)		Mean ε_r	
(ε_r)	staw	(ε_r)	staw	(ε_r)	staw
3.34	0.05	3.46	0.17	3.40	0.13

Table 2.32: Relative permittivity of flour 2:1.

Flour 2:1 - Cohesion and friction coefficient (n = 135)				
	Cohesion (Pa)	staw	Friction coefficient	staw
Initial	108.41	54.15	0.655	0.020
Stable sliding	79.43	42.55	0.622	0.019
Reactivation	87.85	58.39	0.677	0.022

Table 2.33: Cohesion of flour 2:1 derived from ring-shear test results.

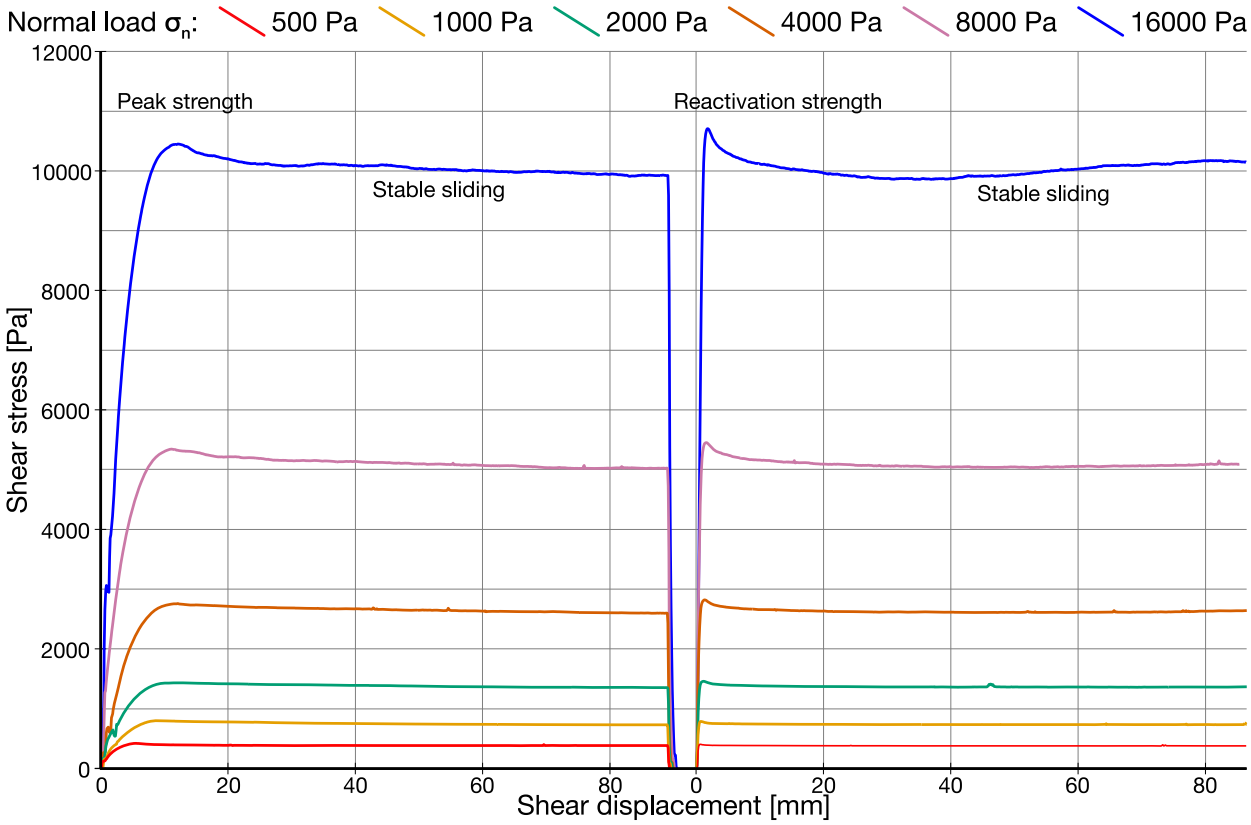

Figure 2.52: Shear stress - displacement curve (shear curve) for flour 2:1 under different normal loads.

2.4.7.4 Flour 1:1

Material description:

White, opaque, slightly beige powder with black and green coloured quartz markers, poorly sorted with spherical to aggregated grains. See Flour and G23T for individual compound characteristics.

Application and handling:

This is a higher-density version of the 2:1 flour mix. It is used as a slightly cohesive, non-toxic, brittle top crust analogue and sieves easily into uniform layers. Its high cohesion and fine grain size resolve even the smallest structures in detail. The mixture of 1 part G23T and 1 part flour as achieved by adding black and green coloured grains to the colourless flour for DIC compatibility. For each part of flour, ⅓ part of black G23T, ⅓ part of green G23T and ⅓ part of colourless G23T is added. Flour is highly hygroscopic and changes its properties with adsorbed water content. Working with flour can cause significant dust generation. The mixture is easily recycled after experimental runs. Handling and sifting flour causes electrostatic charging. The grains are small

enough to be attracted to surfaces by the electrostatic charge and stick to utensils and surfaces.

Measured properties:

Flour 1:1 - Cohesion and friction coefficient (n = 135)				
	Cohesion (Pa)	staw	Friction coefficient	staw
Initial	115.77	71.08	0.652	0.026
Stable sliding	82.77	81.71	0.618	0.028
Reactivation	117.42	155.76	0.665	0.054

Table 2.34: Cohesion of flour 1:1 derived from ring-shear test results.

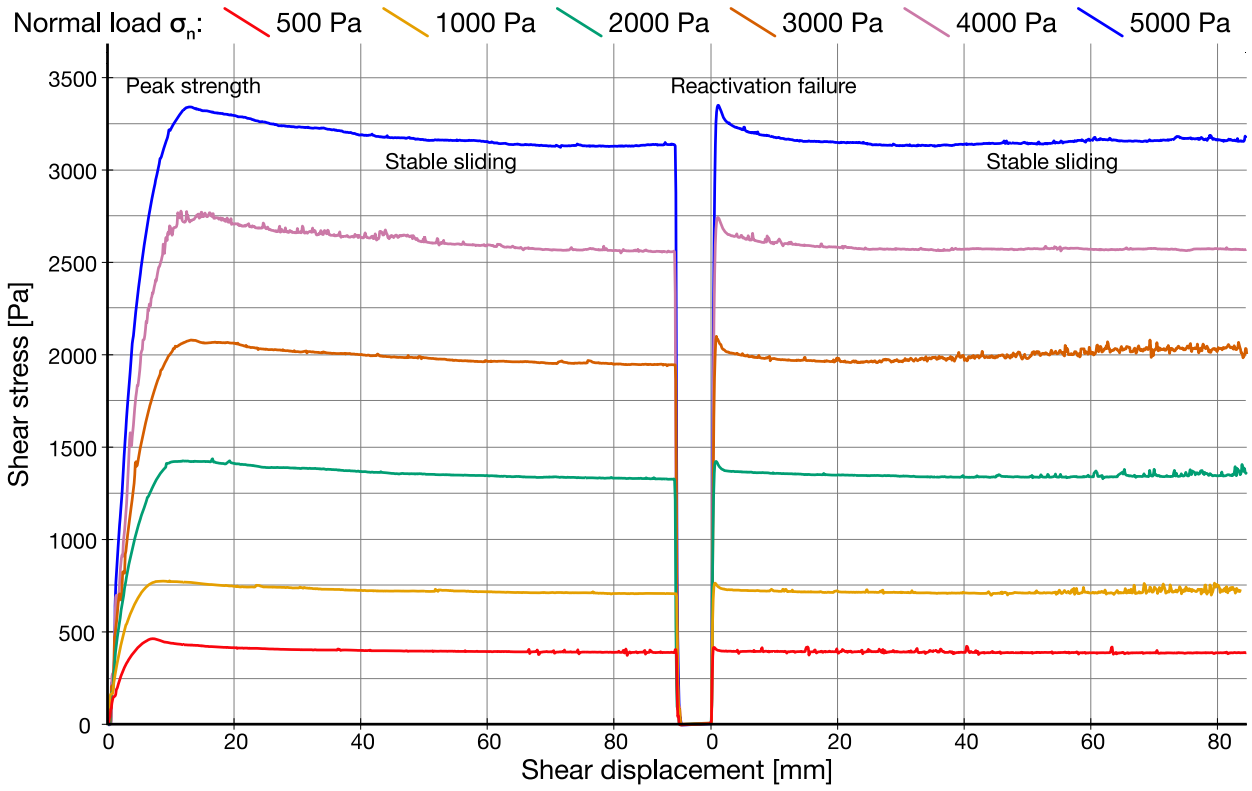

Figure 2.53: Shear stress - displacement curve (shear curve) for of flour 1:1 under different normal loads.

2.4.8 Viscous materials

Brief list of viscous materials used in the UHH-Tec laboratory

2.4.8.1 Water

Material description:

Tap water is used as a reference for our measurements of density.

Measured properties:

Tap water - density ρ		Tap water - relative permittivity
Density (kg/m^3)	staw	(ε_r)
1003.020	2.998	81

Table 2.35: Density of water mesured in the cylinder. Permittivity value from the literature.

2.4.8.2 PDMS

Material description:

Transparent, high-viscosity newtonian fluid. Polydimethylsiloxane (PDMS) type Korasilon® G30M supplied by Kurt Obermeier GmbH, Germany.

Application and handling:

High-viscosity fluid often used to model ductile lower crust or salt. Leaves stains on surfaces when wiped off. Materials can be easily recycled after experimental runs without any changes in material properties.

References:

Detailed rheological description by Rudolf et al. (2016).

Properties:

Specific density of $\rho = 967$ kg/m^3, viscosity $\eta = 3 \times 10^4$ Pa s

2.4.8.3 PDMS + corundum

Material description:

Dark reddish opaque high viscosity near-Newtonian fluid. Mixture of PDMS type Korasilon® G30M supplied by Kurt Obermeier GmbH, Germany and fine corundum powder.

Application and handling:

The mixture of 0.94 kg of PDMS (section 2.4.8.2) and 1 kg of fine corundum powder (section 2.4.2.1) is used as the primary application for experiments imaged by CT-Scans. The addition of corundum powder to PDMS increases the bulk density and viscosity. The

increased density enhances the contrast while imaging (Zwaan & Schreurs, 2017). Over periods of several months, corundum particles sink to the bottom and separate from the mixture. Material preparation is very time consuming as the two components do not easily mix. It leaves stains on surfaces when being wiped off. Materials can be easily recycled multiple times without any changes in material properties. The mixture is highly abrasive, which can increase wear on clear acrylic glass and mechanical components.

References:

Detailed rheological description published by Zwaan et al. (2018). Application as lower crustal analogue by Eisermann et al. (2021).

Properties:

Specific density $\rho = 1603$ kg/m^3, viscosity $\eta = 1.5 \times 10^5$ Pa s

2.4.8.4 Laponite

Material description:

Transparent to slightly blue tinted water-based gel with controllable viscosities based on the concentration of laponite. Laponite-RD is supplied as a white powder by BYK-Chemie GmbH, Germany. It is used as a rheological additive.

Application and handling:

Synthetic clay-based rheological adaptive additive mixed with deionised water to form a gel with complex viscoelastic-plastic rheology. The viscosity depends on the % wt concentration of suspended Laponite-RD. Depending on targeted viscosity, it can be used as a brittle upper crust and a viscous lower crust analogue. High viscosity solutions are difficult to prepare and handle. In higher viscosity solutions, adaptive materials such as expanded glass or corundum can be suspended to change the density without settling. Evaporation of water will affect the resulting viscosity and properties over short periods of time. Freezing of the material is not possible due to uneven expansion leading to cracking and undesired extrusion. The material can be used multiple times.

References:

Material properties and rheology have been characterised by Arachchige et al. (2021).

2.5. Discussion

2.5.1 Ring shear data

Shear curves of flour 2:1 show moderate strain hardening prior to initial failure, especially at low normal loads associated with compaction of the loose flour (Fig. 2.52). Initial failure peaks occur just above stable sliding. At low normal loads, deformation passes directly to plastic deformation. Upon reactivation, the mixture barley shows any strain hardening as the material is already fairly compacted. On reactivation, 2:1 flour shows a much higher reactivation strength proportional to the normal load. Failure on reactivation quickly leads to stable sliding (Fig. 2.52). Conversely, flour 2:1 has a higher reactivation strength than the initial failure. This is due to the high degree of compaction at initial failure and stable sliding. As the normal load increases, work hardening causes the reactivation strength to be higher than the initial failure strength. The extrapolated cohesion of flour 2:1 is initially about 108 Pa and decreases after compaction (Table 2.33).

The shear curves of flour 1:1 are comparable to flour 2:1. Strain hardening occurs prior to initial failure, particularly at low normal loads. Initial failure peaks are just above stable sliding (Fig. 2.53). On reactivation, the mixture barley shows any strain hardening. On reactivation, flour 1:1 shows significant reactivation strength proportional to normal load. Failure on reactivation quickly leads to stable sliding (Fig. 2.53). Conversely, flour 1:1 has a higher reactivation strength than the initial failure. This is due to the high degree of compaction at initial failure and stable sliding. The reactivation strength is higher than the initial failure strength. The extrapolated cohesion of flour 1:1 is initially about 115 Pa and decreases after compaction (Table 2.34).

Measurements conducted with the ring-shear tester provided us with valuable insights into the specific Mohr-Coulomb failure criterion of the granular flour quartz sand mixtures. Consistent with the assumption of the Mohr-Coulomb failure criterion, the data show a linear increase with normal load. However the failure criterion for initial and reactivation are not parallel (Figs. 2.54, 2.55). The behaviour that both flour-quartz mixtures exhibit are characteristic for materials that weakens by a reduction of internal friction while shearing. This behaviour may be due to starch aggregates, which can separate into individual starch granules when shear is imposed on the grain surface (Fig. 2.30). Flour 2:1 and flour 1:1 mixtures have properties that are unrealistic for nature in terms of reactivation strength at high normal loads. Materials capable of representing natural rocks are expected to exhibit a lower reactivation strength due to pre-weakening from previous localised failure. It is only at the lowest normal load tested that I observe the initial failure strength to be higher than the reactivation strength (Figs. 2.54b, 2.55b). I attribute this effect to the angular grain size of the flour (Fig. 2.30). As compaction increases, the grains are able to interlock more closely, increasing friction. This behaviour should make the interpretation of secondary and reactivated faults in analogue experiments difficult. However, most of the experiments are conducted under low normal loads. The overburden load at the bottom of analogue experiments used to

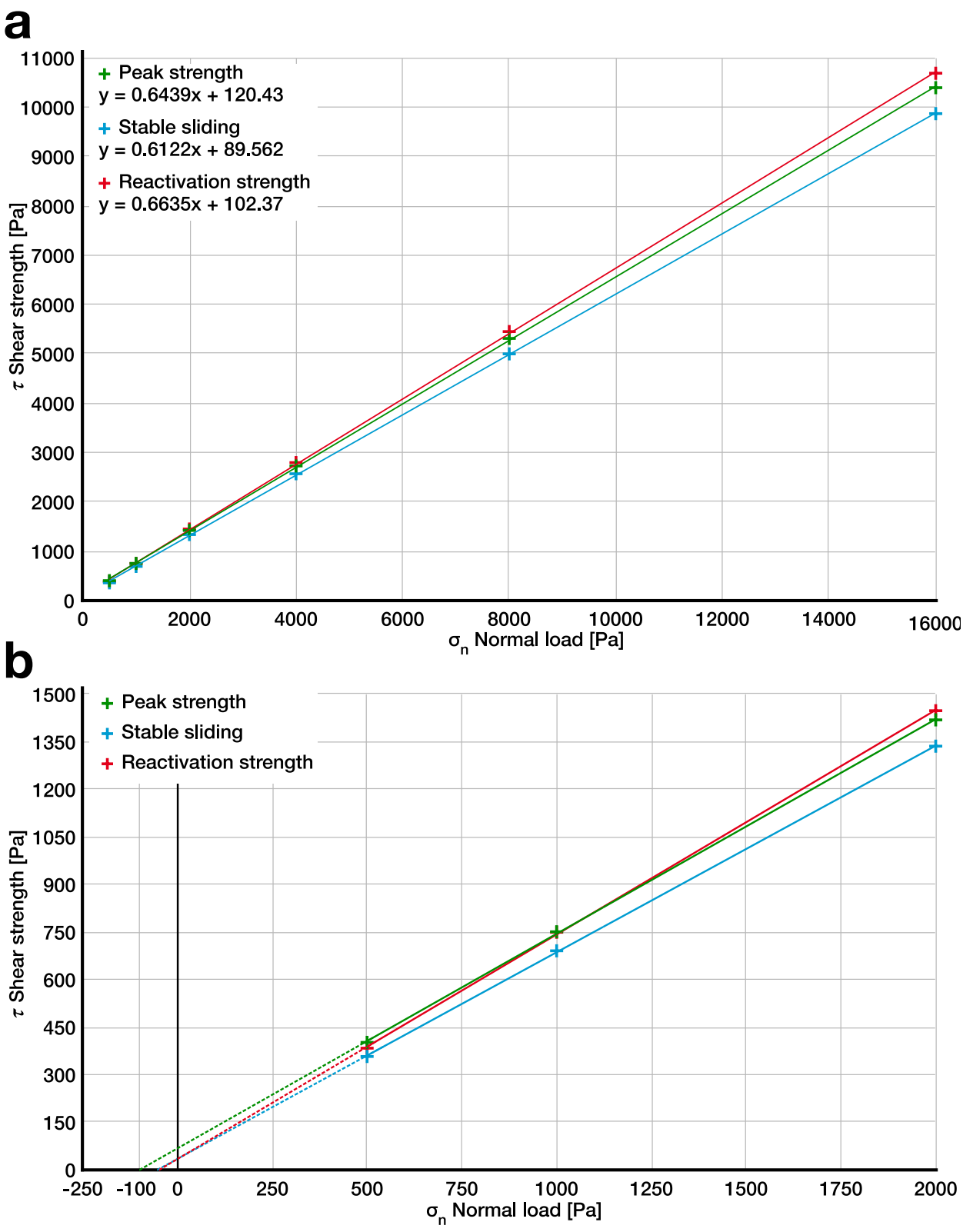

Figure 2.54: Shear strength of flour 2:1 as function of normal load (a) Mohr-Coulomb failure criterion for the full range of tested normal loads. (b) Magnified area of low normal loads with projected behaviour and cohesion at low and negative normal loads.

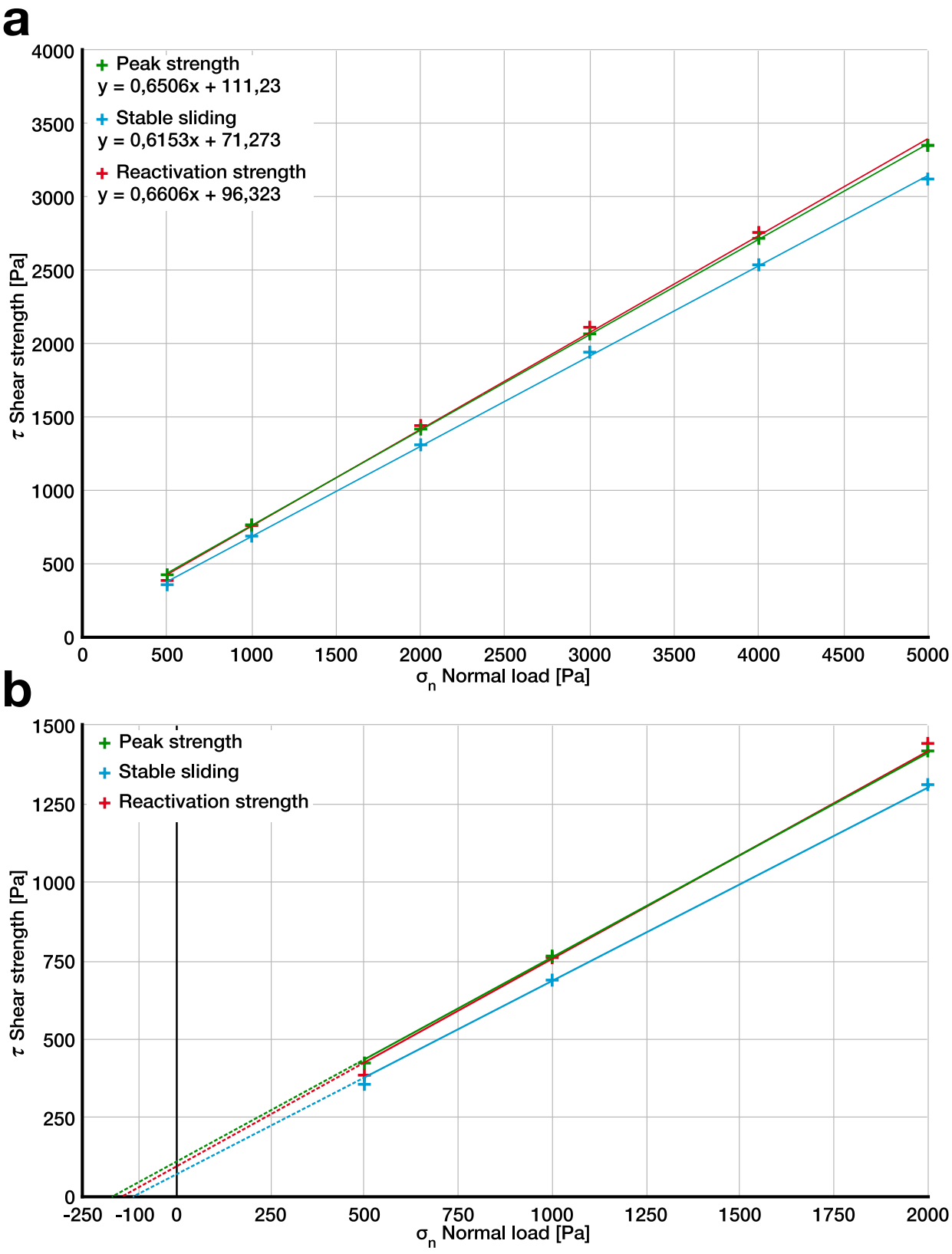

Figure 2.55: Shear strength of flour 1:1 as function of normal load (a) Mohr-Coulomb failure criterion for the full range of tested normal loads. (b) Magnified area of low normal loads with projected behaviour and cohesion at low and negative normal loads.

model crater modification processes range between 1 – 3 cm resulting in normal load of approximately 94 Pa to 282 Pa (ρgh = 961 kg/m^3 × 9.81ms^{-2} × h). At these low levels of overburden loading, the predicted Mohr-Coulomb criterion for reactivation is lower than the initial failure. The effects observed at higher normal loads are not significant for most experimental setups due to its low bulk density. This makes it a valid analogue material even for second order faults. Both mixtures do not exhibit excessively high cohesion values compared to quartz sand (Tables 2.33, 2.34). As the quartz sand content is reduced, an increase in cohesion is observed. It can still be compared to the most cohesive quartz sands, which are in the range of 20 – 100 Pa (Klinkmüller et al., 2016).

2.5.3 Material relative permittivity

GPR works by measuring the time between the transmitted electromagnetic pulse and the received reflection, known as the two-way travel time (TWT) (Fig. 2.2). To calculate the true depth of a reflection, the propagation velocity of the electromagnetic wave needs to be known. The relative permittivity (ε_r) can be used to estimate how fast electromagnetic waves travel through a homogeneous material. The higher the relative permittivity, the slower an electromagnetic wave travels through the material and vice versa. The specific relative permittivity (ε_r) of a given material is important for the interpretation of GPR measurements. This is especially true when interpreting multilayer analogue experiments. A reflection is produced at the interface when the relative permittivity changes. The strength of the reflection is proportional to the difference in relative permittivity at a material interface. The larger the contrast, the larger will be the reflected electromagnetic energy. In addition, the transition from higher to lower and vice versa affects the amplitude of the reflected electromagnetic wave. A transition from a higher to a lower relative permittivity will produce a negative reflection. A transition from a material with a lower dielectric constant to a material with a higher dielectric constant produces a positive reflection. The range of permittivity values ranges from 1 for air to 81 for water. The differences in relative permittivity between the most commonly used analogue materials tend to be small (Table 2.36). These small differences produce only weak reflections, rendering their detection difficult. Brittle materials used in analogue modelling tend to be highly porous, making it almost impossible to detect reflections from small air-filled cracks. In general, analogue materials are not well suited for GPR to adequately image subsurface processes. Because analogue materials are selected for their mechanical properties to suit a particular experiment, it is not easy to consider the correct relative permittivity contrasts required for GPR measurements. While additives such as iron powder or corundum used in CT scanning can diminish the problem, the experimental design may need to be severely compromised.

$\Delta\varepsilon_r$	Air	Expanded glass	Rubber blue	Rubber green	Flour	G23T	G23T DIC	G12T	Flour 2:1	Salt grit	Starch	Spheres course	Spheres fine	Corundum	Tap water
Air	0	0.87	1.16	1.25	1.94	2.16	2.20	2.23	2.40	2.60	2.67	3.00	3.25	3.30	80.00
Expanded glass	-0.87	0	0.29	0.38	1.07	1.29	1.33	1.36	1.53	1.73	1.80	2.13	2.38	2.43	79.13
Rubber blue	-1.16	-0.29	0	0.09	0.78	1.00	1.04	1.07	1.24	1.44	1.51	1.84	2.09	2.14	78.84
Rubber green	-1.25	-0.38	-0.09	0	0.69	0.91	0.95	0.98	1.15	1.35	1.42	1.75	2.00	2.05	78.75
Flour	-1.94	-1.07	-0.78	-0.69	0	0.22	0.26	0.29	0.46	0.66	0.73	1.06	1.31	1.36	78.06
G23T	-2.16	-1.29	-1.00	-0.91	-0.22	0	0.04	0.07	0.24	0.44	0.51	0.84	1.09	1.14	77.84
G23T DIC	-2.20	-1.33	-1.04	-0.95	-0.26	-0.04	0	0.03	0.20	0.40	0.47	0.80	1.05	1.10	77.80
G12T	-2.23	-1.36	-1.07	-0.98	-0.29	-0.07	-0.03	0	0.17	0.37	0.44	0.77	1.02	1.07	77.77
Flour 2:1	-2.40	-1.53	-1.24	-1.15	-0.46	-0.24	-0.20	-0.17	0	0.20	0.27	0.60	0.85	0.90	77.60
Salt grit	-2.60	-1.73	-1.44	-1.35	-0.66	-0.44	-0.40	-0.37	-0.20	0	0.07	0.40	0.65	0.70	77.40
Starch	-2.67	-1.80	-1.51	-1.42	-0.73	-0.51	-0.47	-0.44	-0.27	-0.07	0	0.33	0.58	0.63	77.33
Spheres course	-3.00	-2.13	-1.84	-1.75	-1.06	-0.84	-0.80	-0.77	-0.60	-0.40	-0.33	0	0.25	0.30	77.00
Spheres fine	-3.25	-2.38	-2.09	-2.00	-1.31	-1.09	-1.05	-1.02	-0.85	-0.65	-0.58	-0.25	0	0.05	76.75
Corundum	-3.30	-2.43	-2.14	-2.05	-1.36	-1.14	-1.10	-1.07	-0.90	-0.70	-0.63	-0.30	-0.05	0	76.70
Tap water	-80.00	-79.13	-78.84	-78.75	-78.06	-77.84	-77.80	-77.77	-77.60	-77.40	-77.33	-77.00	-76.75	-76.70	0

Table 2.36: Matrix for determining the difference in relative permittivity (ε_r) at a layer interface. The rows represent the source material and the columns the target material. By selecting a starting material in the row and finding the target material in the column, the overlapping cell will indicate the difference in relative permittivity. Low values will produce weak reflections, indicating a minimal impedance mismatch between the two materials. Negative values in the matrix indicate that the reflected wave undergoes a phase reversal.

2.5.4 Grain size distribution

The range of grain sizes was measured by laser diffraction. This method works best for opaque, individual, rounded to angular grains, as the clarity of the diffraction pattern is related to the optical properties of a material. This is generally not an issue for the most common analogue materials such as quartz sand or corundum. As the measurements require the use of a water-based suspension medium, water-soluble materials such as salts cannot be measured as they would dissolve. In addition, determining the grain size of the transparent glass spheres is challenging as they not only transmit light but also actively diffract and reflect light due to their round shape. However, the measurements we obtained were sufficiently consistent with the manufacturer's quoted grain size range that I decided to include them. The fine glass spheres show fractions of grain sizes in the 150 – 500 µm range that should not be present (Fig. 2.20). From the SEM images it appears that the larger grain size is due to contamination with larger spheres, but their grain size is not related to the coarse spheres (Fig. 2.21). This may, therefore, be attributed to measurement artefacts and/or contamination. However, the mean grain size is within the expected range. The measurement of organic grains is challenging as they often form aggregates or, as in the case of rubber, have elongate shapes (Fig. 2.36). Grain sizes for these materials cannot be determined with high accuracy as their orientation in the suspension affects the measurement. I have included these measurements as I expect the random orientation of elongate aggregates to be a representative average of the expected grain size.

2.6. Conclusion

The study of laboratory-scale geodynamic processes begins with experimental design, which includes the choice of materials. Material science is a fundamental aspect of modern quantitative analogue modelling. New materials are constantly being identified and added to the list of possible crustal analogues. Different disciplines such as physics and sedimentology are involved. Knowledge of physical material properties is a prerequisite for proper scaling of experiments and their comparability to nature. The preparation and execution of practical experiments requires not only knowledge of physical parameters, but also practical skills acquired through hands-on experience. To ensure transparency and comparability between laboratories, I present a comprehensive catalogue of materials used at the UHH-Tec laboratory at Universität Hamburg, Germany, which serves both as a detailed reference for studies performed in the laboratory. It also serves as a practical reference for users of such laboratories. It should be noted that each material is unique and suitable for different applications. Thus, a general comparison between individual materials is not meaningful.

2.6.1. Disclosure of competing interests

G12T and G23T were provided to us free of charge by Schlingmeier Quarzsand GmbH & Co. KG. The expanded glass was provided free of charge by Liaver GmbH & Co. KG, Germany. The materials supplied by ARTEKA e.K., Germany, were purchased on a regular basis. All materials were provided for scientific research purposes. No oversight of the above companies was exercised during the data collection.

3. Structural consequences of sill formation below lunar craters inferred from scaled analogue experiments

Abstract

Localized deformation in form of radial and concentric crater floor fractures are prominent post-cratering structural vestiges of lunar impact craters. Two mechanisms were proposed to explain the formation of floor fractures: isostatic re-equilibration of crust underlying crater floors, and emplacement of horizontal igneous sheets below craters. Due to thick and cool lunar upper crust, the latter mechanism has been regarded as the more likely. I used scaled analogue experiments to model the deformational behaviour of upper crust following crater formation, in order to explore the structural and kinematic consequences of sill formation below crater floors with different depths and diameters. Granular material simulating the Moon's brittle upper crust was filled into a tank. Craters with specified morphologies, depths and radii were excavated into the material by a rotating blade. Sills were simulated by variably sized flat, circular balloons, emplaced into the granular material below model craters and inflated by a pumped-in fluid. For each experiment, the sill was first inflated and then deflated to model intrusion and evacuation of magma, respectively. Surface deformation within the crater was monitored, allowing us to quantify key parameters including surface uplift and the distribution and evolution of strain. Our experiments showed that inflation of balloons caused radial and concentric dilatational fractures after inflation in the overlying granular material. Fracture patterns were more controlled by the depth of balloons below the surface rather than by crater floor morphology. For the duration of fluid inflation into shallow model sills, surface uplift was focused on the crater centre and associated with prominent polygonal fracture patterns. Upon deflation, concentric normal faults developed at the inner crater rim, consistent with the terraced crater margins ubiquitously observed at lunar craters. Interestingly, model craters are characterised by more diverse fracture patterns compared to lunar craters. These diverse fracture patterns may develop from brittle deformation above sills during inflation, allowing for magma to immediately erupt from natural sill reservoirs. Therefore, I conclude that it is

unlikely that natural lunar sill systems attain the structural maturity of our modelled equivalents. Hence, evacuation during inflation in natural systems can account for the presence of less prominent fracture patterns compared to the ones in modelled, more "mature" sill systems.

3.1. Introduction

Impact cratering is one of the most universal geodynamic processes in the Solar System (Kenkmann et al., 2014). The collision of solid matter has affected every planetary body. The result of such collisions leaves well recognisable morphological features in the form of impact craters. The pristine morphology of craters is best seen on rocky bodies that are largely free of atmospheric and endogenetic processes, such as the Moon (Shoemaker, 1962). Since the invention of the telescope, the characteristics of lunar craters have been studied and described in detail. Apollo and Lunar Reconnaissance Orbiter data have provided increasingly detailed information on lunar craters. One notable observation is a class of more than 170 lunar impact craters characterised by anomalously flat and shallow floors cut by fractures, known as Floor-Fractured Craters (FFC) (Hall et al., 1981; Jozwiak et al., 2015). Lunar FFCs are up to 300 km in diameter, and therefore primarily affect complex crater morphologies with central peaks and terraced crater walls (Jozwiak et al., 2012). The average diameter of lunar FFCs is 62 km (Jozwiak et al., 2015). A characteristic, morphological attribute within FFCs are radial and/or concentric oriented Crater Floor Fractures (CFF), which can be tens of kilometres long (Baldwin, 1968; Schultz, 1976; Hall et al., 1981; Jozwiak et al., 2012; Jozwiak et al., 2015; Pathak et al., 2021; Luzzi et al., 2023). Other structures observed in FFCs include moats, ridges and patches or fillings of mare material (Jozwiak et al., 2012). In addition, most craters have distinct terraced rim margins. Understanding the development of FFCs is of great interest to better understand the magmatic history of the Moon.

Impact cratering is typically considered to be a rapid process, occurring in a matter of minutes (Melosh, 1989; Kenkmann et al., 2014). The CFFs and the other observable structures of lunar FFCs are generally considered to be prominent post-crater structural vestiges that form in a not well constrained time frame after the impact event (Hall et al., 1981). There are two main conceptual models for the formation of FFCs: isostatic re-equilibration of the crust beneath the crater floor (Hall et al., 1981; Wichman & Schultz, 1993; Riller, 2005; Hecht et al., 2008) and emplacement of horizontal igneous sheets beneath the crater floor (Fig. 3.1; Schultz, 1976; Michaut, 2011; Jozwiak et al., 2012; Thorey & Michaut, 2014; Jozwiak et al., 2015). Both mechanisms are assumed to be

independently capable of uplifting the crater floor, resulting in radial stretching of the crater floor achieved by extensional fractures. Isostatic re-equilibration of the crust beneath large craters is attributed to the sudden mass deficit caused by the ballistic ejection of target rock during cratering (Melosh, 1989). This process requires a lithosphere capable of viscous deformation. Upward flexing of the crater floor is thought to be compensated by subsidence of the crater rim and periphery (Hall et al., 1981). The 'igneous intrusion model' is based on the presence of lava flows, which are commonly found in and around large lunar craters, and in the proximity of CFFs to mare regions (Jozwiak et al., 2012). Due to the thicker and cooler lunar upper crust, the igneous intrusion mechanism is considered more plausible by previous authors to explain the formation of CFFs in lunar craters (Zuber et al., 1994; Wichman & Schultz, 1995; Michaut, 2011; Jozwiak et al., 2012; Jozwiak et al., 2015; Walwer et al., 2021).

On impact, energy is transferred from the projectile to the ground. The initial shock wave compresses the target rock. This is followed by the excavation phase, during which the crater is formed. Some of the target rock is ejected. Shock-induced unloading causes impact melt to form and accumulate in the crater. The shock wave fractures the rock forming a brecciated lens below the crater (Collins et al., 2012; Kenkmann et al., 2014). The remaining excavation of the crater cavity causes local crustal unloading, which has the potential to generate melt and initiate magma ascent within the lunar crust (Michaut & Pinel, 2018; Walwer et al., 2021). Decompression due to surface unloading creates a relative magma overpressure that facilitates magma movement in existing fractures. The magma travels in a dike before transitioning into a sill (Fig. 3.1a; Michaut et al., 2020; Walwer et al., 2021). When the dyke encounters the brecciated, less dense region below the crater, the magmatic driving pressure is insufficient to continue vertical magma propagation, but the pressure in the stalled dyke below the crater still exceeds the local

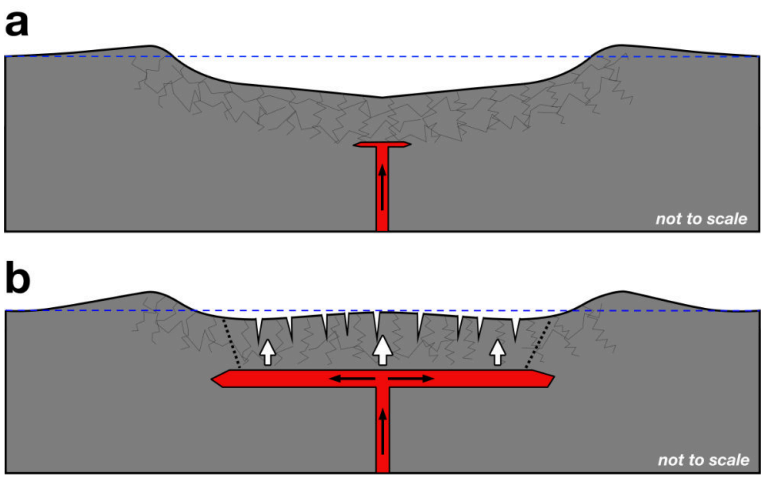

Figure 3.1: Schematic diagram outlining the emplacement of horizontal igneous sheets beneath the crater floor; one of two main conceptual models for the formation of FFCs and the focus of investigation of this research. (a) Crater profile before the onset of crustal relaxation. Melt rises as a dike until it stalls below the fracture lens in the target rock. (b) Stalled melt expands horizontally, uplifting the crater floor. Stretching of the uplifted crater floor causes brittle extensional fractures.

lithostatic pressure (Head & Wilson, 2017). The sill does not propagate beyond the diameter of the crater because of increased overburden pressure from the crater wall and rim, which pinch off the sill (Jozwiak et al., 2015). The sill then continues to inflate, lifting and fracturing the brittle crater floor (Fig. 3.1b).

Earth analogues of dykes have shown that topography-related stress perturbations can influence magma pathways (Michaut et al., 2020). Previous studies of sill induced FFC formation have been limited by considering only 2D systems or low-resolution numerical modelling (Wichman & Schultz, 1995; Jozwiak et al., 2012; Thorey & Michaut, 2014; Michaut et al., 2020). However, the structural consequences of magmatic inflation on surface deformation in combination with crater morphology have not been systematically analysed in 3D. In this study, I performed scaled analogue experiments to study the surface deformation induced by the emplacement of an intrusion beneath an impact crater. The focus of this study is not to investigate the mechanisms responsible for magma ascent and sill formation in the lunar crust. Rather, I take the emplacement of a horizontal intrusion as the starting point for our structural analysis. I analysed the resulting surface deformation associated with sill inflation and evacuation at different crater diameters: in a shallow q_n = 7.5 km and deep q_n = 15 km location below the crater floor (Walwer et al., 2021).

3.1.1 Lunar examples

Lunar FFCs have distinct morphological characteristics. Most notably, the crater floors are cut by escarpments and chains of pits interpreted as surface expressions of fractures (Baldwin, 1968; Schultz, 1976; Xiao et al., 2010; Luzzi et al., 2023). The manifestation of CFFs can vary greatly in size and scale. CFFs generally do not extend beyond the crater rim and they may be obscured by younger impact craters, ejecta material or maria basalt (Schultz, 1976; Jozwiak et al., 2012; Kimi et al., 2023). The occurrence of FFCs is generally associated with the presence of lunar mare in the vicinity (Fig. 3.2; Jozwiak et al., 2012). Based on gravitational measurements these areas are associated with thinner crust (Thorey & Michaut, 2014; Jozwiak et al., 2015). Positive Bouguer anomalies are associated with FFCs, which were interpreted to be an indication of the presence of dense magma beneath the crater (Thorey & Michaut, 2014; Jozwiak et al., 2015).

Regardless of the extent of visible fracturing, all lunar FFCs have anomalously flat and shallow floors as they differ from fresh impact craters in the predicted ratio of depth to diameter (Pike, 1977). The craters Geminus, Aristoteles, Tycho and Copernicus, with an average diameter of 87.5 km, are prime examples of mare-filled FFCs (Fig. 3.2a). Flat

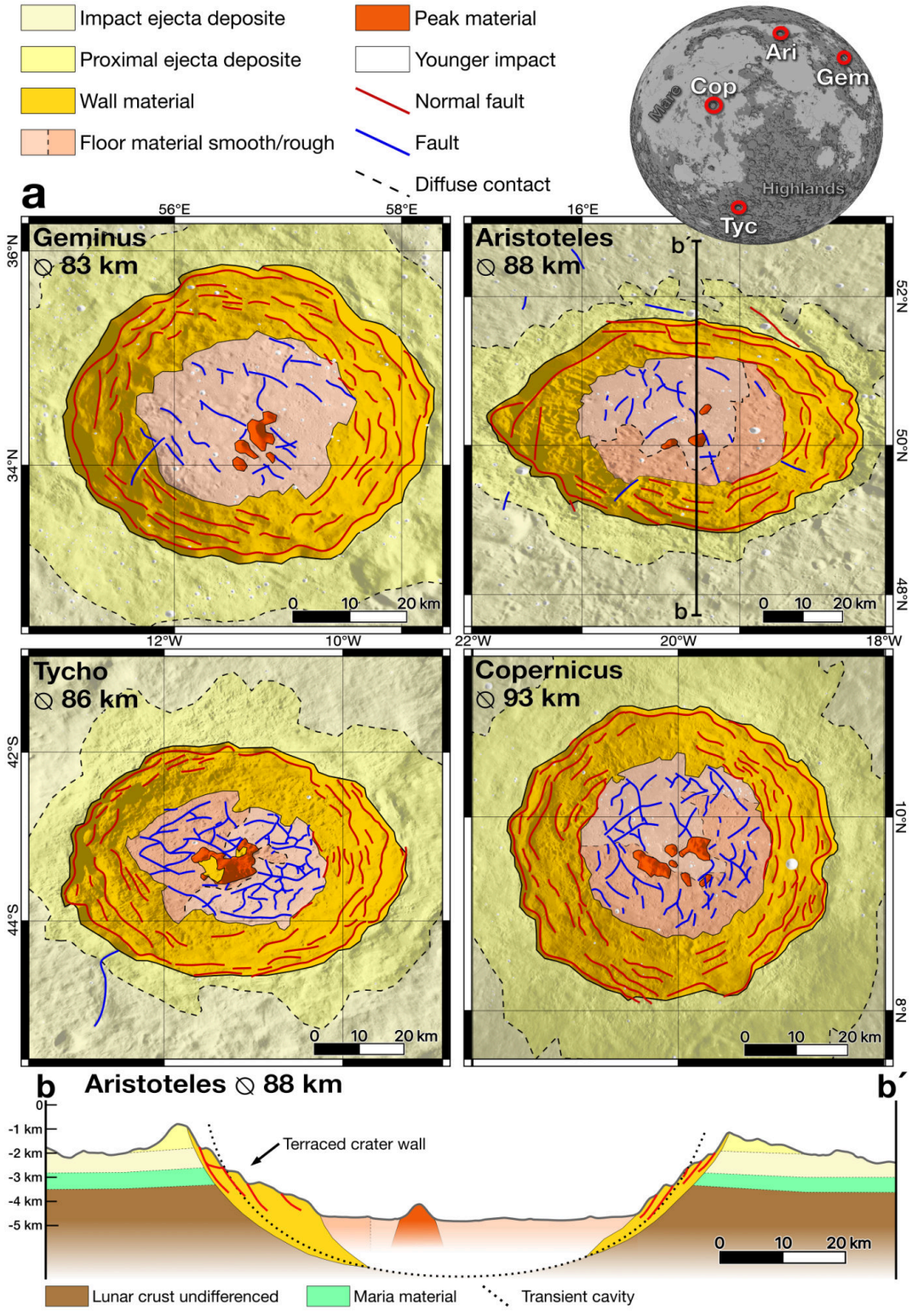

Figure 3.2: Examples of complex floor fractured lunar craters Geminus, Aristoteles, Tycho and Copernicus, showing flat and mare-filled floors. (a) Concentric normal faults of the terraced crater wall are indicated by red lines. Radial and concentric faults are indicated by blue lines. Lithologies and cross section based on USGS Geological Atlas of the Moon: 13, 27, 58, 112. NASA LROC-WAC image data. Ellipticity of crater due to projection. (b) Cross section of Aristoteles crater with interpreted structures based on outcropping lithologies and the USGS Geological Atlas of the Moon. The subsurface structures are not well constrained.

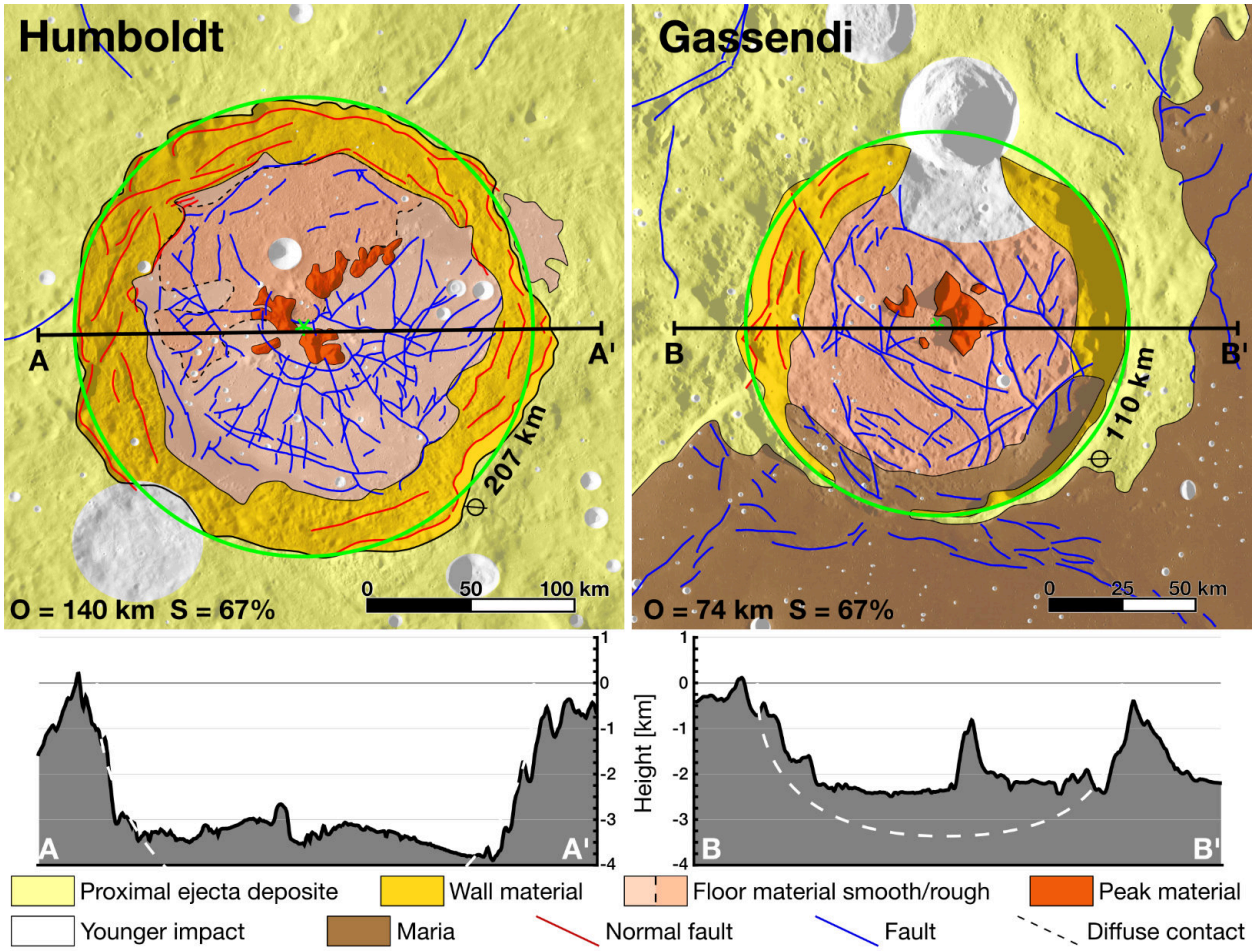

Figure 3.3: Floor fractured lunar craters Humbolt and Gassendi show flat and mare-filled floors. Concentric normal faults of the terraced crater wall are indicated by red lines. Radial and concentric fractures are indicated by blue lines. Lithologies based on USGS Geological Atlas of the Moon criteria. Cross section of craters with high vertical exaggeration showing the convex floor of Humbolt and the flat floor of Gassendi. NASA LROC-WAC image data and cross section from NASA LRO data.

floors in these craters are associated with being filled with younger mare material. Furthermore, some FFCs contain only isolated patches of mare material (Schultz, 1976; Jozwiak et al., 2012; Jozwiak et al., 2015). These fills generally show no visible signs of inflow or lithological connection to the surrounding mare material, being separated by the crater wall lithology (Fig. 3.2b). Central peaks are typically less pristine and irregular. The central peaks are drowned out by the fill of the surrounding mare. CFFs are radial and concentric but can overprint themselves to more chaotic, polygonal appearance (Figs 3.2, 3.3). The craters Tycho and Copernicus show complex polygonal CFF patterns (Fig. 3.2a). Humboldt crater has well developed radial and concentric fractures, while Gassendi fractures are very chaotic (Fig. 3.3; Baldwin, 1968). In Geminus and Aristoteles craters, CFFs appear to be partially covered by mare basalts, visible fractures suggesting a chaotic appearance (Fig. 3.2). Furthermore, the floors of FFCs such as

Humboldt can show a convex upward profile and a moat surrounding the crater wall (Fig. 3.3).

Terraces are prominent structures in lunar crater walls greater than 10 km in diameter (Cintala et al., 1977; Settle & Head III, 1979). Their presence is a defining characteristic of complex crater morphology. Terraces are also common in FFCs (Fig. 3.2). These terraces are characterised by steep concentric scarps oriented towards the crater centre and relatively flat surfaces arranged in a stepped pattern along the crater wall (Fig. 3.2b). The tops of the terraces are generally close to horizontal (Fig. 3.2b). The mechanism of terrace formation is assumed to be part of the cratering process, in which the rim of the transient crater cavity is translated inward along concentric listric faults. Hereby widens the crater while becoming flatter (Kenkmann et al., 2014; Krüger et al., 2017). The morphology of the terraces suggests that slumping occurs as a series of coherent blocks descending into the cavity (Settle & Head III, 1979; Krüger et al., 2017). Rim slumping increases the diameter of a crater by widening the rim and flattening the crater wall (Fig. 3.2b).

3.2. Experimental setup

Our experimental setup uses a polycarbonate tank, 50 cm by 50 cm wide and 15 cm deep (Fig. 3.4a). The tank was filled with a granular material representing the brittle upper crust of the Moon. The top 10 cm was filled with a 2:1 mixture of flour and quartz sand (see chapter 2.4.7.3). Below, a 5 cm layer of foam acted as an elastic filler, reducing the overall volume of the container (Fig. 3.4a).

3.2.1 Sill formation

Formation of the sill was simulated by inflation of a circular balloon embedded in the granular crust analogue. The balloon is made of two round sheets of polyethylene fused together at the edges ((HDPE)+LDPE polymer, thickness 10 µm). The material used is very thin and flexible, yet tear resistant. In the middle of the bottom sheet, a cut-out housed a 3D printed inlet that was taped in place. The inlet allowed for the connection of tubing between the balloon and a pump (Fig. 3.4a). I used self-made balloons with diameters of 15, 20, 25 and 30 cm. The inflated volume of each balloon was determined experimentally. Each balloon diameter was inflated on a flat surface without any overburden to a uniform thickness of 5 mm corresponding to 2.5 km in nature. The corresponding volumes of 15 cm - 90 ml, 20 cm - 180 ml, 25 cm - 290 ml and 30 cm - 420 ml determined the maximum infill into the balloon. The balloon was connected to a

computer-controlled peristaltic pump (Shenchen LabF3 Peristaltic Dispensing Pump, YZ1515x (PPS) pump head) which connected to a water reservoir (Fig. 3.4a). The method for modelling the volcanic plumbing system with an inflatable balloon was similar in function to other analogue models studying caldera collapses (Walter & Troll, 2001; Troll et al., 2002; Luzzi et al., 2021).

3.2.2 Setup process

Each experiment was set up according to a predefined protocol to ensure reproducibility. The polycarbonate box was equipped with a central hole (Fig. 3.4a). A hollow 3D printed spacer tube was first embedded in the centre of the box, which was yet to be filled. The spacer tube acted as a channel for the tubing and as a height reference for positioning the balloon (Fig. 3.4a). Different versions of the spacer tube with

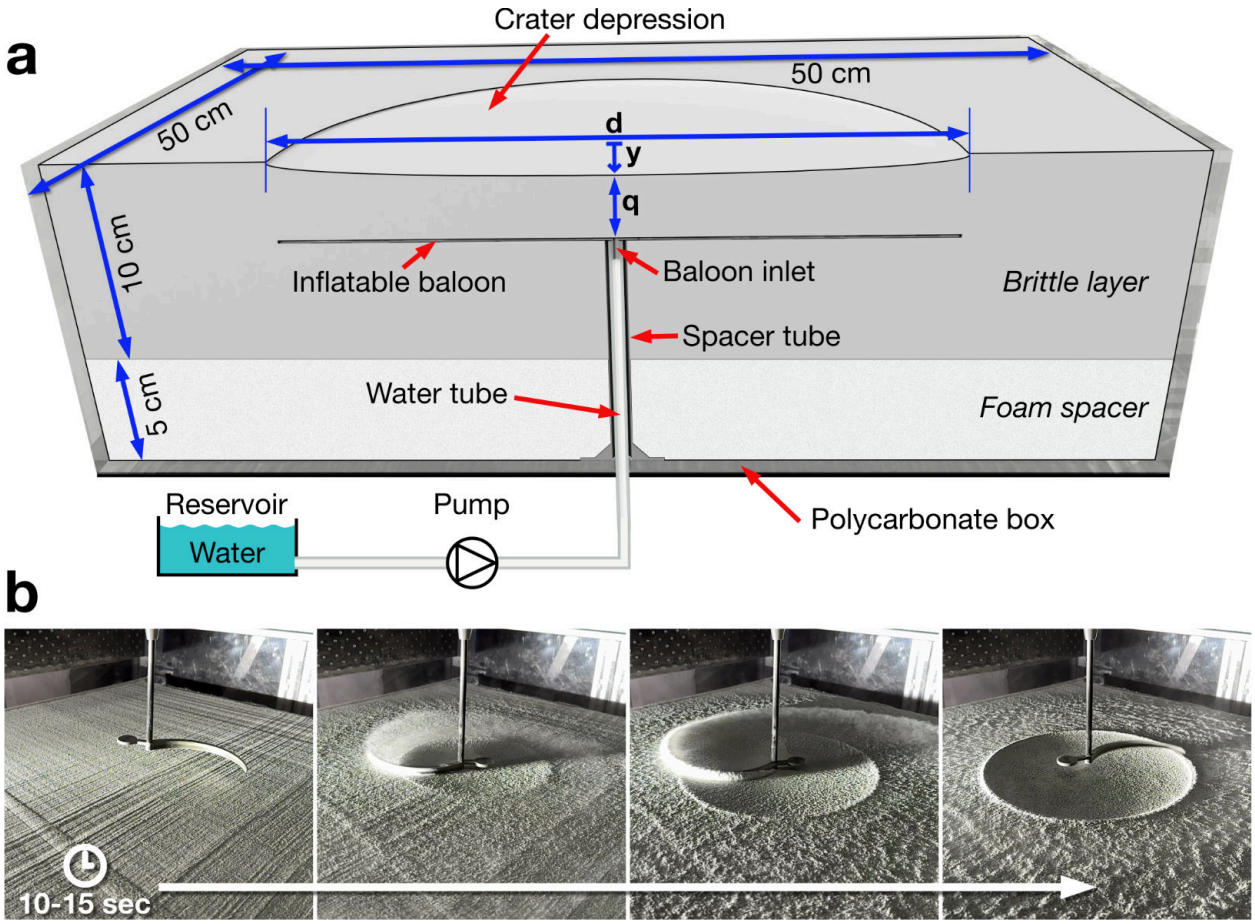

Figure 3.4: Images showing the experimental setup and the generation of model impact craters in granular material (2. generation). (a) Sketch illustrating the general experimental setup with internal placement of the inflatable balloon. d: crater diameter, y: crater depth at the centre, q: depth of balloon below crater centre. (b) Positioning of the curved plastic blade attached to a carbon fibre shaft into the granular material. Rapid rotation of the blade ejected the granular material outwards. Excavated crater and ejected material around the crater rim after completion of the morphology.

specific lengths corresponding to the specific crater diameter being modelled were used. The individual spacer tubes compensated for the increase in crater depth y with increasing diameter d (Table 3.1). This ensured that the balloon was always placed at the exact depth q_m below the crater centre. After initial setup, foam spacers were placed and the granular layer was sieved on top until the surface was consistent with the top of the spacer tube (Fig. 3.4a). A square aluminium bar attached to a set of spacers was used to scrape off excess material and create a level surface at a specified depth for the balloon to rest on. The spacer glides along two sides of the rectangular tank. The spacers were again individually matched to the length of the spacer tube with less than 0.5 mm clearance between the spacer tube and the aluminium bar. The balloon inlet was fitted with a brim which rests on the top of the spacer tube (Fig. 3.4a). Once the balloon was placed and connected to the feed tube inside the spacer tube, the rest of the tank was filled to the top. The two sides of the rectangular tank again acted as a reference for scraping the top surface. This method ensured a perfectly uniform surface with a tolerance of less than ± 0.2 mm in all experimental runs.

3.2.3 Crater generation

A rotating stencil excavated the initial crater shape into the granular layer (Fig. 3.4b). The precise creation of realistic model craters in granular material is critical for comparison with lunar FFC case studies (Fig. 3.2). The model craters were achieved using a curved plastic blade with a base in the shape of the inverse radial crater profile. The final concave shape of the craters, derived from the numerical results, was constructed using Computer Aided Design, based on the calculated and scaled depth and diameter of a fresh lunar crater. The curved blade was made using a 3D printer and attached to a carbon fibre rod, which in turn was attached to a portable drill (Fig. 3.4b). A small counterweight at the tip of the plastic blade reduced rotational imbalance (Fig. 3.4b). A gantry ensured the vertical orientation of the rod and the horizontal orientation of the plastic blade. As it rotated, the plastic blade was gently lowered into the upper part of the granular material, 'carving' and excavating a specific crater profile (Fig. 3.4b). Crater generation usually takes less than 10 seconds. The added value of this procedure is that, during excavation, the ejected material was evenly distributed around the model crater, similar to the distribution of natural ejecta deposits, which decrease in thickness with increasing distance from the carter margin (Fig. 3.4b). The actual impact process is not modelled in our approach, as our experiments were run after the main crater formation process has been completed.

3.2.4 Experimental sets

Four distinct experimental sets were designed to systematically explore the structural effects of sill generation on lunar crater floors (Table 3.1). For each experiment, the balloon was first inflated (Subscript I) to the maximal volume stated in Table 3.1 to simulate intrusion of the sill. After maximal inflation the same volume was pumped out to simulate evacuation of magma (Subscript E). To assess the reproducibility of results, experiments of Set 1, 2 and 4 were repeated at least twice. The control experiments proved high repeatability between experimental runs therefore I chose to only show one experiment result of each run, e.g. 26 out of 49 conducted.

Experiment set 1 consists of 8 experiments where the balloon diameter is equal to the diameter of the crater. Between experiments 1 to 4 and 5 to 8, the diameter is increased in 5 cm increments from 15 cm in experiments 1 and 5 to 30 cm in experiments 4 and 8 (Table 3.1). Experiment set 2 consists of 6 experiments in which the crater diameter remains smaller than the diameter of the balloon, maintaining a fixed diameter of 30 cm. The diameter of the crater is respectively increased in 5 cm increments from 15 cm to 25 cm in experiments 9 to 11 and in experiments 12 to 14. Experiments 4 and 8 correspond to the continuation of this series with the crater diameter matching the balloon diameter of 30 cm (Table 3.1). Experiment set 3 consists of 4 experiments in which the balloon diameter is equal to the crater diameter. Between these experiments, both diameters are increased in 5 cm increments from 15 cm in experiments 15 and 17 to 20 cm in experiments 16 and 18. The centre of the circular balloon is offset by 2.5 cm from the centre of the crater (Table 3.1). Experiment set 4 consists of 8 experiments where the balloon diameter is increased in 5 cm increments between experiments, however without a crater being present. Between experiments 19 to 22 and 23 to 26, the balloon diameter is increased in 5 cm increments from 15 cm in experiments 19 and 23 to 30 cm in experiments 22 and 26 (Table 3.1).

3.2.5 Digital Image Correlation

For quantitative analysis of surface deformation, the experiments were recorded with a 3D Stereo Digital Image Correlation (DIC) StrainMaster system manufactured by LaVision GmbH (Germany). Two M-lite 12M CMOS cameras (12-megapixel) were mounted on a framework above the model surface. The images were recorded with a Device Control Unit X (DCU X) running DaVis 10.2 by LaVision GmbH (Germany). A set of Nikon lenses with 24 mm focal lengths were used. Stereo DIC permits the computation of 3D surface displacement fields by cross-correlation of sequentially recorded stereo image pairs (Adam et al., 2005; Eisermann et al., 2021). Simultaneous

application of stereo image reconstruction generates a highly accurate 3D model of the surface topography. The brittle layer included black and green dyed quartz grains serving as marker particles for DIC cross-correlation (see thesis chapter 2). Calibration of the cameras prior to each experiment and before the preparation of the crater both identified and corrected lens distortions and set the correct length scale to ensure high-precision calculations. The vertical and horizontal accuracy of the recorded surface was in the sub-millimetre range. For displacement vector field calculation using DIC, the software DaVis 10.2 was also used, allowing us to precisely monitor the morphological evolution of the surface by calculating the cumulative displacement vector field for each experiment. Derived from the vector field we can plot local divergence to image strain.

3.3. Scaling

Accurate scaling of the experiment is a prerequisite to ensure physical comparability between model (Subscript m) and nature (Subscript n) (Hubbert, 1937). Our experiments were scaled to lunar conditions. The length scale of our experiments was set to $L = l_m/l_n = 2 \times 10^{-6}$, i.e., $l_m = 1$ cm in the model corresponds to $l_n = 5$ km in nature. The chosen length scale allows representation of natural craters with diameters between 75 km and 150 km and fresh crater depths between 2.97 km and 3.78 km (Table 3.1). In Experiment Sets 1, 2 and 3, the balloon for simulation of the sill was placed either $q_m = 1.5$ cm or $q_m = 3$ cm below the crater centre. This resulted in natural equivalents of sill formation at depths of $q_n = 7.5$ km and $q_n = 15$ km (Fig. 3.4, Table 3.1). In Experiment Set 4, due to the lack of crater morphology, the balloon rests deeper below the surface with shallow sills $q_m = 2.09 – 2.25$ cm and deeper sills $q_m = 3.59 – 3.75$ cm below the crater centre (Table 3.1). This results in natural equivalents of sill formation at depths of $q_n = 10.45 – 11.25$ km and $q_n = 17.95 – 18.75$ km (Table 3.1).

Diameters and depths of freshly formed lunar craters were modelled numerically using the down2earth.eu impact calculator (Collins et al., 2005). The following parameters were chosen to calculate crater dimensions. We set the density of the target rock, simulating basaltic feldspar-rich highland crust, to 2600 kg/m^3, the density of the projectile, representing a solid stone impactor, to 3000 kg/m^3, the impact velocity to 15 km/s and the impact angle to 45° (Kiefer et al., 2012). Resulting in the crater diameter (d) and central crater depth (y) (Table 3.1), both of which were considered in the experimental design. The resulting crater represented the morphological shape of a complex crater.

The flour-quartz sand mixture used to simulate brittle upper crust consists of standard wheat flour type 405 and quartz sand type G23T (see 2.4.7.3 flour 2:1 for

Model										Nature			
Experiment No.	d_m [cm]	y_m [cm]	q_m [cm]	D_m sill [cm]	V_m sill [ml]	O_{mI} [cm]	O_{mE} [cm]	S_I	S_E	d_n [km]	y_n [km]	q_n [km]	D_n sill [km]
Set 1													
1	15	0.59	1.5	15	90	5.9	5.5	39%	37%	75	2.97	7.5	75
2	20	0.64	1.5	20	180	8.8	11.7	44%	59%	100	3.24	7.5	100
3	25	0.7	1.5	25	290	13.9	17.1	56%	68%	125	3.51	7.5	125
4	30	0.75	1.5	30	420	19.3	21.4	64%	71%	150	3.78	7.5	150
5	15	0.59	3	15	90	5	4.7	33%	31%	75	2.97	15	75
6	20	0.64	3	20	180	5.9	6.2	30%	31%	100	3.24	15	100
7	25	0.7	3	25	290	7.3	6.8	29%	27%	125	3.51	15	125
8	30	0.75	3	30	420	8.1	7.9	27%	26%	150	3.78	15	150
Set 2													
9	15	0.59	1.5	30	420	9.3	8.8	31%	29%	75	2.97	7.5	150
10	20	0.64	1.5	30	420	10.6	10.4	35%	35%	100	3.24	7.5	150
11	25	0.7	1.5	30	420	13.1	13.1	44%	44%	125	3.51	7.5	150
12	15	0.59	3	30	420	5.9	5.2	20%	17%	75	2.97	15	150
13	20	0.64	3	30	420	6.7	6.1	22%	20%	100	3.24	15	150
14	25	0.7	3	30	420	8.8	8.3	29%	28%	125	3.51	15	150
Set 3													
15	15	0.59	1.5	15	90	6.3	5.7	42%	38%	75	2.97	7.5	75
16	20	0.64	1.5	20	180	9.4	9.3	47%	47%	100	3.24	7.5	100
17	15	0.59	3	15	90	6.9	5.9	46%	39%	75	2.97	15	75
18	20	0.64	3	20	180	6.3	5.5	32%	28%	100	3.24	15	100
Set 4													
19			2.09	15	90	7.7	7.2	51%	48%			10.45	75
20			2.14	20	180	11.7	13.6	59%	68%			10.7	100
21			2.2	25	290	12.1	14.5	48%	58%			11	125
22			2.25	30	420	19.5	19.4	65%	65%			11.25	150
23			3.59	15	90	5.5	5.5	37%	37%			17.95	75
24			3.64	20	180	7.5	7.1	38%	36%			18.2	100
25			3.7	25	290	6.8	6.7	27%	27%			18.5	125
26			3.75	30	420	12.1	11.5	40%	38%			18.75	150

Table 3.1: Model parameters and their natural equivalents for each experiment. d: crater diameter; y: crater depth; q balloon depth; D: balloon diameter; V: balloon volume; O: polygonal area diameter; S: polygonal fracture proportion.

detailed description). The Mohr-Coulomb properties of this granular material adhere to brittle (Subscript B) deformation. Specifically, the mixture has a density of ρ_{mB} = 961 kg/m^3, a cohesion of approximately 108 Pa s and an angle of internal friction of ϕ = 46.39° (Table 2.31). The respective material properties, in particular the angle of repose

and density, were determined in our laboratory, whereas the cohesion and shear strength were measured using a ring shear apparatus at GFZ Potsdam, Germany (see Chapter 2.4.7). I ensured that humidity did not affect the strength of the granular material by keeping the humidity in the laboratory below 20%. Using the average density of the feldspar-rich highland crust ρ_{nB} = 2600 kg/m^3 (Kiefer et al., 2012), the density scale is defined as P = ρ_{mB}/ρ_{nB} = 0.4 for the upper crust. The gravity scaling ratio is G = g_m/g_n = 6.

Inflation and evacuation of the sill was performed at a linear flow rate of 20 ml per minute. The balloon was filled with 21°C tap water with a density ρmW = 998 kg/m^3. Given the density of a lunar basaltic melt ρ_{nW} = 2800 kg/m^3 (Walwer et al., 2021), the density scaling factor amounts to P = ρ_{mW} / ρ_{nW} = 3.6 x 10^{-1}. The water is characterised by a Newtonian viscosity of η_{mW} = 9.77 x 10^{-4} Pa s. Given the effective viscosity of a low-viscosity lunar basaltic melt η_{nW} = 100 Pa s (Galland et al., 2014), the viscosity scaling factor is H = η_{mW}/η_{nW} = 9.8 x 10^{-6}. The melt buoyancy relation in the model is given by ρ_{mW} / ρ_{mB} = 1.039 and in nature by ρ_{nW} / ρ_{nB} = 1.077. Values greater than 1 indicate negative buoyancy. The lunar crust has a lower density than basaltic magmas, so magmas on the Moon have negative buoyancy (Walwer et al., 2021). I only considered the resulting brittle deformation in our models. Brittle deformation is independent of strain rate and therefore kinematic scaling of velocities, viscosity and density is not necessary.

To quantify the extent of polygonal fracturing within the crater centre, I measured the diameter O of a circle containing all polygonal fractures (Table 3.1). The ratio between the diameter O and the balloon diameter D_m gives the proportion of polygonal fractures S.

3.4. Model limitations

The experimental series was designed to test the widely accepted igneous intrusion model as the main driver for lunar FFC generation. I limited the number of physical variables to ensure reproducibility and comparability of experiments, as is common in analogue models. I was not able to test the unconfined fluid injection, as the replication of an unconfined experimental setup is a challenge in terms of the reproducibility of key parameters. The experimental setup forces the formation of a sill using a flat, horizontal balloon (Fig. 3.3). The geometry of the sill is predetermined by its maximum diameter, depth, location, and shape. Evacuation of magma in the sill can only be simulated by pumping fluid out of the balloon, i.e., in opposite direction with regard to magma evacuation in nature. Fluid inflow and outflow were both linear. Minor leakages of the

balloon occurred during some of the experiments. In case a leakage was detected, the respective experiment was re-run and excluded from the main line of experiments, instead serving as an additional control experiment. Our models only reproduce and account for brittle deformation. The strength of the granular analogue is uniform and does not account for the weakening and ductile (continuous) deformation generated by the impact.

3.5. Results

I present the results of 26 experiments in which I varied five parameters in a controlled manner: initial balloon depth (q), crater diameter and related depth (d+y), crater to balloon diameter ratio, crater morphology, and crater to sill alignment. Four sets of experiments can be derived from the variation of the parameters (Table 3.1).

3.5.1 Set 1: Balloon and crater at equal diameter

After inflation, fractures in the uplifted area are extensional while the crater rim is contracting. After evacuation, a reversal of the fracture kinematics is observed. At maximum inflation of deep balloons (q_m = 3 cm), weak local compactation extending beyond the crater rim is observed (Fig. 3.5 experiments 5I, 6I, 7I, 8I). Fractures in crater with shallow balloons (q_m = 1.5 cm) are limited by the crater rim (Fig. 3.5, experiments 1I, 2I, 3I, 4I). After evacuation, deformation is localised in the form of concentric extensional fractures. The fracture pattern in a crater with shallow balloon (q_m = 1.5 cm) is strongly polygonal after maximum inflation. The polygonal fracture area does not extend to the rim but is surrounded by concentric fractures (Fig. 3.5, experiments 1I, 2I, 3I, 4I). The polygonal fracture area increases with increasing crater diameter. After maximum evacuation, the fracture pattern extends with concentric extensional fractures forming at approximately ½ the crater radius (Fig. 3.5, experiments 1E, 2E, 3E, 4E). In contrast, the fracture pattern of crater with a deep balloon (q_m = 3 cm) is barley altered and strongly dominated by radial fractures. The central area shows some polygonal fractures, but their extent is largely uniform between crater diameters (Fig. 3.5, experiments 5E, 6E, 7E, 8E).

3.5.2 Set 2: Balloon larger than crater

The fractures in all experiments of set 2 are barley influenced by the crater rim. The fracture patterns in the shallow balloon craters (q_m = 1.5 cm) are distinctly polygonal after maximum inflation (Fig. 3.6, experiments s9I, 10I, 11I). The fracture pattern of a crater

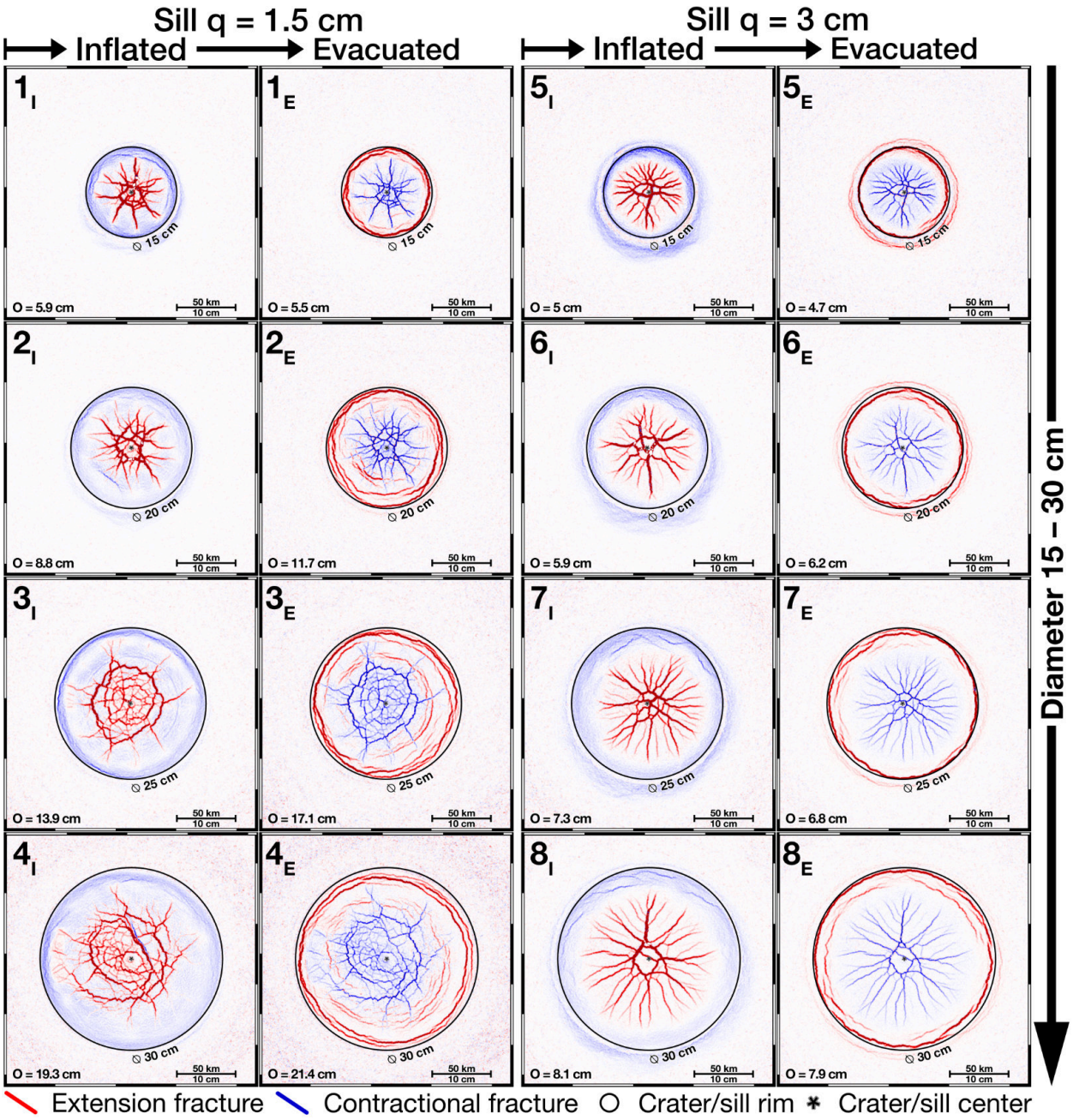

Figure 3.5: Experiment set 1 consists of 8 experiments where the sill diameter is equal to the diameter of the crater morphology. The sill depth was varied to be either 1.5 or 3 cm below the crater floor. The solid circle indicates the perimeter of the crater and the perimeter of the sill. Colour intensity represents fracture dominance. Blue colours indicate compression, while red colours indicate extension. Subscript I shows the cumulative fracturing of a given experiment from initial crater morphology to maximum inflation, while subscript E shows the cumulative fracturing from maximum inflation to complete evacuation.

with deep balloon (q_m = 3 cm) is dominated by radial fractures with a polygonal fracture pattern in the centre (Fig. 3.6, experiments 12I, 13I, 14I). A reversal of the fracture kinematics is observed upon evacuation. After evacuation, the fracture pattern remains virtually unchanged. After evacuation, deformation is localised in the form of concentric extensional fractures around the balloon rim (Fig. 3.6, experiments 9-14E). Fractures extend beyond the crater rim in experiments 9, 10, 12 and 13 (Fig. 3.6). These fractures are predominantly radial and feather out beyond the crater rim. Experiments 11 and 14 show concentric fractures localised outside the crater rim, but no central fractures extending beyond the crater wall (Fig. 3.6).

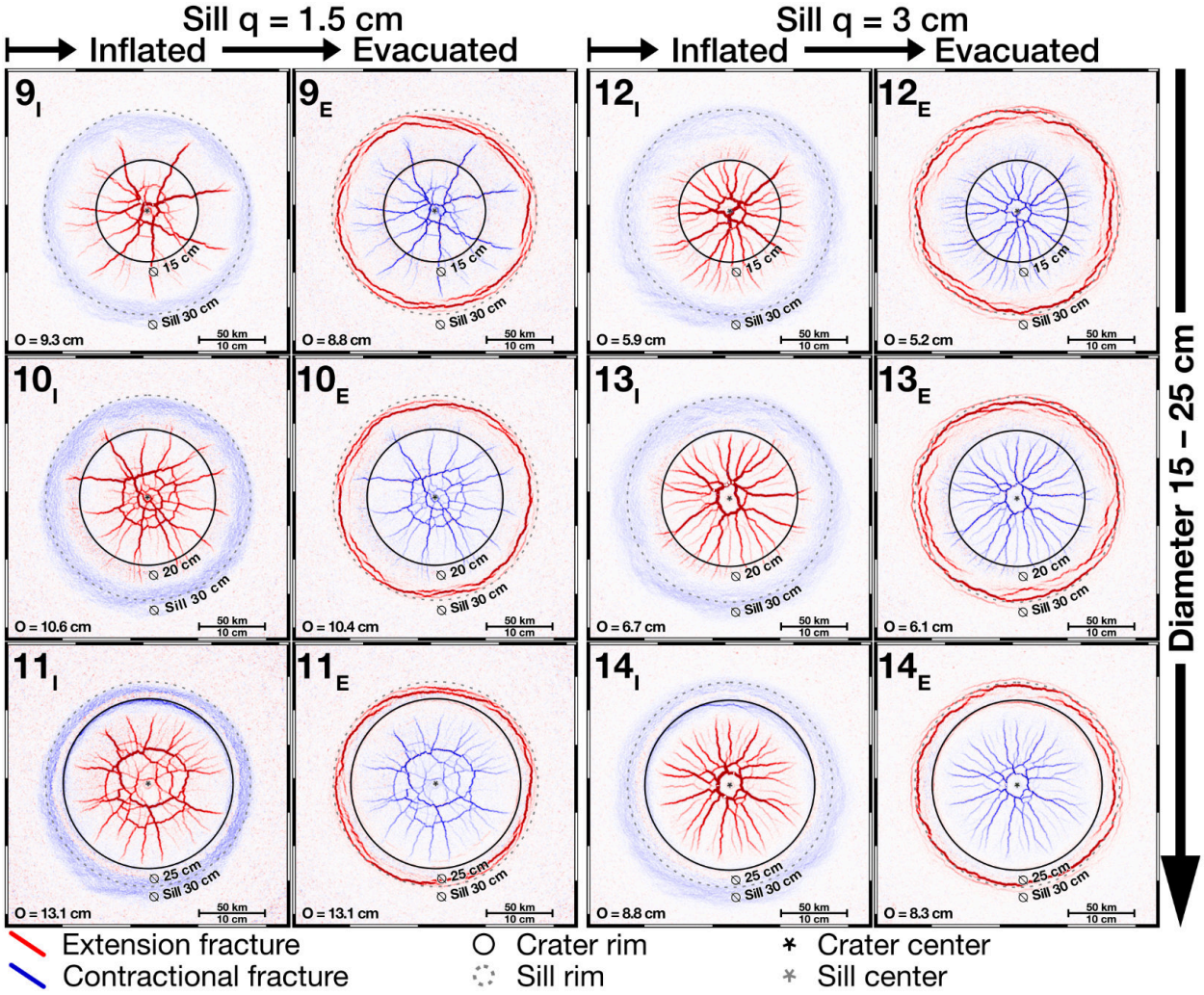

Figure 3.6: Experiment set 2 consists of 6 experiments in which the sill maintains a fixed diameter of 30 cm. The crater diameter is increased in 5 cm increments from 15 to 25 cm. The depth of the sill is varied so that it is either 1.5 or 3 cm below the crater floor. The solid circle indicates the perimeter of the crater, while the dashed line indicates the rim of the sill. The intensity of the colours represents fracture dominance. Blue colours indicate compression, while red colours indicate extension. Subscript I shows the cumulative fracturing of a given experiment from initial crater morphology to maximum inflation, while subscript E shows the cumulative fracturing from maximum inflation to complete evacuation.

3.5.3 Set 3: Balloon offset from crater

Fractures are mainly located above the balloon extending beyond the crater rim (Fig. 3.7). Fracture patterns in craters with shallow balloons (q_m = 1.5 cm) are distinctly polygonal after maximum inflation (Fig. 3.7, experiments 15I, 16I). The fracture pattern of craters with a deep balloon (q_m = 3 cm) is dominated by radial fractures with some polygonal fractures in the centre (Fig. 3.7, experiments 17I, 18I). Fractures inside the craters are more pronounced than outside. In experiments 15 and 16 the centre of the polygonal fractures is approximately 1.25 cm offset from the crater centre, while in experiments 17 and 18 the centre of the radial fractures is approximately 1.5 cm offset from the crater centre (Fig. 3.7). A reversal of the fracture kinematics is observed after evacuation. After maximum evacuation, the central fracture pattern remains virtually unchanged (Fig. 3.7, experiments 15 – 18 E). After evacuation, deformation is localised in the form of concentric extensional fractures following the balloon rim. Concentric fractures are deflected as they cut the crater rim at a low angle (Fig. 3.7, experiments 15-18E). In experiments 15 and 16, concentric fractures are also localised on the

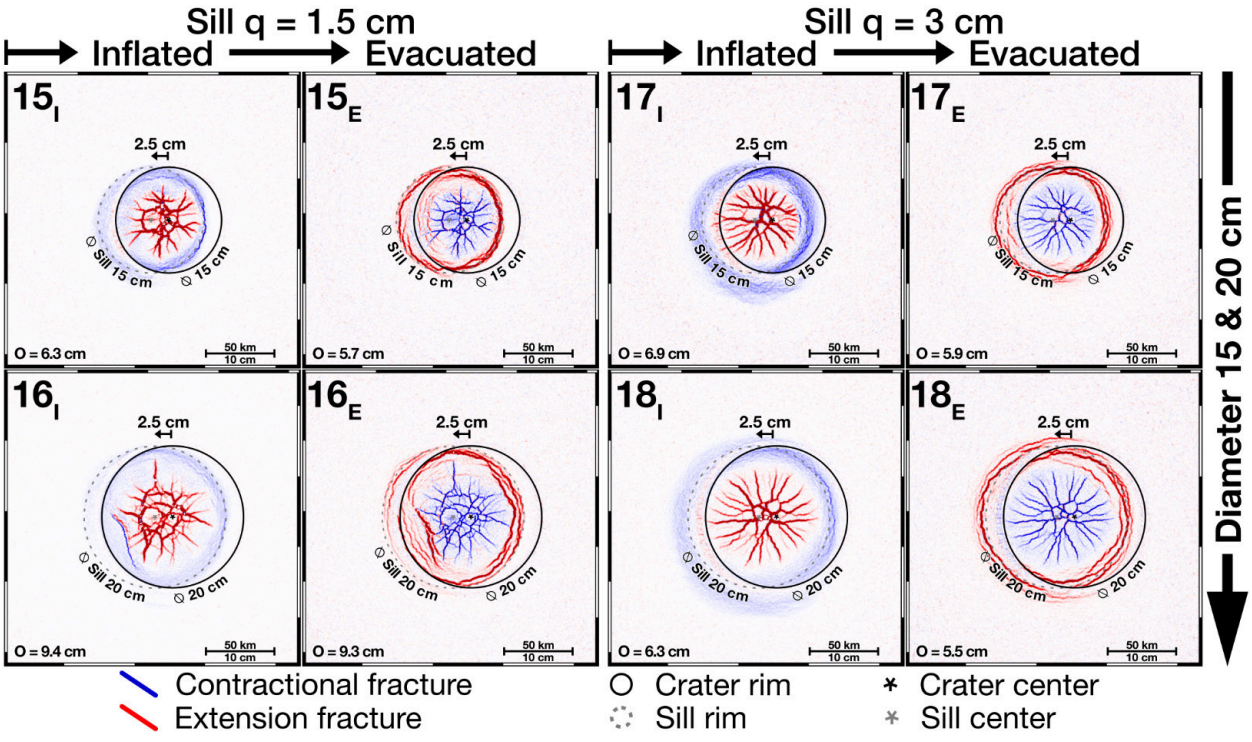

Figure 3.7: Experiment set 3 consists of 4 experiments where the sill diameter is equal to the crater diameter. The position of the circular sill is offset by 2.5 cm from the centre of the crater. The depth of the sill is varied to be either 1.5 or 3 cm below the crater floor. The solid circle indicates the perimeter of the crater, while the dashed line indicates the rim of the sill. The intensity of the colours represents fracture dominance. Blue colours indicate compression, while red colours indicate extension. Subscript I shows the cumulative fracturing of a given experiment from initial crater morphology to maximum inflation, while subscript E shows the cumulative fracturing from maximum inflation to complete evacuation.

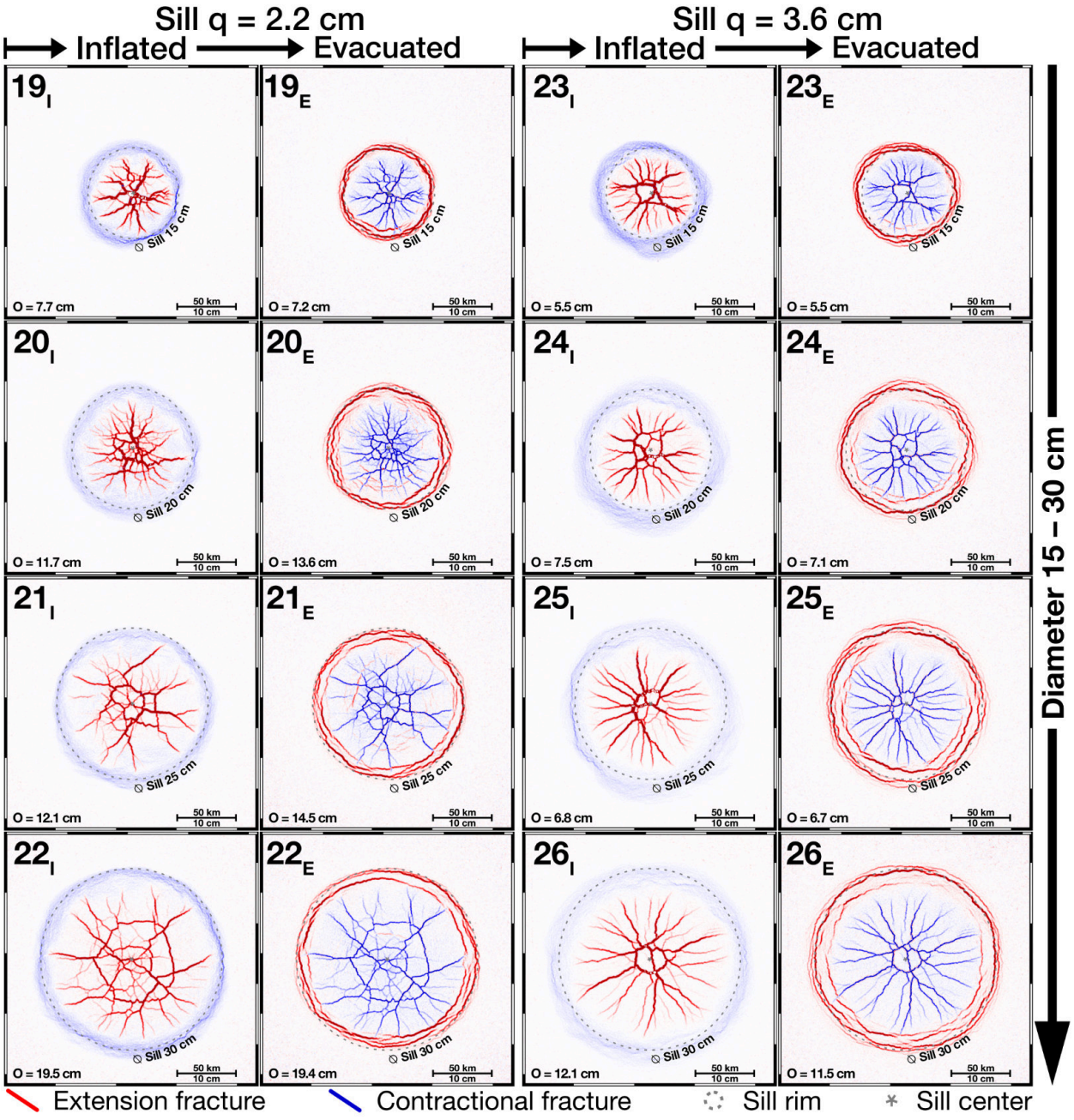

Figure 3.8: Experiment set 4 consists of 8 experiments where no crater morphology is present. The sill diameter is increased in 5 cm increments between experiments. Due to the lack of crater cavity, the sill depth is varied to be either 2.2 or 3.6 cm below the crater floor. The dashed circle indicates the rim of the sill. Colour intensity represents fracture dominance. Blue colours indicate compression, while red colours indicate extension. Subscript I shows the cumulative fracturing of a given experiment from initial crater morphology to maximum inflation, while subscript E shows the cumulative fracturing from maximum inflation to complete evacuation.

crosscut crater wall. Overall, the fracture patterns in set 3 experiments become slightly asymmetric (Fig. 3.7).

3.5.4 Set 4: Balloon without crater

The fracture pattern in the crater with the balloon at shallow depth (q_m = 2.2 cm) is distinctly polygonal after maximum inflation (Fig. 3.8, experiments 19I, 20I, 21I, 22I). The polygonal fracture area increases with increasing crater diameter. After maximum evacuation a few concentric extensional fractures form at about ½ crater radius, but the fracture pattern remains virtually unchanged (Fig. 3.8, experiments 19E, 20E, 21E, 22E). The fracture pattern of deep balloon craters (q_m = 3.6 cm) is dominated by radial fractures, while the central region is dominated by radial to polygonal fractures (Fig. 3.8, experiment 23I, 24I, 25I, 26I). A reversal of the fracture kinematics is observed after evacuation. At maximum inflation of a deep balloon, weak localised deformation is observed extending beyond the balloon rim (Fig. 3.8, experiments 23I, 24I, 25I, 26I). Fractures of a shallow balloon crater are limited by the balloon rim (Fig. 3.8, experiments 19I, 20I, 21I, 22I). After evacuation, deformation at the balloon rim is localised in the form of concentric extensional fractures (Fig. 3.8, experiments 19 – 26 E).

3.5.5 Crater floor uplift

As our experiments only consider brittle deformation no time scaling has been applied. The rate of inflow and outflow into the balloon is linear therefore I can evaluate the relative evolution of floor uplift and fracture formation. The time series of experiments 3 and 7 from set 1, with identical crater and sill diameter of 25 cm, are representative of the evolution of all experiments conducted. While starting conditions of crater morphology are identical, the empty balloon in experiment 3 is located at a shallow q_m = 1.5 cm and in experiment 7 at a deep q_m = 3 cm below the crater (Fig. 3.9; Table 3.1; Supplementary figure S3.10). Inflation of the balloon causes the crater floor to uplift and flex upwards. In experiment 3, after the onset of inflation, uplift begins to concentrate in the centre of the crater, creating a distinct central peak with steep slopes (Fig. 3.9; Supplementary figure S3.10). The magnitude of the uplift as it approaches the depth of the crater causes the formation of large extensive fractures confined to the uplifted area and the slopes. As the shallow balloon continues to inflate, the uplifted area begins to widen and the fractured area increases, forming polygonal blocks. In contrast, in experiment 7 the uplift begins to be more distributed, lifting the crater centre and flattening the crater floor (Fig. 3.9; Supplementary figure S3.10). This leads to the early localisation of fractures that span at least half of the crater radius. As inflation continues,

the central area begins to become convex with gentle slopes. The magnitude of the uplift is radially symmetric with a decrease in uplift towards the crater rim. At maximum uplift, the central part of the crater is flattened and a moat forms between the uplifted area and the crater rim. The central part of the crater floor extends above the crater rim (Figs. 3.9, 3.10). Concentric fractures begin to localise on the crater wall. With the beginning of the evacuation of the balloon, the crater floor subsides uniformly. Distinct concentric fractures begin to localise on the crater wall. Floor fractures localised during uplift remain active. After complete evacuation, the crater morphology approximates the initial crater morphology in the experiments (Fig. 3.10). Concentric fractures along the crater wall displace individual blocks downwards. Displacement along these faults is very small in the model (Fig. 3.10). Fractures are stepped along the crater wall (Fig. 3.10). Uplift magnitudes and morphological profiles differ between balloon depths. The crater floor

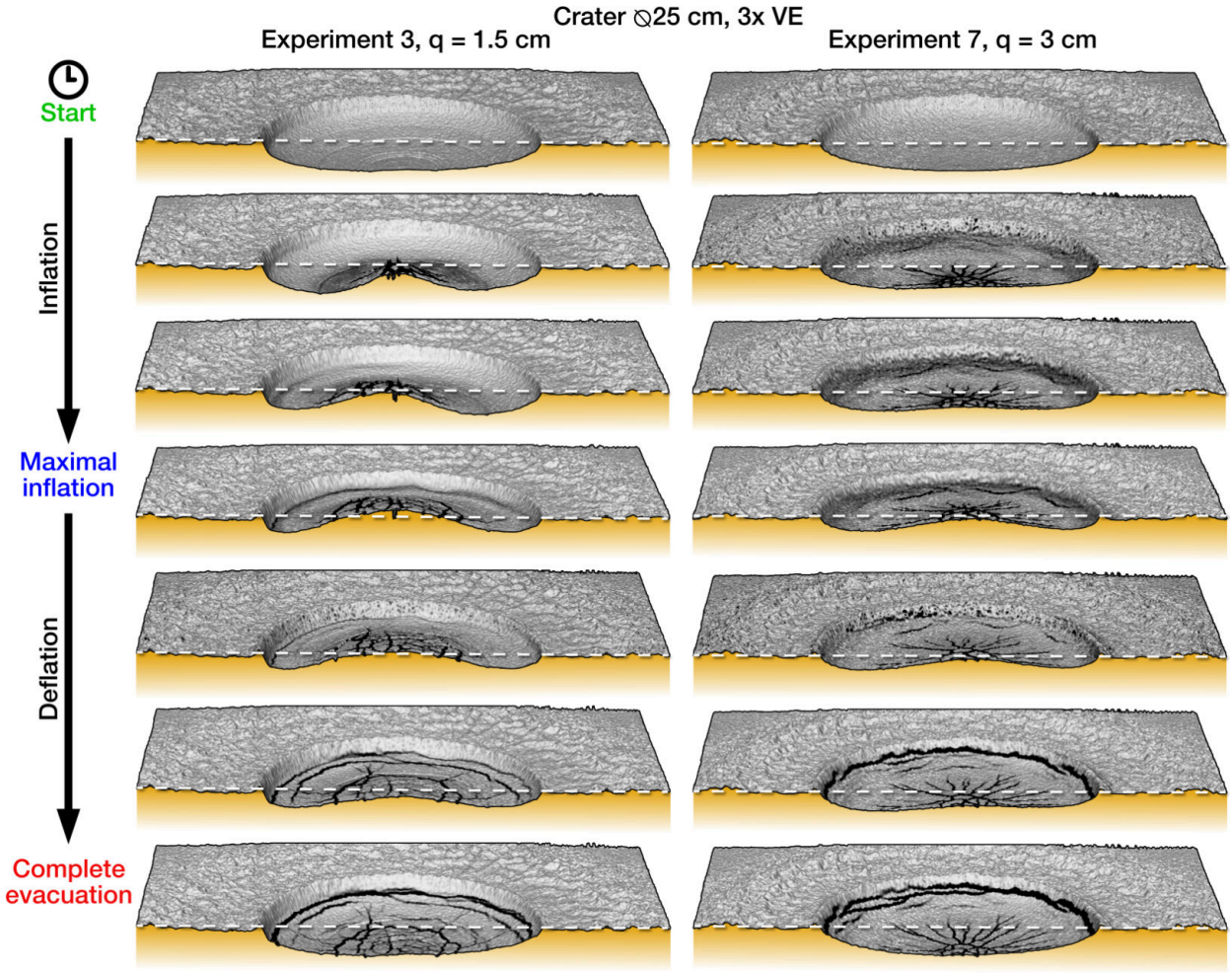

Figure 3.9: Cross-section and temporal evolution of experiments 3 and 7 from set 1, where the sill diameter is equal to the crater diameter of 25 cm, representing craters with diameters of 125 km each. Experiment 3 has a shallow sill while 7 has a deep sill. Each panel represents the morphology at approximately 20 minute intervals during linear inflation and deflation of the balloon. Black lines indicate measured fractures that are undifferentiated in their kinematics. Morphology 3x vertically exaggerated.

of experiment 3 after maximum inflation of the shallow balloon has a near horizontal floor (Fig. 3.10). At approximately half of the crater radius the slope increases, forming a moat. The crater floor of experiment 7 after maximum inflation of the deep balloon has a uniform slope falling towards the crater wall. The slope decreases towards the crater wall, forming a moat. The deeper balloon in Experiment 7 uplifts the crater floor uniformly (Fig. 3.10).

3.6. Discussion

I evaluate the igneous intrusion model as a mechanism for crater modification on the Moon. Our experiments provide insight into the resulting crater floor fracture pattern and morphological changes, which serve as an analogue to natural FFCs. The analogue experiments, which took place under the influence of the laws of physics in a 3D space, allow us to gain a detailed insight into the spatio-temporal evolution of brittle deformation. By design, our experiments take into account detailed multi-scale processes, complex material properties, randomisation and natural inhomogeneities that exceed the capabilities of numerical models (Zwaan et al., 2022).

The range of modelled craters, spanning from 75 to 150 km, has been chosen to focus on the most prevalent FFCs diameter. Properties of lunar crust as well as endogenic processes are inferred from remote sensing and applied terrestrial observations (Jozwiak et al., 2012). Sill depths below crater floors are not well constrained. On the assumption that ascending melt stalls into a sill at the reach of the breccia lens, I chose to test the sill stalling at a shallow 7.5 km and a deep 15 km below the crater (Wilson & Head, 2018). However, the proposed sill formation mechanism based on density is challenged by the fact that lunar magmas, which are expected to be denser than the host rock, show no buoyancy (Walwer et al., 2021). On that assumption other mechanisms are necessary to accumulate magma below a crater. The ascent mechanism is beyond the scope of this work. Furthermore, sill depth in nature might show more variability than modelled (Wichman & Schultz, 1995). However, the tested depths yield a broader understanding of the depth influence of a given intrusion on the resulting fracture pattern.

The four sets of experiments presented examine different aspects of sill depth and orientation and their structural consequences (Table 3.1). Experiment set 1 obeys to the proposed mechanism of the igneous intrusion model by assuming that the developing sill is centred and cannot extend beyond the crater rim. It is the prime objective of this study and tests the proposed intrusion model (Fig. 3.5). Experiment set 2 tested a more open system, allowing the sill to extend beyond the crater rim if favourable. It is assumed

that the maximum extent of the sill is centred (Fig. 3.6). Experiment set 3 tested what the fracture pattern would look like if the sill would not form crater centred and could partially extend beyond the crater rim (Fig. 3.7). Experiment Set 4 tested, as a reference, how the fracture pattern would develop without the presence of the crater morphology, akin to collapse caldera formation on Earth (Walter & Troll, 2001; Troll et al., 2002; Holohan et al., 2007; Galland et al., 2018). In addition, in the absence of a particular crater morphology, the balloons are located deeper below the surface than in sets 1, 2 and 3 (Fig. 3.8).

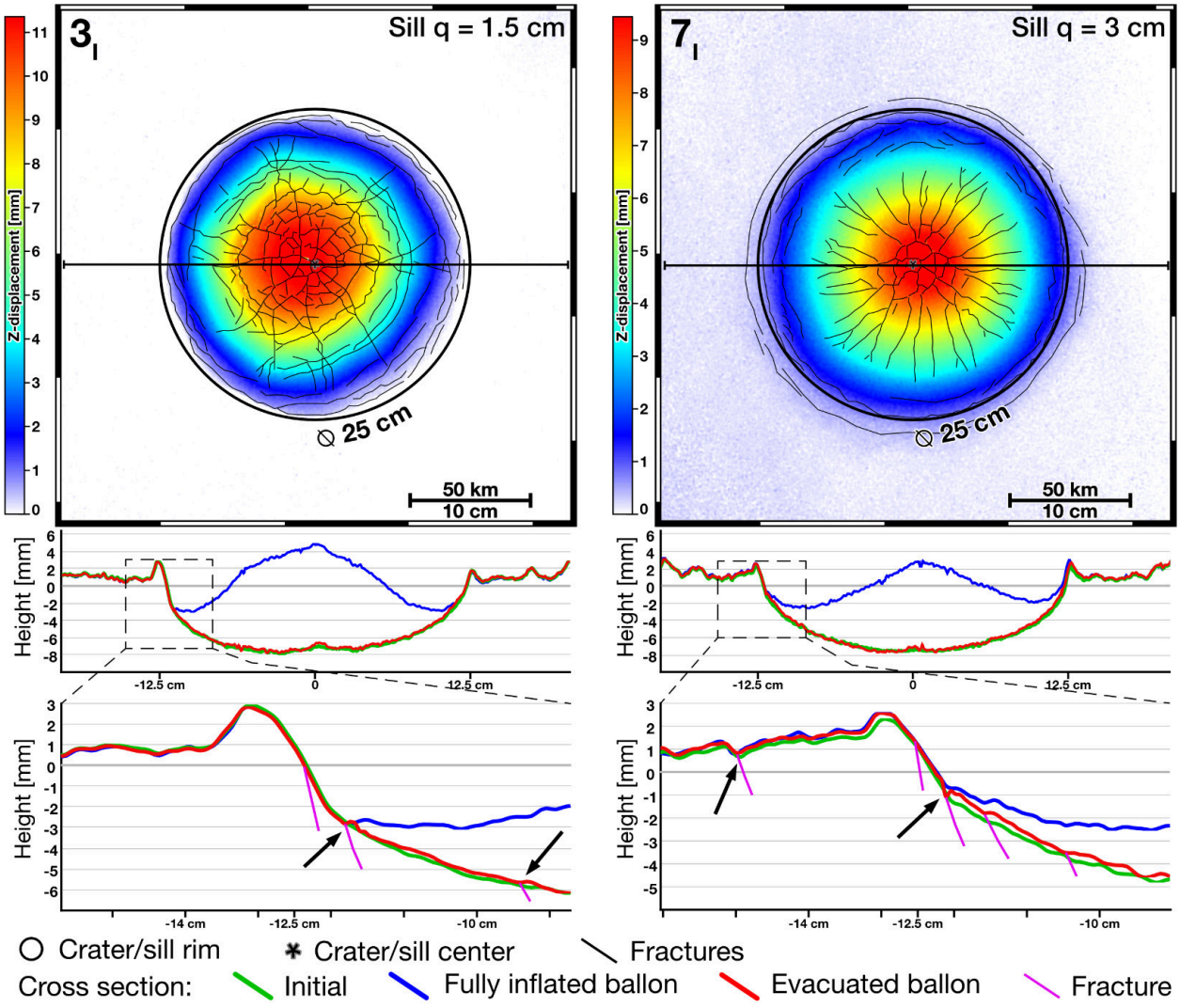

Figure 3.10: Cumulative vertical displacements of experiments 3 and 7 with different sill depths after maximum inflation. Solid lines indicate fracture traces. Initial, maximum inflated and evacuated topography profiles, indicated by green, blue and red curves respectively. Observed crater wall fractures are indicated by purple lines.

3.6.1 Fractures

The observations show that inflation of a sill below a crater is capable of lifting its floor (Fig. 3.9; Supplementary figures S3.10). Floor uplift causes upwards flexing of the crater floor which induces primarily extensional fractures in the overlying granular material. During inflation, fractures are primarily extensional, whereas after evacuation a reversal of the fracture kinematics is observed. Surface fractures can be categorized by being either radial or concentric in orientation relative to the crater centre. Overprint of both fracture orientations become difficult to categorize leading to an overall polygonal appearance. Especially as orientations of overprinted block boundaries quickly become chaotic. With the exception of purely concentric crater wall fractures, all fractures in our experiments can generally be categorized as either primary radial or polygonal.

The polygonal fractured area is typically radially symmetric, and its centre is aligned with the balloon centre (Fig. 3.5, experiment 2l). Measuring the diameter of the polygonal fractured area and relating it to the balloon diameter, gives the area that can be lifted to a maximum. This allows us to calculate the dimensionless parameter S, which is equivalent to the percentage of the area affected by polygonal fracturing (Table 3.1). By plotting S, I can quantify changes in the fracture pattern in relation to balloon depth. Due to an insufficient number of data points, I have excluded set 3 from the interpretation in terms of S (Table 3.1).

The proportion of polygonal CFFs strongly shows correlation with the depth of the balloon below the crater floor (Fig. 3.5, experiment 4 and 8). Shallowly buried balloons generally show higher proportions of polygonal fracturing than deeply located balloons, regardless of crater or balloon diameter (Fig. 3.11). Inflation and evacuation of shallowly buried balloons are further altering the area of polygonal fracturing. After evacuation, the

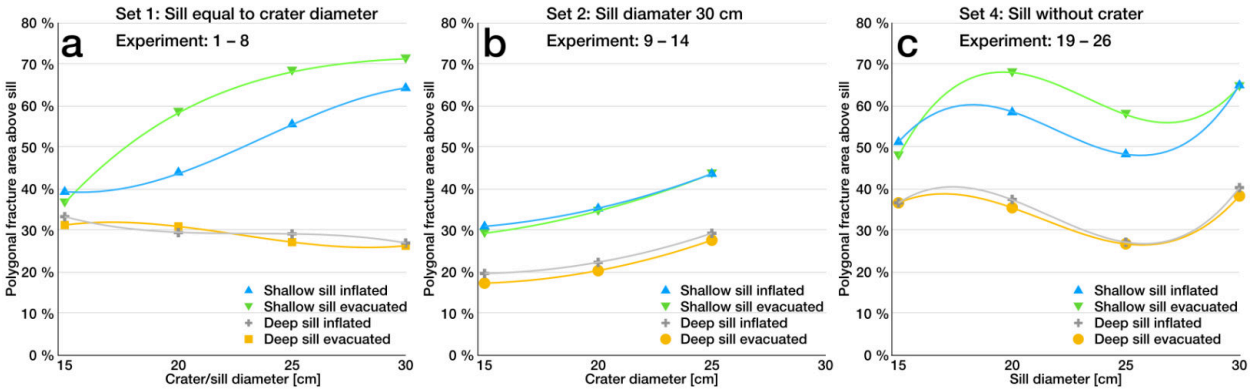

Figure 3.11: Graphs showing the magnitude of polygonal fractures S in crater centres. The depth of the sill plays an important role, with deeper placements producing significantly less polygonal surface fractures. (a) Set 1 experiments with increasing sill and crater diameter. (b) Experiments from set 2 as a function of fixed sill diameter. (c) Set 4 experiments with increasing sill diameter.

polygonal fractured area increases while in deeply seated balloons it barley localises more fractures than initiated by inflation (Fig. 3.11a, c). In set 2 with decreasing area of sill extending beyond the crater margin, S increases in both shallowly and deeply seated balloons (Fig. 3.11b). In absence of any crater morphology, the fractured area does not increase with sill diameter. Shallowly buried balloons have a variation in S of 20%, while deeper balloons show a variation of 15% (Fig. 3.11c). With a distinct crater morphology present, variation in S within shallow balloons is 30% with increasing diameter, while deeper seated sill analogues have a variation as little as 5% with a slight decrease towards increasing diameter (Fig. 3.11a). This shows us that the fracture pattern is primarily influenced by the balloon depth.

Prior experiments testing the isostatic relaxation model show that the occurrence of radial and concentric CFFs follows a uniform transition, based on strength of crust below the crater floor (see thesis chapter 4). The occurrence of predominantly polygonal fractures over shallowly buried sill analogues, and radial fractures over deeply seated analogues, leads to the assumption that with increasing sill depth the proportion of concentric fractures becomes smaller, while radial fractures remain. However, model sills in set 4, which are located deeper below the surface, maintain the trend of fractures observed in set 1 experiments (Fig. 3.11c). Overburden pressure at the time of sill formation might play a role.

Taking into account our model results, the fracture patterns in lunar FFCs may indicate the emplacement depth of the sill. Specifically, large craters with shallow sills, as modelled in experiment 4, develop a complex polygonal fracture pattern (Fig. 3.5, experiment 4E). Polygonal blocks are formed from primary radial and concentric fractures. The observed fracture pattern shares a high resemblance with fractures observable in the Humboldt crater with a diameter of 207 km (Fig. 3.3). In Humboldt, we can approximate S to be around 67%, which matches well the observed 64% after inflation in experiment 4. The fracture pattern observed in Tycho and Copernicus affects the whole crater floor, and S approximates 50% (Fig. 3.2). Overall, lunar FFCs are dominated by radial and concentric fractures showing geometric similarity with experiments characterized by shallow model sills, indicating that sills in nature seem to be rather shallow (Wichman & Schultz, 1995). Interestingly, model craters are characterized by more diverse fracture patterns, compared to lunar craters (Figs. 3.5, 3.2). This may be due to low resolution in remote sensing data, compared to DIC which can detect the smallest discontinuities in granular materials (Luzzi et al., 2023). Furthermore, evacuation of the sill early during inflation could hinder the sill becoming mature, which keeps floor uplift below expected magnitudes reducing the overall amount of expected deformation.

3.6.2 Influence of crater morphology

Crater morphology, such as any topography, causes stress perturbations in the upper crust. Such perturbations can influence fluid ascend (Michaut et al., 2020). While fluid pathways in our setup are constrained by the balloon, allowing little deviation from determined pathways, surface morphology may cause pressure gradients through changes in the overburden thickness. However, the crater depth-to-diameter relation is much smaller in nature than vertically exaggerated profiles might imply (Figs. 3.3, 3.4a). After impact cratering, the resulting crater morphology reaches a topographically metastable condition in the matter of hours (Collins et al., 2002; Ivanov, 2005).

I hypothesised that the sill would first expand horizontally before uniformly uplifting the crater floor in a piston-like manner (Jozwiak et al., 2012; Thorey & Michaut, 2014; Jozwiak et al., 2015; Wilson & Head, 2018). However, I observed that the uplift was not uniformly distributed above the balloon (Figs. 3.9, 3.10). Accumulation of fluid and uplift was mainly concentrated at the centre of the crater due to the flexural rigidity of the overlaying crust. The centre is typically the deepest point of a crater, with the least overburden above the sill and mechanically the weakest point. For a horizontal sill below a crater, the overburden, and hence the mechanical strength, increases towards the crater rim as the crater depth decreases. Higher fluid pressure is required for sill emplacement towards the crater rim (Fig. 3.4a). The concentrated uplift caused the formation of extensional fractures to develop. Based on the experiments, it is apparent that these fractures would lead to an evacuation of the magma-analogue if it were not constrained by the skin of the balloon (Fig. 3.9). In addition, non-uniform uplift caused a moat to form between the uplifted area and the crater rim. In case of the deeper balloon, uplift was much more uniform and the resulting moat is less distinct (Figs. 3.10, 3.3). The intrusion of a sill modifies the crater morphology by uplifting its floor. The uplift is not uniform, but is influenced by the deepest point of the crater.

I hypothesised that the sill would stop extending past the crater rim (Jozwiak et al., 2012; Thorey & Michaut, 2014; Jozwiak et al., 2015; Wilson & Head, 2018). In the experiments of set 2 with a balloon lager than the crater, the crater rim had little influence on stopping the expanding sill from expanding laterally. Experiment 9I and 12I show that fractures extend beyond the crater rims (Fig. 3.6). However, these fractures develop late into the inflation. In experiment 9I, the fractures show no sign of influence from the presence of crater morphology. Therefore, the increase in overburden above the balloon of y_m = 0.59 cm (y_n = 2.97 km) does not add enough pressure to stop the balloon from inflating. In experiment 12I, radial fractures transecting the crater rim diverge and split into smaller fractures. This indicates that overburden hinders fluid emplacement and uplift-induced fracture localization beyond the rim. The modelled crater in experiment

12I is identical to that in experiment 9I, so the difference in fractures between the two must be attributed to the deeper location of the sill and, therefore, its higher overburden. In the series of experiments where the balloon centre is offset from the centre of the crater by 2.5 cm (Fig. 7, experiment 16 and 18), the developing fracture patterns are offset by only 1.25 cm. In case of the offset balloon, the developing fractures, which are normally balloon-centred, are offset by 1.25 cm. This is less than the total offset of 2.5 cm. The fracture pattern is offset towards the crater centre, i.e., towards the point of least overburden thickness. However, our experiments show that the influence of the crater topography is much smaller in both cases of balloon depth than previously expected. The crater margin was unable to stop the expansion of the sill beyond the rim.

3.6.3 Terraced crater walls

Terraced crater walls are typical for lunar craters (Figs. 3.2, 3.3; Krüger et al., 2017). The mechanism of terrace formation is part of the cratering process, in which the rim of the crater cavity is translated inwards along concentric normal faults (Settle & Head III, 1979; Krüger et al., 2017). The mare filling of the crater floors has sharp, partly overflowing contacts with terraced wall blocks (Fig. 3.2b). Terraces are not considered in our initial crater morphology (Fig. 3.10). When the rotating blade excavates the final crater morphology, as part of the experiment preparation, I do not observe any wall collapse (Fig. 3.4b). In all our experiments I observed the development of concentric normal faults on the crater wall during evacuation of the analogue sills (Figs. 3.5, 3.10). The resulting fractures displace blocks of the crater wall in a step-like manner (Fig. 3.10). As terrace formation is part of the cratering process which I do not model, I still can observe spontaneous formation of these fractures in our models. However, concentric fractures also develop beyond the crater rim at the balloon rim in the Set 2 experiments which is not known to be the case in nature (Fig. 3.6). It is, therefore, likely that their development in our experiments is solely related to the hinge zone of the flexed crater floor. On inflation, the upwards flexing balloon rim is compacted but shows poor fracture localisation (Fig. 3.5). On deflation, the compacted hinge is stretched, localising extensional fractures. In addition, the model faults showed differential displacements between the blocks (Fig. 3.10). The formation of terraces is more dispersed in the case of a deep sill (Fig. 3.5, experiment 5E). This observation suggests that the dominant presence of terraced walls in lunar fractures may not be exclusively related to the impact process (Figs 3.2, 3.3). Their occurrence in our experiments could also be an indication that a subsiding crater floor could be able to reactivate terrace faults contributing to further slumping at a later stage.

3.6.4 Magmatic system

FFCs are generally associated with surface expressions of magmatic activity (Jozwiak et al., 2015; Head & Wilson, 2017; Giguere et al., 2020). The clear correlation between FFCs and the presence of volcanic activity on the surface ensures the presence of magma. The observed fracture patterns, which are consistent with lunar examples, support the assumption that igneous intrusion is a possibility of crater floor uplift. Lunar floor fractured craters measure up to 300 km in diameter (Fig. 3.2). The igneous intrusion model expects the resulting sill to form to almost equal diameters as the crater (Thorey & Michaut, 2014). The most prevalent FFCs have a diameter of 62 km, which is still a tremendous diameter for an intrusive sill (Michaut, 2011). A sill of this diameter is exceptionally large when compared to terrestrial examples (Galerne et al., 2008; Jaxybulatov et al., 2014). Large terrestrial crater such as Sudbury (Canada) and Vredefort (South Africa) have been eroded by a couple of kilometres (Grieve & Therriault, 2000; Grieve et al., 2008; Huber et al., 2022). Even though we have deep exposure at these sites there are no known sills beneath large terrestrial craters. Lunar sills may extend further laterally than terrestrial ones due to lower viscosity of lunar magmas (Head & Wilson, 2017). FFCs are generally half as deep as fresh, unmodified craters (Pike, 1977). Crater floor uplift solely accomplished by igneous intrusion necessitates sill thicknesses of a couple of kilometres (Figs. 3.2b, 3.3). Again, exceptionally thick when compared to terrestrial examples, although due to the lower gravity greater thicknesses can be reached (Galerne et al., 2008; Jaxybulatov et al., 2014). The thickness of the maximal inflated balloon in our experiments was designed to lift the crater floor uniformly by 5 mm or 2.5 km in nature. This is consistent with expected thicknesses of the lunar sills (Jozwiak et al., 2015; Wilson & Head, 2018). While maximal inflation of model sills resulted in central uplift regarded as unrealistic (Fig. 3.10). Our experiments show that sill inflation does not uniformly uplift the crater floor (Fig. 3.10). For a sill or laccolith to be able to lift the crater floor to the observed depth reduction, a large volume of melt must be generated and mobilised. The required volume of ascending magma would necessitate mass relocation at lower crustal levels, potentially necessitating lower crustal flows to maintain mass balance.

Due to the sheer size of the intrusions required to uplift the crater to the observed levels, I consider the development of a fully mature sill to be unrealistic. Our experiments show that uniform, piston like uplift of the crater floor is not accomplished under the most ideal conditions. The similarity between experimental fracture pattern and lunar CFFs do not exclude the roll of an igneous intrusion as the driver for uplift, but not to the extent previously hypothesised.

FFCs show smooth lava filled floors (Fig. 3.2). These fillings are attributed to be most likely mare material post-dating the impact structure (Giguere et al., 2020; Pathak et al., 2021; Kimi et al., 2023). If the younger lava originated externally, an inflow is required to fill the crater floor. Smooth floor fillings are generally disconnected by older slumped crater wall lithologies from the surrounding mare materials (Fig. 3.2). External inflow is visible at Gassendi however mare filling is clearly separated from the elevated floor filling (Fig. 3.3, Giguere et al., 2020). Therefore, in case of Gassendi filling must originate from within the crater and has experienced crater floor uplift. The possibility of erupting ascending magma into the crater has been proposed previously (Gornitz, 1973; Srivastava et al., 2013; Michaut & Pinel, 2018). Impact-induced weaknesses in the crater floor are a prerequisite for magma pathways (Michaut & Pinel, 2018). In our experiments, I observed that local accumulation and vertical floor uplift were favoured over horizontall fluid migration. The experiments show that it is more efficient for accumulating magma to overcome the pressure of the overburden than to spread horizontally. In addition, gas and volatiles in the magma reaching surface begin to expand due to the vacuum, foaming the magma and reduce its density (Head & Wilson, 2017). Our experiments support the idea that early eruption of accumulating magma is the most likely outcome. It is therefore unlikely that the sill will reach full maturity as previously thought. Infill might play a bigger role in shallowing the crater than previously expected.

Doming structures in the vicinity of mare regions have been interpreted as large laccolith intrusions unrelated to impacts (Wöhler et al., 2006; Wöhler et al., 2007; Wöhler & Lena, 2009). Their morphology shows low angle convex up-doming of mostly flat lunar mare material. However, their diameter and uplift does not approach the diameter expected for FFCs (Wöhler et al., 2006; Wöhler et al., 2007). Their surfaces only show minimal fracturing. Most of the observable linear graben cut the surrounding mare plain and the doming structure (Wöhler et al., 2006; Wöhler et al., 2007; Wöhler & Lena, 2009). With the lack of visible surface fractures none of the doming structures are relatable to the fractures observed in experimental set 4 (Fig. 3.8). The lack of surface fractures on the proposed laccolith is unexpected, as doming over the laccolith induces fractures that are visible on the surface (Schmiedel et al., 2017). Relating the proposed laccolith to our results of set 4 shows that these may actually not be laccoliths.

The majority of FFCs possesses a morphological central peak (Figs 3.2, 3.3, Jozwiak et al., 2012). However, peaks in FFCs are typically less pristine, not coherent and drowned from the surrounding mare fill (Fig. 3.2). Areas between individual sub-peaks are filled by mare material. Furthermore, FFCs such as Humboldt feature large pits in-between peaks (Fig. 3.3). While our experiments neglect the initial presence of a central peak, I observed strong peak-like uplift early in the inflation. Fractures at the early stage

of floor uplift are strongly dilatational and concentrated to the central area (Fig. 3.9, exp. 3). From our observations it is therefore possible that crater floor uplift could contribute to the modification of peaks observed in lunar crater (Fig. 3.2b). As the evacuation of the sill is expected to occur around the crater centre the peak might be affected by the volcanic activity. Observed pits between peaks are indication for potential volcanic vents associated with sill evacuation on mare filling of crater floors (Head & Wilson, 2017). This may identify as the vents involved in evacuation of the sill.

3.6.5 Sill emplacement model

Derived from the observations of our experiments, I propose a revised igneous intrusion model for the formation of lunar FFCs. Crustal unloading causes the formation of melt below the crater (Fig. 3.12a). Melt starts to accumulate and migrate upward and transitions into a horizontal intrusion. Inflation causes crater floor uplift. At first, accumulation of magma is limited to the crater centre with the lowest overburden (Fig. 3.12b). The intrusion takes a laccolith shape. Central uplift and upwards bending of the crater floor forces the formation of large extensive fractures. In conjunction with an already brecciated host rock these fractures will ultimately favour evacuation of the intrusion before a mature sill can develop. Evacuation of the laccolith will cause the crater floor to subside while the crater fills with lava (Fig. 3.12c). Lava filling will partly fill the crater morphology with seemingly disconnected mare material, contributing to a shallowing of its initial morphology. CFFs will adsorb part of the mare filling pausing their presence to the surface (Head & Wilson, 2017). Subsidence of the crater floor reactivates concentric crater wall fractures of terraces. The intrusion may only evacuate partly contributing to an overall shallowing of the crater floor (Fig. 3.12c). Our proposed model differs from the generally accepted model by emphasizing that the intrusion does not reach the maturity previously stated.

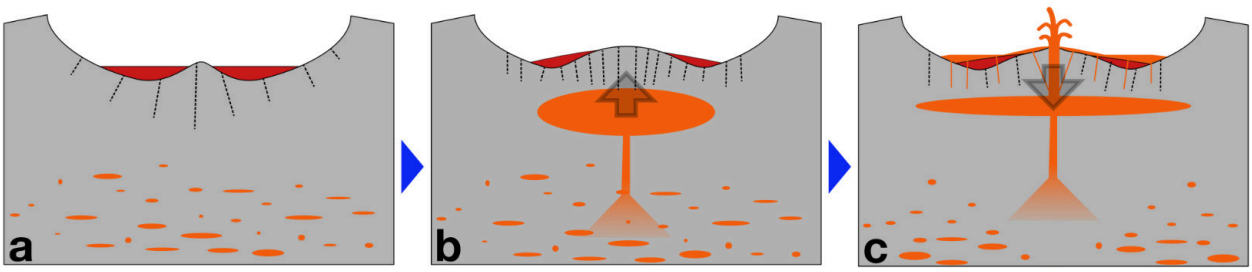

Figure 3.12: Synoptic block diagram showing the proposed evolution of intrusion-induced crater modification. (a) Final crater with fresh, unaltered morphology. (b) Accumulation of melt below the crater at. Uplift of the crater floor. (c) Partial evacuation of the crater floor through fractures in the crater centre. Melt filling the crater floor. Subsidence of the crater floor due to evacuation of the underlying sill. See text for detailed explanation.

3.7 Conclusions

Our experiments show that the inflation of a sill below a crater is capable to uplift the crater floor shallowing its depth. Floor uplift causes upwards bending of the crater floor inducing fractures in the overlying granular material. Fracture patterns were primarily controlled by the depth below crater floor of balloons rather than by crater floor morphology. In shallow model sills polygonal fracture pattern dominated the crater floor, whereas deep model sills developed a primarily radial fracture pattern. For the onset of fluid inflation into shallow model sills, surface uplift was focused on the crater centre and associated with rather prominent fractures. Accumulation of magma is controlled by the deepest point of the crater. The majority of natural lunar craters are dominated by polygonal fractures and therefore the emplacement of a shallow sill is the most realistic assumption. Upon evacuation, concentric normal faults developed at the inner crater wall which correspond to the terraced crater margins ubiquitously observed at lunar craters. Overall, our experiments closely resemble lunar floor fractured craters structurally supporting the igneous intrusion model. Interestingly, model craters are characterized by more diverse fracture patterns, compared to lunar craters, which may be due to resolution constraints in remote sensing data. Furthermore, focused brittle deformation above sills during onset of inflation likely creates pathways allowing for magma to erupt from natural sill reservoirs, explaining the presence of disconnected mare fill of most FFCs. Central peaks are often only preserved as multiple peaks, which may further collapse during crater floor uplift. Our data shows that the igneous intrusion model is capable of explaining lunar FFCs. However, it is unlikely that natural sill systems attain the maturity previously proposed by the literature. Proposed magnitudes of sills are unknown in terrestrial analogues. I call into question the generalized model proposed by the literature regarding uncertainties on magma ascend and sill formation. Evacuation during inflation in natural systems can account for the presence of less prominent fracture patterns compared to the ones in modelled, more “mature” sill systems.

4. Long-term Isostatic Relaxation of Large Terrestrial Impact Structures: Structural Characteristics Inferred from Scaled Analogue Experiments

Abstract

Crater floor fractures are prominent post-cratering structural vestiges that are known from large impact craters on rocky planetary bodies. Two mechanisms were proposed to explain the formation of floor fractures: emplacement of igneous sheets below crater floors and isostatic re-equilibration of crust underlying target rocks, i.e., crustal relaxation. Here, I use two-layer analogue experiments modelling the deformational behaviour of lower and upper crust following crater formation, scaled to the physical conditions on Earth, to explore the structural and kinematic consequences of crustal relaxation. Specifically, the structural evolution of model upper crust was systematically analysed for various initial depths and diameters of crater floors, gleaned from numerical models for average continental crust. The analogue modelling results provide quantitative estimates of the duration, geometry and distribution of deformation zones in upper crust and, for the first time, a quantitative relationship between diameter, depth and fracture geometry of crater floors. The experiments show also that crater floor uplift is accomplished by long-wavelength subsidence of the crater periphery and may operate on time scales of thousands of years in nature. I conclude that patterns of observed floor fractures, including impact melt rock dykes known from the Sudbury and Vredefort impact structures, can be caused by long-term uplift of the crater floor, compensated by lateral crustal flow toward the crater centre.

4.1. Introduction

Meteorite impact is recognized as a fundamental geological process of the solar system. Knowledge on large impact crater formation in particular has gained significantly in importance in the Earth Sciences for understanding punctuated geological events entailing drastic changes of climate (Artemieva et al., 2017; Gulick et al., 2019), the evolution of life (Goderis et al., 2021; Kring & Bach, 2021; Lowery et al., 2021) and generation of giant natural resource deposits (Lightfoot, 2017). Large impact crater formation is typically regarded as a matter of minutes (Melosh, 1989). Accordingly, numerical models of large impact cratering are generally tailored to elucidating cratering mechanisms on this time scale (Melosh & Ivanov, 1999; Wünnemann & Ivanov, 2003; Ivanov, 2005; Collins et al., 2012; Morgan et al., 2016). Despite the importance for understanding deformation processes resulting in the morphology and structure of crater floors as well as the redistribution of impact melt within target rock, long-term crater modification, spanning thousands of years after cratering, has not been analyzed systematically in 3-D space (Melosh, 1976; Schultz, 1976; Schultz & Orphal, 1978; Wichman & Schultz, 1993; Riller, 2005; Hecht et al., 2008; Jozwiak et al., 2012; Jozwiak et al., 2015; Huber & Kovaleva, 2020; Huber et al., 2022).

The pristine morphology of craters is evident best on rocky celestial bodies that are largely devoid of atmospheric and endogenetic processes causing resurfacing of the bodies. Notably on the Moon, the flat floors of many large impact craters have long known to be characterized by prominent fractures and are, thus, known as floor-

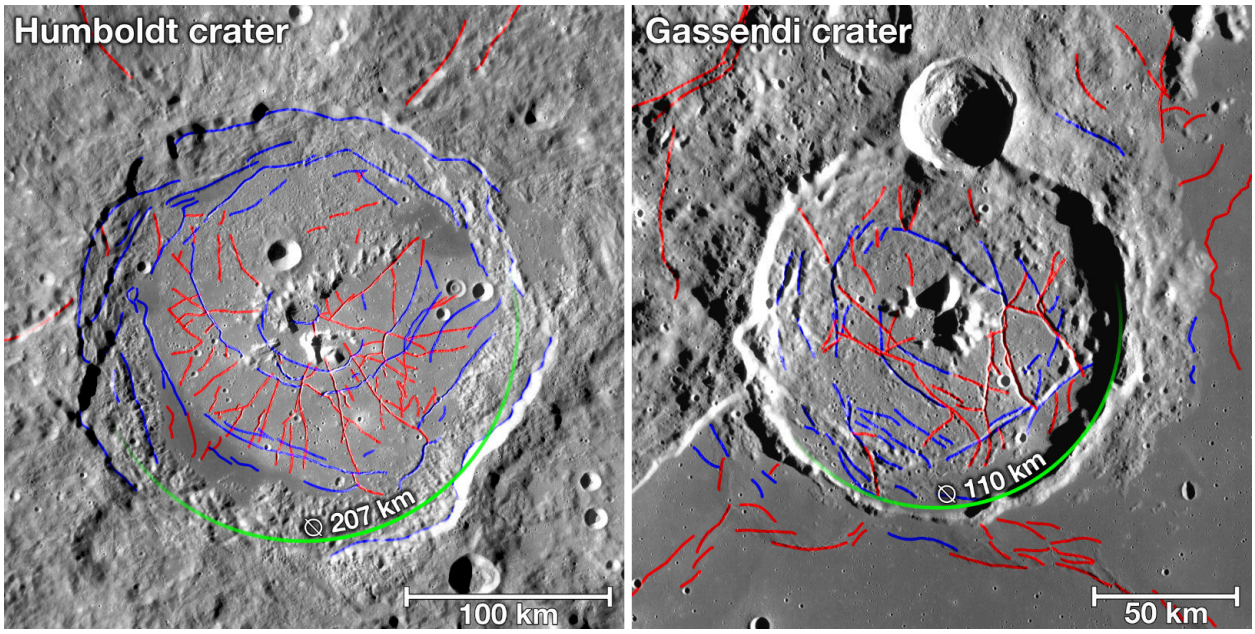

Figure 4.1: Examples of complex lunar craters showing radial and concentric floor fractures, indicated by red and blue lines, respectively, for the Humboldt and Gassendi craters.

fractured craters (Melosh, 1976; Schultz, 1976; Hall et al., 1981; Dombard & Gillis, 2001; Mohit & Phillips, 2006; Jozwiak et al., 2012; Thomas R. Watters et al., 2012; Thorey & Michaut, 2014; Jozwiak et al., 2015). Crater floor fractures (CFFs) can be tens of kilometers long and may form radial, concentric and polygonal patterns, in places even beyond crater margins (Fig. 4.1). Floor-fractured craters are known also from Mars,

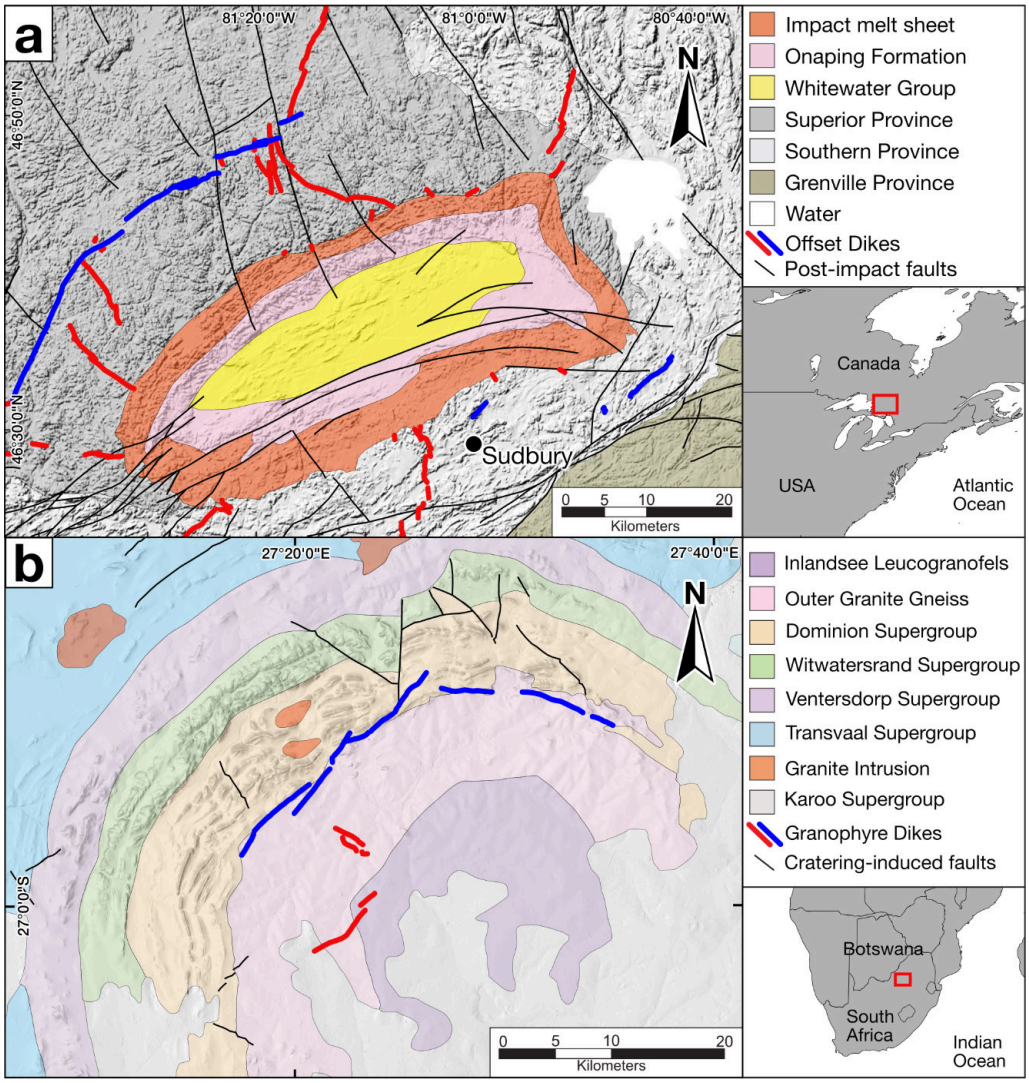

Figure 4.2: Examples of the largest known impact structures on Earth hosting radial and concentric impact melt-rock dykes, indicated in red and blue, respectively. (a) Sudbury impact structure, Canada. Geometry of Offset Dykes are based on Pilles et al. (2018). (b) Vredefort impact structure, South Africa. Geometry of Granophyre Dykes are based on Lieger and Riller (2012) and Huber et al. (2020).

Enceladus, Ceres, Venus and Mercury. Martian CFFs are less distinct due to vigorous atmospheric processes of the planet (Schultz & Orphal, 1978; Korteniemi et al., 2006; Mohit & Phillips, 2007). The nearly 1000 km wide Caloris Basin on Mercury is, perhaps, the most impressive floor-fractured crater known in the solar system. It is characterized by a distinct radial pattern of CFFs and grabens in its centre (Watters et al., 2005;

Murchie et al., 2008; Freed et al., 2009; Mohit et al., 2009; Watters et al., 2009; Klimczak et al., 2010; T. R. Watters et al., 2012; Klimczak et al., 2013) and concentric CFFs and compressional ridges, so-called wrinkle ridges, which developed close to the margin of the impact structure (Freed et al., 2012).

On Earth, evidence of floor-fractured craters is less obvious, as large impact structures are partially eroded, covered by sedimentary strata or are deformed (Grieve & Therriault, 2000; Grieve et al., 2008). Two impact structures, Sudbury (Canada) and Vredefort (South Africa), which are most likely more than 200 km in diameter, are well known for hosting impact melt-rock dykes, i.e., melt rock-filled CFFs (Wichman & Schultz, 1993). At Sudbury (Fig. 4.2a), the dykes are known, due to post-emplacement tectonic segmentation, as Offset Dykes (Grant et al., 1984). The dykes are disposed concentrically and radially around the relic of the deformed impact melt rock sheet (Grieve, 1991; Riller, 2005), to which some of the radial ones are connected (Hecht et al., 2008; Lightfoot, 2017; Pilles et al., 2018). Similar to Sudbury, the Vredefort impact structure hosts impact melt rock dykes, known as Granophyre Dykes (Reimold & Gibson, 2006). These dykes are disposed mostly concentrically around the crater centre and line the interface between granitoid rocks and supracrustal strata (Fig. 4.2b). Similar to the Offset Dykes at Sudbury, the Granophyre Dykes are interpreted to be derived from the overlying, now eroded, impact melt rock sheet (Lieger & Riller, 2012; Huber & Kovaleva, 2020; Huber et al., 2020; Huber et al., 2022).

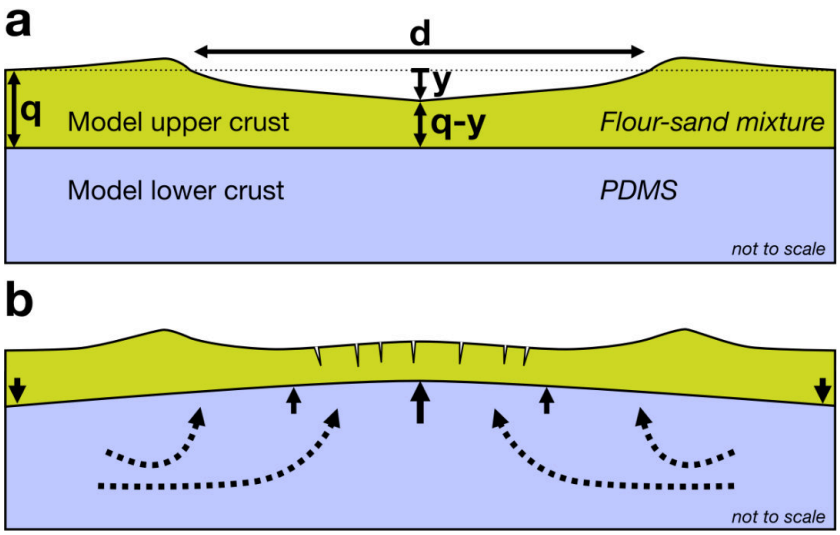

Figure 4.3: Sketch outlining crustal flow during isostatic relaxation of crust below meteorite impact craters. (a) Crater profile prior to onset of crustal relaxation. q: Thickness of granular layer, d: Initial rim-to-rim crater diameter, y: Depth of crater centre. (b) Crustal flow indicated by stippled arrows during crustal relaxation.

There are two major conceptual models for the formation of CFFs: emplacement of horizontal igneous sheets below the crater floor (Schultz, 1976; Jozwiak et al., 2012) and isostatic re-equilibration of crust underlying the crater floor (Hall et al., 1981; Huber et al., 2022). Both mechanisms are assumed to independently cause uplift of the crater floor resulting in radial stretching of the crater floor accomplished by extensional

fractures. The “igneous sheet hypothesis” is based on the presence of lava flows frequently found within, and in the vicinity of, large lunar craters, and proximity of CFFs to mare regions (Jozwiak et al., 2012). Isostatic re-equilibration of crust (Fig. 4.3) below large craters is attributed to the mass deficit caused by ballistic ejection of target rock during cratering (Melosh, 1989). This process requires a viscously deforming lithosphere. Upward flexing of the crater floor is thought to be compensated by subsidence of the crater margin and its periphery (Fig. 4.3b).

Here, I explore the viability of isostatic re-equilibration, i.e., relaxation, of crust underlying large impact craters, and the evolution of CFFs in terms of patterns and kinematics during this process, using two-layer scaled analogue experiments. Specifically, I systematically analyze the influence of initial depths and diameters of model craters on CFF formation. Using state-of-the art digital image correlation, the results of our physical experiments enable us to quantitatively project the duration of vertical displacements, horizontal surface motion and localization of brittle deformation at surface to natural equivalents. Modelling results are compared to the Chicxulub, Sudbury and Vredefort impact structures, the three largest ones presently known on Earth (Grieve et al., 2008). Taking into account crustal thickness, the analogue experiments provide, for the first time, a quantitative relationship between morphology and diameter of crater floors with fracture geometry.

4.2. Experimental setup

A rectangular tank measuring 75 cm x 75 cm x 8 cm was filled with an 8 cm thick layer of polydimethylsiloxane (PDMS), representing viscous middle and lower crust, and granular material, simulating the brittle upper crust, sieved on top of the PDMS layer (Fig. 4.4a). The granular layer consisted of a 2:1 mixture of respectively flour and quartz sand (see 2.4.7.3 flour 2:1 for detailed description). To avoid unwanted experimental artefacts due to large variation in the thickness of the granular layer, its top surface was levelled by scraping off excess granular material utilizing spacers at the tank edges as reference. This procedure resulted in a variation of the top surface of less than ± 0.7 mm. Scraped surfaces served as topography reference planes for crater depths.

As I explore long-term crater modification, the actual mechanisms of impact cratering are unimportant for our physical experiments. We, therefore, use the crater shapes resulting immediately after cratering as starting conditions. The generation of most accurately shaped model craters in granular material without altering mechanical material properties is key for achieving meaningful modelling results. Based on natural prototypes, computer-aided design and a 3D printer were used to manufacture curved

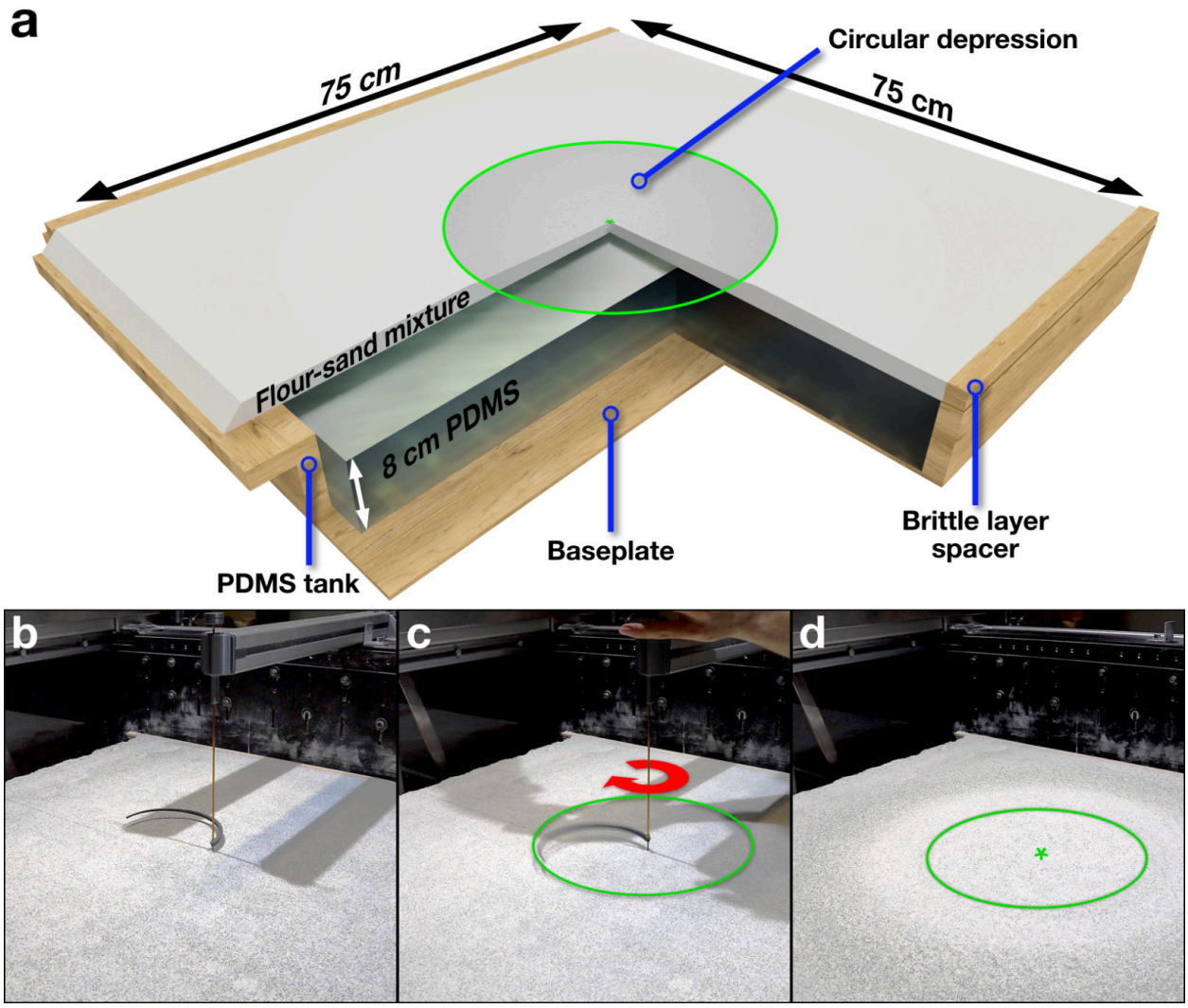

Figure 4.4: Images showing the experimental setup and generation of model impact craters in granular material (1. generation). (a) Sketch illustrating the general experimental setup. (b) Positioning of the curved plastic blade attached to a hollow metal axis into the granular material. (c) Fast rotation of the blade ejects granular material. (d) Excavated crater and ejected material around the crater margin (green circle) after removal of the curved blade.

plastic blades modelling the desired depths, diameters and morphologies of model craters. Crater floor depths were maximal in the centres and decreased linearly to about 1 mm near crater margins. The plastic blades were attached to a hollow metal axis and lowered over a fixed metal axis into the into the granular material (Fig. 4.4b). Fast rotation of the plastic blade, propelled with a portable drill held in position by a gantry, ejected granular material radially outward and excavated craters of any desired diameters and shapes in granular material (Fig. 4.4c). An added value of this procedure is that ballistically ejected material is evenly distributed around model craters (Fig. 4.4d), akin to the distribution of natural ejecta deposits, decreasing in thickness with increasing distance to crater margins.

4. Isostatic relaxation model

Experiment No.	Nature q_n [km]	d_n [km]	y_n [km]	$q_n - y_n$ [km]	Model q_m [cm]	d_m [cm]	y_m [cm]	$q_m - y_m$ [cm]	y_m End [cm]	Uplift [cm]	Nature S_n	U_n	Model S_m	U_m Start	U_m End	Concentric fractures [%]	Radial fractures [%]
1	7	87.5	1.14	5.86	2	25	0.311	1.689	0.022	0.326	0.0670	0.0130	0.0676	0.0124	0.0009	6.6	93.4
2	7	87.5	1.14	5.86	2	25	0.394	1.606	0.008	0.367	0.0670	0.0130	0.0642	0.0158	0.0003	10.3	89.7
3	7	105	1.21	5.79	2	30	0.370	1.629	-0.055	0.385	0.0551	0.0115	0.0543	0.0123	-0.0018	9.3	90.7
4	7	105	1.21	5.79	2	30	0.492	1.508	-0.056	0.525	0.0551	0.0115	0.0503	0.0164	-0.0019	28.7	71.3
5	7	122.5	1.25	5.75	2	35	0.356	1.644	0.021	0.334	0.0469	0.0102	0.0470	0.0102	0.0006	13.8	86.2
6	7	122.5	1.25	5.75	2	35	0.393	1.607	-0.012	0.452	0.0469	0.0102	0.0459	0.0112	-0.0003	31.7	68.3
7	7	122.5	1.25	5.75	2	35	0.461	1.539	-0.048	0.487	0.0469	0.0102	0.0440	0.0132	-0.0014	39.8	60.2
8	7	140	1.31	5.69	2	40	0.406	1.594	-0.029	0.438	0.0406	0.0094	0.0399	0.0102	-0.0007	8.3	91.7
9	7	140	1.31	5.69	2	40	0.519	1.481	0.052	0.486	0.0406	0.0094	0.0370	0.0130	0.0013	18.6	81.4
10	7	140	1.31	5.69	2	40	0.566	1.434	-0.044	0.650	0.0406	0.0094	0.0359	0.0142	-0.0011	48.7	51.3
11	7	157.5	1.36	5.64	2	45	0.446	1.554	-0.024	0.509	0.0358	0.0086	0.0345	0.0099	-0.0005	22.9	77.1
12	7	157.5	1.36	5.64	2	45	0.619	1.381	-0.079	0.733	0.0358	0.0086	0.0307	0.0138	-0.0018	94.5	5.5
13	7	157.5	1.36	5.64	2	45	0.674	1.326	-0.024	0.710	0.0358	0.0086	0.0295	0.0150	-0.0005	81.8	18.2
14	7	175	1.4	5.6	1	25	0.342	0.658	-0.038	0.358	0.0320	0.0080	0.0263	0.0137	-0.0015	94.1	5.9
15	7	175	1.4	5.6	1	25	0.441	0.559	-0.103	0.536	0.0320	0.0080	0.0224	0.0176	-0.0041	100	0
16	7	210	1.48	5.52	1	30	0.478	0.522	-0.059	0.556	0.0263	0.0070	0.0174	0.0159	-0.0020	90.4	9.6
17	7	210	1.48	5.52	1	30	0.593	0.407	-0.052	0.643	0.0263	0.0070	0.0136	0.0198	-0.0017	83.5	16.5
18	7	245	1.52	5.48	1	35	0.551	0.449	-0.017	0.562	0.0224	0.0062	0.0128	0.0157	-0.0005	80	20
19	7	245	1.52	5.48	1	35	0.605	0.394	-0.021	0.636	0.0224	0.0062	0.0113	0.0173	-0.0006	88.5	11.5
20	7	280	1.62	5.38	1	40	0.329	0.671	-0.042	0.329	0.0192	0.0058	0.0168	0.0082	-0.0010	81.2	18.8
21	7	280	1.62	5.38	1	40	0.524	0.476	-0.032	0.583	0.0192	0.0058	0.0119	0.0131	-0.0008	69.7	30.3

q: Brittle layer thickness; d: Crater diamater; y: Crater cavity depth; q-y: Floor thickness brittle layer (center); S: Floor thickness-crater diameter ratio; U: Depth-diameter ratio

Table 4.1: Model parameters and their natural equivalents for each experiment.

For quantitative analysis of surface deformation, the experiments were recorded with a 3D Stereo Digital Image Correlation (DIC) StrainMaster system manufactured by LaVision GmbH (Germany). Two M-lite 12M CMOS cameras (12-megapixel) where mounted on a framework above the model surface. The images were recorded with a Device Control Unit X (DCU X) running DaVis 10.2 by LaVision GmbH (Germany). A set of Nikon lenses with 24 mm focal lengths were used. Stereo DIC permits the computation of 3D surface displacement fields by cross-correlation of sequentially recorded stereo image pairs (Adam et al., 2005; Eisermann et al., 2021). Simultaneous application of stereo image reconstruction generates a highly accurate 3-D model of the surface topography. The brittle layer included black dyed quartz grains serving as marker particles for DIC cross-correlation. Calibration of the cameras prior to preparation of model craters identified and corrected lens distortions and set the correct length scale to ensure high-precision calculations. The vertical and horizontal accuracy of the recorded surface was in the sub-millimetre range. For displacement vector field calculation using DIC, the software DaVis 10.2 was used as well. This allowed us to precisely monitor the morphological evolution of the surface, commencing immediately upon crater formation, by calculating the cumulative displacement vector field for each experiment.

4.3. Scaling

Accurate scaling of the experiment is a prerequisite to ensure physical comparability between model (Subscript m) and nature (Subscript n) (Hubbert, 1937). Our experiments were scaled to Earth. Diameters and depths of freshly formed terrestrial craters as well as ejecta thicknesses were modelled numerically using the "Earth Impact Effects Program" (Collins et al., 2005). I set the density of target rock, simulating average continental crust, at 2700 kg/m^3, the density of the projectile, representing a solid stone impactor, at 3000 kg/m^3, the impact velocity at 20 km/s, and the impact angle at 45°. Projectile diameters were increased incrementally resulting in an increase of crater diameter (d) and central crater depth (y) (Table 4.1), both considered in the experimental setup.

Limited by the size of our modelling box, two sets of physical experiments differing in length scaling were conducted to model surface deformation in and around craters representing natural equivalents of up to 280 km in diameter. The length scale of set 1 experiments was set to $L_{set1} = l_m/l_n = 2.9 \times 10^{-6}$, i.e., the brittle layer thickness q_m = 2 cm, to model surface deformation within and around craters representing natural equivalents between 87.5 km and 157.5 km in diameter (experiments 1 to 13 in Table 1). The length scale of set 2 experiments was set to $L_{set2} = l_m/l_n = 1.43 \times 10^{-6}$, with q_m = 1 cm, to account for diameters of natural crater between 175 km and 280 km (experiments 14 to 21 in Table 4.1). Given the same grain size of the granular material in both experimental setups, the spatial resolution of set 2 experiments is somewhat reduced compared to set 1 experiments.

The flour-quartz sand mixture consists of standard wheat flour type 405 and G23T quartz sand type. The Mohr-Coulomb properties of this granular material adheres to brittle (Subscript B) deformation typical for upper continental crust. Specifically, the mixture has a density of ρ_{mB} = 961.5 kg/m^3, a cohesion of approximately 108 Pa s and an internal friction angle of ϕ = 46.39° (Table 2.31). I ensured that humidity did not affect the strength of the granular material by always keeping the air humidity in the lab below 20%. The respective material properties, notably angle of repose and density, were determined in our laboratory, whereas cohesion and shear strength were measured with a ring shear apparatus at the GFZ Potsdam, Germany (see 2.4.7.3 flour 2:1 for detailed description). PDMS simulating viscous (Subscript D) deformation consisted of KORASILON® Öl G 30 M manufactured by Kurt Obermeier GmbH & Co. KG. At low strain rates, this material, which has a specific density of ρ_{mD} = 967 kg/m^3, is characterized by an effective near Newtonian viscosity of $\eta_m = 3 \times 10^4$ Pa s as indicated by the manufacturer and verified at the GFZ Postdam laboratory for the material batch used in our experiments (see 2.4.8.2 PDMS for detailed description). Given the effective

viscosity of the lower continental crust η_n = 1020 Pa s (Shinevar et al., 2015), the viscosity scaling factor amounts to $H = \eta_m/\eta_n = 3 \times 10^{-16}$.

Using the average density of the brittle upper crust ρ_{nB} = 2660 kg/m^3 and ρ_{nD} = 2700 kg/m^3 for the lower crust (Christensen & Mooney, 1995), the density scale is defined as $P_B = \rho_{mB}/\rho_{nB}$ = 0.361 for the upper crust and $P_D = \rho_{mD}/\rho_{nD}$ = 0.358 for the lower crust. The density ratio between upper and lower crust is $P_n = \rho_{nB}/\rho_{nD}$ = 0.985 and $P_m = \rho_{mB}/\rho_{mD}$ = 0.993 in the model and, thus, rather similar. The time scale ratio:

$$T = \frac{t_m}{t_n} = \frac{H}{P_D * L * G}$$

Where G = g_m/g_n = 1 is the gravity ratio. In set 1 experiments, 1 s in the model corresponds to 0.92 years in nature, in contrast to 1.85 years in set 2 experiments. It should be kept in mind that the time scaling is highly dependent on the chosen viscosity for the natural lower crust (η_n).

4.4. Results

The relationship between long-term viscous relaxation of crust and evolution of CFF patterns, characterized either as radial, concentric or polygonal, was examined in terms of initial diameters and depths of model craters (Table 4.1). For a given crater diameter, different crater depths, qualitatively denoted as shallow, intermediate and deep, were examined (Fig. 4.5). The shallowest ones of these are respectively closest to the numerically obtained ones for the Earth.

4.4.1 Vertical surface displacements

Magnitudes and rates of uplift of crater floor centres relate to initial diameters and depths of craters. Notably, large and deep model craters result in respectively larger magnitudes and rates of uplift than do small and shallow craters (Fig. 4.5; Supplementary figures S4.7). While the rates of crater floor uplift are high initially and decay exponentially, the magnitude of uplift increases with time. Specifically, set 1 experiments, adhering to craters with diameters between 87.5 km and 157.5 km, 90% of the crater floor uplift occurs within about 50 minutes, corresponding to some 2.700 years in nature (Fig. 4.5a). In set 2 experiments, modelling craters with diameters between 170 and 280 km, 90% of crater floor uplift is accomplished after about one hour, translating to approximately 6.700 years in nature (Fig. 4.5b). Thus, floor uplift rates in set 2 craters are lower than in set 1 craters and isostatic equilibrium is reached after

about t_m = 2.5 hours (t_n ≈ 8.500 years) in set 1, and t_m = 1.5 hours (t_n ≈ 10.000 years) in set 2 craters.

The spatial variation in total vertical displacements of crater floors characterized chiefly by radial and chiefly by concentric CFFs is illustrated respectively for experiments 6 and 13 (Table 4.1, Fig. 4.6a, b). The largest uplift magnitudes occur in the crater centres, notably in areas delimited by concentric fractures. Uplifted crater floors are mostly flat and lined by a moat at the crater rim (Fig. 4.6c, d). Crater floor uplift is accompanied by subsidence of the proximal crater periphery, covered largely by ejecta deposits, while the crater rims do not seem to undergo significant vertical displacements. On the other hand, distal peripheral areas bordering on the zones of subsidence undergo surface uplift (Fig. 4.6b; Supplementary Figures S4.3, S4.4). Often, the transition between the peripheral zones of subsidence and uplift are marked by weakly localized concentric reverse faults. Overall, vertical displacements occur over rather wide areas, i.e., large wavelengths of surface elevation changes, with the final crater floors approaching the level of the reference surface (Figs. 4.5, 4.6a–d). Interestingly, low-wavelength topographic anomalies are largely preserved during relaxation (Fig. 4.6c, d).

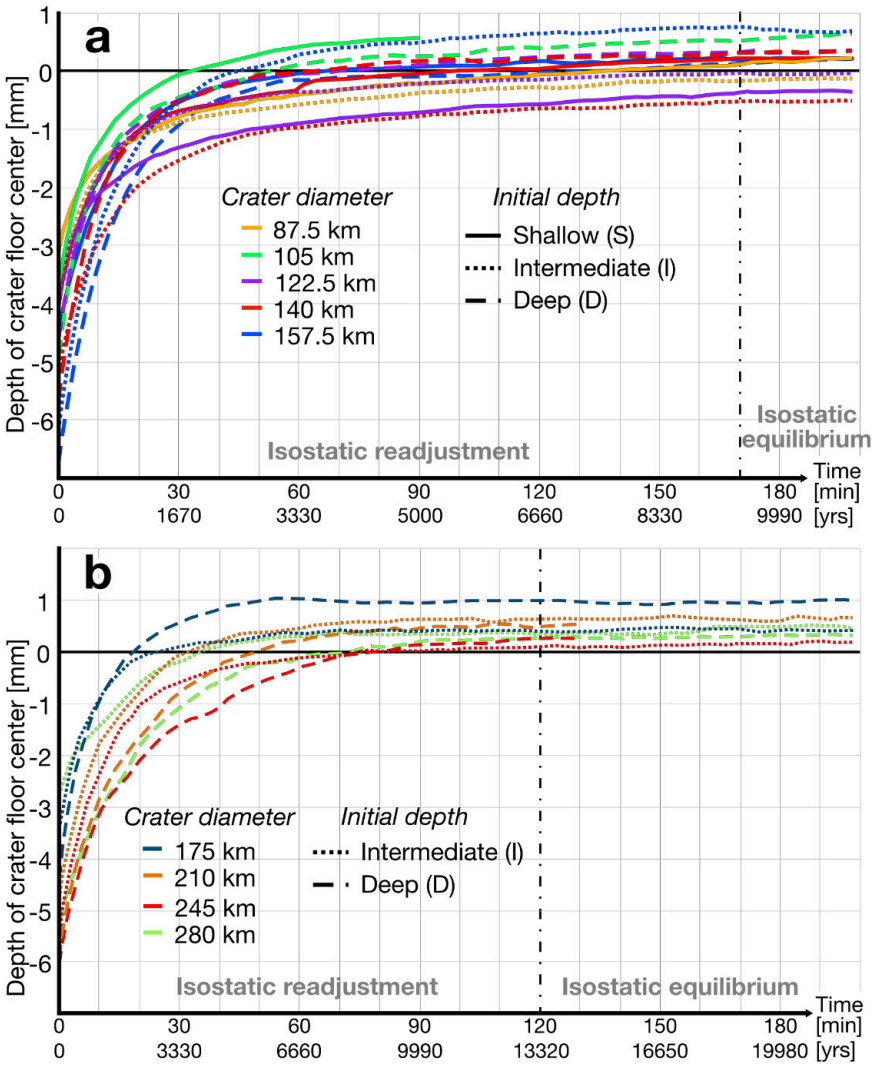

Figure 4.5: Diagrams displaying the magnitude and rate of floor uplift at model crater centres. Colors indicate the specific diameters of modelled craters in nature. The initial depths of each crater are indicated by different line styles of the curves (a) Experiments of set 1. (b) Experiments of set 2.

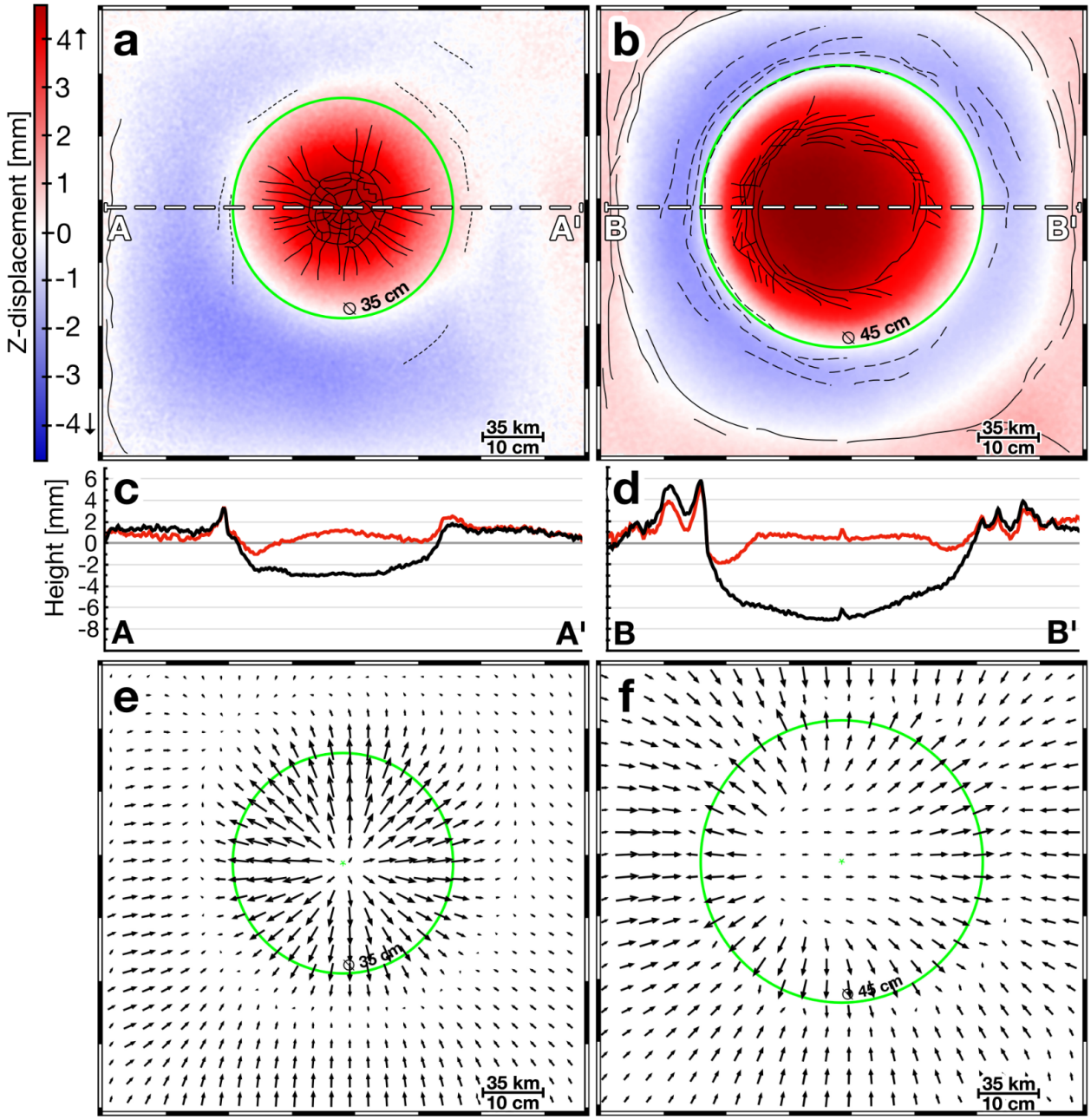

Figure 4.6: Spatial variation of cumulative displacements of model craters and their peripheries characterized chiefly by radial and chiefly by concentric floor fractures, i.e., experiments 6 and 13 (Table 1), respectively. (a, b) Cumulative vertical displacements of experiments 6 and 13, representing respectively craters with diameters of 122.5 km and 157.5 km. Solid and stippled lines indicate respectively traces of extension fractures and reverse faults. The outer zone of uplift in (b) is possibly an artefact caused by the proximity of this zone to the box walls inhibiting radial outward flow and, thus, causing uplift of the material. (c, d) Initial and final topography profiles, indicated respectively by black and red curves, of experiment 6 and experiment 13 craters. (e, f) Cumulative horizontal displacement vector fields of experiments 6 and 13.

4.4.2 Horizontal surface displacements

Gradients in the total displacement of surface particles are paramount for understanding the kinematics of model upper crust, and, by inference, that of the underlying viscous layer during relaxation (Fig. 4.6e, f; Supplementary figures S4.1, S4.2). Overall, the orientations of displacement vectors are radial, collectively forming centro-symmetric displacement vector fields, with a few exceptions attributed to somewhat imperfect model preparation. Notably, large gradients in the vector lengths with identical orientations are spatially associated with concentric extension fractures, whereas strongly divergent vector components adhere to zones of radial extension fractures. Conversely, areas of convergent displacement vectors provoke reverse faults. Hence, crust affected by radial CFFs is stretched gradually outward (Fig. 4.6a), whereas concentric dilation fractures enclose crustal portions retaining their structural coherence and, thus, characterize zones of velocity discontinuities decoupling crustal portions moving outward (Fig. 4.6b). The outward motion diminishes towards the crater rim, which itself is not displaced. Upper crust underlying the proximal crater periphery moves uniformly towards the crater rim where displacement magnitudes decrease to nill (Fig. 4.6a, b; Supplementary figures S4.1, S4.2).

4.4.3 Fracture patterns

Deformation in the slightly cohesive flour-sand mixture is evident by distinct fractures (Figs. 4.6, 4.7, 4.8). The fractures dissected the entire granular layer, evident upon removal of the layers after each experiment. Fractures visualized by DIC were screened in terms of geometric disposition, i.e., concentric versus radial, and type, i.e., extensional versus reverse, and displayed for each experiment (Figs. 4.7, 4.8). While uplifted surfaces, notably upward flexed crater floors, show mostly extensional fractures, subsided surfaces host dominantly reverse faults (Figs. 4.6, 4.7, 4.8; Supplementary figures S4.3, S4.4). The relative importance of the two geometric dispositions can be quantified by the percentages of their respective cumulative lengths compared to the total length of all fractures of an experiment (Table 4.1; Figs. 4.7, 4.8). For the smallest crater with the shallowest floor of set 1 experiments, i.e., experiment 1, 93.4% of all fractures are radial (Table 4.1; Fig. 4.7). Within this experiment set, the cumulative length of radial fractures decreases systematically with an increase in crater diameter and initial crater depth to some 5 to 18%, i.e., experiments 12 and 13. The respective increase in the cumulative length of concentric fractures, evident in this set of experiments, peaks at 100% in set 2 experiments, modelling the largest and initially deepest craters (Table 4.1; Fig. 4.8). Hence, there is a systematic increase in the total

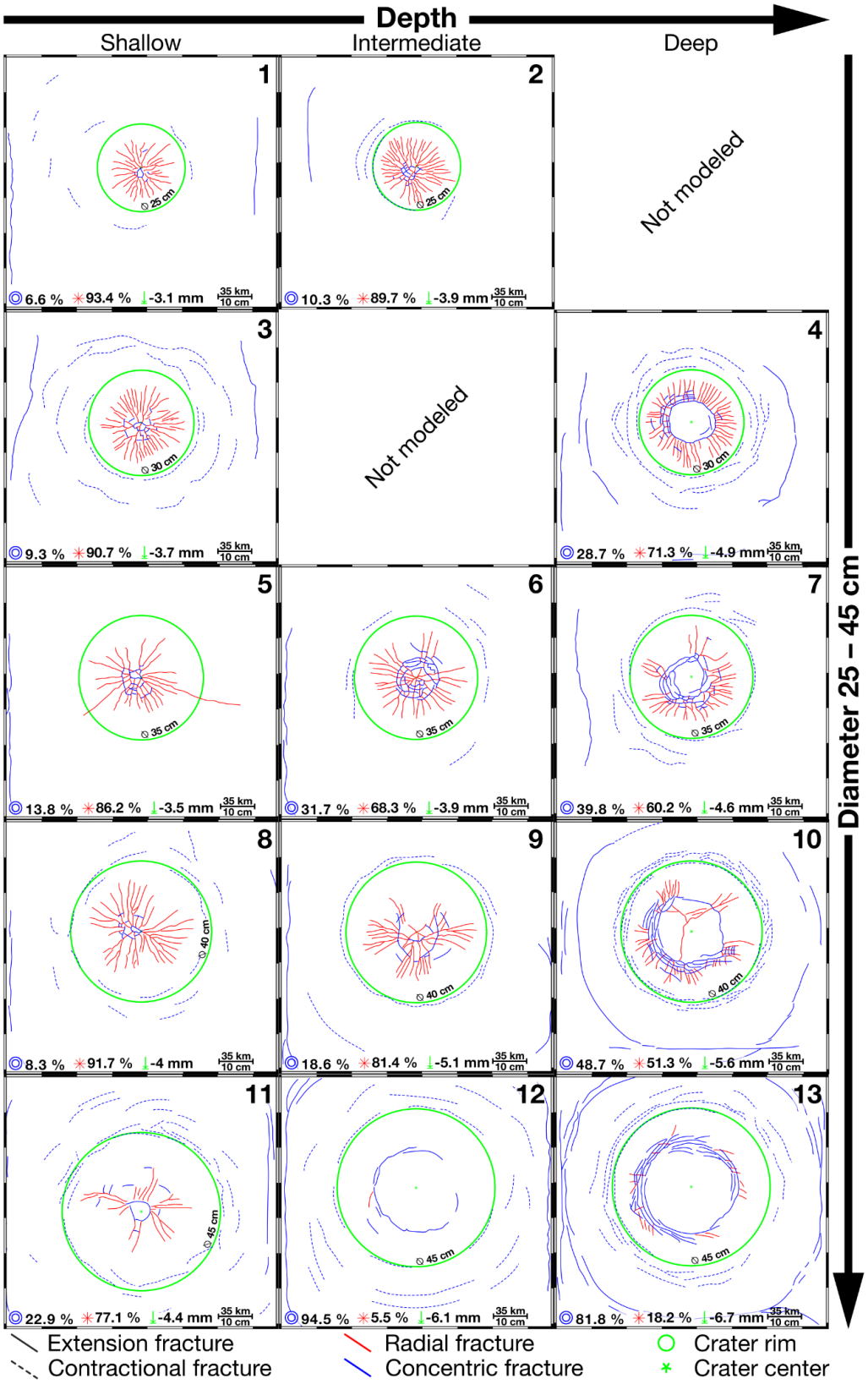

Figure 4.7: Radial (red) and concentric (blue) fractures of final set 1 experiments. Experiment numbers are indicated in the top right of each panel. Images of experiments are arranged by initial depths (rows) and diameters (columns) of craters. Solid and stippled lines indicate respectively traces of extension fractures and reverse faults. The percentage of cumulative concentric and radial fault lengths with respect to total fracture length as well as the depth of crater floors is indicated at the bottom of each panel.

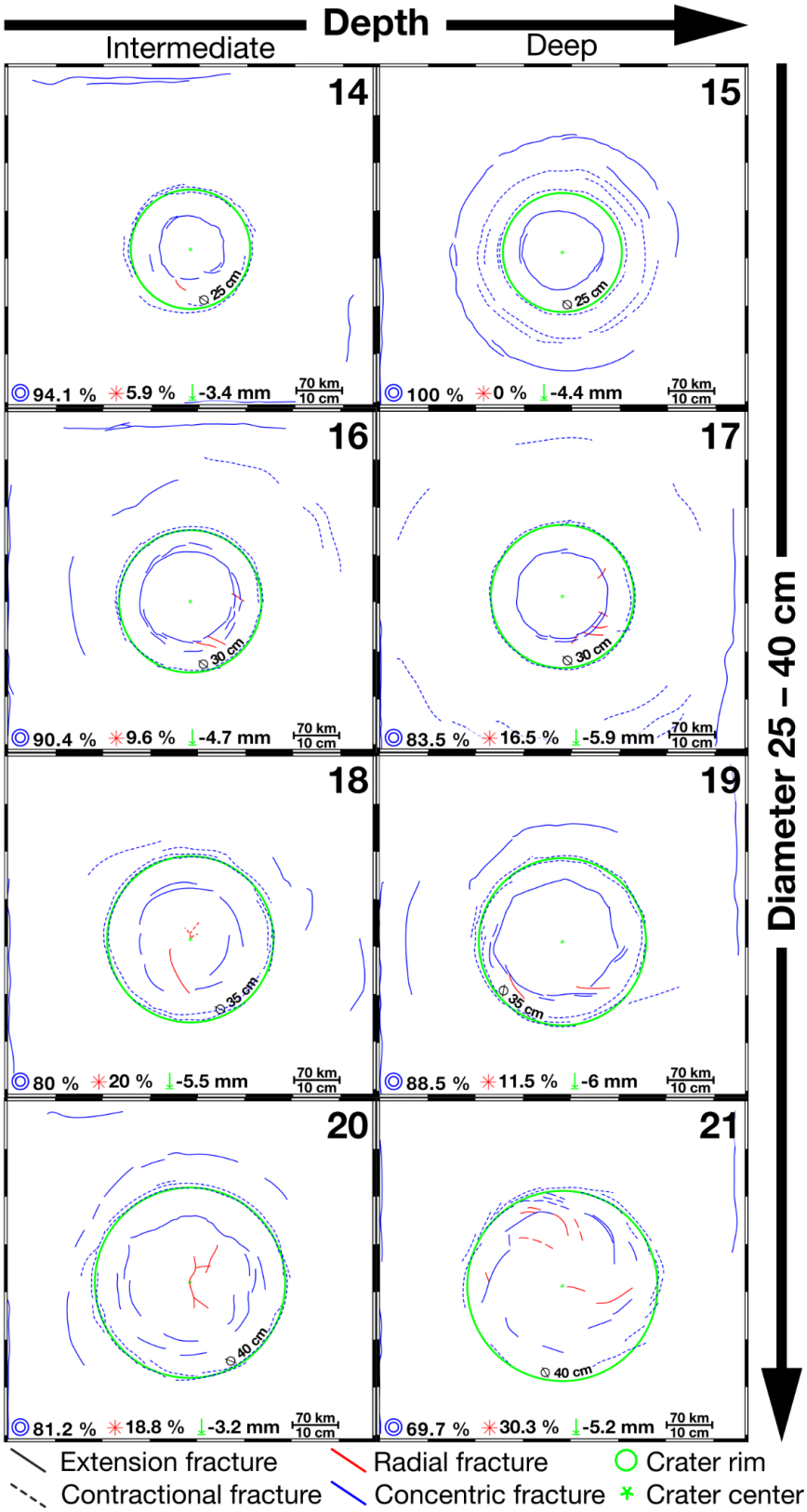

Figure 4.8: Radial (red) and concentric (blue) fractures of final set 2 experiments. Experiment numbers are indicated in the top right of each panel. Images of experiments are arranged by initial depths (rows) and diameters (columns) of craters. Solid and stippled lines indicate respectively traces of extension fractures and reverse faults. The percentage of cumulative concentric and radial fault lengths with respect to total fracture length as well as the depth of crater floors is indicated at the bottom of each panel.

length of concentric fractures with increasing crater diameter and initial depth, at the expense of radial fractures. The development of both fracture types leads to polygonal fracture patterns, mostly seen in the crater centres (Fig. 4.7).

As crater floor uplift is maximal in the crater centre, fracturing starts in, and thus emanates from, the centre towards the rim with the formation of radial CFFs. During floor uplift, the fractures widen, while they propagate and taper outwards. The width of fractures, as measured by DIC, in set 1 experiments translates to 35 – 250 m, and in set 2 experiments to 70 – 560 m in nature (Supplementary Figures S4.5, S4.6). Overall, concentric faults initiate later than radial ones and form first in the crater and later in its periphery, where they show up as normal faults (Figs. 4.7, 4.8; Supplementary figure S4.4). In general, they tend to develop at distances of approximately ½ and ¾ crater radii from crater ceters. In places, the concentricity of most distal fractures in set 1 experiments is influenced by their proximity to the straight box walls (Fig. 4.8).

4.5. Discussion

4.5.1 Buoyancy and material strength in experiments

Post-cratering floor uplift of large impact craters is controlled chiefly by isostasy and the mechanical strength of impacted rock masses (Melosh & Ivanov, 1999). Notably for layered target rocks, such as on Earth, more rigid and less dense, buoyant layers float on top of viscous layers (Göttl & Rummel, 2009). According to Archimedes' Principle, the buoyancy force F_A equals the weight of the viscous material it displaces and is counteracted by its down-pulling weight force:

$$F_g = m * g$$

Therefore, if $F_A > F_G$, the rigid layer will float. According to the Airy-Heiskanen model of isostasy (Heiskanen, 1950), a rigid layer will sink into a viscous one until isostatic equilibrium, i.e., $F_A = F_G$, is attained. At that stage, topography of the rigid layer will depend on the density contrast of the layers. The spatial variation in topography will, therefore, point to respective variations in buoyancy and weight force equilibrium. To minimize variations, i.e., attain isostatic equilibrium, on the scale of large impact craters, the layers will adjust their thicknesses through deformation. While viscous layers will deform by coherent material flow, rigid layers will deform discontinuously by overcoming cohesion and internal friction (Schultz & Watters, 2001). Accordingly, the mechanical strength of target rocks, i.e., its resistance in attaining isostatic equilibrium, is paramount in controlling viscous relaxation of crust below crater floors.

To relate viscous relaxation to deformation of (model) crustal material, two dimensionless parameters, *U* and *S*, are used. The parameter *U* is the depth-diameter

ratio of a crater and relates to crater floor buoyancy (Wünnemann & Ivanov, 2003). As *U* increases with crater depth, positive values of *U* relate to a mass deficit and thus will induce crater floor uplift, whereas negative values of *U* point to excess mass causing floor subsidence. As the crater depth changes during the experiments, I calculate *U* at the beginning and at the end of experiments (Table 4.1). The ratio between thickness of brittle crust and crater diameter is a crude measure of crater floor strength:

$$S = \frac{(q - y)}{d}$$

Positive values of *S* indicate a strong crater floor, whereas *S = 0* signifies total loss of crater floor strength. As the brittle layer thickness of the crater floor remains constant in all experiments, *S* remains constant as well. Since *S* does not account for weakening of the brittle layer, either by fracturing or heating, this parameter is only meaningful in the beginning of experiments (Table 4.1).

Our experiments point to a straightforward empirical relationship between parameters *U* and S, and crater diameter and fracture types (Fig. 4.9). Specifically, for a given crater diameter, the cumulative length of concentric fractures increases with increases in initial floor depth and *U*, while *S* decreases. Conversely, strong crater floors, characterized by large values of *S*, tend to form chiefly radial fractures, whereas weak crater floors will develop more concentric fractures. The values of *U* and *S* of numerically modelled craters for Earth match remarkably well those of set 1 craters with shallow floors (labelled “S” in Figure 4.9), but depart significantly from set 2 craters, modelled with the shallowest possible floors (labelled “I” in Figure 4.9). I

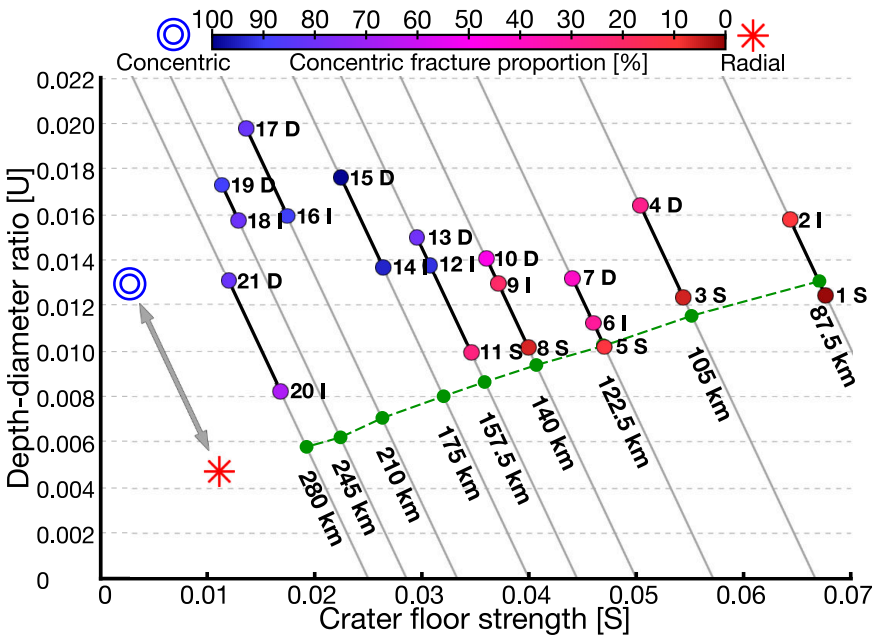

Figure 4.9: Diagram showing the relationship between crater floor depths and fracture type with regard to *U* and *S* in terms of concentric fracture proportion for each experiment and equivalent natural crater diameter. D, I and S indicate respectively deep, intermediate and shallow depths of model craters. Symbols indicate trends in fracture type. Notably, the proportion of concentric fractures increases with increasing crater depth. Green dots indicate parameters of numerically modeled craters for Earth.

attribute this difference to the fact that depth-diameter ratios of set 1 craters can be experimentally implemented more accurately than those of set 2 craters.

The spatial variation in topography, and thus buoyancy, controls material flow and deformation kinematics of crustal relaxation. In the experiments, the pre-cratering reference surface is the isopotential surface towards which material tends to move to attain isostatic equilibrium during relaxation. While DIC measures most accurately displacements of the top surfaces, the kinematics of the hidden interface between the PDMS and the granular layer needs to be inferred from surface deformation. I justify this approach by the strong mechanical coupling of the layers, which likely transmits displacements across their interface.

4.5.2 Kinematics of crustal relaxation

Upon crater formation, most of the crater floor will be located below, and the crater rim and its proximal periphery, due to the presence of ejected material, above, the reference surface (Fig. 4.10). Thus, crater floors and their periphery will not be in isostatic equilibrium immediately after cratering. Notably, large buoyancy forces will drive material underlying the crater floor upward, whereas material below the rim and its immediate periphery will subside due to large weight forces. These differential vertical surface motions are mimicked by the interface of the PDMS and granular layers, evident upon removal of the latter after completion of each experiment. Specifically, as the crater floor is flexed upward and the brittle layer stretched horizontally, the interface will most likely change shape to form a broad dome, akin to the horizontal gradient in material uplift, below the crater floor (Fig. 4.10). This process will cause redistribution of mobile PDMS.

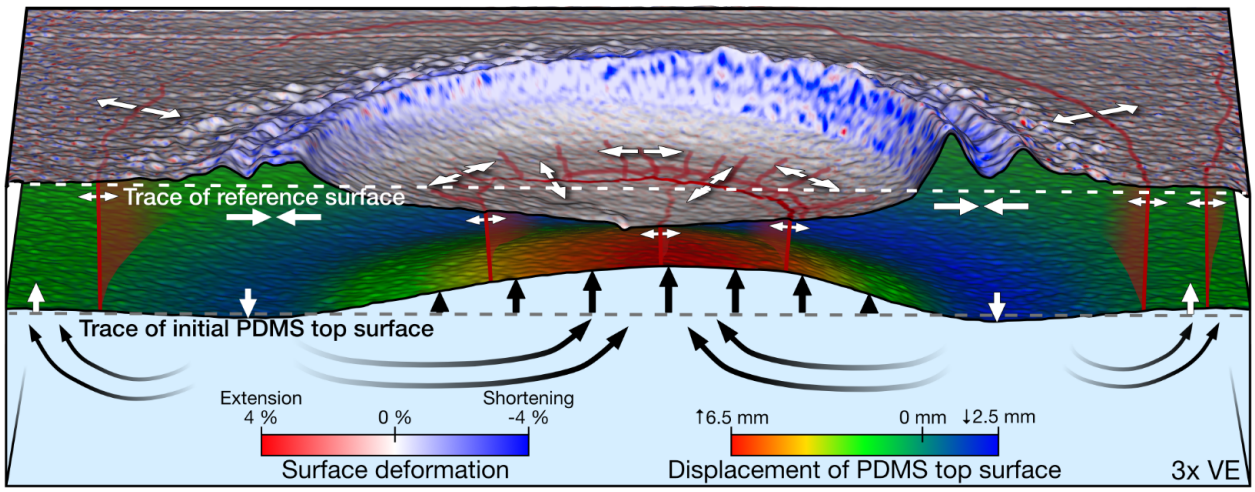

Figure 4.10: Synoptic 3D block image displaying components of modelled crustal flow below a crater as a consequence of crustal relaxation. For explanation see text.

Notably, PDMS from below the subsiding crater periphery will be drawn toward, and into the emerging dome below, the crater, to adjust to the centro-symmetric surface flow field (Fig. 4.6, e, f; Supplementary figures S4.1, S4.2). Furthermore, horizontal shortening characterizing crater rims, imparted by convergent flow on either side of the rims (Fig. 4.10; Supplementary figures S4.1-S4.6), must lead to vertical thickening of the rims. However, DIC shows that the rim surfaces do not undergo vertical displacements (Fig. 4.6a, b). Hence, vertical thickening of the rims along with their elevated topography are likely compensated for by subsidence of the PDMS-granular layer interface, possibly resulting in concentric downward bulges of the interface below rims. Such bulges may additionally force PDMS to flow towards the crater centre and possibly toward the crater periphery.

Following transient cavity formation, lasting approximately half a minute, cratering is controlled by gravity (Ivanov & Deutsch, 1999; Melosh & Ivanov, 1999). Hydrocode models, typically portraying about 10 minutes of cratering, show that collapse of the cavity results in crater floor uplift and widening of the crater diameter, both diminishing exponentially in magnitude (Collins et al., 2002; Ivanov, 2005). Our experiments show that the exponential behavior of this motion continues at lower strain rates during long-term relaxation of model crust below the crater and its periphery (Fig. 4.5).

4.5.3 CCFs in nature and experiment

To test the structural significance of experiments, the surface flow field during relaxation and, hence, the resulting geometry of model CFFs, are compared to prominent post-cratering structures observed at the Chicxulub, Sudbury and Vredefort impact structures. The Chicxulub impact structure, Mexico, is estimated at 180 to 200 km in diameter and hosts a topographic peak ring located at a radial distance of about 40 km from the crater centre (Morgan et al., 1997; Collins et al., 2002; Collins et al., 2008). Due to burial of the impact structure under approximately 1 km thick post-impact sedimentary rock, CFFs are unknown from this impact structure. However, recent drilling of the peak ring (Morgan et al., 2016) revealed that rocks making up the ring are characterized by the pervasive presence of shear bands indicating horizontal extension (Riller et al., 2018). Experiments 14 and 15, modeling Chicxulub-size craters, show concentric dilational CFFs at the equivalent position of the peak ring (Supplementary figure S4.4). Thus, horizontal extension of the Chicxulub peak ring agrees with the relaxation-induced crater flow field in the experiment.

The rim-to-rim diameters of the Sudbury and Vredefort impact structures are not well known, due to respectively orogenic deformation and erosion. For Sudbury, diameter

estimates are on the order of 200 km to 260 km, and for Vredefort estimates are up to 300 km (Grieve et al., 2008). In both impact structures, impact melt dykes, formed from CFFs (Hecht et al., 2008; Lieger & Riller, 2012; Pilles et al., 2018; Huber et al., 2020), are radial in the central portions and concentric at radial distances of about 35 km (Fig. 4.2). For radial CFFs, this matches well with experiments 16 to 21, corresponding to the crater diameters of both impact structures (Supplementary figure S4.4). However, modelled CFFs in these experiments are located much further outwards, compared to observed impact melt dykes of the impact structures. As concentric dykes in both impact structures line interfaces between crystalline basement and metasedimentary cover rocks, lithological heterogeneity of target rocks may significantly influence the location of impact-melt dykes. Interestingly, the impact melt sheet at Sudbury solidified about 104 years after impact (Zieg & Marsh, 2005), constraining the duration of impact melt-filled CFF formation at Sudbury. As this duration corresponds well to the experimentally inferred duration of crustal relaxation, we believe that our time scaling of this process is realistic and a key message of our experimental work. Collectively, patterns, kinematics and duration of activity of experimental CFFs resulting from crustal relaxation seem to agree reasonably well with first-order, post-impact deformation structures of the larges impact structures known on Earth.

4.5.4 Model limitations

The two-layer experimental setup and materials used are mechanically rather simple and do not do justice to the mechanical complexity of continental crust. Material properties do not change during experiments. Thus, our experiments do not consider the influence of initial target rock heterogeneity and changes in rock rheology, caused, for example, by mechanical weakening of crust by pervasive impact-induced fracturing and thermal softening, on strain localization. Moreover, our experimental setups do not model the structural influence of specific variations in crater floor morphology, such as peak rings. The experiments are scaled to Earth's gravity and continental crust, limiting direct inference to other celestial rocky bodies. Imperfect preparation of model setups notably regarding crater depth in set 2 experiments may well have caused variations in CFF patterns. Finally, DIC measured sub-millimeter length changes, which are susceptible to background noise caused by vibration and thermal extension of the deformation rig during ongoing experiments.

4.6. Conclusions

Physical experiments involving an upper brittle layer and a lower viscous layer were conducted to systematically explore the kinematics and structural effects of crustal relaxation of target rock underlying craters, ranging in diameter from 87.5 km to 280 km in nature. The experiments are characterized by uplift of crater floors and concomitant subsidence of the immediate crater periphery. The vertical surface motions translate to convergent lateral flow of viscous crust from the periphery towards crater centres. Uplift rates of crater floors are characterized by exponential decay and depend on buoyancy and strength of crust below floors, approximated in experiments respectively by the diameter-depth ratio and thickness of brittle crust of craters. The formation of prominent concentric and radial fractures in uplifted crater floors is a structural hallmark of crustal relaxation. The cumulative length of concentric fractures increases with increasing initial floor depth and crater diameter at the expense of radial fractures, whereby polygonal fracture patterns may develop in crater centres. Post-cratering floor fracture patterns and deformation kinematics of the largest known impact structures on Earth agree reasonably well with experimental results indicating that crustal relaxation is an important process in the long-term crater modification. Although our experiments are physically scaled to Earth, they may help to constrain the rheology of layered crust on rocky celestial bodies at the time of impact.

5. Conclusion

The aim of the thesis is to address important knowledge gaps in planetary geology. In particular, the thesis aims to improve our knowledge of long-term crater modification, which is one of the most common geodynamic processes in the Solar System. Two mechanisms have been proposed to explain the formation of floor-fractured craters: emplacement of horizontal igneous sheets beneath the crater floor (Fig. 1.2a; Schultz, 1976; Jozwiak et al., 2012) and isostatic re-equilibration of crust underlying the crater floor (Fig. 1.2b; Hall et al., 1981; Riller, 2005; Hecht et al., 2008).

Using scaled analogue experiments, I systematically investigated the structural consequences of both mechanisms on long-term crater floor deformation. Knowledge of the physical properties of materials is a prerequisite for proper scaling of experiments and their comparability to nature. I used a novel flour-sand material mixture to model crater modification processes, designed to model isostasy-driven crater modification. Its low cohesion and small grain size allowed the preservation of the smallest fractures. By determining its Mohr-Coulomb failure criterion and other mechanical properties such as density, I was able to ensure its suitability for my experiments. The rather unrealistic behaviour of flour 2:1, with reactivation strength higher than initial strength at high normal loads, did not affect my experiments negatively as we mainly observed first order faults at low normal loads. Detailed knowledge of the mechanical properties of the granular materials used in the experiments was crucial to the interpretation of the observed processes.

The experimental surfaces were monitored using 3D digital image correlation, which allowed me to quantify key structural parameters such as surface motion and the distribution and evolution of surface fractures. The addition of custom-coloured marker grains enabled me to achieve sub-millimetre accuracy. The results of my scale models allowed me to quantify the duration, geometry and distribution of brittle deformation of the upper crust. Most importantly, the analogue experiments provided, for the first time, a quantitative relationship between the diameter, depth and fracture geometry of crater floors.

My experiments showed that inflation of a sill below a crater is capable of uplifting the crater floor. Floor uplift caused upward bending of the crater floor and induces fractures. The fracture patterns were primarily controlled by the depth of the balloons below the crater rather than the morphology of the crater floor. For the duration of fluid inflation into shallow model sills, surface uplift was focused on the crater centre and associated with prominent polygonal fracture pattern. Deep model sills developed distinct radial fracture pattern. Upon evacuation, concentric normal faults developed at the inner crater rim, corresponding to the terraced crater rims, ubiquitous in lunar craters. Overall, our experiments of shallow model sills resembled lunar FFCs. Interestingly, model craters are characterised by more diverse fracture patterns compared to lunar craters. Focused brittle deformation above sills during the onset of inflation is likely to create pathways that allow magma to erupt from natural sill reservoirs. Our data show that the igneous intrusion model is still capable of explaining observed lunar FFCs. I call into question the simplified model proposed in the literature. The experiments suggest that natural sill systems are unlikely to reach the extent previously suggested by other authors. Magma accent and sill formation on the Moon is still associated with uncertainties.

Experiments involving an upper brittle layer and a lower viscous layer showed that crustal relaxation is capable of uplifting the crater floor as well. The experiments are characterised by uplift of the crater floor and associated subsidence of the crater periphery. The surface uplift is translated into a convergent lateral flow of viscous crust from the periphery towards the crater centres. Crater floor uplift rates are characterised by exponential decay and depend on the buoyancy and strength of the crust beneath the floors. The formation of prominent concentric and radial fractures in uplifted crater floors is a structural characteristic of relaxation of crust below craters. The experiments show also that crater floor uplift is accomplished by long-wavelength subsidence of the crater periphery and may operate on time scales of thousands of years in nature. This kind of surface motion has not been observed for the inflation of model sills.

The post-cratering floor fracture patterns and deformation kinematics of the largest known impact structures on Earth agree reasonably well with experimental results, indicating that crustal relaxation is an important process in long-term crater modification, although our experiments are physically scaled to Earth.

It is not advisable to draw a direct comparison between the two experiments, as they are scaled to lunar and Earth analogues, respectively. This also recognises the differences in crustal configuration between the two. However, upon initial inspection, both examined processes for modifying craters display similarities in their results. Our study has shown that both isostatic relaxation and the emplacement of an igneous

intrusion can lift and fracture the crater floor. This finding effectively satisfies the definition for FFC genesis for both processes but in reality, it is more nuanced. Both crater modification mechanisms are linked to specific conditions that are necessary for them to work, which I addressed in our experimental series. Isostatic relaxation requires a viscous lower crust and somewhat flexible upper crust. This requirement is well met on Earth but the Moon has a thicker and cooler crust than Earth (Zuber et al., 1994). Due to lower gravity, the Moon's surface preserves much larger topographic variation than the Earth's crust, indicating a stiffer lunar upper crust (Watts, 2001; Göttl & Rummel, 2009). This hinders isostatic relaxation on the moon (Wichman & Schultz, 1995). The igneous intrusion model requires the emplacement of large amounts of magma below a crater. Lunar FFCs are most common around the Lunar mare regions, characterized by strong volcanic activity. However, large terrestrial craters such as Sudbury (Canada) and Vredefort (South Africa) have been eroded by a few kilometres (Grieve & Therriault, 2000; Grieve et al., 2008). Although there is deep exposure of the impactite's stratigraphy at these sites, there are no known sills beneath these craters. My experiments have shown that crater-centred intrusions did not uniformly uplift the crater floor. The Laccolith forming in the crater centre would eventually lead to evacuation of the magma before a uniform sill would be able to uplift the complete crater floor. With the premature evacuation the sill may never reach expected levels of uplift. Lava fillings capable of shallowing the crater to observed amounts would completely mask any fractures originating from the inflation phase. But lunar crater clearly preserved characteristic radial and concentric grooves and trenches being masked by a thin layer of lava at best (Head & Wilson, 2017). While I think it is realistic to assume that lava infill and limited laccolith inflation can account for some of the uplift, isostatic relaxation may still play a role. Both mechanisms do not necessarily need to be independent from each other (Wichman & Schultz, 1995). Increased heat flow and the presence of melt could favour isostatic relaxation even in thicker lunar crust. Previous studies have already predicted that isostatic relaxation is possible on the Moon, but found that it alone cannot explain the shallowing of FFCs (Wichman & Schultz, 1995; Jozwiak et al., 2015). The verdict of our experiments is that crater-centred intrusions on the Moon would underperform if considered as the only acting process. I show that crater modification and floor fracture formation cannot be attributed to a single process.

On Earth CFFs are evidently associated with impact melt rock (Lieger & Riller, 2012; Huber et al., 2020; Huber et al., 2022). Their genetic relationship excludes a deeper crustal origin. Therefore impact melt must have filled CFFs from top down. This is in line with our experimental observations. Fractures developing from isostatic relaxation follows a exponential decay with most strain manifesting shortly after cratering.

Upwards flexure of the crater floor causes extensional fractures on the dilated surface. These fractures would easily be capable of beeing filled with impact melt. Our experiments demonstrated that crater floor uplift caused by crustal relaxation is much more dynamic than previously thought, even for smaller, shallower craters. I conclude that the viscous relaxation model is the most likely mechanism for crater modification on Earth. As the viscous relaxation model is much simpler in the prerequisite conditions necessary it may be more universally applicable for large crater.

5.1 Outlook

The conclusions that can be drawn from our experiments show that refined experimental studies could help to further improve our knowledge of the driver behind crater modification. As FFCs are widely observed throughout the Solar System, the process behind them must be more universally applicable. Therefore, it may be interesting to conduct further experimental studies to evaluate different parameters. The way forward is to evaluate a model that can be applied to the Earth and Moon simultaneously, including Mars and Mercury. For the lunar analogue, it would be helpful to design experiments that model the emplacement of the sill with a less constrained setup to evaluate not only surface structures but also the underlying magmatic system to gain insight into the timing of lunar FFC generation. By calibrating the surface uplift and fracture pattern of crustal relaxation experiments to different upper crustal thicknesses, rigidities and lower crustal viscosities, we may be able to derive a proxy for determining the lower crustal viscosity of other celestial bodies from imaged crater morphologies. Testing different thicknesses of brittle upper crust could also further assess the role of crustal relaxation in lunar and Mercury FFC. By incorporating realistic central peaks and peak rings into the initial crater morphology, experiments can be further refined to better approximate nature and study their influence on crustal relaxation. In addition, larger craters can be better represented. However, at a certain crater size the curvature of the planet begins to play a role, so the analogue models are not infinitely scalable. It would also be interesting to combine the two experimental setups to study the interplay between crustal relaxation and igneous intrusion. By including a viscous lower crust in the emplacement of a sill below the crater, the sill will also be subject to isostatic equilibrium.

6. Acknowledgments

Writing this thesis would not have been possible without the much appreciated help of many people. First of all, I would like to thank my supervisor, Prof. Dr. Ulrich Riller for all the support he gave me. Ulrich not only gave me the opportunity to write this thesis, but also to set up and manage the analogue modelling laboratory. He also taught me everything I know about design and scientific work with great patience and dedication. The freedom he gave me during my thesis gave me the opportunity to learn valuable skills that I can leverage as I move forward. It was a great time, with great projects we worked on together over the years. I would like to thank my family Sabine + Horst Eisermann and my grandmother Edith Conrad for supporting me in doing what I love. My greatest appreciation goes to Prof. Dr. Christian Betzler and Dr. habil. Sebastian Lindhorst, who gave me great moral support, aided me in formatting the thesis and were always there to give me advice. My greatest appreciation to Dr. Olivier Galland, who taught me everything about scaling and how to perform analogue experiments on volcanic systems. I thank Dr. Yvonne Milker for helping me with the SEM. I thank Dr. Paul Göllner and Felix Schulte for the great discussions we had in the group. I thank Piet Lehmann and Talitha Knauer for their help in measuring material properties as part of their student assistantship. I thank Louisa Kanzler for her help with the sill experiment series, great discussions and proofreading. I thank Matthias Rosenau for his guidance at a very early stage of the project. He made it possible to carry out the ring shear tests in person at the laboratory of the GFZ Potsdam. Thanks to Mr. Schönbeck who helped with the post-processing of the ring shear test data. I would like to thank Stephanie Teuber for discussions and very early pilot experiments on crustal relaxation in her master thesis. Reviewer Prof. Dr. Gareth Collins for insightful comments. Dr. Megan Withers for great discussions, proofreading and insightful comments. Thanks to the ZDF for making a movie. Thanks to LaVision GmbH for making our measurements possible. I would also like to thank the following people for their moral support. Without them, this would not have been half as much fun: Nina Lenz, Linus Budke, Maryse Schmidt, Vanessa Ehlies, Dirk Eggers. Great Scott! If you put your mind to it, you can accomplish anything. Roads? Where we're going, we don't need roads. (Brown, 1985).

The RELAX project was funded by the German Science Foundation (DFG) (grant Ri 916/22-1).

7. References

Adam, J., Urai, J. L., Wieneke, B., Oncken, O., Pfeiffer, K., Kukowski, N., (2005). Shear localisation and strain distribution during tectonic faulting—new insights from granular-flow experiments and high-resolution optical image correlation techniques. *Journal of Structural Geology, 27*(2), 283-301.

Arachchige, U. N., Cruden, A. R., & Weinberg, R. (2021). Laponite gels - visco-elasto-plastic analogues for geological laboratory modelling. *Tectonophysics, 805*, 228773. https://www.sciencedirect.com/science/article/pii/S0040195121000573

Artemieva, N., Morgan, J., & Party, E. S. (2017). Quantifying the Release of Climate-Active Gases by Large Meteorite Impacts With a Case Study of Chicxulub. *Geophysical Research Letters, 44*(20), 10,180-110,188. https://agupubs.onlinelibrary.wiley.com/doi/abs/10.1002/2017GL074879

Baldwin, R. B. (1968). Rille pattern in the lunar crater Humboldt. *Journal of Geophysical Research (1896-1977), 73*(10), 3227-3229. https://doi.org/10.1029/JB073i010p03227

Beekman, F., Willingshofer, E., Sokoutis, D., Pueyo, E. L., Casas, A. M., Peiro, A., (2019). *Ring shear test data of iron powder – quartz sand mixture: a new marker material for analog modelling in a CT scanner at Utrecht University (The Netherlands) (EPOS TNA call 2017)*. Retrieved from https://gfzpublic.gfz-potsdam.de/pubman/item/item_5000659

Blott, S. J., & Pye, K. (2001). GRADISTAT: a grain size distribution and statistics package for the analysis of unconsolidated sediments. *Earth Surface Processes and Landforms, 26*(11), 1237-1248. https://onlinelibrary.wiley.com/doi/abs/10.1002/esp.261

Boutelier, D. (2016). TecPIV—A MATLAB-based application for PIV-analysis of experimental tectonics. *Computers & Geosciences, 89*, 186-199.

Bralower, T. J., Cosmidis, J., Fantle, M. S., Lowery, C. M., Passey, B. H., Gulick, S. P. S., (2020). The Habitat of the Nascent Chicxulub Crater. *AGU Advances, 1*(4), e2020AV000208. https://agupubs.onlinelibrary.wiley.com/doi/abs/10.1029/2020AV000208

C. Lightfoot, P. (2006). Timing of sulphide saturation and ore formation in the Sudbury Igneous Complex. *ASEG Extended Abstracts, 2006*(1), 1-9. https://www.publish.csiro.au/paper/ASEG2006AB095

Christensen, N. I., & Mooney, W. D. (1995). Seismic velocity structure and composition of the continental crust: A global view. *Journal of Geophysical Research: Solid Earth, 100*(B6), 9761-9788. https://agupubs.onlinelibrary.wiley.com/doi/abs/10.1029/95JB00259

Cintala, M. J., Wood, C. A., & Head, J. W. (1977). *The effects of target characteristics on fresh crater morphology-Preliminary results for the moon and Mercury.* Paper presented at the In: Lunar Science Conference, 8th, Houston, Tex., March 14-18, 1977, Proceedings. Volume 3.(A78-41551 18-91) New York, Pergamon Press, Inc., 1977, p. 3409-3425.

Collins, G., Kenkmann, T., Osinski, G., & Wünnemann, K. (2008). Mid-sized complex crater formation in mixed crystalline-sedimentary targets: Insight from modeling and observation. *Meteoritics & planetary science, 43*(12), 1955-1977.

Collins, G. S., Melosh, H. J., & Marcus, R. A. (2005). Earth impact effects program: A web-based computer program for calculating the regional environmental consequences of a meteoroid impact on Earth. *Meteoritics & planetary science, 40*(6), 817-840.

Collins, G. S., Melosh, H. J., Morgan, J. V., & Warner, M. R. (2002). Hydrocode Simulations of Chicxulub Crater Collapse and Peak-Ring Formation. *Icarus, 157*(1), 24-33. https://www.sciencedirect.com/science/article/pii/S0019103502968223

Collins, G. S., Melosh, H. J., & Osinski, G. R. (2012). The Impact-Cratering Process. *Elements, 8*(1), 25-30. https://doi.org/10.2113/gselements.8.1.25

Dengate, H. N., Baruch, D. W., & Meredith, P. (1978). The Density of Wheat Starch Granules: A Tracer Dilution Procedure for Determining the Density of an Immiscible Dispersed Phase. *Starch - Stärke, 30*(3), 80-84. https://onlinelibrary.wiley.com/doi/abs/10.1002/star.19780300304

Dombard, A. J., & Gillis, J. J. (2001). Testing the viability of topographic relaxation as a mechanism for the formation of lunar floor-fractured craters. *Journal of Geophysical Research: Planets, 106*(E11), 27901-27909.

Eisermann, J. O., Göllner, P. L., & Riller, U. (2021). Orogen-scale transpression accounts for GPS velocities and kinematic partitioning in the Southern Andes. *Communications Earth & Environment, 2*(1), 167. https://doi.org/10.1038/s43247-021-00241-4

Folk, R. L., & Ward, W. C. (1957). Brazos River bar [Texas]; a study in the significance of grain size parameters. *Journal of sedimentary research, 27*(1), 3-26.

Freed, A. M., Blair, D. M., Watters, T. R., Klimczak, C., Byrne, P. K., Solomon, S. C., (2012). On the origin of graben and ridges within and near volcanically buried craters and basins in Mercury's northern plains. *Journal of Geophysical Research: Planets, 117*(E12).

Freed, A. M., Solomon, S. C., Watters, T. R., Phillips, R. J., & Zuber, M. T. (2009). Could Pantheon Fossae be the result of the Apollodorus crater-forming impact within the Caloris basin, Mercury? *Earth and Planetary Science Letters, 285*(3-4), 320-327.

Galerne, C. Y., Neumann, E.-R., & Planke, S. (2008). Emplacement mechanisms of sill complexes: Information from the geochemical architecture of the Golden Valley Sill Complex, South Africa. *Journal of Volcanology and Geothermal Research, 177*(2), 425-440. https://www.sciencedirect.com/science/article/pii/S0377027308003442

Galland, O., Burchardt, S., Hallot, E., Mourgues, R., & Bulois, C. (2014). Dynamics of dikes versus cone sheets in volcanic systems. *Journal of Geophysical Research: Solid Earth, 119*(8), 6178-6192. https://agupubs.onlinelibrary.wiley.com/doi/abs/10.1002/2014JB011059

Galland, O., Holohan, E., van Wyk de Vries, B., & Burchardt, S. (2018). Laboratory Modelling of Volcano Plumbing Systems: A Review. In C. Breitkreuz & S. Rocchi (Eds.), *Physical Geology of Shallow Magmatic Systems: Dykes, Sills and Laccoliths* (pp. 147-214). Cham: Springer International Publishing.

Ge, Z., Rosenau, M., Warsitzka, M., & Gawthorpe, R. L. (2019). Overprinting translational domains in passive margin salt basins: insights from analogue modelling. *Solid Earth, 10*(4), 1283-1300. https://se.copernicus.org/articles/10/1283/2019/

Giguere, T. A., Hawke, B. R., Gillis-Davis, J. J., Lemelin, M., Boyce, J. M., Trang, D., (2020). Volcanic Processes in the Gassendi Region of the Moon. *Journal of Geophysical Research: Planets, 125*(9), e2019JE006034. https://doi.org/10.1029/2019JE006034

Goderis, S., Sato, H., Ferrière, L., Schmitz, B., Burney, D., Kaskes, P., (2021). Globally distributed iridium layer preserved within the Chicxulub impact structure. *Science Advances, 7*(9), eabe3647. https://doi.org/10.1126/sciadv.abe3647

Goehring, L., Morris, S. W., & Lin, Z. (2006). Experimental investigation of the scaling of columnar joints. *Physical Review E, 74*(3), 036115. https://link.aps.org/doi/10.1103/PhysRevE.74.036115

Gornitz, V. (1973). Igneous vs impact processes for the origin of the mare lavas. *The Moon, 6*(3), 357-379. https://doi.org/10.1007/BF00562211

Göttl, F., & Rummel, R. (2009). A geodetic view on isostatic models. *Pure and applied geophysics, 166*, 1247-1260.

7. References

Grant, R., Bite, A., Pye, E., Naldrett, A., & Giblin, P. (1984). Sudbury quartz diorite offset dikes. In *The geology and ore deposits of the Sudbury structure* (Vol. 1, pp. 275-300): Ontario Geological Survey.

Grieve, R. A. F., & Therriault, A. (2000). Vredefort, Sudbury, Chicxulub: Three of a Kind? *Annual Review of Earth and Planetary Sciences, 28*(1), 305-338. https://doi.org/10.1146/annurev.earth.28.1.305

Grieve, R. A. F. (1991). Terrestrial impact: The record in the rocks*. *Meteoritics, 26*(3), 175-194. https://doi.org/10.1111/j.1945-5100.1991.tb01038.x

Grieve, R. A. F., Reimold, W. U., Morgan, J., Riller, U., & Pilkington, M. (2008). Observations and interpretations at Vredefort, Sudbury, and Chicxulub: Towards an empirical model of terrestrial impact basin formation. *Meteoritics & planetary science, 43*(5), 855-882. https://doi.org/10.1111/j.1945-5100.2008.tb01086.x

Gulick, S. P. S., Bralower, T. J., Ormö, J., Hall, B., Grice, K., Schaefer, B., (2019). The first day of the Cenozoic. *Proceedings of the National Academy of Sciences, 116*(39), 19342-19351. https://www.pnas.org/doi/abs/10.1073/pnas.1909479116

Hall, J. (1815). II. On the Vertical Position and Convolutions of certain Strata, and their relation with Granite. *Earth and Environmental Science Transactions of the Royal Society of Edinburgh, 7*(1), 79-108.

Hall, J. L., Solomon, S. C., & Head, J. W. (1981). Lunar floor-fractured craters: Evidence for viscous relaxation of crater topography. *Journal of Geophysical Research: Solid Earth, 86*(B10), 9537-9552.

Head, J. W., & Wilson, L. (2017). Generation, ascent and eruption of magma on the Moon: New insights into source depths, magma supply, intrusions and effusive/explosive eruptions (Part 2: Predicted emplacement processes and observations). *Icarus, 283*, 176-223. https://www.sciencedirect.com/science/article/pii/S0019103516302366

Hecht, L., Wittek, A., Riller, U., Mohr, T., Schmitt, R. T., & Grieve, R. A. F. (2008). Differentiation and emplacement of the Worthington Offset Dike of the Sudbury impact structure, Ontario. *Meteoritics & planetary science, 43*(10), 1659-1679. https://onlinelibrary.wiley.com/doi/abs/10.1111/j.1945-5100.2008.tb00635.x

Heiskanen, W. A. (1950). *On the isostatic structure of the earth's crust*: Isostatic Institute of the International Association of Geodesy.

Holohan, E. P., van Wyk de Vries, B., & Troll, V. R. (2007). Analogue models of caldera collapse in strike-slip tectonic regimes. *Bulletin of Volcanology, 70*(7), 773-796.

Hubbert, M. K. (1937). Theory of scale models as applied to the study of geologic structures. *Bulletin of the geological society of America, 48*(10), 1459-1520. http://dx.doi.org/10.1130/GSAB-48-1459

Huber, M. S., & Kovaleva, E. (2020). Identifying Gaps in the Investigation of the Vredefort Granophyre Dikes: A Systematic Literature Review. *Geosciences, 10*(8).

Huber, M. S., Kovaleva, E., Clark, M. D., Riller, U., & Fourie, F. D. (2022). Evidence from the Vredefort Granophyre Dikes points to crustal relaxation following basin-size impact cratering. *Icarus, 374*, 114812. https://www.sciencedirect.com/science/article/pii/S0019103521004589

Huber, M. S., Kovaleva, E., & Riller, U. (2020). Modeling the geochemical evolution of impact melts in terrestrial impact basins: Vredefort granophyre dikes and Sudbury offset dikes. *Meteoritics & planetary science, 55*(10), 2320-2337.

Ivanov, B. A. (2005). Numerical Modeling of the Largest Terrestrial Meteorite Craters. *Solar System Research, 39*(5), 381-409. https://doi.org/10.1007/s11208-005-0051-0

Ivanov, B. A., & Deutsch, A. (1999). Sudbury impact event: Cratering mechanics and thermal history. In B. O. Dressler & V. L. Sharpton (Eds.), *Large meteorite impacts and planetary evolution; II* (Vol. 339): Geological Society of America.

Jaxybulatov, K., Shapiro, N. M., Koulakov, I., Mordret, A., Landès, M., & Sens-Schönfelder, C. (2014). A large magmatic sill complex beneath the Toba caldera. *Science, 346*(6209), 617-619. https://doi.org/10.1126/science.1258582

Jozwiak, L. M., Head, J. W., & Wilson, L. (2015). Lunar floor-fractured craters as magmatic intrusions: Geometry, modes of emplacement, associated tectonic and volcanic features, and implications for gravity anomalies. *Icarus, 248*, 424-447.

Jozwiak, L. M., Head, J. W., Zuber, M. T., Smith, D. E., & Neumann, G. A. (2012). Lunar floor-fractured craters: Classification, distribution, origin and implications for magmatism and shallow crustal structure. *Journal of Geophysical Research: Planets, 117*(E11).

Kenkmann, T., Poelchau, M. H., & Wulf, G. (2014). Structural geology of impact craters. *Journal of Structural Geology, 62*, 156-182. https://www.sciencedirect.com/science/article/pii/S0191814114000285

Kiefer, W. S., Macke, R. J., Britt, D. T., Irving, A. J., & Consolmagno, G. J. (2012). The density and porosity of lunar rocks. *Geophysical Research Letters, 39*(7). https://agupubs.onlinelibrary.wiley.com/doi/abs/10.1029/2012GL051319

Kimi, K. B., Harish, & Vijayan, S. (2023). Mare filled craters on the Moon. *Icarus, 390*, 115298. https://www.sciencedirect.com/science/article/pii/S0019103522003906

Klimczak, C., Ernst, C. M., Byrne, P. K., Solomon, S. C., Watters, T. R., Murchie, S. L., (2013). Insights into the subsurface structure of the Caloris basin, Mercury, from assessments of mechanical layering and changes in long-wavelength topography. *Journal of Geophysical Research: Planets, 118*(10), 2030-2044.

Klimczak, C., Schultz, R. A., & Nahm, A. L. (2010). Evaluation of the origin hypotheses of Pantheon Fossae, central Caloris basin, Mercury. *Icarus, 209*(1), 262-270.

Klinkmüller, M., Schreurs, G., Rosenau, M., & Kemnitz, H. (2016). Properties of granular analogue model materials: A community wide survey. *Tectonophysics, 684*, 23-38. https://www.sciencedirect.com/science/article/pii/S0040195116000548

Korteniemi, J., Aittola, M., Öhman, T., & Raitala, J. (2006). *Floor-fractured craters on the terrestrial planets—The Martian perspective.* Paper presented at the Proceedings of the First International Conference on Impact Cratering in the Solar System, SP.

Krawczyk, C. M., Buddensiek, M. L., Oncken, O., & Kukowski, N. (2013). Seismic imaging of sandbox experiments – laboratory hardware setup and first reflection seismic sections. *Solid Earth, 4*(1), 93-104. https://se.copernicus.org/articles/4/93/2013/

Kring, D. A., & Bach, W. (2021). Hydrogen Production from Alteration of Chicxulub Crater Impact Breccias: Potential Energy Source for a Subsurface Microbial Ecosystem. *Astrobiology, 21*(12), 1547-1564. https://doi.org/10.1089/ast.2021.0045

Krüger, T., Kenkmann, T., & Hergarten, S. (2017). Structural uplift and ejecta thickness of lunar mare craters: New insights into the formation of complex crater rims. *Meteoritics & planetary science, 52*(10), 2220-2240. https://onlinelibrary.wiley.com/doi/abs/10.1111/maps.12925

Lieger, D., & Riller, U. (2012). Emplacement history of Granophyre dikes in the Vredefort Impact Structure, South Africa, inferred from geochemical evidence. *Icarus, 219*(1), 168-180. https://www.sciencedirect.com/science/article/pii/S0019103512000747

Lightfoot, P. C. (2017). Chapter 4 - The mineral system characteristics of the Sudbury Ni-Cu-Co-PGE sulfide ore deposits. In P. C. Lightfoot (Ed.), *Nickel Sulfide Ores and Impact Melts* (pp. 296-440): Elsevier.

Lowery, C. M., Jones, H. L., Bralower, T. J., Cruz, L. P., Gebhardt, C., Whalen, M. T., (2021). Early Paleocene Paleoceanography and Export Productivity in the Chicxulub Crater. *Paleoceanography and Paleoclimatology, 36*(11). https://doi.org/10.1029/2021PA004241

7. References

Luzzi, E., Nodjoumi, G., Massironi, M., Pozzobon, R., & Rossi, A. P. (2023). A Semiautomated Analysis of Displacement-To-Length Scaling of the Grabens Affecting Lunar Floor-Fractured Craters. *Journal of Geophysical Research: Planets, 128*(4). https://doi.org/10.1029/2022JE007265

Luzzi, E., Rossi, A. P., Massironi, M., Pozzobon, R., Corti, G., & Maestrelli, D. (2021). Caldera Collapse as the Trigger of Chaos and Fractured Craters on the Moon and Mars. *Geophysical Research Letters, 48*(11). https://agupubs.onlinelibrary.wiley.com/doi/abs/10.1029/2021GL092436

Melosh, H. J. (1976). *On the origin of fractures radial to lunar basins.* Paper presented at the Lunar and planetary science conference proceedings.

Melosh, H. J. (1989). *Impact cratering : a geologic process*. New York : Oxford University Press : Clarendon Press.

Melosh, H. J., & Ivanov, B. A. (1999). IMPACT CRATER COLLAPSE. *Annual Review of Earth and Planetary Sciences, 27*(1), 385-415. https://doi.org/10.1146/annurev.earth.27.1.385

Michaut, C. (2011). Dynamics of magmatic intrusions in the upper crust: Theory and applications to laccoliths on Earth and the Moon. *Journal of Geophysical Research: Solid Earth, 116*(B5). https://agupubs.onlinelibrary.wiley.com/doi/abs/10.1029/2010JB008108

Michaut, C., & Pinel, V. (2018). Magma Ascent and Eruption Triggered by Cratering on the Moon. *Geophysical Research Letters, 45*(13), 6408-6416. https://agupubs.onlinelibrary.wiley.com/doi/abs/10.1029/2018GL078150

Michaut, C., Pinel, V., & Maccaferri, F. (2020). Magma ascent at floor-fractured craters diagnoses the lithospheric stress state on the Moon. *Earth and Planetary Science Letters, 530*, 115889. https://www.sciencedirect.com/science/article/pii/S0012821X19305813

Mohit, P. S., Johnson, C. L., Barnouin-Jha, O., Zuber, M. T., & Solomon, S. C. (2009). Shallow basins on Mercury: Evidence of relaxation? *Earth and Planetary Science Letters, 285*(3-4), 355-363.

Mohit, P. S., & Phillips, R. J. (2006). Viscoelastic evolution of lunar multiring basins. *Journal of Geophysical Research: Planets, 111*(E12).

Mohit, P. S., & Phillips, R. J. (2007). Viscous relaxation on early Mars: A study of ancient impact basins. *Geophysical Research Letters, 34*(21).

Montanari, D., Agostini, A., Bonini, M., Corti, G., & Ventisette, C. D. (2017). The Use of Empirical Methods for Testing Granular Materials in Analogue Modelling. *Materials, 10*(6), 635. https://www.mdpi.com/1996-1944/10/6/635

Morgan, J. V., Warner, M., the Chicxulub Working, G., Brittan, J., Buffler, R., Camargo, A., (1997). Size and morphology of the Chicxulub impact crater. *Nature, 390*(6659), 472-476. https://doi.org/10.1038/37291

Morgan, J. V., Gulick, S. P. S., Bralower, T., Chenot, E., Christeson, G., Claeys, P., (2016). The formation of peak rings in large impact craters. *Science, 354*(6314), 878-882. https://doi.org/10.1126/science.aah6561

Müller, G. (1998). Starch columns: Analog model for basalt columns. *Journal of Geophysical Research: Solid Earth, 103*(B7), 15239-15253. https://agupubs.onlinelibrary.wiley.com/doi/abs/10.1029/98JB00389

Murchie, S. L., Watters, T. R., Robinson, M. S., Head, J. W., Strom, R. G., Chapman, C. R., (2008). Geology of the Caloris basin, Mercury: A view from MESSENGER. *Science, 321*(5885), 73-76.

Panien, M., Buiter, S. J. H., Schreurs, G., & Pfiffner, O. A. (2006). Inversion of a symmetric basin: insights from a comparison between analogue and numerical experiments. *Geological Society, London, Special Publications, 253*(1), 253. 10.1144/GSL.SP.2006.253.01.13. http://sp.lyellcollection.org/content/253/1/253.abstract

Panien, M., Schreurs, G., & Pfiffner, A. (2006). Mechanical behaviour of granular materials used in analogue modelling: insights from grain characterisation, ring-shear tests and analogue experiments. *Journal of Structural Geology, 28*(9), 1710-1724.

Pathak, S., Dagar, A. K., Bhattacharya, S., Moitra, H., Chauhan, M., & Gupta, S. (2021). Geological insights into lunar floor-fractured crater Atlas. *Icarus, 360*, 114374. https://www.sciencedirect.com/science/article/pii/S0019103521000658

Pike, R. J. (1977). *Size-dependence in the shape of fresh impact craters on the Moon.* Paper presented at the Impact and explosion cratering: Planetary and terrestrial implications.

Pilles, E. A., Osinski, G. R., Grieve, R. A., Smith, D., & Bailey, J. (2018). Formation of large-scale impact melt dikes: A case study of the Foy Offset Dike at the Sudbury impact structure, Canada. *Earth and Planetary Science Letters, 495*, 224-233.

Pohlenz, A., Rudolf, M., Kemnitz, H., & Rosenau, M. (2020). *Ring shear test data of glass beads 40-70 µm used for analogue experiments in the Helmholtz Laboratory for Tectonic Modelling (HelTec) at the GFZ German Research Centre for Geosciences in Potsdam*. Retrieved from Potsdam: https://gfzpublic.gfz-potsdam.de/pubman/item/item_5003070

Poppe, S., Holohan, E. P., Galland, O., Buls, N., Van Gompel, G., Keelson, B., (2019). An Inside Perspective on Magma Intrusion: Quantifying 3D Displacement and Strain in Laboratory Experiments by Dynamic X-Ray Computed Tomography. *Frontiers in Earth Science, 7*. Original Research. https://www.frontiersin.org/articles/10.3389/feart.2019.00062

Poppe, S., Holohan, E. P., Pauwels, E., Cnudde, V., & Kervyn, M. (2015). Sinkholes, pit craters, and small calderas: Analog models of depletion-induced collapse analyzed by computed X-ray microtomography. *Geological Society of America Bulletin, 127*(1-2), 281-296.

Ranalli, G. (2001). Experimental tectonics: from Sir James Hall to the present. *Journal of Geodynamics, 32*(1), 65-76. https://www.sciencedirect.com/science/article/pii/S0264370701000230

Reimold, W. U., & Gibson, R. L. (2006). The melt rocks of the Vredefort impact structure – Vredefort Granophyre and pseudotachylitic breccias: Implications for impact cratering and the evolution of the Witwatersrand Basin. *Geochemistry, 66*(1), 1-35. https://www.sciencedirect.com/science/article/pii/S0009281905000528

Riller, U. (2005). Structural characteristics of the Sudbury impact structure, Canada: Impact-induced versus orogenic deformation—A review. *Meteoritics & planetary science, 40*(11), 1723-1740. https://onlinelibrary.wiley.com/doi/abs/10.1111/j.1945-5100.2005.tb00140.x

Riller, U., Poelchau, M. H., Rae, A. S. P., Schulte, F. M., Collins, G. S., Melosh, H. J., (2018). Rock fluidization during peak-ring formation of large impact structures. *Nature, 562*(7728), 511-518. https://doi.org/10.1038/s41586-018-0607-z

Ritter, M. C., Leever, K., Rosenau, M., & Oncken, O. (2016). Scaling the sandbox-Mechanical (dis) similarities of granular materials and brittle rock. *Journal of Geophysical Research: Solid Earth, 121*(9), 6863-6879.

Ritter, M. C., Leever, K., Rosenau, M., & Oncken, O. (2016). Scaling the sandbox—Mechanical (dis) similarities of granular materials and brittle rock. *Journal of Geophysical Research: Solid Earth, 121*(9), 6863-6879.

Rosenau, M., Corbi, F., & Dominguez, S. (2017). Analogue earthquakes and seismic cycles: experimental modelling across timescales. *Solid Earth, 8*(3), 597-635. https://se.copernicus.org/articles/8/597/2017/

Rosenau, M., Lohrmann, J., & Oncken, O. (2009). Shocks in a box: An analogue model of subduction earthquake cycles with application to seismotectonic forearc evolution. *Journal of Geophysical Research: Solid Earth, 114*(B1). https://doi.org/10.1029/2008JB005665

7. References

Rosenau, M., Nerlich, R., Brune, S., & Oncken, O. (2010). Experimental insights into the scaling and variability of local tsunamis triggered by giant subduction megathrust earthquakes. *Journal of Geophysical Research: Solid Earth, 115*(B9). https://agupubs.onlinelibrary.wiley.com/doi/abs/10.1029/2009JB007100

Rosenau, M., & Oncken, O. (2009). Fore-arc deformation controls frequency-size distribution of megathrust earthquakes in subduction zones. *Journal of Geophysical Research: Solid Earth, 114*(B10). https://agupubs.onlinelibrary.wiley.com/doi/abs/10.1029/2009JB006359

Rosenau, M., Pohlenz, A., Kemnitz, H., & Warsitzka, M. (2018). *Ring-shear test data of quartz sand G23 used for analogue experiments in the Helmholtz Laboratory for Tectonic Modelling (HelTec) at the GFZ German Research Centre for Geosciences in Potsdam*. Retrieved from Potsdam: https://gfzpublic.gfz-potsdam.de/pubman/item/item_3903923

Rosenau, M., Warsitzka , M., & Zavada, P. (2022). *Ring-shear test data of glass beads 100-200 µm used for analogue experiments in the tectonic modelling labs at GFZ Potsdam and the Institute of Geophysics of the Czech Academy of Sciences, Prague*. Retrieved from Potsdam: https://gfzpublic.gfz-potsdam.de/pubman/item/item_5014543

Rudolf, M., Boutelier, D., Rosenau, M., Schreurs, G., & Oncken, O. (2016). Rheological benchmark of silicone oils used for analog modeling of short- and long-term lithospheric deformation. *Tectonophysics, 684*, 12-22. https://www.sciencedirect.com/science/article/pii/S0040195115006605

Schmiedel, T., Galland, O., & Breitkreuz, C. (2017). Dynamics of Sill and Laccolith Emplacement in the Brittle Crust: Role of Host Rock Strength and Deformation Mode. *Journal of Geophysical Research: Solid Earth, 122*(11), 8860-8871.

Schreurs, G., Buiter, S. J. H., Boutelier, D., Corti, G., Costa, E., Cruden, A. R., et al. (2006). Analogue benchmarks of shortening and extension experiments. In *Analogue and Numerical Modelling of Crustal-Scale Processes* (Vol. 253): Geological Society of London.

Schultz, P. H., & Orphal, D. (1978). Floor-fractured craters on the Moon and Mars. *Meteoritics, 13*, 622-625.

Schultz, P. H. (1976). Floor-fractured lunar craters. *The Moon, 15*(3), 241-273. https://doi.org/10.1007/BF00562240

Schultz, R. A., & Watters, T. R. (2001). Forward mechanical modeling of the Amenthes Rupes Thrust Fault on Mars. *Geophysical Research Letters, 28*(24), 4659-4662. https://doi.org/10.1029/2001GL013468

Settle, M., & Head III, J. W. (1979). The role of rim slumping in the modification of lunar impact craters. *Journal of Geophysical Research: Solid Earth, 84*(B6), 3081-3096. https://agupubs.onlinelibrary.wiley.com/doi/abs/10.1029/JB084iB06p03081

Sherlock, D. H., & Evans, B. J. (2001). The Development of Seismic Reflection Sandbox Modeling. *AAPG Bulletin, 85*(9), 1645-1659. https://doi.org/10.1306/8626CCE9-173B-11D7-8645000102C1865D

Shinevar, W. J., Behn, M. D., & Hirth, G. (2015). Compositional dependence of lower crustal viscosity. *Geophysical Research Letters, 42*(20), 8333-8340.

Shoemaker, E. M. (1962). Interpretation of lunar craters. *Physics and Astronomy of the Moon*, 283-359.

Srivastava, N., Kumar, D., & Gupta, R. P. (2013). Young viscous flows in the Lowell crater of Orientale basin, Moon: Impact melts or volcanic eruptions? *Planetary and Space Science, 87*, 37-45. https://www.sciencedirect.com/science/article/pii/S0032063313002286

Stamhuis, E., & Thielicke, W. (2014). PIVlab–towards user-friendly, affordable and accurate digital particle image velocimetry in MATLAB. *Journal of open research software, 2*(1), 30.

Thorey, C., & Michaut, C. (2014). A model for the dynamics of crater-centered intrusion: Application to lunar floor-fractured craters. *Journal of Geophysical Research: Planets, 119*(1), 286-312.

Toramaru, A., & Matsumoto, T. (2004). Columnar joint morphology and cooling rate: A starch-water mixture experiment. *Journal of Geophysical Research: Solid Earth, 109*(B2). https://agupubs.onlinelibrary.wiley.com/doi/abs/10.1029/2003JB002686

Troll, V. R., Walter, T. R., & Schmincke, H.-U. (2002). Cyclic caldera collapse: Piston or piecemeal subsidence? Field and experimental evidence. *Geology, 30*(2), 135-138. https://doi.org/10.1130/0091-7613(2002)030<0135:CCCPOP>2.0.CO;2

Walter, T. R., & Troll, V. R. (2001). Formation of caldera periphery faults: an experimental study. *Bulletin of Volcanology, 63*(2), 191-203. https://doi.org/10.1007/s004450100135

Walwer, D., Michaut, C., Pinel, V., & Adda-Bedia, M. (2021). Magma ascent and emplacement below floor fractured craters on the Moon from floor uplift and fracture length. *Physics of the Earth and Planetary Interiors, 312*, 106658. https://www.sciencedirect.com/science/article/pii/S0031920121000169

Warsitzka, M., Ge, Z., Schönebeck, J.-M., Pohlenz, A., & Kukowski, N. (2019). Ring-shear test data of foam glass beads used for analogue experiments in the Helmholtz Laboratory for Tectonic Modelling (HelTec) at the GFZ German Research Centre for Geosciences in Potsdam and the Institute of Geosciences, Friedrich Schiller University Jena, GFZ Data Services. *GFZ Data Services*.

Warsitzka, M., Zavada, P., & Rosenau, M. (2022). *Ring-shear test data of wheat flour used for analogue experiments in the laboratory of the Institute of Geophysics of the Czech Academy of Science, Prague*. Retrieved from Potsdam: https://gfzpublic.gfz-potsdam.de/pubman/item/item_5011169

Watters, T. R., Murchie, S. L., Robinson, M. S., Solomon, S. C., Denevi, B. W., André, S. L., & Head, J. W. (2009). Emplacement and tectonic deformation of smooth plains in the Caloris basin, Mercury. *Earth and Planetary Science Letters, 285*(3-4), 309-319.

Watters, T. R., Nimmo, F., & Robinson, M. S. (2005). Extensional troughs in the Caloris Basin of Mercury: Evidence of lateral crustal flow. *Geology, 33*(8).

Watters, T. R., Robinson, M. S., Banks, M. E., Tran, T., & Denevi, B. W. (2012). Recent extensional tectonics on the Moon revealed by the Lunar Reconnaissance Orbiter Camera. *Nature Geoscience, 5*(3), 181-185.

Watters, T. R., Solomon, S. C., Klimczak, C., Freed, A. M., Head, J. W., Ernst, C. M., (2012). Extension and contraction within volcanically buried impact craters and basins on Mercury. *Geology, 40*(12), 1123-1126.

Watts, A. B. (2001). *Isostasy and Flexure of the Lithosphere*. United Kingdom: Cambridge University Press.

Wichman, R., & Schultz, P. (1993). Floor-fractured crater models of the Sudbury Structure, Canada: Implications for initial crater size and crater modification. *Meteoritics, 28*(2), 222-231.

Wichman, R., & Schultz, P. (1995). Floor-fractured craters in Mare Smythii and west of Oceanus Procellarum : implications of crater modification by viscous relaxation and igneous intrusion models. *Journal of Geophysical Research, 100*, 21201-21218.

Wilson, L., & Head, J. W. (2018). Lunar floor-fractured craters: Modes of dike and sill emplacement and implications of gas production and intrusion cooling on surface morphology and structure. *Icarus, 305*, 105-122. https://www.sciencedirect.com/science/article/pii/S001910351730622X

Wöhler, C., & Lena, R. (2009). Lunar intrusive domes: Morphometric analysis and laccolith modelling. *Icarus, 204*(2), 381-398. https://www.sciencedirect.com/science/article/pii/S0019103509003236

7. References

Wöhler, C., Lena, R., Lazzarotti, P., Phillips, J., Wirths, M., & Pujic, Z. (2006). A combined spectrophotometric and morphometric study of the lunar mare dome fields near Cauchy, Arago, Hortensius, and Milichius. *Icarus, 183*(2), 237-264. https://www.sciencedirect.com/science/article/pii/S0019103506000960

Wöhler, C., Lena, R., & Phillips, J. (2007). Formation of lunar mare domes along crustal fractures: Rheologic conditions, dimensions of feeder dikes, and the role of magma evolution. *Icarus, 189*(2), 279-307. https://www.sciencedirect.com/science/article/pii/S0019103507000565

Wünnemann, K., Collins, G. S., & Osinski, G. R. (2008). Numerical modelling of impact melt production in porous rocks. *Earth and Planetary Science Letters, 269*(3), 530-539. https://www.sciencedirect.com/science/article/pii/S0012821X08001660

Wünnemann, K., & Ivanov, B. A. (2003). Numerical modelling of the impact crater depth–diameter dependence in an acoustically fluidized target. *Planetary and Space Science, 51*(13), 831-845. https://www.sciencedirect.com/science/article/pii/S0032063303001211

Xiao, Z., Zeng, Z., Xiao, L., Fa, W., & Huang, Q. (2010). Origin of pit chains in the floor of lunar Copernican craters. *Science China Physics, Mechanics and Astronomy, 53*(12), 2145-2159. https://doi.org/10.1007/s11433-010-4174-z

Zieg, M. J., & Marsh, B. D. (2005). The Sudbury Igneous Complex: Viscous emulsion differentiation of a superheated impact melt sheet. *GSA Bulletin, 117*(11-12), 1427-1450. https://doi.org/10.1130/B25579.1

Zuber, M. T., Smith, D. E., Lemoine, F. G., & Neumann, G. A. (1994). The Shape and Internal Structure of the Moon from the Clementine Mission. *Science, 266*(5192), 1839-1843. https://doi.org/10.1126/science.266.5192.1839

Zwaan, F., & Schreurs, G. (2017). How oblique extension and structural inheritance influence rift segment interaction: Insights from 4D analog models. *Interpretation, 5*(1), SD119-SD138.

Zwaan, F., Schreurs, G., & Adam, J. (2018). Effects of sedimentation on rift segment evolution and rift interaction in orthogonal and oblique extensional settings: Insights from analogue models analysed with 4D X-ray computed tomography and digital volume correlation techniques. *Global and Planetary Change, 171*, 110-133. http://www.sciencedirect.com/science/article/pii/S0921818117302369

Zwaan, F., Schreurs, G., Buiter, S. J. H., Ferrer, O., Reitano, R., Rudolf, M., & Willingshofer, E. (2022). Analogue modelling of basin inversion: a review and future perspectives. *Solid Earth, 13*(12), 1859-1905. https://se.copernicus.org/articles/13/1859/2022/

8.1. Supplement to chapter 2

	Density ρ								Friction angle ϕ	
	Grain (kg/m³)	Sifted (kg/m³)	staw	Porosity	Compacted (kg/m³)	staw	Porosity	Δ ρ s-c (kg/m³)	(°)	staw
G12T	2680	1612.044	8.97	39.8 %	1635.896	7.10	39 %	-23.852	31.033	0.34
G23T	2680	1631.788	11.6	39.1 %	1647.238	9.68	38.5 %	-15.450	32.209	0.38
G23T dyed black		1567.968	14.3		1582.474	11.8		-14.506	32.481	0.45
G23T dyed green		1542.578	9.30		1554.078	4.52		-11.500	32.516	0.43
Corundum	4020	1868.216	11.3	53.5 %	2011.692	27.8	50 %	-143.476	34.990	0.45
Iron	7870								33.718	0.69
Spheres fine	2500	1515.530	12.6	39.4 %	1580.644	23.4	36.8 %	-65.114	26.218	0.48
Spheres course	2500	1486.170	9.56	40.6 %	1550.962	12.1	38 %	-64.792	25.328	0.54
Expanded glass	2500	284.404	4.93	88.6 %	292.764	2.55	88.3 %	-8.360	29.501	0.48
Flour	1500	586.398	21.1	60.9 %	687.246	19.8	54.2 %	-100.848	50.372	0.95
Starch	1500	678.588	10.9	54.8 %	746.416	16.0	50.2 %	-67.828	52.972	0.97
Rubber black	1170	508.796	4.34	56.5 %	553.338	5.73	52.7 %	-44.542	42.344	0.83
Rubber green	1170	528.236	4.23	54.9 %	572.172	7.71	51.1 %	-43.936	44.367	0.61
Rubber blue	1170	568.132	7.10	51.4 %	593.828	6.43	49.2 %	-25.696	37.705	0.92
Salt grit	2160	1207.710	9.51	44.1 %	1221.572	8.18	43.4 %	-13.862	32.719	0.46
Salt	2160								30.503	0.44
G23T DIC	2680	1656.016	9.19	38.2 %	1676.618	6.67	37.4 %	-20.602	31.241	0.52
G12T elastic		1279.886	6.76		1409.360	12.0		-129.474	32.547	0.65
Flour 2:1		961.558	5.87		1132.780	18.2		-171.222	46.390	0.63

Table S2.1: Table summarising measured densities, calculated porosities and internal friction angle of all granular materials.

Relative permittivity ε_r						
	GP8800 (0.4-6 GHz)		GSSI (2 GHz)		Mean ε_r	
	(ε_r)	staw	(ε_r)	staw	(ε_r)	staw
G12T	3.26	0.05	3.2	0.10	3.23	0.08
G23T	3.22	0.08	3.1	0.12	3.16	0.12
Corundum	4.06	0.15	4.54	0.05	4.30	0.27
Spheres fine	4.08	0.08	4.42	0.13	4.25	0.21
Spheres	3.92	0.08	4.08	0.08	4.00	0.12
Expanded	1.94	0.05	1.8	0.07	1.87	0.09
Flour	3.08	0.08	2.8	0.12	2.94	0.18
Starch	3.68	0.04	3.66	0.09	3.67	0.07
Rubber green	2.32	0.04	2.18	0.08	2.25	0.10
Rubber blue	2.28	0.04	2.04	0.09	2.16	0.14
Salt grit	3.68	0.04	3.52	0.11	3.60	0.12
G23T DIC	3.26	0.11	3.14	0.15	3.20	0.14
Flour 2:1	3.34	0.05	3.46	0.17	3.40	0.13

Table S2.2: Table summarising measured relative permittivity values of all granular materials.

8.2. Supplement to chapter 3

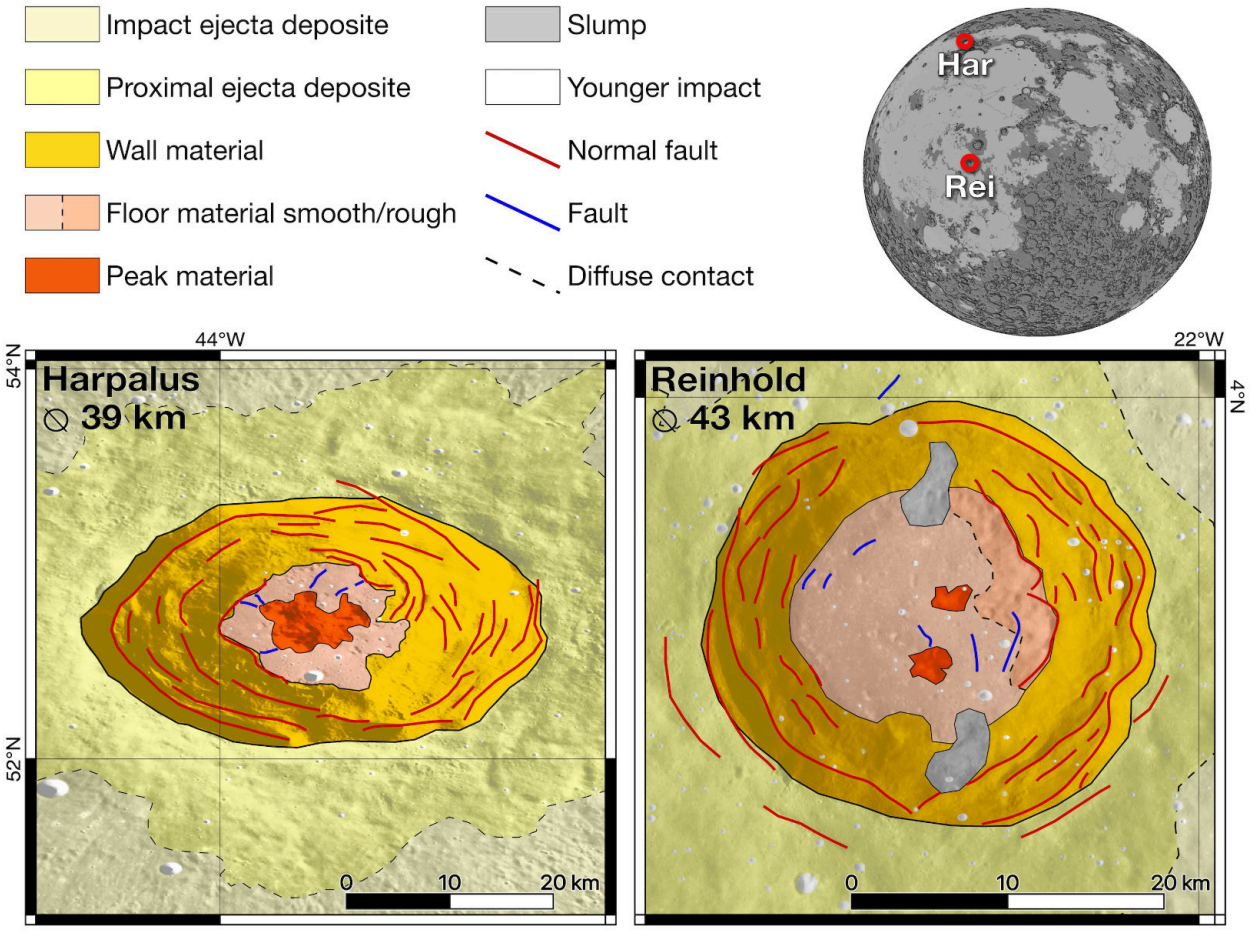

Figure S3.1: Examples of complex floor fractured lunar craters Harpalus and Reinhold, showing flat and mare-filled floors. Concentric normal faults of the terraced crater wall are indicated by red lines. Radial and concentric floor faults are indicated by blue lines. Lithologies and cross section based on USGS Geological Atlas of the Moon: 11, 58. NASA LROC-WAC image data. Ellipticity of crater due to projection.

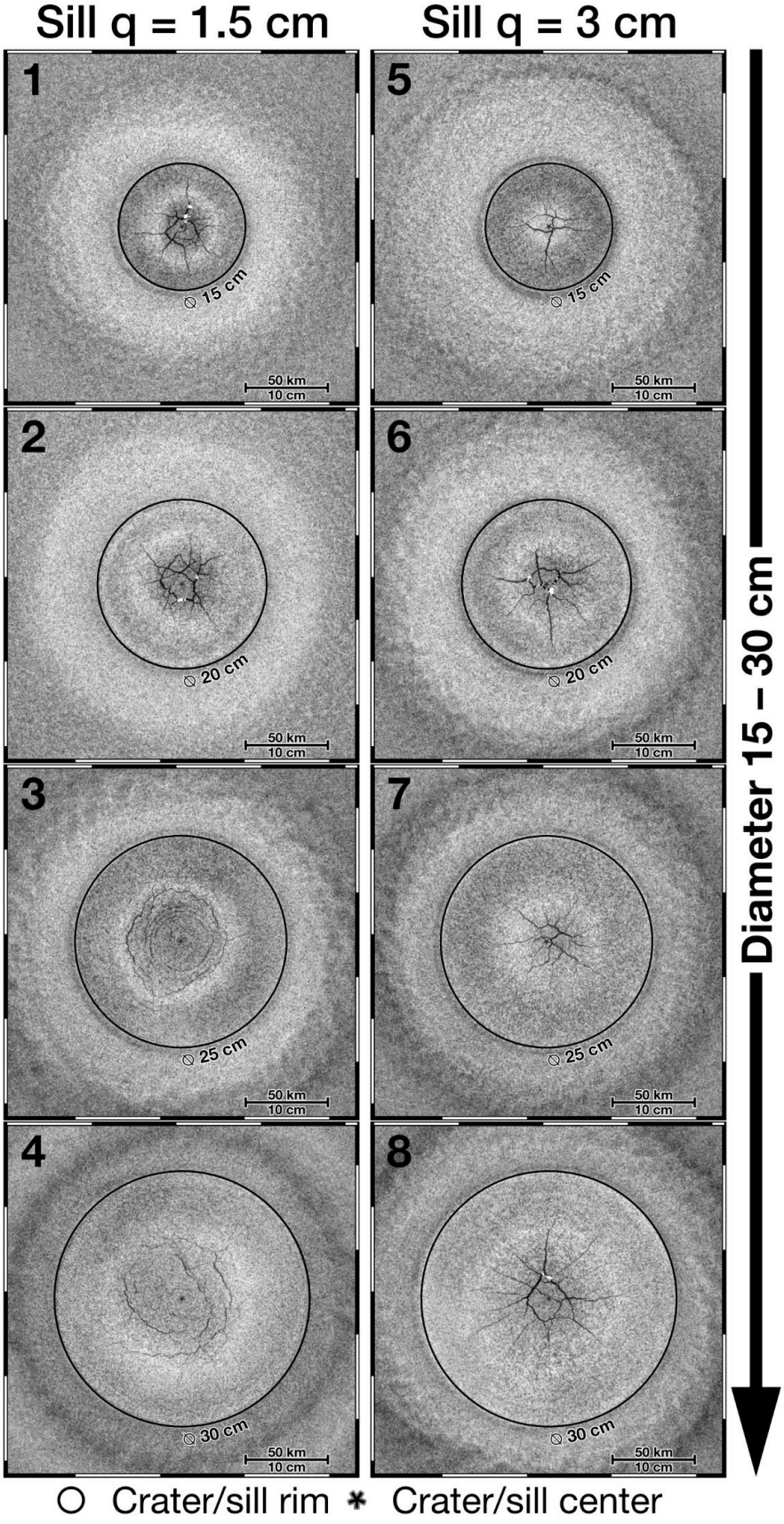

Figure S3.2: Image of the experimental surface from Set 1 after maximum inflation. Black lines are visible surface fractures. The diameter of the model sill is indicated by the black cricle.

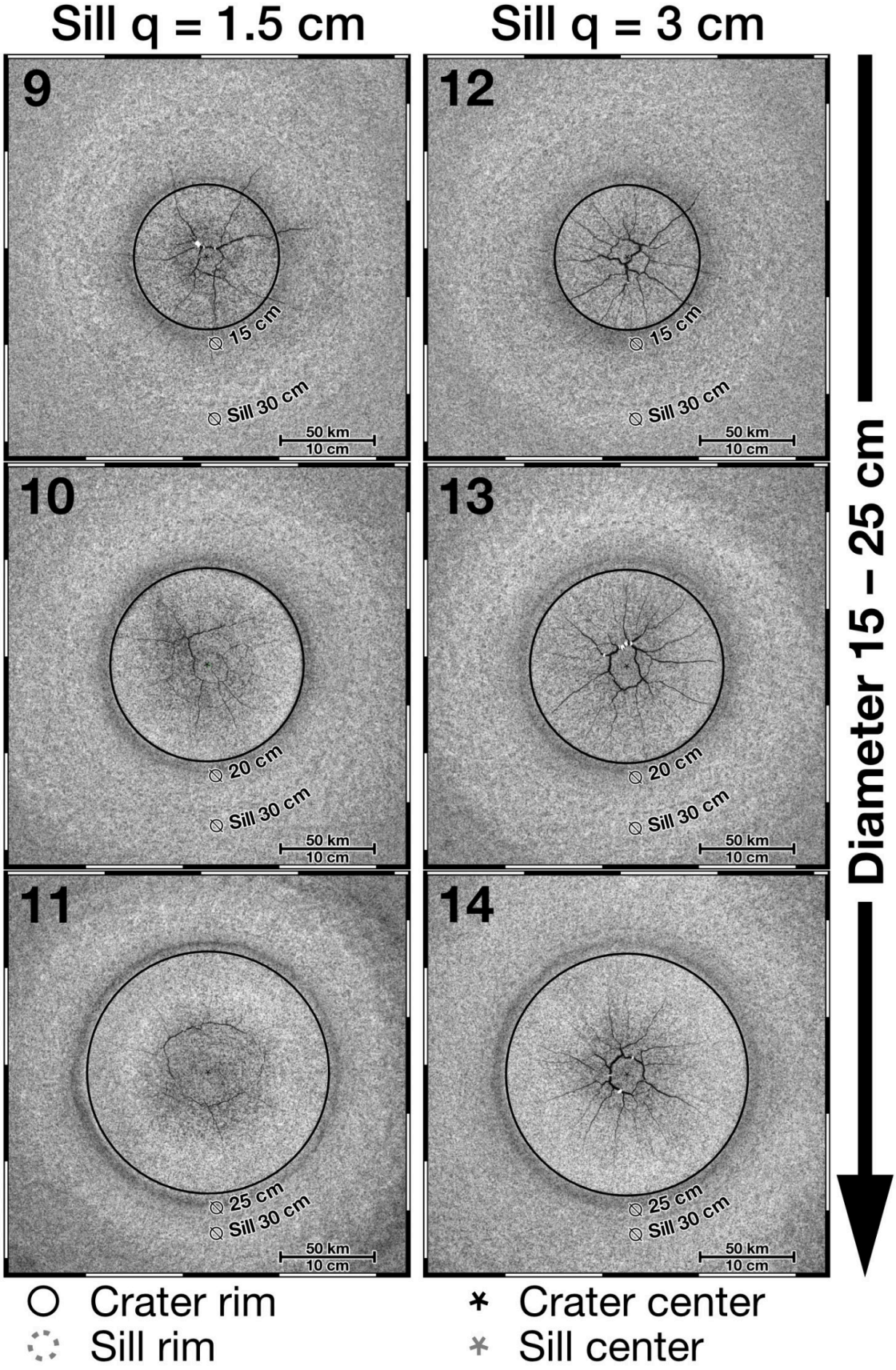

Figure S3.3: Image of the experimental surface from Set 2 after maximum inflation. Black lines are visible surface fractures. The diameter of the model sill is indicated by the dotted line.

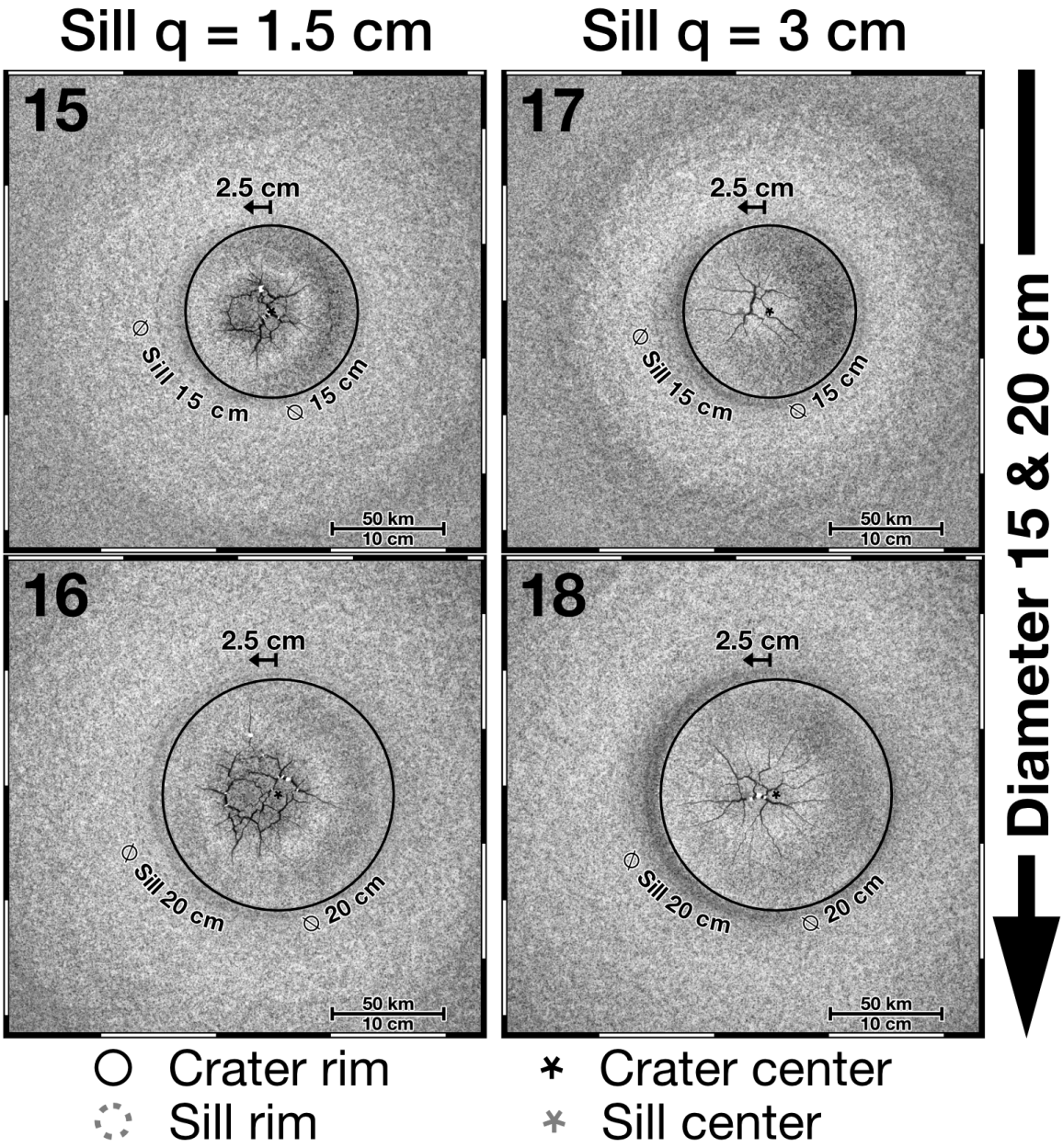

Figure S3.4: Image of the experimental surface from Set 3 after maximum inflation. Black lines are visible surface fractures. The diameter of the model sill is indicated by the dotted line.

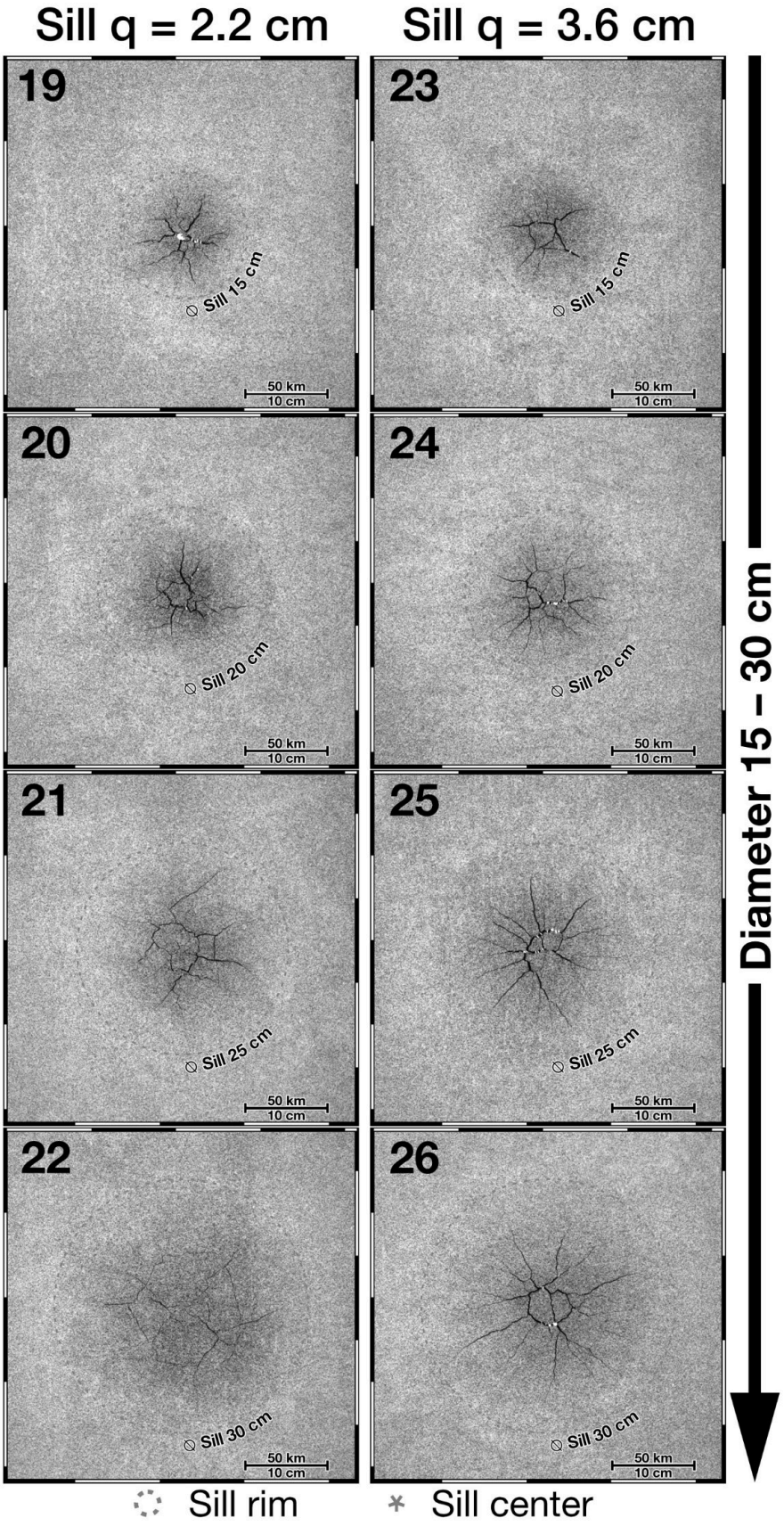

Figure S3.5: Image of the experimental surface from Set 4 after maximum inflation. Black lines are visible surface fractures. The diameter of the model sill is indicated by the dotted line.

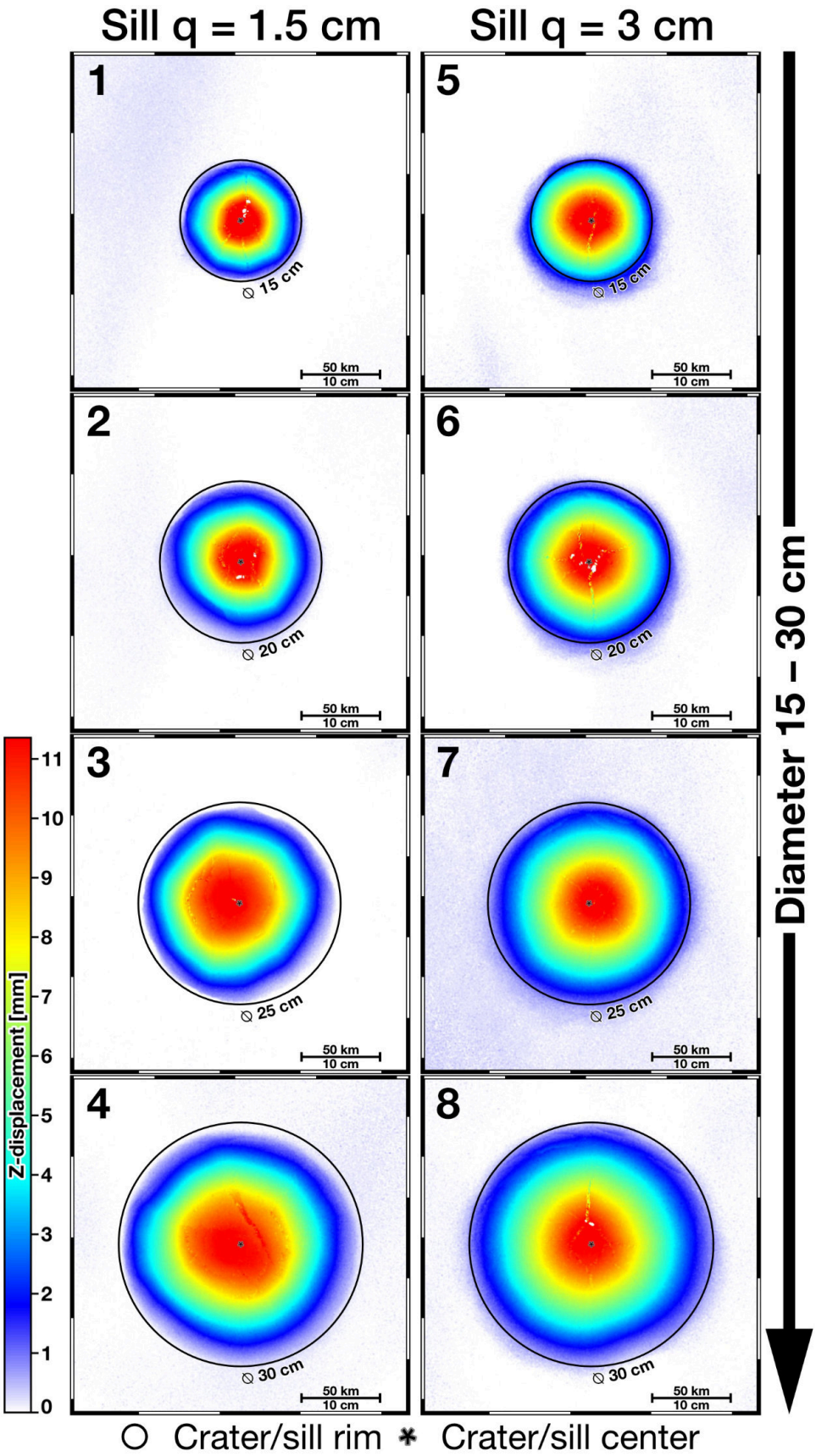

Figure S3.6: Cumulative vertical displacements of experiment Set 1 with model sill depths of q_m = 1.5 cm 1 – 4 and q_m = 3 cm 5 – 8 after maximum inflation.

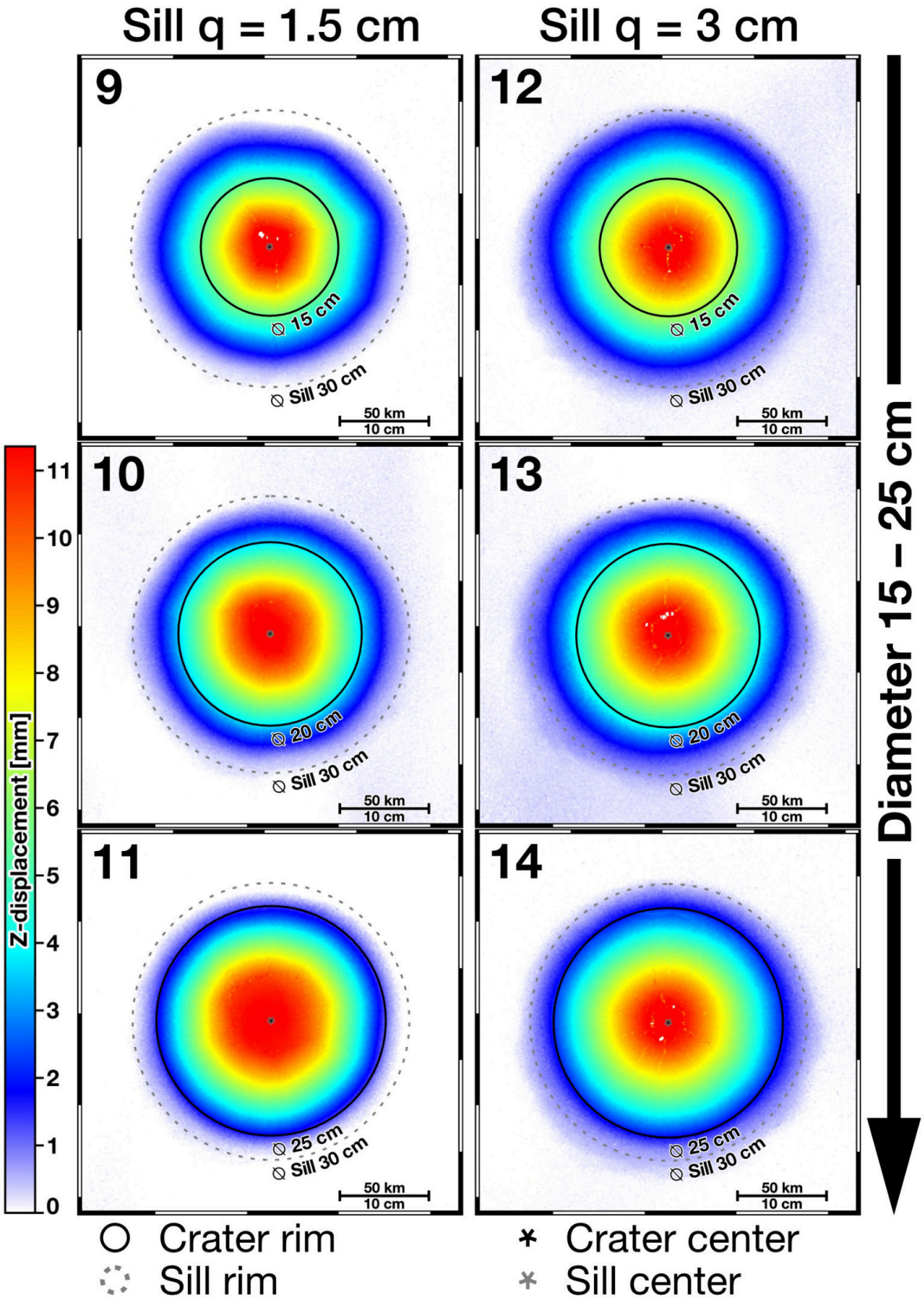

Figure S3.7: Cumulative vertical displacements of experiment Set 2 with model sill depths of q_m = 1.5 cm 9 – 11 and q_m = 3 cm 12 – 14 after maximum inflation. Diameter of model sill indicated by stippled line.

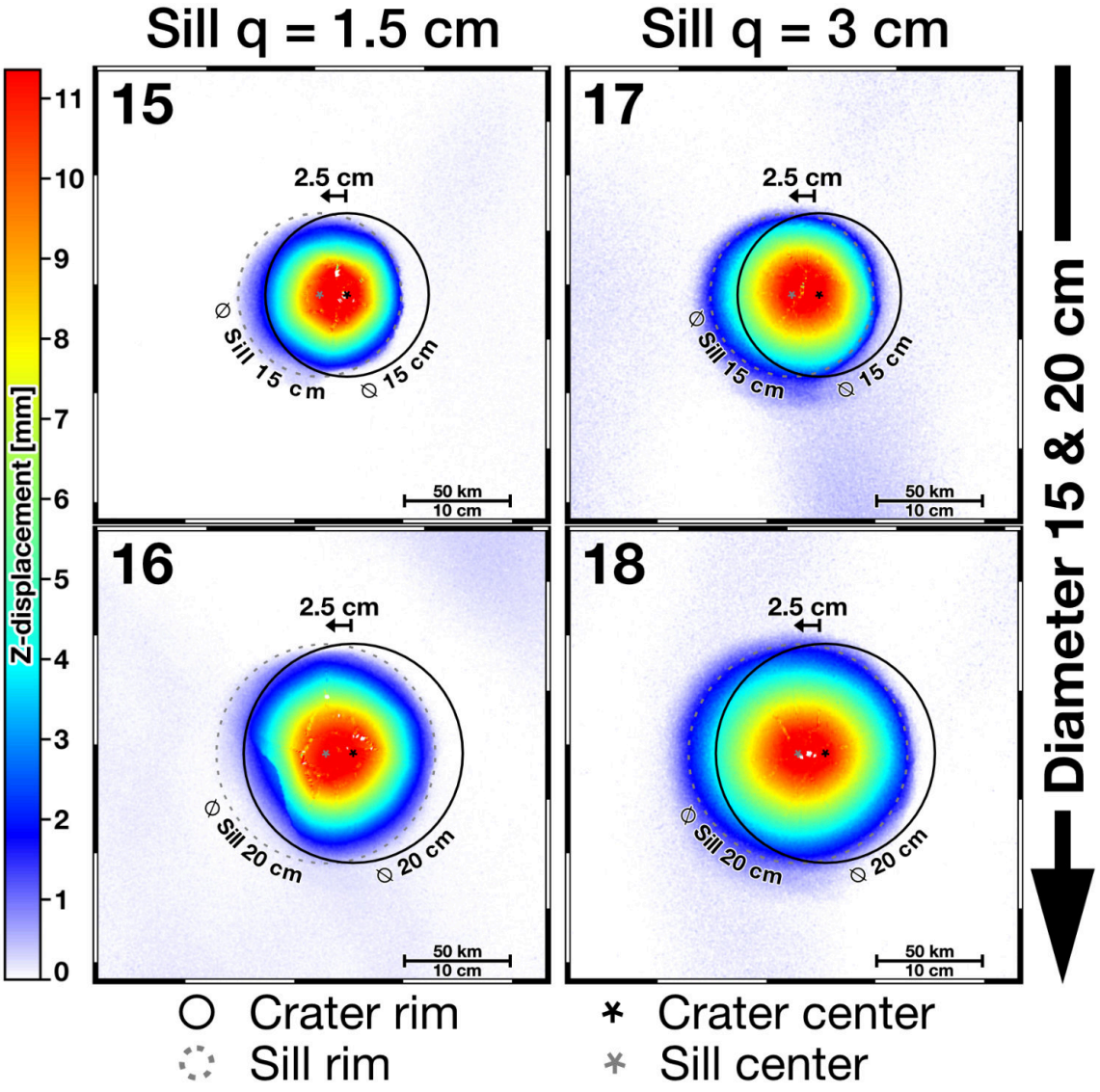

Figure S3.8: Cumulative vertical displacements of experiment Set 3 with model sill depths of q_m = 1.5 cm 15 – 16 and q_m = 3 cm 17 – 18 after maximum inflation. Diameter of model sill indicated by stippled line.

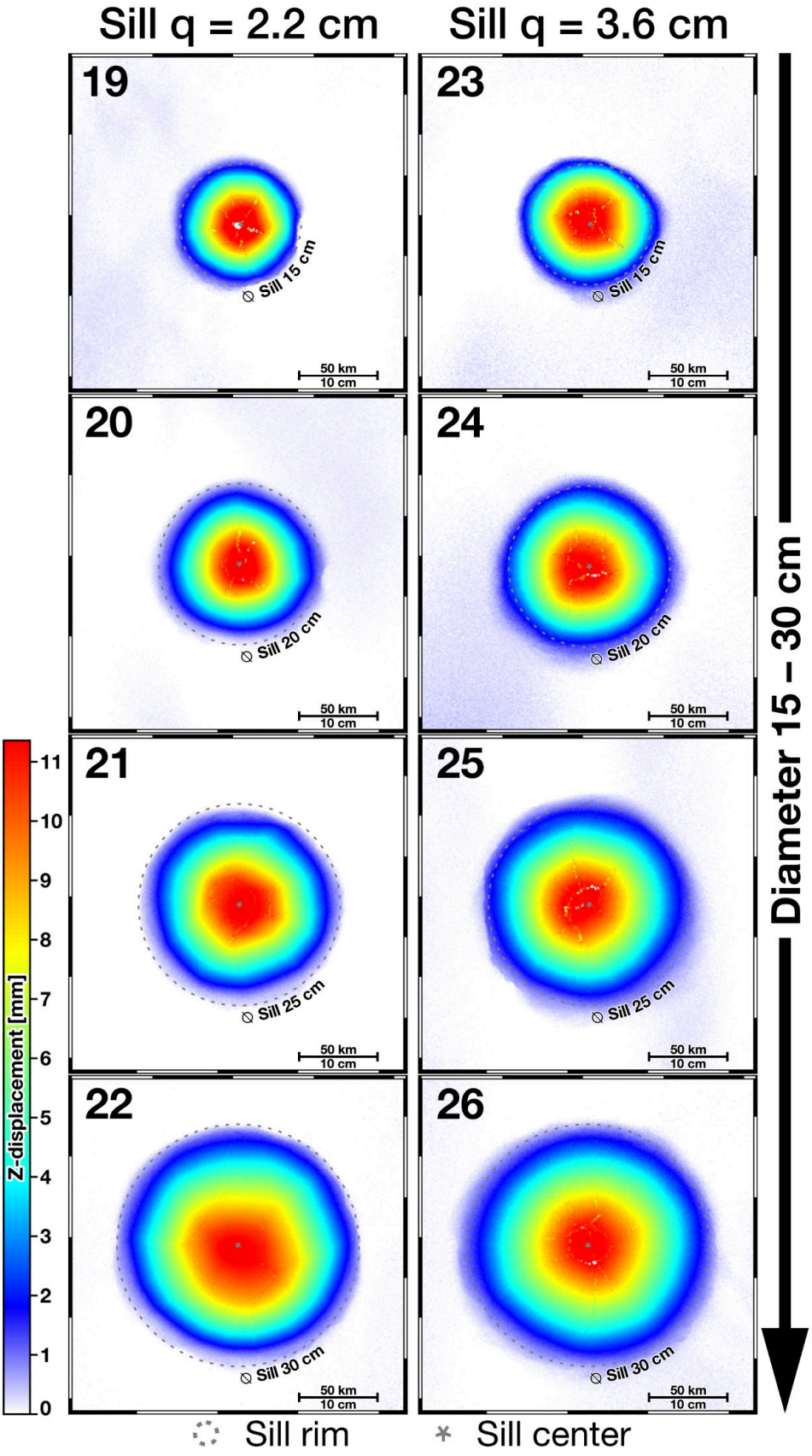

Figure S3.9: Cumulative vertical displacements of experiment Set 4 with model sill depths of q_m = 2.2 cm 19 – 22 and q_m = 3 cm 23 – 26 after maximum inflation. Diameter of model sill indicated by stippled line.

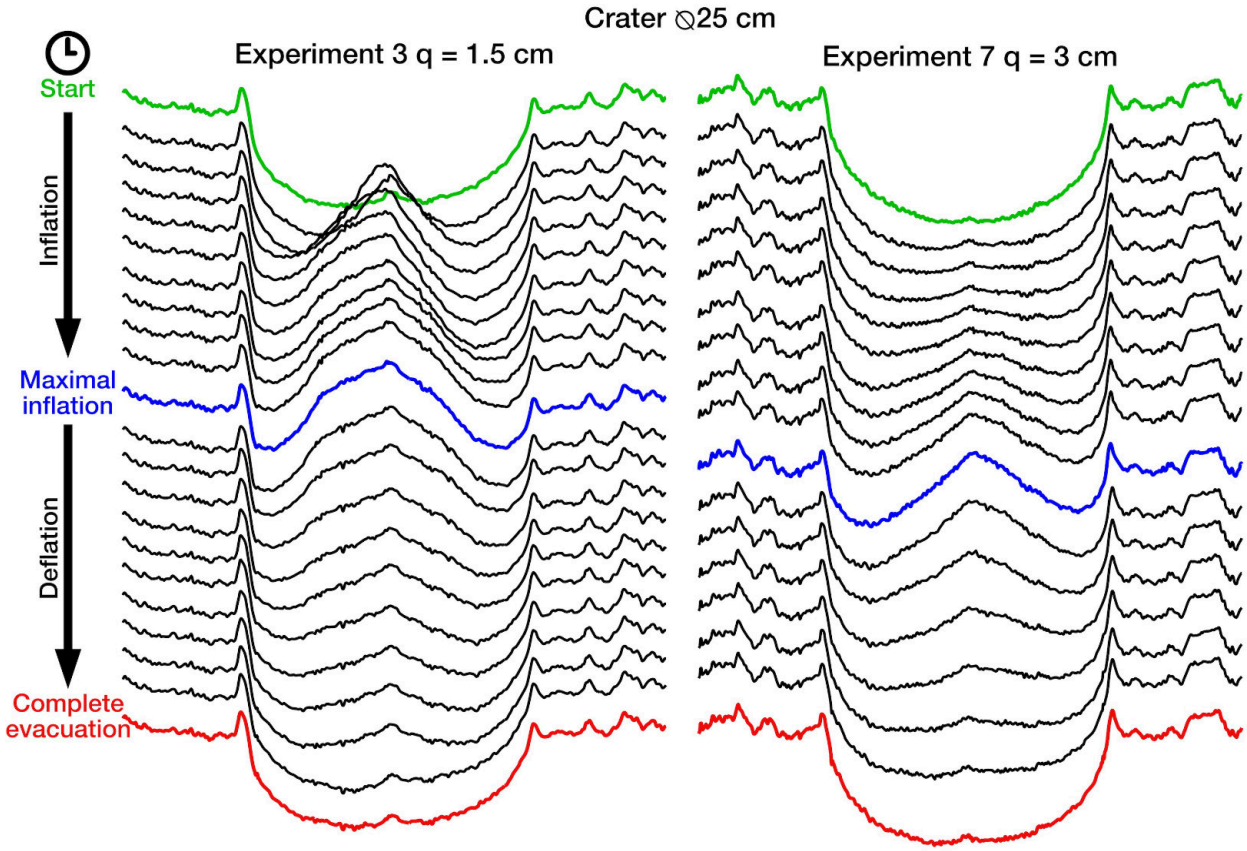

Figure S3.10: Ridgeline plot (cross-section) and temporal evolution of experiments 3 and 7 from set 1, where the sill diameter is equal to the crater diameter of 25 cm, representing craters with diameters of 125 km each. Experiment 3 has a shallow sill while 7 has a deep sill. Each panel represents the morphology at approximately 5 minute intervals during linear inflation and deflation of the balloon. Morphology 5x vertically exaggerated.

8.3. Supplement to chapter 4

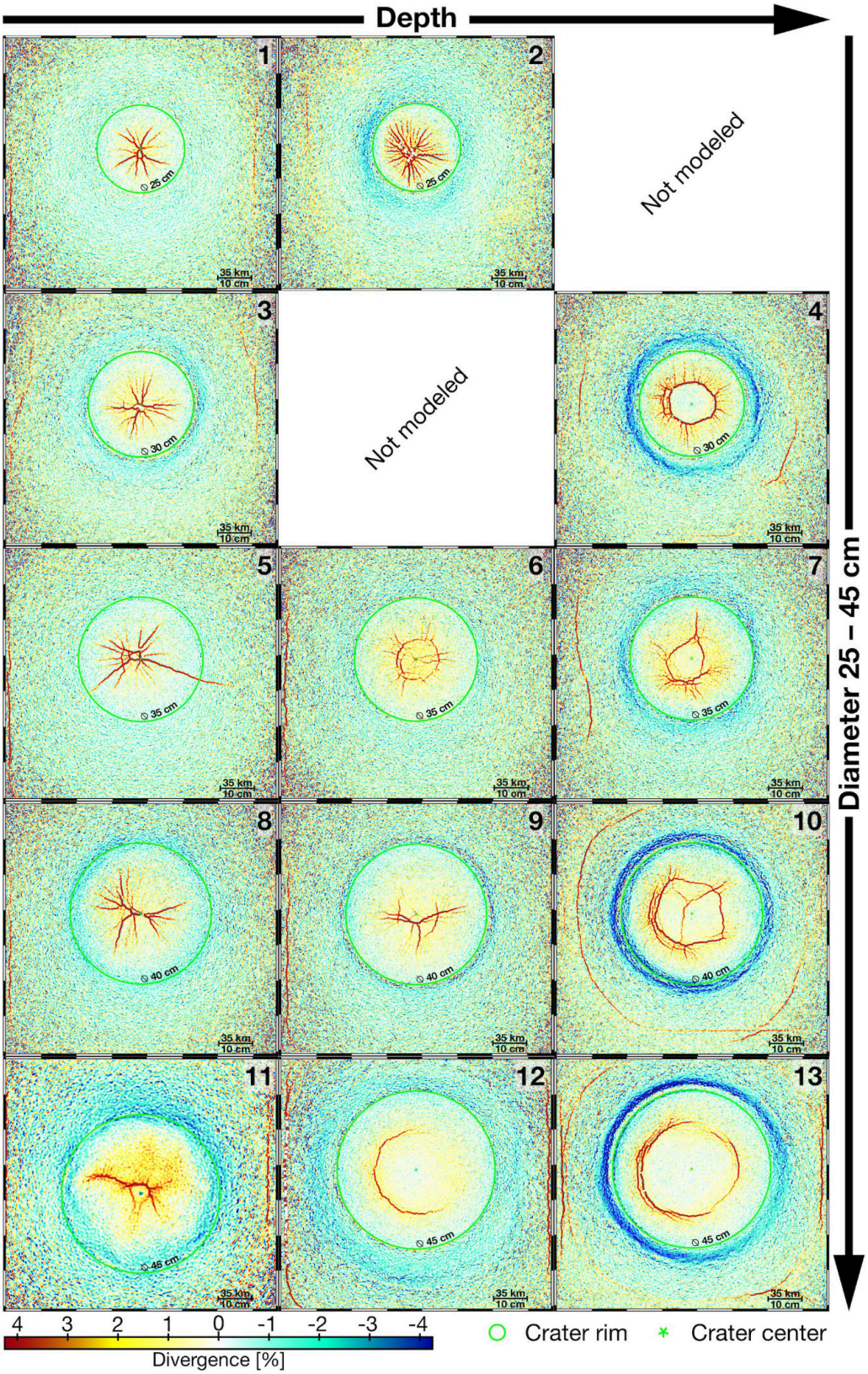

Figure S4.1: Panels showing cumulative divergence of set 1 experiments with convergent particle motion (blue), denoted as negative values, and divergent particle motion (red), indicated as positive values. Experiment numbers are indicated in the top right of each panel. Panels of experiments are arranged with regard to initial depths (rows) and diameters (columns) of craters.

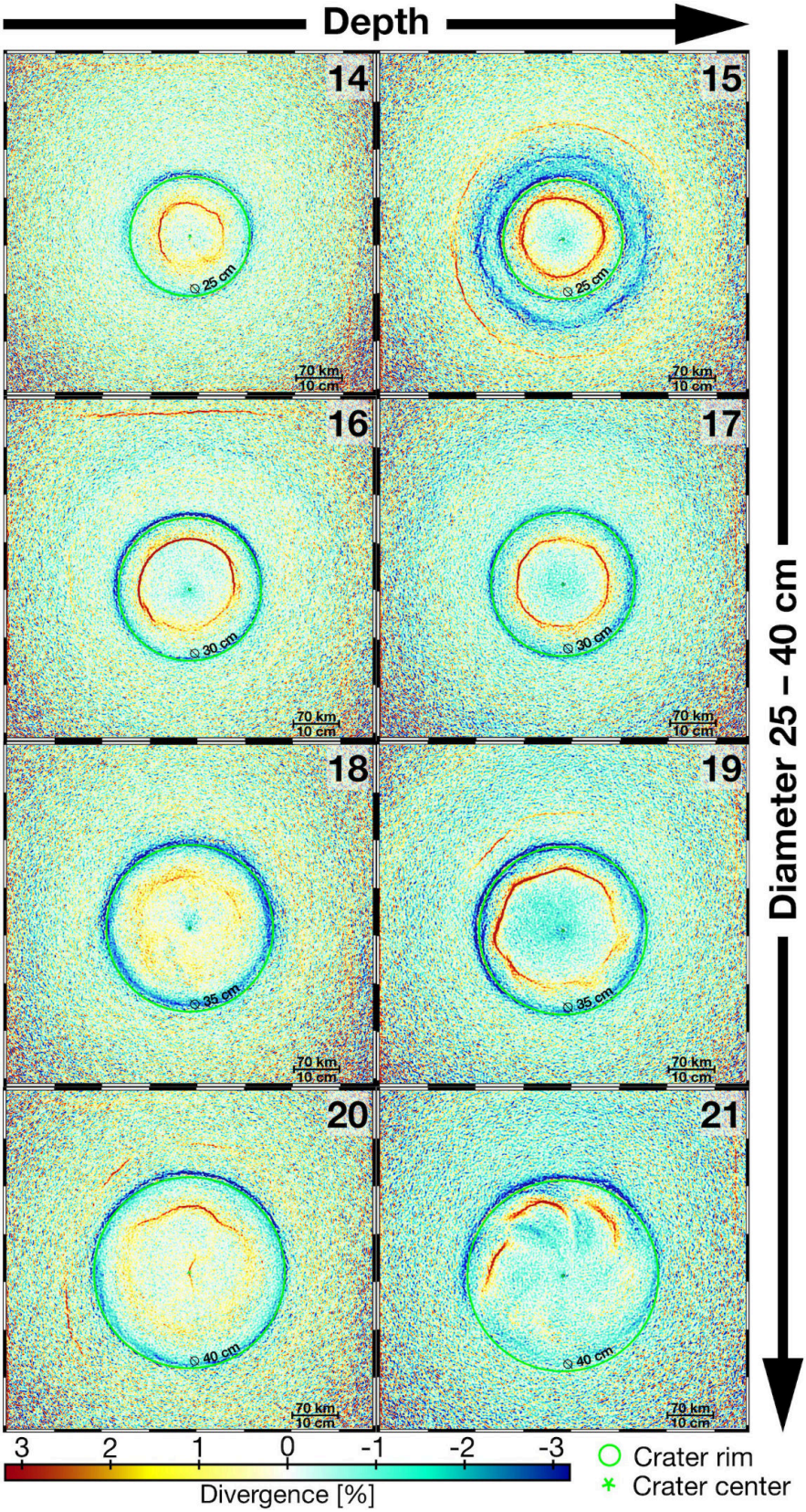

Figure S4.2: Panels showing cumulative divergence of set 2 experiments with convergent particle motion (blue), denoted as negative values, and divergent particle motion (red), indicated as positive values. Experiment numbers are indicated in the top right of each panel. Panels of experiments are arranged with regard to initial depths (rows) and diameters (columns) of craters.

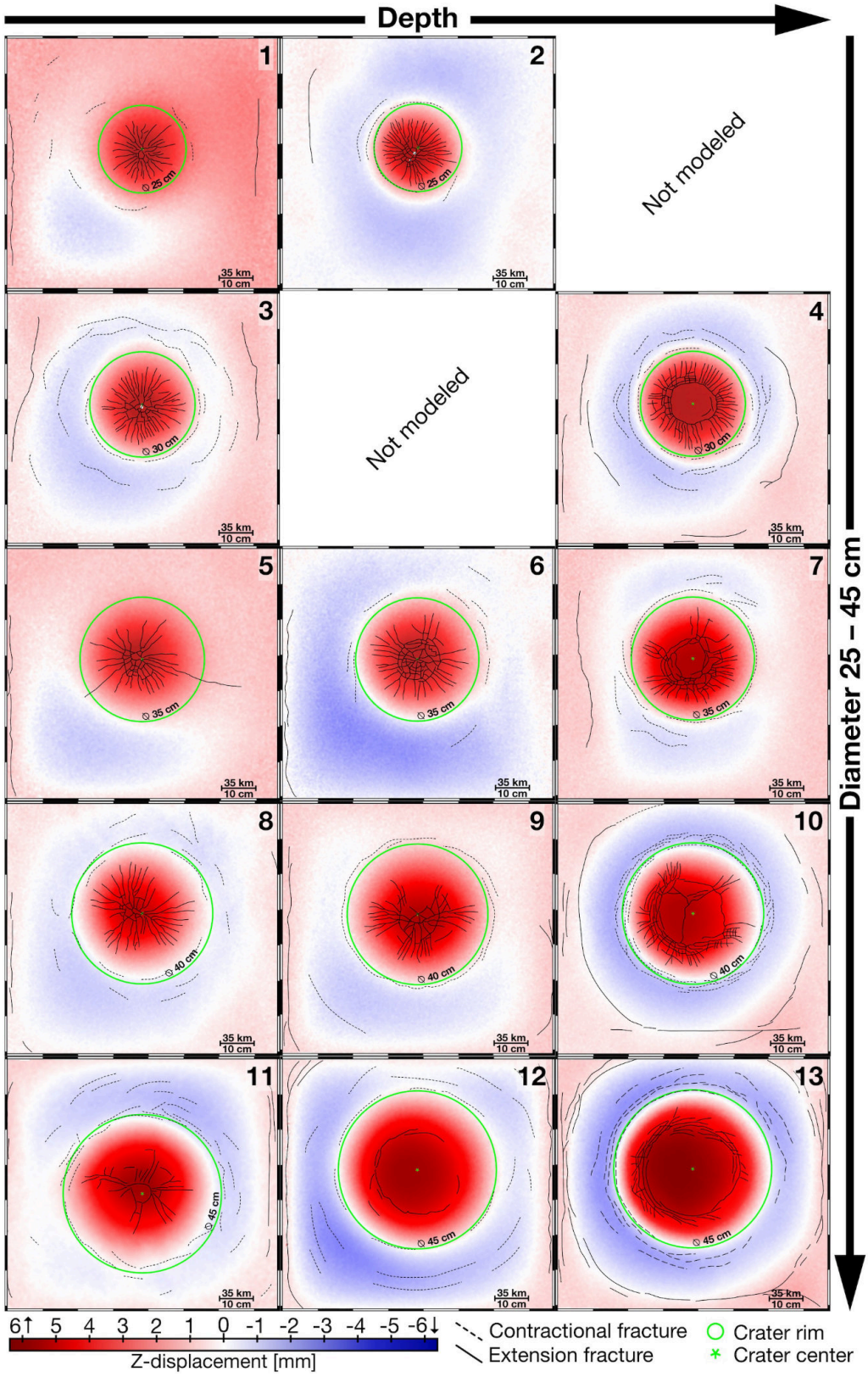

Figure S4.3: Panels showing cumulative surface Z-displacements of set 1 experiments, with particle uplift (red), denoted as positive values, and particle subsidence indicated as negative values (blue). Values indicate deviation from initial topography. Experiment numbers are indicated in the top right of each panel. Images of experiments are arranged by initial depths (rows) and diameters (columns) of craters. Solid and stippled lines indicate respectively traces of extension fractures and reverse faults.

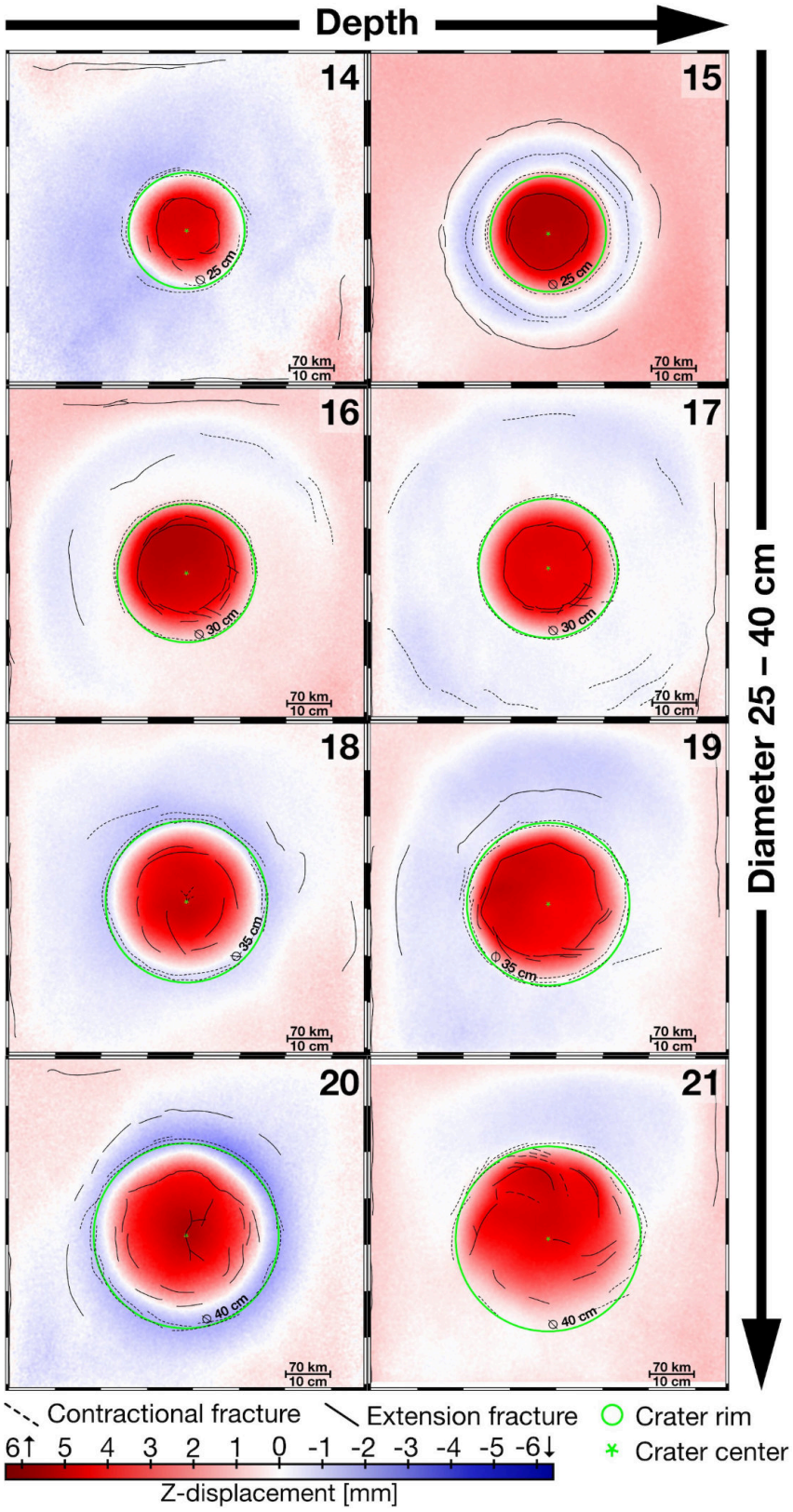

Figure S4.4: Panels showing cumulative surface Z-displacements of set 2 experiments, with particle uplift (red), denoted as positive values, and particle subsidence indicated as negative values (blue). Values indicate deviation from initial topography. Experiment numbers are indicated in the top right of each panel. Images of experiments are arranged by initial depths (rows) and diameters (columns) of craters. Solid and stippled lines indicate respectively traces of extension fractures and reverse faults.

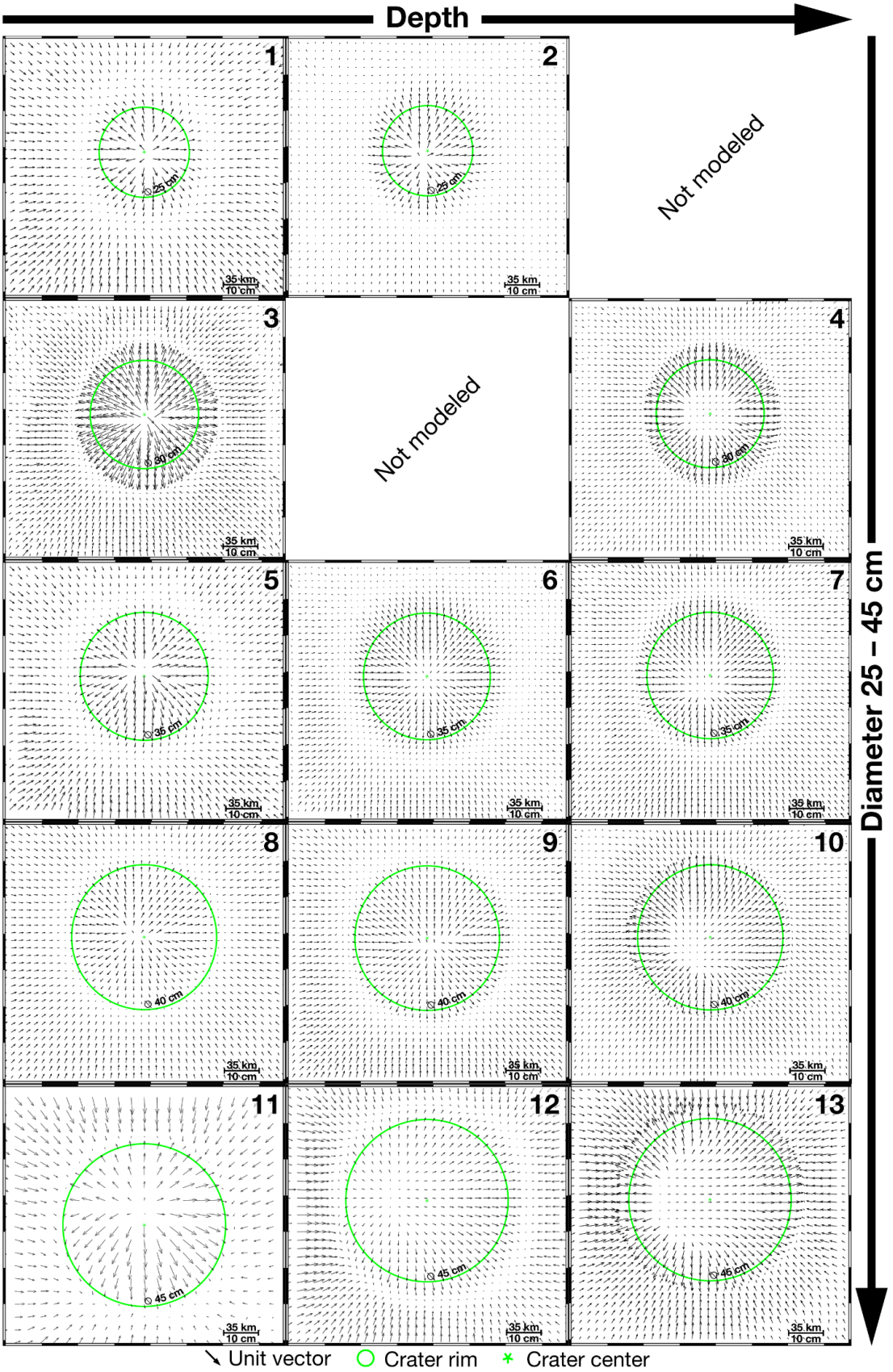

Figure S4.5: Panels showing cumulative horizontal displacement vector fields of set 1 experiments. Vector lengths are not to scale. Experiment numbers are indicated in the top right of each panel. Images of experiments are arranged by initial depths (rows) and diameters (columns) of craters.

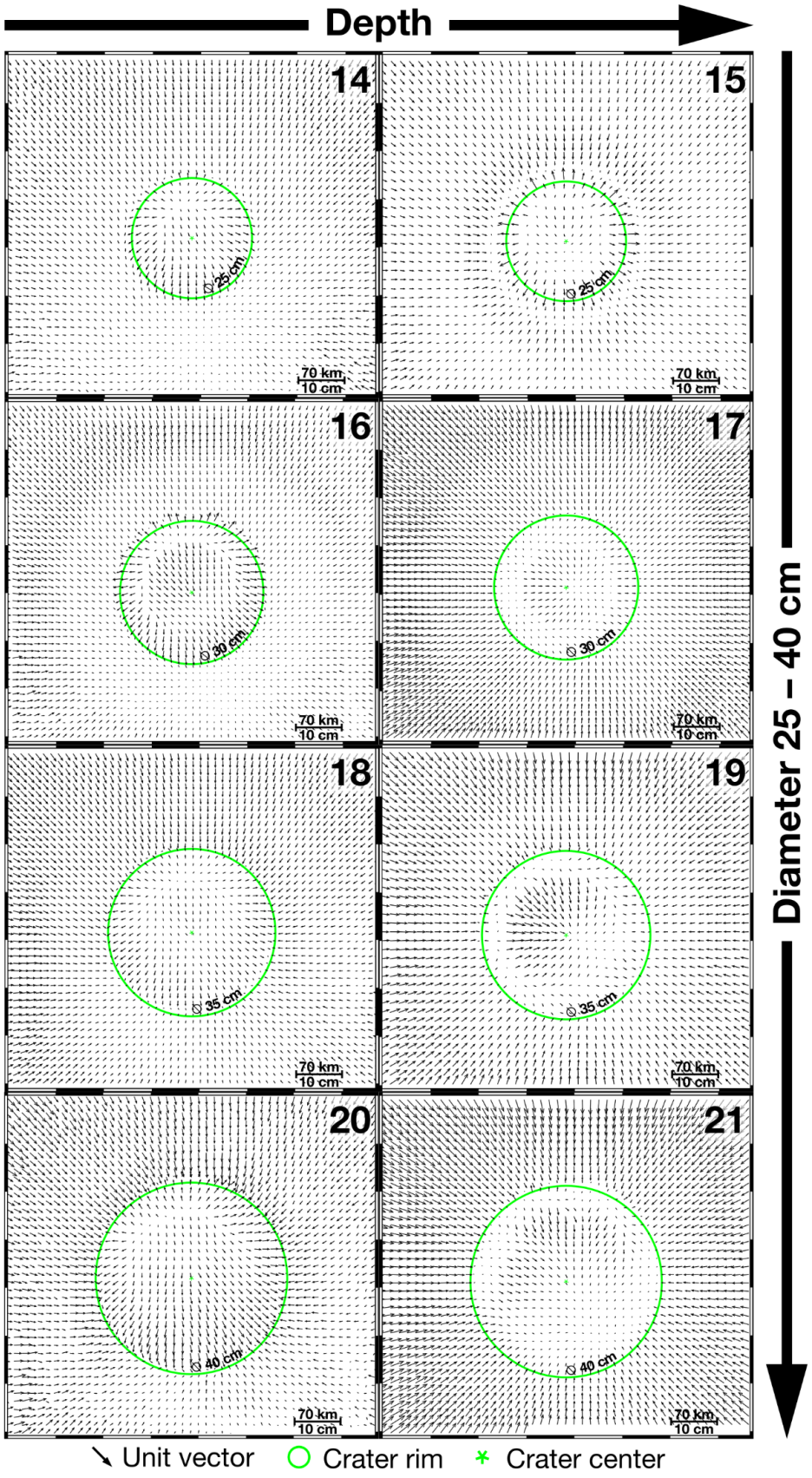

Figure S4.6: Panels showing cumulative horizontal displacement vector fields of set 2 experiments. Vector lengths are not to scale. Experiment numbers are indicated in the top right of each panel. Images of experiments are arranged by initial depths (rows) and diameters (columns) of craters.

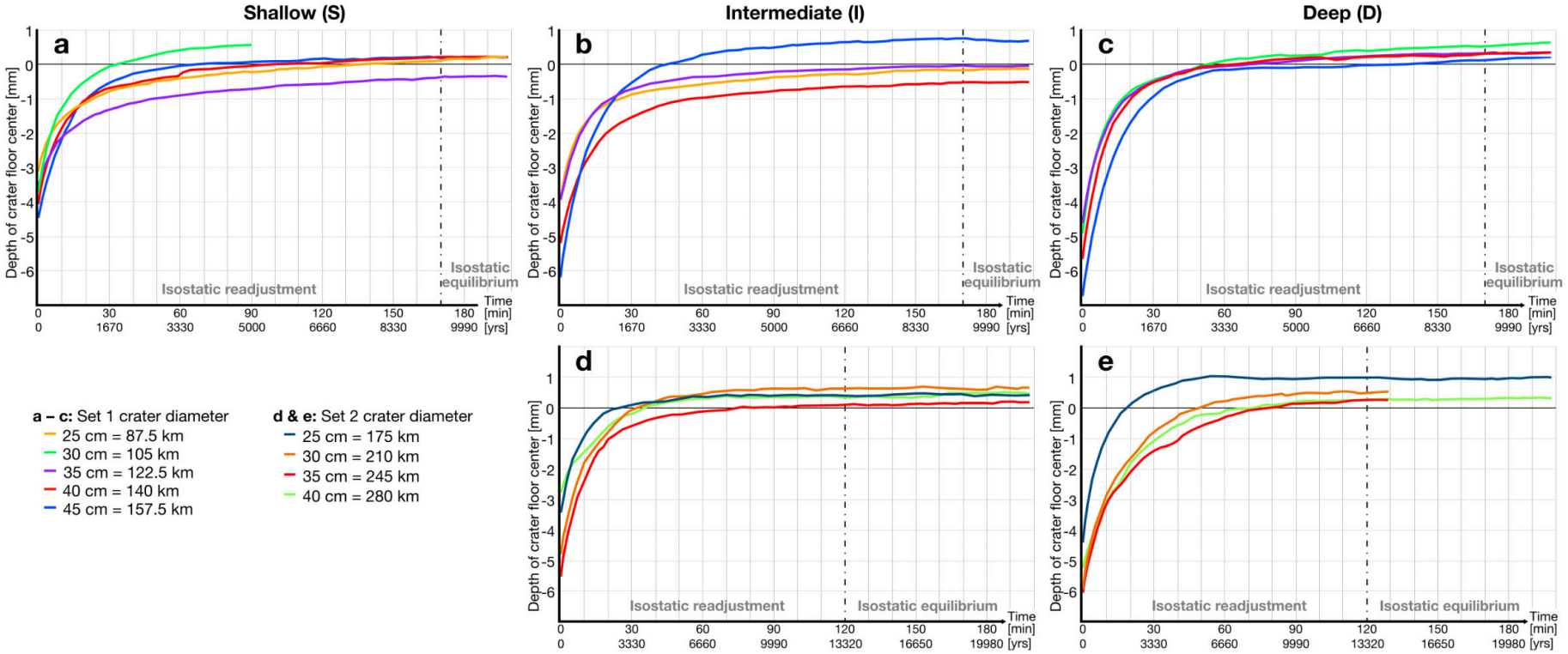

Figure S4.7: Diagrams displaying the magnitude and rate of floor uplift at model crater centres. Colors indicate the specific diameters of modelled craters in nature. The initial depths of each crater are indicated by different line styles of the curves. (a) Experiments of set 1 with shallow initial floors. (b) Experiments of set 1 with intermediate initial floors. (c) Experiments of set 1 with deep initial floors. (d) Experiments of set 2 with intermediate initial floors. (e) Experiments of set 2 with deep initial floors.

Versicherung an Eides statt
Affirmation on oath

Hiermit versichere ich an Eides statt, dass ich die vorliegende Dissertation mit dem Titel: „*Processes of long-term crater modification inferred from scaled analogue experiments*“ selbstständig verfasst und keine anderen als die angegebenen Hilfsmittel – insbesondere keine im Quellenverzeichnis nicht benannten Internetquellen – benutzt habe. Alle Stellen, die wörtlich oder sinngemäß aus Veröffentlichungen entnommen wurden, sind als solche kenntlich gemacht. Ich versichere weiterhin, dass das gebundene Exemplar der Dissertation und das in elektronischer Form eingereichte Dissertationsexemplar und das bei der Fakultät zur Archivierung eingereichte gedruckte gebundene Exemplar der Dissertationsschrift identisch sind.

I hereby declare an oath that I have written the present dissertation on my own with the title: "*Processes of long-term crater modification inferred from scaled analogue experiments*" and have not used other than the acknowledge resources and aids. All passages taken literally or analogously from other publications are identified as such. I further declare declare that the bound copy of the dissertation and the dissertation submitted in electronic form and the printed bound copy of the dissertation submitted to the faculty for archiving are identical.

Hamburg, 28.01.2024

Ort, Datum Unterschrift/signature

Additional contributions during the PhD period:

Colour theme of this thesis:

Made on a Mac